

INIS-BE--0001



BE970001

BE970001



Conformal Radiotherapy : Physics, Treatment Planning and Verification

Proceedings book

*11th Annual Symposium of the
Belgian Hospital Physicist Association*



This year, the 11th Annual Symposium of the Belgian Hospital Physicist Association is organised by the Department of Radiotherapy and Nuclear Medicine of the University of Gent. The central theme of the Symposium is conformal radiotherapy.

The goal of conformal radiotherapy is to establish a dose distribution that conforms tightly to the target volume and to limit radiation to all other normal tissues. The driving force is the insight that conformal radiotherapy - for a number of common tumours - significantly improves both local control and palliation. It has been argued that improved local control will increase survival. It is beyond doubt that better palliation results in a higher quality of life.

Although the idea of conformal external radiotherapy is not new at all, it was only in the advent of the recent technologies that megavoltage X-ray conformal therapy became feasible. Present-day linear accelerators allow fully computerised control of the orientation and geometry of the beam. Sophisticated imaging techniques supply 3-dimensional anatomical and functional data. The resulting images permit the reconstruction of the patient in the virtual world created by the treatment planning software. Current high-performance and reasonably priced workstations and computer methods allow to fix the numerous degrees of freedom in an optimum way. However, the practicable combination of the above methods is still a scientific challenge. In addition, the technological and dosimetric issues regarding dynamic conformal therapy have not been addressed thoroughly yet.

The symposium is intended to provide a multidisciplinary forum for scientific exchange and to optimise interdisciplinary co-operation between physicists, engineers and physicians. After browsing through this Proceedings Book, I obtained two impressions. The first being that the treatment of a patient with radiation is evolving to a chain of activities of which the final quality is determined by the most weak link. The second feeling is that the steadily growing role of physics in this chain is being fully recognised.

The layout of this Proceedings Book has been divided into two parts. The first part contains the abstracts of the invited lectures, proffered papers and poster presentations. The second part contains the corresponding full papers that were received before November 30.

The invited lectures cover the domains of multileaf collimation, 3-dimensional imaging, clinical execution and quality assurance. A total of 39 abstracts have been accepted by the scientific committee. The scientific level of both oral and poster presentations is judged to be high. An overview of all the poster presentations is given by three rapporteurs in the poster session.

I would like to thank all the participants, coming from 11 nations, for their enthusiasm and the 26 exhibitors for their generous support. A list of all participants is added in this Proceedings Book. I finally wish to recognise the help from the organising committee. In particular, I would like to thank Ludwig Fortan.

Carlos De Wagter,

Gent, December 8, 1995

11th Annual Symposium of the Belgian Hospital Physicist Association

Location :

Aula of the University of Gent
Voldersstraat 9
9000 Gent, BELGIUM

Time :

Friday, December 8 and Saturday, December 9, 1995

Organising committee :

C. De Wagter (President)
E. Achten
C. Colle
Y. De Deene
W. De Neve
J. De Poorter
G. De Smet
R. Dierckx
L. Fortan
M. Mareel
J. Schelfhout
L. Vakaet
B. Van Duyse
W. Verweire

Scientific committee :

C. De Wagter
P. Merlo
B. Schaeken
R. Van Loon
S. Vynckier

Guest speakers :

P. Aletti, Centre Alexis Vautrin, Vandœuvre-Les-Nancy, France
W. De Neve, University Hospital, Gent, Belgium
M. van Herk, The Netherlands Cancer Institute, Amsterdam, The Netherlands
J. Wong, W. Beaumont Hospital, Royal Oak, MI, U.S.A.

We like to thank the following companies / institutions for their support :

A2J

Alphatron Electronic Parts bv

Best Planning Systems bv

Bogman Medical Equipment

Canberra Packard Benelux

Chartex - Cerro Metal Products

CURAD Radiation Cure and Protection

Digital Equipment

Dutoit Medical

EG & G, Ortec

General Electric Medical Systems

Helax

Kodak

Landré - Intechmij, Div. Landré & Glinderman

MCR

Novolab bvba

Nucletron

Philips Medical Systems Division

Precision Therapy Europe

Röntgen Technische Dienst bv

Sercolab

Siemens Medical Engineering

Sinmed bv

Theratronics - CIS BIO

Universiteit Gent

Zambon

Zeneca

Exhibition Booth :

J, Peristylum

M, Peristylum

H, Peristylum

K, Peristylum

V, Entrance Hall

EE, Peristylum

Q, Left Balcony 2nd Floor

F, Peristylum

L, Peristylum

G, Peristylum

C, Peristylum

U, 2nd floor

T, Right Balcony 2nd Floor

I, Peristylum

P, Entrance Hall

S, Right Balcony 2nd Floor

A, Peristylum

O, Entrance Hall

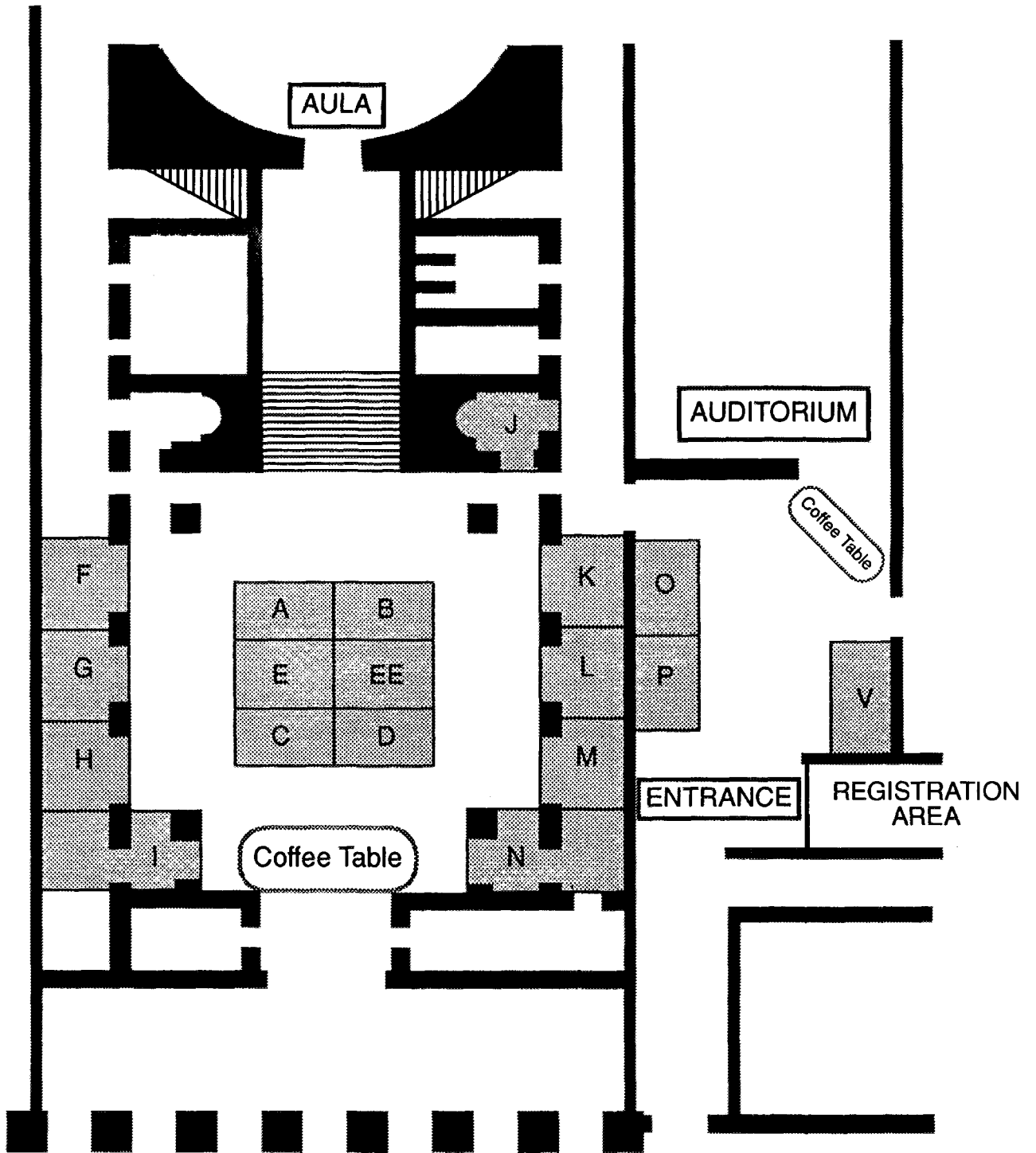
B, Peristylum

R, Left Balcony 2nd Floor

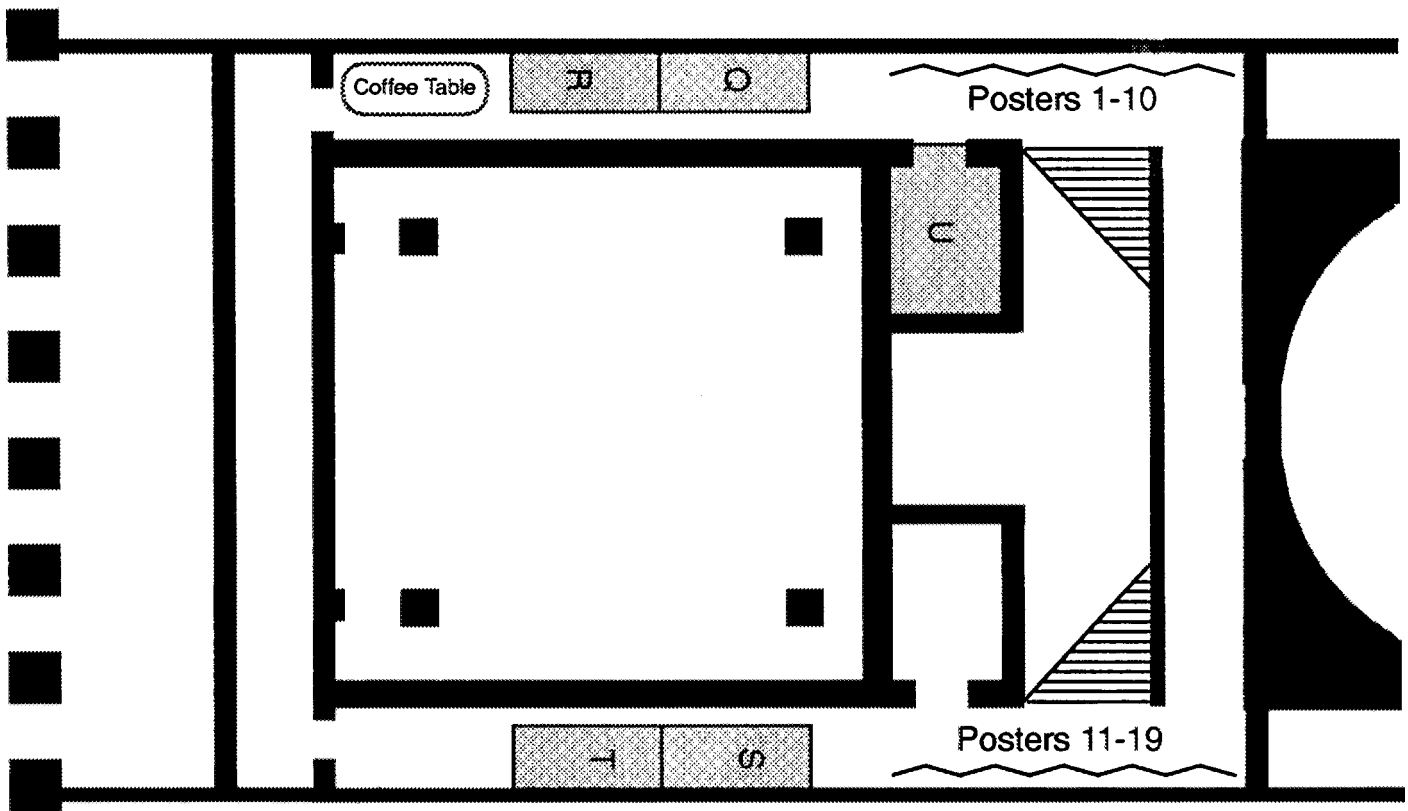
D, Peristylum

E, Peristylum

FLOOR PLAN : FIRST FLOOR



FLOOR PLAN : SECOND FLOOR



v

NEXT PAGE(S)
left BLANK

Program :

Friday, 8 December 1995

12:30 Registration desk + Opening of Technical Exhibition
13:30 - 14:00 Welcome by : J. Willems, Rector Universiteit Gent
R. Van Loon, President Belgian Hospital Physicist Association
C. De Wagter, President Organizing Committee

14:00 - 15:35 Session 1 : Conformal Radiotherapy and Multileaf Collimation

Moderators : B. Proimos and W. De Neve

AULA

- 14:00 L 1.1 Invited lecture :
Wong, J.
Delivery of intensity modulated beams using dynamic multileaf collimation.
- 14:45 L 1.2 Knöös, T., Nilsson, P., and Ask, A.
Conformal three dimensional radiotherapy treatment planning in Lund.
- 14:57 L 1.3 Briot, E., and Julia, F.
Penumbra characteristics of square photon beams delimited by a GEMS collimator.
- 15:09 L 1.4 Ginestet, C., Lafay, E., Malet, C., Mombard, C., Desfarges, Y., and Dupin, G.
Evaluation of the penumbra of a multileaf collimator.
- 15:23 L 1.5 Van Duyse, B., Colle, C., De Wagter, C., and De Neve, W.
Modification of a 3D-planning system for use with a multileaf collimator.
-

15:35 - 16:15 Coffee break + Technical Exhibition

16:15 - 17:24 Session 2 : Three-dimensional Imaging

Moderators : P. Aletti and B. Schaeken

AULA

- 16:15 L 2.1 Invited lecture :
van Herk, M., Gilhuijs, K., Kooy, H., Kwa, S., Lebesque, J., Muller, S., de Munck, J.,
and Touw, A.
Applications of 3D-image registration in conformal radiotherapy.
- 17:00 L 2.2 Rasch, C., Keus, R., Touw, A., Lebesque, J., and van Herk, M.
CT and MRI matching for radiotherapy planning in head and neck cancer.
- 17:12 L 2.3 Bosmans, H., Verbeeck, R., Vandermeulen, D., Suetens, P., Wilms, G., Maaly, M.,
Marchal, G., and Baert, A.L.
Validation of new 3D post processing algorithm for improved maximum intensity
projections of MR angiography acquisitions in the brain.
-

17:24 - 19:00 Technical Exhibition

19:30 **Congress Dinner in Restaurant "De Kleine Brug",
Sint-Pietersnieuwstraat 45, Gent.**

Saturday, 9 December 1995, morning

08:30 - 09:39 Session 3 : Treatment Simulation, Planning and Optimization

Moderators : J. Wong and C. De Wagter

AUDITORIUM

- 08:30 L 3.1 Invited lecture :
De Neve, W.
Conformal radiotherapy : treatment planning and clinical applications.
- 09:15 L 3.2 Schelfhout, J., Derycke, S., Fortan, L., Van Duyse, B., Colle, C., De Wagter, C., and De Neve, W.
Planning and delivering high doses to targets surrounding the spinal cord at the lower neck and upper mediastinal levels : static beam-segmentation technique executed by a multileaf collimator.
- 09:27 L 3.3 Colle, C., Van den Berge, D., De Wagter, C., Fortan, L., Van Duyse, B., and De Neve, W.
Optimization of radiotherapy to target volumes with concave outlines : target-dose homogeneity and selective sparing of critical structures by constrained matrix inversion.

09:39 - 09:57 Break - Changing Aula Rooms

09:57 - 10:45 Session 3bis : Treatment Simulation, Planning and Optimization

Moderators : J. Wong and C. De Wagter

AULA

- 09:57 L 3.4 Nowak, P.J.C.M., van Dieren, E.B., van Sörnsen de Koste, J.R., van Est, H., Heijmen, B.J.M., and Levendag, P.C.
A nationwide Dutch study regarding treatment portals for elective neck irradiation.
- 10:09 L 3.5 Haest, K., Vanregemorter, J., and Van Dam, J.
Virtual simulation of radiotherapeutic treatment of the prostate.
- 10:21 L 3.6 Dessy, E., Hoornaert, M.T., and Malchair, F.
Tomodensitometry images : integration in radiotherapy.
- 10:33 L 3.7 Van den Heuvel, E., De Beukeleer, M., Nys, F., Bijdekerke, P., Robberechts, M., and Van Cauwenbergh, R.
Immobilization for the radiation therapy treatment of the pelvic region.

10:45 - 11:15 Coffee break + Technical Exhibition

11:15 - 12:15 Session 4 : Poster Session

AULA

- 11:15 Poster introduction by 3 rapporteurs;
Presentation of the Award for the best poster.
- 11:45 Individual poster discussions in the poster hall.

12:15 - 13:30 Luncheon at Exhibition Hall

Saturday, 9 December 1995, afternoon

13:30 - 15:03 Session 5 : Quality Assurance

Moderators : M. van Herk and R. Van Loon

AULA

- 13:30 L 5.1 Invited lecture :
Aletti, P.
Conformal radiotherapy using multileaf collimation : quality assurance and *in vivo* dosimetry.
- 14:15 L 5.2 Dirkx, M.L.P., Kroonwijk, M., de Boer, J.C.J., and Heijmen, B.J.M.
Application of an EPID for fast daily *dosimetric* quality control of a full computer-controlled treatment unit.
- 14:27 L 5.3 Kroes, A.P.G., Bruinvis, I.A.D., Lanson, J.H., and Uiterwaal, G.J.
Quality assurance of a conformal treatment technique.
- 14:39 L 5.4 De Ost, B., Bellekens, L., Cardoen, R., Goossens, H., Haest, K., Mertens, N., Pieters, D., Schaeken, B., and Vanregemorter, J.
KWARTA (KWaliteitsverzekering in de RadioTherapiecentra van de provincie Antwerpen) : Quality control of the contact therapy machine and treatment planning system.
- 14:51 L 5.5 Infantino, S., and Malchair, F.
QC in MRI : useful or superfluous ?

15:03 - 15:35 Coffee break + Technical Exhibition

15:35 - 16:23 Session 6 : Dosimetry Topics

Moderators : S. Vynckier and B. Van Duyse

AULA

- 15:35 L 6.1 De Poorter, J., De Wagter, C., and De Deene, Y.
In vivo noninvasive thermometry for hyperthermia applications using the MRI-based proton-resonance-frequency method.
- 15:47 L 6.2 Baas, H.W., Davelaar, J.J., Broerse, J.J., and Noordijk, E.M.
Dosimetry of secondary tumors after radiotherapy.
- 15:59 L 6.3 Rebigan, F.
New relations in basic dosimetry.
- 16:11 L 6.4 Schaeken, B., and Bressers, E.
How to calibrate Grenz-beams in clinical practice ?

16:23 - 16:45 Session 7 : Closing Lecture

AULA

- 16:23 L 7.1 Proimos, B.S.
Conformal radiotherapy made easy through gravity oriented absorbers.

16:45 - 16:50 Closure of the Symposium by C. De Wagter.

- P 1 Transmission dosimetry with a liquid-filled electronic portal imaging device.
Boellaard, R., van Herk, M., and Mijnheer, B.J.
- P 2 *In vivo* dosimetry with L- α -alanine.
Boey, R., Van Der Velden, K., and Schaecken, B.
- P 3 *In vivo* dosimetry using thermoluminescence dosimeters in brachytherapy with a 370 GBq ^{192}Ir source.
Cuepers, S.
- P 4 Film dosimetry in conformal radiotherapy.
Danciu, C., and Proimos, B.S.
- P 5 Three dimensional gel dosimetry by use of nuclear magnetic resonance imaging (MRI).
De Deene, Y., De Wagter, C., De Poorter, J., Van Duyse, B., Achten, E., and De Neve, W.
- P 6 Limits of dose escalation in lung cancer : a dose-volume histogram analysis comparing coplanar and non-coplanar techniques.
Derycke, S., Van Duyse, B., Schelfhout, J., and De Neve, W.
- P 7 Spectrometric methods used in the calibration of radiodiagnostic measuring instruments.
de Vries, W.
- P 8 *In vivo* dosimetry of high-dose fractionated irradiation in an experimental set-up with rats.
Fortan, L., Van Hecke, H., Van Duyse, B., Pattyn, P., De Meerleer, G., Van Rentergem, K., and De Neve, W.
- P 9 *In vivo* dosimetry in radiotherapy : a comparison of the response of semiconductor and thermoluminescence (TLD700) dosimeters.
Greffe, J.L., Loncol, Th., Vanneste, F., Octave-Prignot, M., Denis, J.M., de Patoul, N., and Vynckier, S.
- P 10 Evaluation of the Vidar's VXR-12 digitizer performances for film dosimetry of beams delimited by multileaf collimation.
Julia, E., and Briot, E.
- P 11 Evaluation of ion chamber dependent correction factors for ionisation chamber dosimetry in proton beams using a Monte Carlo method.
Palmans, H., and Verhaegen, F.
- P 12 Human calf muscular metabolism study with a home-made ergometer using ^{31}P NMR spectroscopy.
Peynsaert, J., Achten, E., Claeys, E., and Rousseaux, M.
- P 13 Daily check of the electron beams with a diode system.
Pilette, P.
- P 14 Quality assurance and accuracy in Co-60 radiotherapy.
Scarlat, E., and Rebigan, F.
- P 15 Treatment planning in radiosurgery : parallel Monte Carlo simulation software.
Scielzo, G., Grillo Ruggieri, F., Modesti, M., Felici, R., and Surridge, M.
- P 16 Pulsed dose rate brachytherapy (PDR) : an analysis of the technique at 2 years.
Thienpont, M., van Eijkeren, M., Van Hecke, H., Boterberg, T., and De Neve W.
- P 17 Three dimensional conformal radiation therapy may improve the therapeutic ratio of radiation therapy after pneumonectomy for lung cancer.
Trouette, R., Causse, N., Elkhadri, M., Maire, J.Ph., Houlard, J.P., Recaldini, L., and Demeaux, H.
- P 18 Measurements of the primary and scatter dose in high energy photon beams.
van der Linden, P.M., Tiourina, T.B., and Dries, W.
- P 19 Compton scatter correction for planar scintigraphic imaging.
Van Steelandt, E., Dobbeleir, A., and Vanregemorter, J.

List with Full Papers :

Conformal three dimensional radiotherapy treatment planning in Lund. <i>Knöös, I., Nilsson, P., and Ask, A.</i>	25
Evaluation of the penumbra of a multileaf collimator. <i>Lafay, F., Malet, C., Mombard, C., Ginestet, C., Desfarges, Y., and Dupin, G.</i>	31
Modification of a 3D-planning system for use with a multileaf collimator. <i>Van Duyse, B., Colle, C., De Wagter, C., and De Neve, W.</i>	39
Applications of three-dimensional image correlation in conformal radiotherapy. <i>van Herk, M., Gilhuijs, K.G.A., Kooy, H., Kwa, S., Lebesque, J.V., Muller, S., de Munck, J.C., and Touw, A.</i>	47
Irradiation of target volumes with concave outlines. <i>De Neve, W., Fortan, L., Derycke, S., Van Duyse, B., and De Wagter, C.</i>	63
An analytic solution for calculating the beam intensity profiles useful to irradiate volumes with bi-concave outlines. <i>De Neve, W., Derycke, S., and De Wagter, C.</i>	75
Planning and delivering high doses to targets surrounding the spinal cord at the lower neck and upper mediastinal levels : static beam-segmentation technique executed by a multileaf collimator. <i>Schelfhout, J., Derycke, S., Fortan, L., Van Duyse, B., Colle, C., De Wagter, C., and De Neve, W.</i>	83
Optimization of radiotherapy to target volumes with concave outlines : target-dose homogeneization and selective sparing of critical structures by constrained matrix inversion. <i>Colle, C., Van den Berge, D., De Wagter, C., Fortan, L., Van Duyse, B., and De Neve, W.</i>	87
Tomodensitometry images : integration in radiotherapy. <i>Dessy, E., Hoornaert, M.T., and Malchair, F.</i>	93
Impact of immobilization procedures on the efficiency of radiation therapy treatment in the pelvic region. <i>Van den Heuvel, F., De Beukeleer, M., Nys, F., Bijdekerke, P., Robberechts, M., and Van Cauwenbergh, R.</i>	107
Application of an EPID for fast daily <i>dosimetric</i> quality control of a full computer-controlled dual gantry treatment unit. <i>Dirkx, M.L.P., Kroonwijk, M., de Boer, J.C.J., and Heijmen, B.J.M.</i>	115
QC in MRI : useful or superfluous ? <i>Infantino, S., and Malchair, F.</i>	119
Noninvasive MRI thermometry with the proton resonance frequency (PRF) method : <i>in vivo</i> results in human muscle. <i>De Poorter, J., De Wagter, C., De Deene, Y., Thomsen, C., Ståhlberg, F., and Achten, E.</i>	129
Dosimetry at the location of secondary tumours after radiotherapy. <i>Baas, H.W., Davelaar, J., Broerse, J.J., and Noordijk, E.M.</i>	137
Conformal radiotherapy made easy through gravity oriented absorbers. <i>Proimos, B.S.</i>	143

<i>In vivo</i> dosimetry with L- α -alanine. <u>Boey, R., Van Der Velden, K., Janssens, H., and Schaeken, B.</u>	163
<i>In vivo</i> dosimetry using thermoluminescence dosimeters during brachytherapy with a 370 GBq Ir ¹⁹² source. <u>Cuepers, S., Piessens, M., Verbeke, L., and Roelstraete, A.</u>	173
Film dosimetry in conformal radiotherapy. <u>Danciu, C. and Proimos, B.S.</u>	179
Three dimensional gel dosimetry by use of nuclear magnetic resonance imaging (MRI). <u>De Deene, Y., De Wagter, C., De Poorter, J., Van Duyse, B., De Neve, W., Van Hecke, H., Ravier, A., and Achten, E.</u>	193
Limits of dose escalation in lung cancer : a dose-volume histogram analysis comparing coplanar and non-coplanar techniques. <u>Derycke, S., Van Duyse, B., Schelfhout, J., and De Neve, W.</u>	209
Spectrometric methods used in the calibration of radiodiagnostic measuring instruments. <u>de Vries, W.</u>	217
Treatment planning in radiosurgery : parallel Monte Carlo simulation software. <u>Scielzo, G., Grillo Ruggieri, F., Modesti, M., Felici, R., and Surridge, M.</u>	223
Pulsed dose rate brachytherapy (PDR) : an analysis of the technique at 2 years. <u>Thienpont, M., van Eijkeren, M., Van Hecke, H., Boterberg, T., and De Neve W.</u>	227
Three dimensional conformal radiation therapy may improve the therapeutic ratio of radiation therapy after pneumonectomy for lung cancer. <u>Trouette, R., Causse, N., El Khadri, M., Caudry, M., Maire, J.Ph., Houlard, J.P., Récaldini, L., and Demeaux, H.</u>	231
Implementation of intensity modulation with dynamic multileaf collimation. <u>Wong, J.W., Yu, C., and Jaffray, D.</u>	233
Conformal radiotherapy using multileaf collimation : quality assurance and <i>in vivo</i> dosimetry <u>Aletti, P.</u>	243

Delivery of intensity modulated beams using dynamic multileaf collimation.

J. Wong

W. Beaumont Hospital, Royal Oak, MI, U.S.A.

NO ABSTRACT SUBMITTED.

See Full Paper, pp. 233 - 242

Conformal Three Dimensional Radiotherapy Treatment Planning in Lund

Tommy Knöös¹, Per Nilsson¹, Anders Ask², ¹Dept Radiation Physics and Dept ²Oncology, University Hospital in Lund. S-221 85 Lund, SWEDEN

The use of conformal therapy is based on 3D treatment planning as well as methods and routines for 3D patient mapping, 3D virtual simulation etc. This presentation will discuss the management of patients at our department using state of the art equipment in the treatment chain. The Radiotherapy Department at the University Hospital in Lund treats patients from the Southern region in Sweden with a population of about 1.5 million people within a distance of 250 km. About 2100 new patients are annually treated with external radiotherapy on seven linear accelerators. Three of the accelerators have dual photon energies and electron treatment facilities. A multi-leaf collimator as well as an electronic portal imaging device are available on one machine. Two simulators and an in-house CT-scanner are used for treatment planning. During 1988 to 1992 Scandiplan (Umplan) was used. Since 1992, the treatment planning system is TMS (HELAX AB, Sweden) which is based on the pencil beam algorithm of Ahnesjö. The calculations use patient modulated accelerator specific energy fluence spectra which are compiled with pencil beams from Monte Carlo generated energy absorption kernels. Heterogeneity corrections are performed with results close to conventional algorithms. Irregular fields, either from standard or individual blocks and from multi-leaf collimators are handled by the treatment planning system. The field shape is determined conveniently using the beam's eye view, BEV. The final field shape is exported electronically to either the block cutting machine or the MLC control computer. All patient fields are checked against the BEV during simulation using manual methods. Treatment verification is performed by portal films and in vivo dosimetry with silicon diodes or TL-dosimetry. Today approximately 4400 patients have received a highly individualised 3D conformal treatment. This report will present the 3D radiotherapy process in Lund from a physicist's view.

**PENUMBRA CHARACTERISTICS OF SQUARE PHOTON BEAMS DELIMITED
BY A GEMS MULTILEAF COLLIMATOR**



BE9700004

E. BRIOT, F. JULIA

Physics Department, Institut Gustave-Roussy, Villejuif, France.

BE9700004

This MLC has been designed to replace directly the standard collimator of a SATURNE IV Series linac. It consists of 2 x 32 tungsten leaves and one set of upper block jaws.

Isodose curves and dose profiles were measured for symmetric fields at the depth of the maximum and at reference depths for 6 MV, 10 MV, 18 MV photon beams.

The penumbra (80 % - 20 %) corresponding to the face and the side of the leaves are compared with the standard collimators.

Along the X direction, the field delimitation is performed primarily with the leaves which are continuously variable in position. Along the Y direction, the field is initially approximated by the closure of opposite leaf pairs ; then the Y upper jaws produce the exact size of the required field.

As the leaves move linearly the penumbra (80 % - 20 %) corresponding to the leaf ends is minimized and held constant at all positions by curvature of their faces.

Penumbra obtained with the superposition of leaves and Y jaws depend on their relative position. The penumbra is minimum when the leaf side and the Y jaw edge coincide and the comparison of the measurement values with the conventional collimator shows that the differences are within 1 mm. When the leaves delineating the field are not entirely covered by the Y block upper jaws, the penumbra increases, and at the junction of the opposing leaves, a width increase up to 3.5 mm can be observed.

SEE P. 31-37

86/178
E.B.
1 of 3

Evaluation of the penumbra of a multileaf collim

C. GINESTET*, E. LAFAY*, C. MALET*, C. M
Y. DESFARGES**, G. DUPIN**

* Radiation Physics department - Centre Léon B
** Philips Medical Systems - LYON - FRANCE

E.

(Supported by a grant of the "ligue de l'Ain")

Since January 1995, we use a new Philips SL20 linear accelerator which is connected to a multileaf collimator. Computer-controlled multileaf collimators open up the opportunity to practice conformal radiotherapy. Its aim is to adjust as well as possible the Planning Target Volume (P.T.V) to the effective treated volume with an homogeneous dose distribution in the PTV, and to protect healthy tissues and delicate organs.

This is already possible with a multileaf collimator by increasing the number of complex fields with different incidences during a same session. Moreover, the "Beam's Eye View" (BEV) function of the three-dimensional treatment planning system allows to define the shape of complex fields. But if we want the beam to stick exactly to the P.T.V, we have to know precisely the penumbra.

For rectangular fields, the penumbra is defined by the distance between the 80% and 20% isodoses relative to the beam axis. It also seems us interesting to analyse the distances between, respectively, the 95% and 50% isodoses, the 90% and 50% isodoses, the 50% and 20% isodoses relative to the beam axis.

Today, when the leaves are set up automatically from a BEV or a simulation film, the optimization system doesn't take into account the penumbra.

This work is an evaluation of the different penumbras according to their different origins and of the different margins we have to take into account when we realize a treatment planning.

We therefore compared results obtained with different types of measures : several kinds of ionization chamber and several film densitometers.

The result of this work will give us the tool to adjust the reference isodose to the P.T.V, either by integrating this result into the dosimetry softwares, or by taking it into account for drawing the PTV.

SEP P39-41

Modification of a 3D-planning system for use with a multileaf collimator.

Van Duyse, B., Colle, C., De Wagter, C., and De Neve, W.

Department of Radiotherapy, Nuclear Medicine and Experimental Cancerology, University Hospital, Gent, BELGIUM.

Recently, the Philips SL25 linear accelerator of the Radiotherapy Department at the University Hospital of Gent was retrofitted with a multileaf collimator (MLC). To allow treatment planning with the MLC, the currently used GRATIS™ 3D-planning system (developed by G. Sherouse) needed some adaptations. The availability of the C source code of this planning system allowed us to do so.

The Virtual Simulator™ section was extended so that the leaves are graphically set in the Beams Eye View. The leaves can be set manually or automatically, based on a previously defined margin around the target. Once the leaves are set, a data file is created for each beam, containing the leaf settings. This file is finally transferred to the MLC computer over the network or by floppy.

The entire process does not require any manual transfer of leaf settings, not only adding a time-saving but also an error preventing factor to the GRATIS™ 3D-planning system. Measurements to verify the accuracy of the adaptations of the planning system will be presented.

SEP P 47-61

APPLICATIONS OF 3-D IMAGE REGISTRATION IN CONFORMAL RADIOTHERAPY.

M. van Herk, K. Gilhuijs, H. Kooy, S. Kwa, J. Lebesque, S. Muller, J. de Munck and A. Touw

Radiotherapy department, The Netherlands Cancer Institute, Amsterdam, The Netherlands

The development of techniques for the registration of CT, MRI and SPECT creates new possibilities for improved target volume definition and quantitative image analysis. Our technique, based on chamfer matching, is suitable for automatic 3-D matching of CT with CT, CT with MRI, CT with SPECT and MRI with SPECT. The following applications will be discussed: *Target volume definition.* By integrating CT with MRI, the diagnostic qualities of MRI are combined with the geometric accuracy of the planning CT. Significant differences in the delineation of the target volume for brain, head and neck and prostate tumors have been demonstrated when using integrated CT and MRI compared with using CT alone. In addition, integration of the planning CT with pre-operative scans improves knowledge of possible tumor extents. *Quantification of organ motion.* By first matching scans based on the bony anatomy and subsequently matching on an organ of study, relative motion of the organ is quantified accurately. In a study with 42 CT scans of 11 patients, magnitude and causes of prostate motion have been analysed. The most important motion of the prostate is a forward-backward rotation around a point near the apex caused by rectal volume difference. Significant correlations were also found between motion of legs and prostate. *Follow-up studies.* By integrating functional images made before and after radiotherapy with the planning CT, the relation between local change of lung function and delivered dose has been quantified accurately. The technique of chamfer matching is a convenient and more accurate alternative for the use of external markers in a CT/SPECT lung damage study. Also, damage visible in diagnostic scans can be related to radiation dose, thereby improving follow-up diagnostics.

It can be concluded that 3-D image integration plays an important role in assessing and improving the accuracy of radiotherapy and is therefore indispensable for conformal therapy. However, user-friendly implementation of these techniques remains to be done to facilitate clinical application on a large scale.

BE9700008



BE9700008

C.Rasch, R.Keus, A.Touw, J.Lebesque, M.van Herk. Department of Radiotherapy, Netherlands Cancer Institute/Antoni van Leeuwenhoekhuis, Plesmanlaan 121, 1066 CX Amsterdam, The Netherlands

CT and MRI matching for radiotherapy planning in head and neck cancer.



BE9700009

Aim of the study: To evaluate the impact of matched CT and MRI information on target delineation in radiotherapy planning for head and neck tumors.

Material and methods: MRI images of eight patients with head and neck cancer in supine position, not necessarily obtained in radiotherapy treatment position were matched to the CT scans made in radiotherapy position using automatic three-dimensional chamfer-matching of bony structures . Four independent observers delineated the Gross Tumor Volume (GTV) in CT scans and axial and sagittal MR scans. The GTV's were compared, overlapping volumes and non-overlapping volumes between the different datasets and observers were determined.

Results: In all patients a good match of CT and MRI information was accomplished in the head region. The combined information provided a better visualisation of the GTV, oedema and normal tissues compared with CT or MRI alone. Determination of overlapping and non-overlapping volumes proved to be a valuable tool to measure uncertainties in the determination of the GTV.

Conclusions: CT-MRI matching in patients with head and neck tumors is feasible and makes a more accurate irradiation with higher tumor doses and less normal tissue complications possible. Remaining uncertainties in the determination of the GTV can be quantified using the combined information of MRI and CT.

BE9700009

Validation of new 3D post processing algorithm for improved maximum intensity projections of MR angiography acquisitions in the brain

H. Bosmans, R. Verbeek, D. Vandermeulen, P. Suetens, G. Wilms, M. Maaly, G. Marchal, A.L. Baert

Purpose: to validate a new post processing algorithm for improved maximum intensity projections (mip) of intracranial MR angiography acquisitions

Material and methods: The core of the post processing procedure is a new brain segmentation algorithm. Two seed areas, background and brain, are automatically detected. A 3D region grower then grows both regions towards each other and this preferentially towards white regions. In this way, the skin gets included into the final 'background region' whereas cortical blood vessels and all brain tissues are included in the 'brain region'. The latter region is then used for mip. The algorithm runs less than 30min on a full dataset on a Unix workstation.

Images from different acquisition strategies including multiple overlapping thin slab acquisition, magnetization transfer (MT) MRA, Gd-DTPA enhanced MRA, normal and high resolution acquisitions and acquisitions from mid field and high field systems were filtered. A series of contrast enhanced MRA acquisitions obtained with identical parameters was filtered to study the robustness of the filter parameters.

Results: In all cases, only a minimal manual interaction was necessary to segment the brain. The quality of the mip was significantly improved, especially in post Gd-DTPA acquisitions or using MT, due to the absence of high intensity signals of skin, sinuses and eyes that otherwise superimpose on the angiograms.

Conclusion: The filter is a robust technique to improve the quality of MR angiograms.

Conformal radiotherapy : treatment planning and clinical applications.

W. De Neve

University Hospital, Dept. of Radiotherapy and Nuclear Medicine, Gent, BELGIUM.

NO ABSTRACT SUBMITTED.

See Full Papers, pp. 63 - 82

~~SEE P 63-82~~

~~SEE P 83-86~~

Planning and delivering high doses to targets surrounding the spinal cord at the lower neck and upper mediastinal levels : static beam-segmentation technique executed by a multileaf collimator.

Schelfhout, I., Derycke, S., Fortan, L., Van Duyse, B., Colle, C., De Wagter, C., and De Neve, W.

Department of Radiotherapy, Nuclear Medicine and Experimental Cancerology, University Hospital, Gent, BELGIUM.

If a planning target volume of a head and neck cancer extends at a level below the shoulders, a technical challenge arises in limiting the dose at the spinal cord below tolerance. No standard solution allowing the delivery of a homogeneous dose much higher than the tolerance dose of the spinal cord, exists. This problem belongs to a class of problems which involves the design of 3D-conformal dose distributions for concave targets. All the methods using beam intensity modulation involve the use of dedicated planning systems and none of them are easily portable to the general radiotherapy department.

We investigated the possibility to plan and deliver beam intensity modulated radiotherapy using a general purpose 3D-planning system (Sherouse's GRATIS™) and a linear accelerator equipped with a standard multileaf collimator (Philips MLC). During the planning process, dose homogeneization at the target is obtained by calculation of weights, given to beam segments of specific, predetermined geometry. This specific geometry maximises the area of each segment and thus reduces the number of segments. With a virtual patient in supine position, a first planning using a single isocenter, with gantry positions of -60°, -30°, 0°, 30° and 60°, was performed. Medial edges of all segments were located tangential to the spinal cord. The resulting dose distribution allowed to encompass the target by an isodose surface of 66-70 Gy without exceeding spinal cord tolerance but required 42 segments distributed over 5 gantry angles. Therefore we determined by dose-volume histogram analysis if : 1) for some gantry positions, all beam segments could be omitted; 2) at the remaining gantry angles, segments could be omitted; 3) at least 2 segments could be traded off against 1 additional gantry angle. This procedure resulted in a final plan containing 22 segments spread over 8 gantry angles. Preliminary dosimetric results on a RANDO phantom support the robustness of the method. The first clinical applications are planned for November 1995. Although up to 99 beam segments can be programmed on the Philips SL25 linear accelerator, it remained impossible to use these segments synchronized with the MLC. Such a synchronization protocol similar to that used for enabling of the automatic wedge would decrease the number of operator interventions and increase the speed of execution by a factor of more than 2 (beam-off time between consecutive segments would be reduced from 1-2 minutes to 18 seconds). Truly dynamic leaf control would further increase speed of execution since linac on-off would only occur while changing gantry angles. From a clinical viewpoint, the proposed treatment for irradiating lower neck and upper mediastinal targets could be used as a standard against which other solutions might be tested.

Acknowledgements : This work was supported by grants of the "Centrum voor Gezwekziekten, University Gent" and the "Sportvereniging tegen Kanker". The "UZG-project Conformal Radiotherapy" is funded by the "Vereniging voor Kankerbestrijding".



Optimization of radiotherapy to target volumes with concave outlines : target-dose homogenization and selective sparing of critical structures by constrained matrix inversion.

Colle, C. (*), Van den Berge, D. (†), De Wagter, C. (*), Fortan, L. (*), Van Duyse, B. (*), and De Neve, W. (*)

(*) Department of Radiotherapy, UZ-Gent, and (†) Department of Radiotherapy, AZ-VUB, Brussels, BELGIUM.

A class of problems in conformal radiotherapy involves the design of 3D-conformal dose distributions for targets with concave outlines. For these targets, it is impossible to find beam incidences for which the target volume can be isolated from the tissues at risk. Commonly occurring examples are most thyroid cancers and the targets located at the lower neck and upper mediastinal levels related to some head and neck. We recently developed a solution to this problem, using beam intensity modulation executed with a multileaf collimator by applying a static beam-segmentation technique. The method includes the definition of beam incidences and beam segments of specific shape as well as the calculation of segment weights. Tests on Sherouse's GRATIS™ planning system allowed to escalate the dose to these targets to 65 - 70 Gy without exceeding spinal cord tolerance. Further optimization by constrained matrix inversion was investigated to explore the possibility of further dose escalation. The cost function to be minimized $\sum_i (D_i - d_i)^2 + w \sum_j D_j$ consisted of 2 terms;

$\sum_i (D_i - d_i)^2$, where D_i and d_i were the calculated and desired doses at the i -th voxel inside the target; and $w \sum_j D_j$, where D_j

was the calculated dose at the j -th voxel inside the spinal cord and w was an empirically determined weight factor. This weight factor defined the importance of dose to the spinal cord relative to dose homogeneity at the target ($d_i = \text{constant}$). In this model, D_i and D_j were linear combinations of weighted functions of all beams. The partial derivative of each beam's function yields n equations with n (unknown) beam weights, that were determined by constrained matrix inversion, the constraint being zero or positive values for all beam weights. To implement this method, Sherouse's external beam module was modified. For a predefined w value, beam weights were optimized within a few seconds on a DEC alpha 3000. In practice, 5-10 w values had to be tested, making optimization a less-than-five-minute procedure. This optimization procedure allowed further target dose escalation to (theoretically) 120-150 Gy without exceeding spinal cord tolerance.

Acknowledgements : This work is supported by a grant of the "Centrum Gezwelziekten, University Gent"; the "Comprehensive Project Conformal Radiotherapy, UZG" is funded by the "Vereniging voor Kankerbestrijding".

A nationwide Dutch study regarding treatment portals for elective neck irradiation. P.J.C.M. Nowak, E.B. van Dieren, J.R. van Sörnsen de Koste, H. van Est, B.J.M. Heijmen, P.C. Levendag. Dr. Daniel den Hoed Cancer Center, Rotterdam, the Netherlands. Email: Dieren@kfh.azr.nl

Purpose/Objective: To assess the variation in treatment portals for elective radiotherapy of the neck, and the three-dimensional dosimetric consequences of this variation.

Materials & Methods: Experienced radiation oncologists ($n=16$) from all major head & neck cooperative groups in the Netherlands ($n=11$) were asked to define RT-portals on a lateral and/or AP simulation film, for (routine) elective neck irradiation for a T2 tumor of the mobile tongue and a T3 tumor of the supraglottic larynx. Treatment portals were compared and evaluated using a three-dimensional treatment planning system and CT data with contoured critical structures and target volume. The CT-defined clinical target volume was mutually agreed upon by ENT-surgeons and radiation oncologists.

Results: Large differences were seen in treated volume (a factor of five). In addition, due to the variation in the cranial boundary of the RT-portals, the estimated NTCP varied considerably (0-50%). Moreover, several of the RT-portals did not adequately cover the CT-defined target volume.

Conclusion: Even amongst experienced head and neck radiation oncologists, there seems to be little agreement regarding treatment technique and size of the treatment portals in case of elective neck irradiation. This results in a considerable variation in treated volume. As a consequence, there is a large difference in the anticipated probability of normal tissue complication, and possibly in tumor control probability. Therefore, a definition of target volume and, consequently, a standardization of elective neck portals is mandatory. This is even more important if the primary tumor and clinically node-negative neck are to be treated by 3D conformal RT using multiple CT-slices for target delineation and positioning of BEV blocks in order to spare the normal tissue function with maximum tumor control probability.



VIRTUAL SIMULATION OF RADIOTHERAPEUTIC TREATMENT OF THE PROSTATE

K. Haest (1), J. Vanregemorter (1), J. Van Dam (2)
 Depts of Radiotherapy, A.Z. Middelheim Antwerp (1) and K.U. Leuven (2)

Virtual simulation allows to simulate the radiotherapeutic treatment by computer, based on a CT scan of the patient in treatment position.

We used the routinely obtained CT scans of prostate cancer patients in treatment position after conventional simulation for a parallel virtual simulation. In a first step the three-dimensional electron density data of the CT were used to outline the prostate and critical organs as three-dimensional volumes of interest. Based on the 3D information of the pre-defined target volume and a pre-set 3D margin, beams and beam blocks were automatically generated according to the beam set-up. A beam's-eye view of the volumes of interest was calculated for each beam, superimposed on a digitally reconstructed radiograph using the actual divergence of the beam. At the same time the dose distribution was computed for the fields and blocks generated by the virtual simulator. The resulting Dose Volume Histograms for prostate, rectum and bladder were reviewed and compared with the Dose Volume Histograms obtained from the conventional simulation process. During both virtual and conventional simulation, time commitments required for all the members of the radiotherapy treatment team were recorded.

We report on the following: (a) routine use of virtual simulation is possible in a busy radiation oncology department; (b) virtual simulation results in most cases in smaller field sizes than conventional simulation; (c) Dose Volume Histograms show that virtual simulation of the prostate minimises the dose delivered to the bladder; (d) a shift in workload can be expected from technicians towards physicists and medical doctors with an overall decrease in time for both personnel and patient.

TOMODENSITOMETRY IMAGES : INTEGRATION IN RADIOTHERAPY.

F. Dessy¹, M.T. Hoornaert¹, F. Malchair².

With a view to utilization of CT scan images in radiotherapy, we have measured the effective energy and the linearity of four different scanners (Siemens somatom CR, HiQS, Plus and Picker PQ 2000) and two "non standard scanners", simulators with CT option (Webb 1990) (Varian Ximatron and Oldelft Simulx CT) using the method described by White and Speller in 1980. When the linearity relation is presented using the density or the electron density as the abscissa, we obtain a "blurred area" where two different components of equal density or electron density can have two different Hounsfield's numbers. Using the linearity relation, we determined the "density" of Rando's lung heterogeneity. We calculated a treatment planning (T.P.) using this value and made a comparison between the T.P. and the real absorbed dose which was measured using diodes. The comparison between the TP and the relative absorbed doses showed a difference of up to 4,5 %. We only made one measurement. This will be explored in a near future.

¹ Hopital de Jolimont, Service d'oncologie et de médecine nucléaire, Hains St Paul..

² Biomed Engineering, Bonnelles..

IMMOBILIZATION FOR THE RADIATION THERAPY TREATMENT OF THE PELVIC REGION. .

F. Van den Heuvel, M. De Beukeleer, F. Nys, P. Bijdekerke, M. Robberechts, R. Van Cauwenbergh

Academic Hospital, Free University of Brussels Brussels, Belgium

Introduction: Previous experience with the treatment of the pelvic region has shown that geometric setup errors are considerable in extent and incidence. A proposal to alleviate this problem is the introduction of immobilization devices in analogy with head and neck treatment. The goal of this paper is to investigate the practicality and efficacy of such a technique and to compare it with an earlier proposed technique using interactive adjustment and Electronic Portal Imaging (EPI).

Methods and Materials: A group of 13 patients treated in the pelvic region using external radiation therapy was immobilized using an Orfit®-like cast. Every fraction for every patients was imaged using an EPID. Immediately after obtaining an image it was compared to a digitized simulation image using the in-house developed OPIDUM system. Patient position was adjusted when an error in one of the main directions (transversal or longitudinal) exceeded 5mm. Time measurements were carried out in order to assess the impact of the immobilization procedure on the patient throughput.

Preliminary results (27 fields-6 patients) In 68% of the cases a corrective action was necessary. The fraction of total treatment time was 50% for 26% of the fields. The range of errors measured in the longitudinal direction was between 29 and -22 mm. In the transversal direction the range was from -7 to 6mm

Analysis: In this paper a full analysis will be carried out for 13 patients yielding statistics for more than 200 fields. The analysis will concentrate on determining the nature of the errors (random or systematic) and the impact on patient throughput.

Conformal radiotherapy using multileaf collimation : quality assurance and *in vivo* dosimetry.

P. Aletti

Centre Alexis Vautrin, Vandœuvre-Les-Nancy, France.

NO ABSTRACT SUBMITTED.

See Full Paper, pp. 243 - 260

**Application of an EPID for fast daily *dosimetric* quality control
of a fully computer-controlled treatment unit**



BE9700019

M.L.P. Dirkx, M. Kroonwijk, J.C.J. de Boer and B.J.M. Heijmen
Dr. Daniel den Hoed Cancer Center, Rotterdam, The Netherlands.

Rec P. 117-118

The MM50 Racetrack Microtron, suited for sophisticated three-dimensional computer-controlled conformal radiotherapy techniques, is a complex treatment unit in various respects. Therefore, for a number of gantry angles, daily quality control of the absolute output and the profiles of the *scanned* photon beams is mandatory. A fast method for these daily checks, based on *dosimetric* measurements with the Philips SRI-100 Electronic Portal Imaging Device, has been developed and tested. Open beams are checked for four different gantry angles; for gantry angle 0, a wedged field is checked as well. The fields are set up one after another under full computer control. Performing and analyzing the measurements takes about ten minutes.

The applied EPID has favourable characteristics for dosimetric quality control measurements: absolute measurements reproduce within 0.5 % (1 SD) and the reproducibility of a relative (2D) fluence profile is 0.2% (1 SD). The day-to-day sensitivity stability over a period of a month is 0.6% (1 SD). EPID-signals are within 0.2% linear with the applied dose.

The 2D fluence profile of the 25 MV photon beam of the MM50 is very stable in time: during a period of one year, a maximum fluctuation of 2.6% was observed. Once, a deviation in the cGy/MU-value of 6% was detected. Only because of the performed morning quality control checks with the EPID, erroneous dose delivery to patients could be avoided; there is no interlock in the MM50-system that would have prevented patient treatment. Based on our experiences and on clinical requirements regarding the acceptability of deviations of beam characteristics, a protocol has been developed including action levels for additional investigations. Studies on the application of the SRI-100 for in vivo dosimetry on the MM50 have been started.

BE9700019

Quality assurance of a conformal treatment technique.

A.P.G. Kroes, I.A.D. Bruinvis, J.H. Lanson and G.J. Uiterwaal.

The Netherlands Cancer Institute / Antoni van Leeuwenhoek Huis, Amsterdam, The Netherlands.

Purpose. For a parotid gland irradiation technique with a pair of oblique wedged photon beams the target coverage near the surface was investigated. The planning target volume extends to 5 mm under the skin; a minimum target dose of 95% is required when the dose at the centre is set to 100%.

Methods. The treatment technique was simulated on a water phantom with a beam of 45 degree gantry angle, 55 degree wedge, 8 x 10 cm² field size and the isocentre at 2 cm depth. Beam energies of 4, 6 and 8 MV were used. The dose distributions were measured in two orthogonal planes through the isocentre perpendicular to the water surface. In each plane the dose was measured with a p-type silicon diode along lines through the isocentre every 45 degrees. Dose distributions were calculated in these planes with our 3-D planning system (U-Mplan, University of Michigan planning system), which model parameters are fitted to depth dose curves and profiles of open and wedged normally incident beams.

Results. From the measurements the location of the 95% isodose was determined in 5 points near the surface. For 4, 6 and 8 MV the depths of the 95% isodose were 6.0, 10.3 and 11.0 mm, respectively. The depths of the 95% points of single normally incident open fields were 6.0, 9.0 and 11.5 mm, respectively. The treatment planning system (TPS) calculated the 95% isodose for the parotid technique at 5.5, 7.3 and 11.5 mm depths, for 4, 6 and 8 MV, respectively. Thus for 6 MV the 95% was 3 mm deeper than calculated by the TPS; 2 mm were caused by the inaccuracy of the open field depth dose curve fit in the build-up region.

Conclusions. The depth near the surface of the 95% isodose for this treatment technique can be estimated from single open field depth dose curves with acceptable accuracy. This result is not obvious, however, because the effects of the wedge and oblique incidence on the dose distribution are also involved. The TPS performed well for the 4 and 8 MV beams, but for treatments with 6 MV target underdosage could have remained undetected. Because of the better target coverage, the 4 MV beam was chosen for future parotid gland treatments.



KWARTA (KWaliteitsverzekering in de RadioTherapiecentra van de provincie Antwerpen) :
Quality control of the contact therapy machine and treatment planning system.

B. De Ost (1), L. Bellekens (2), R. Cardoen (3), H. Goossens (4), K. Haest (5), N. Mertens (5), D. Pieters (3),
 B. Schaeken (1), J. Vanregemorter (1).

During the first year of the provincial QA project, joint procedures were set up for the routine quality control of linear accelerators, Cobalt treatment machines and simulators. A set of standard forms was produced for use in all centres, respecting the differences of each individual machine. Since these forms are now in use in all centres the second year of the project mainly focused on the QA/QC of the contact therapy machine and treatment planning system.

QC measurements for the contact therapy machines were performed in air or in a phantom. Since the output was checked with the same ionisation chamber (0.33 cc flat chamber calibrated for 50 kV) and the same type of electrometer in all centres, the results could be compared mutually and with the reference values.

The major parameter groups, tested for the treatment planning system were: isodose distribution (visual control of all square fields in the database of the system), PDD data (analysing of 10x10 cm², 20x20 cm², 30x30 cm² and 40x40 cm² open or wedged fields), output factors, wedge and tray factors, inverse square law, geometrical testing of the digitiser - screen - printer and geometrical and densitometrical testing of the CT images - screen - printer. Between 496 and 1243 parameters were investigated in the different centres (depending on the presence of the electron data). Irregularities (0 % to 4 % of the total investigated parameters) were reported to the respective physicist.

(1) Algemeen ziekenhuis Middelheim, Lindendreef 1, 2020 Antwerpen / (2) Sint Vincentius Ziekenhuis, Sint Vincentiusstraat 20, 2018 Antwerpen / (3) Medisch Instituut St. Augustinus, Oosterveldlaan 24, 2610 Wilrijk / (4) Sint Elizabeth Ziekenhuis, Rubensstraat 166, 2300 Turnhout / (5) Sint Norbertus Ziekenhuis, Rooienberg 25, 2570 Duffel

QC in MRI : useful or superfluous ?

S. Infantino & F. Malchair (Biomed Engineering, Bonnelles)

A European task group has developed a protocol of quality controls (QC) in MRI. It essentially relates on control of image properties (uniformity of the signal, signal-to-noise ratio (SNR), resolution, distortion,...).

We applied this protocol to the Magnetom SP (Siemens) of the CHU in Liège. We had to use the Siemens multi-purpose phantom that doesn't permit a QC as complete and accurate as the Test Objects used in the protocol. The phantom simulates the magnetic properties of the body. We tested the body and head coils with and without a loading annulus that simulates the body conductivity and we obtained interesting results :

- body coil : the signal, SNR, uniformity and artifacts were satisfactory just after a maintenance but had changed significantly and became unacceptable two weeks later.
- head coil : the uniformity of the signal and SNR were satisfactory without the annulus. With the annulus the signal increased from the right to the left of the phantom of nearly 20 % ! This came from a lack of correction of uniformity in the static field.

Other parameters (slice width and spacing, resolution and distortion) were satisfactory.

Since the head coil problem didn't appear during the maintenance we suggest Siemens' QC should include observation of intensity profiles. The images obtained should be archived so that the evolution of performances of the scanner is known.

In vivo noninvasive thermometry for hyperthermia applications using the MRI-based proton-resonance-frequency method

J. De Poorter, C. De Wagter, and Y. De Deene; MR Department, University Hospital, Gent, Belgium

SEC P129-136

The lack of noninvasive temperature monitoring is seriously limiting hyperthermia treatment of deep-seated tumors [1]. MRI methods have shown to be promising [2]. These methods exploit the temperature dependence of a physical property whose spatial distribution can be visualized. We examined the Proton Resonance Frequency (PRF) as physical property because phantom studies prove the high accuracy that can be obtained using this parameter.

Thermal experiments were performed in human lower legs. Our results show that in muscle tissue the three-dimensional temperature distribution can be evaluated with a mean spatial distribution of 2 millimeters, a temporal resolution of 2 minutes and an accuracy of about 1°C. However, it is not possible to retrieve the temperature distribution in fat tissue using the PRF-method due to the predominance of susceptibility effects in fat. The susceptibility effects are a consequence of the temperature dependence of the susceptibility constants. Experimental data on these dependencies were obtained and the magnitude of these effects was modelled for some specific configurations. The susceptibility effects in muscle tissue can be neglected when precautions are made.

We conclude that the PRF method is an attractive tool to study time-varying temperature changes in muscle tissue.

References

- [1] BOLOMEY, J. C., AND HAWLEY, M. S. *Noninvasive Control of Hyperthermia* in 'Methods of Hyperthermia Control' (Ed. M. Gautherie). Springer-Verlag, Berlin, 1990, pp. 35-111.
- [2] DE POORTER, J., DE WAGTER, C., DE DEENE, Y., THOMSEN, C., STÅHLBERG, F., AND ACHTEN, E. *Journal of Magnetic Resonance, Series B* 103 (1994), 234-241.

DOSIMETRY OF SECONDARY TUMORS AFTER RADIOTHERAPY

SEC P137-142

H.W. Baas, J.J. Davelaar, J.J. Broerse, E.M. Noordijk
University Hospital, Clinical Oncology, Leiden

After a latency period of many years the incidence of a secondary tumor is considered a serious late effect of radiotherapy. Analysis of about 200 patients, treated radiotherapeutically for Hodgkin's disease in our hospital, shows an actuarial risk for the incidence of a secondary tumor of about 7 % after 10 years. The chance of tumor induction depends on the dose at the location of the tumor and therefore a good dose estimation is mandatory. Radiotherapy was given with Co-60 in the early years and with linear accelerators thereafter, exposing the target areas to 36 - 40 Gy. For dose estimations at the penumbra and outside the beam, where tumor incidence is expected to be high, we used a. o. Monte Carlo calculations. We developed an EGS4 computer simulation for a treatment beam from a linear accelerator irradiating a mathematical phantom representing the patient geometry (GSF ADAM phantom). The isodose curves at certain energies were obtained for a water phantom and fitted quite well with measurements. In addition to Monte Carlo calculations we also used existing treatment planning systems. We will discuss the dose estimations of a number of patients and the derived risk per unit of dose, which is important for both radiotherapy as well as radiation protection in general.



BE9700024

NEW RELATIONS IN BASIC DOSIMETRY

F. Rebigan

Institute of Atomic Physics, Bucharest, Romania



BE9700025

In this paper four new relations are derived, for the first time, based on the definitions of the fundamental dosimetric quantities given in the last ICRU reports. These relations have the general form $A \cdot B = A \cdot B$, where A and A , B and B are, the dosimetric quantities and their rates, respectively. Thus, the author found $\psi \cdot \Phi = \phi \cdot \Psi$, for a monoenergetic beam of photons, in any point of this beam and at any time. Here ψ is the energy fluence rate, ϕ particle fluence rate, Ψ energy fluence, and Φ the particle fluence. The second relation is $K \cdot \psi = K \cdot \Psi$, where K and K are kerma and kerma rate. The third relation, for absorbed dose D and its rate \dot{D} is $D \cdot \psi = \dot{D} \cdot \Psi$. Finally, for electron fluence Φ_e , and ϕ_e electron fluence rate the corresponding relation is $D \cdot \phi_e = \dot{D} \cdot \Phi_e$. At the end the author states interesting remarks regarding an exhaustive description of an ionizing radiation beam or radiation field closely related to their interaction with matter.

How to calibrate Grenz-beams in clinical practice?

B. Schaeken⁽¹⁾, E. Bressers⁽²⁾.

(1) A.Z. Middelheim, Lindendreef 1, 2020 Antwerpen.

(2) Virga Jesse Ziekenhuis, Stadsomvaart 11, 3500 Hasselt.

In recent years, a considerable effort has been made in improving precision and consistency in the whole process of calibration of high energy photon and electron beams (national protocols, primary calibration facilities...). Despite its 100 th anniversary, the calibration of low energy x-ray beams is still a delicate and cumbersome work for all hospital physicists.

We compared the reading in air of 5 different ionisation chambers (NE2532, NE2536, NE2571, PTWM23342, Markus) in an X-ray beam (RT50, HVL=0.35 mm Al). All NE chambers were provided with a calibration factor N_k , the PTW chamber was directly calibrated in dose to water $N_{D,w}$. The polarisation and recombination effects were measured. In our reference field (ssd=4cm, field diameter 40 mm), the readings in air for the dedicated plan parallel chambers deviated by not more than 8%. The measurements with the NE2571 chamber did not correspond very well with the other measurements. For the equipment at AZM the dose rate in air for the reference field was measured from 1971 on and found to be very stable : 17.36 Gy/min \pm 0.48 (1sd).

We tried to measure the BSF for the field defining cones used in clinical practice using a Markus plane parallel chamber, but the resulting BSF did not correspond to those reported in BJR/suppl.17. Special attention will be paid in calibrating beams with field size comparable to the dimension of the chamber window / chamber body.

CONFORMAL RADIOTHERAPY MADE EASY THROUGH GRAVITY ORIENTED ABSORBERS

Basil S. Proimos

Dept. of Medical Physics, University of Patras, Greece

In the '50s and the '60s we developed simple technics modulating the beam intensity in synchronism with the rotation, either of the vertical patient (M.I.T.) or of the machine around the horizontal patient (Greek Anticancer Institute of Athens, Memorial Hospital of New York, etc).

An absorber, which is similar in shape to a vital organ, intercepts the beam, casting its protective "shade" over the organ, for all positions of rotation. This way the organ is protected during all of the patient's irradiation time T . On any transverse cross, any point outside of the organ's cross-section is protected for only a fraction of T , which is decreasing with the distance of that point from the organ. Consequently, the dose to the protected organ is smaller than (a) the dose it would absorb without protection (b) the dose to the surrounding (less vital) healthy tissue and (c) of course, the dose to the neighbouring tumour.

The device is attached to the head of the machine, through its base-plate, which slides in two parallel grooves, provided for the insertion of ordinary wedge-filters. A freely rotating shaft of suspension holds the absorbers at its front end and a counter weight at its rear end. Only the absorbers are in the beam.

The beam's central ray always meets both the suspension axis of the device and the rotation axis of the machine, perpendicularly. These two parallel axes define the "principal plane", on which lies the source, too. During the rotation gravity keeps the absorbers parallel to themselves, just as it does for the riders of the big "Ferris wheel" at a "Luna Park".

Consider a plane perpendicular to the "principal plane" and passing through the source. It cuts the organ and its protector in two cross-sections, which remain always "homiotheta", with center of "homiothesis" the source. This way the protector's cross-section is projected by the beam on the organ's cross-section for all positions of rotation.

The larger the cross-section of the organ and the smaller the required protection, the smaller must be the attenuation coefficient μ of the material the protector is made of.

A series of slides show the dose distributions in a series of actual cases, such as head tumours with eyes protection, neck or chest tumours with spinal cord protection, cervix tumours with rectum and bladder protection, etc. In most cases, if the vital organs are not overprotected, the 90% or 80% isodose surface fits to or conforms with the surface of the Planning Target Volume (PTV) no matter how irregular (convex and concave) it is.



Transmission dosimetry with a liquid-filled electronic portal imaging device.

R.Boellaard, M. van Herk and B.J. Mijnheer

The Netherlands Cancer Institute, Amsterdam, The Netherlands.

BE9700027

The aim of transmission dosimetry is to correlate transmission dose values with patient dose values. A liquid-filled electronic portal imaging device (EPID) has been developed in our institution. After determination of the dose response relationship, i.e. the relation between pixel value and dose rate, for clinical situations we found that the EPID is applicable for two-dimensional dosimetry with an accuracy of about 1%. The aim of this study is to investigate transmission dose distributions at different phantom-detector distances to predict exit dose distributions from transmission dose images. An extensive set of transmission dose measurements below homogeneous phantoms were performed with the EPID. The influence of several parameters such as field size, phantom thickness, phantom-detector distance and phantom-source distance on the transmission dose and its distribution were investigated. The two-dimensional transmission dose images were separated into two components: a primary dose and a scattered dose distribution. It was found that the scattered dose is maximal at a phantom thickness of about 10 cm. The scattered dose distribution below a homogeneous phantom has a gaussian shape. The width of the gaussian is small at small phantom-detector distances and increases for larger phantom-detector distances. The dependence of the scattered dose distribution on the field size at various phantom-detector distances has been used to estimate the dose distribution at the exit site of the phantom. More work is underway to determine the exit dose distributions for clinical situations, including the presence of inhomogeneities.

IN VIVO DOSIMETRY WITH L- α -ALANINE

Boey R.(1), Van Der Velden K.(1), Schaeken B.(2)

(1)Industriële Hogeschool van het Gemeenschapsonderwijs Limburg, Maastrichterstraat 100, B3500 Hasselt

(2)Department of Radiotherapy

Academisch Ziekenhuis Middelheim, Lindendreef 1, B2020 Antwerp, Belgium

IN VIVO DOSIMETRY WITH L- α -ALANINE

When organic substances are irradiated, stable unpaired electrons can be formed. The concentration of these electrons is detected via electron paramagnetic resonance (EPR), a non-destructive form of dosimetry. L- α -alanine is extremely suited as a detector because of its high stability and high yield of unpaired electrons.

With an EMS 104 spectrometer, we measure the peak-to-peak value of the first derivative of the resonance-spectrum. This value is proportional to the concentration of unpaired electrons and therefore with the absorbed dose.

Prior to the in vivo measurements in teletherapy, a calibration curve had to be established. This clearly showed a linear relationship between the EPR-signal and the absorbed dose, except for very low dose where precision was low (20% 1SD). This indicates that the background signal of the dosimeter is strongly orientation dependent. For this reason we decided to use pre-irradiated detectors.

With this in mind we performed a number of in vivo measurements, from which it became clear that error propagation plays a major role with the calculation of the measured absorbed dose, in the range 1 Gy-6 Gy. Contrary to in vivo measurements in brachytherapy, where higher doses are measured, large uncertainties (30% 1SD) on our entry dose calculations were perceived.

We therefore propose to use a statistical method of reducing this standard deviation to an acceptable level. Our method, consisting of 2 detectors and the usage of weightcoefficients on our standard deviations, gave promising results.

However, theoretical calculations and in vivo measurements show that this method is still not satisfactory to reduce the uncertainty to an acceptable standard in clinical situations.

In vivo dosimetry using thermoluminescence dosimeters during brachytherapy with a 370 GBq Ir¹⁹² source.

S. Cuepers, M. Piessens, L. Verbeke, A. Roelstraete.
Radiotherapy and Oncology, O.L.V. Ziekenhuis, Aalst, Belgium.

When using LiF thermoluminescence dosimeters in brachytherapy, we have to take into account the properties of a high dose rate Ir¹⁹² source (energy spectrum ranging from 9 to 885 keV, steep dose gradient in the vicinity of the source) and these of the dosimeters themselves (supralinearity, reproducibility, size). All these characteristics combine into a set of correction factors which have been determined during in phantom measurements. These results have then been used to measure the dose delivered to organs at risk (e.g. rectum, bladder, etc.) during high dose rate brachytherapy with a 370 GBq Ir¹⁹² source for patients with gynaecological tumours.

FILM DOSIMETRY IN CONFORMAL RADIOTHERAPY

Claudia Danciu and Basil S. Proimos

Dept. of Medical Physics, University of Patras, Greece

Conformal Radiotherapy aims to achieve:

- a) an isodose surface fitting geometrically to the surface of the "Planning Target Volume"(PTV), which volume must receive at each point a dose at least equal to the minimum dose, required by the radiotherapist
- b) protection of the vital organs, so that they absorb a dose smaller than the maximum one, specified by the radiotherapist.

In other words, Treatment Planning in Conformal Radiotherapy aims to solve the "inverse problem".

Dosimetry, through a film sandwiched in a transverse cross-section of a solid phantom, is a method of choice in Conformal Radiotherapy because:

- a) the blackness ("density") of the film at each point offers a measure of the total dose received at that point
- b) the film is easily calibrated by exposing a film strip in the same cross-section, through a stationary field

For this, the film must have the following two properties :

- a) It must be "slow", in order not to be overexposed, even if the therapeutic dose of 200 cGy is given in any region of it.
- b) The response of the film ("density versus dose curve") must be independent of the photon energy spectrum.

After testing a few "slow" films, we decided that the Kodak "X-Omat V for therapy verification" was the best.

To investigate whether the film response was independent of the photon energy, we have derived the response curves for six depths, starting from the depth of maximum dose to the depth of 25 cm, in a solid phantom. The vertical beam was perpendicular to the anterior surface of the phantom, which was at the distance of 100 cm from the source and the field was 15x15 cm at that distance. We repeated this procedure for photon beams emitted by a Cobalt -60 unit, two 6 MV and 15 MV Linear Accelerators, as well as a 45 MV Betatron . For each of those four different beams the film response was the same for all six depths. The results, as shown in the diagrams, are very satisfactory.

We have also derived the response curve under a geometry similar to that actually applied, when the film is irradiated in a transverse cross-section of the phantom. The horizontal beam was almost parallel (angle of 85) to the plane of the film. The same was repeated with the central ray parallel to the film (angle 90) and at a distance of 1.5 cm from the horizontal film. The field size was again 15x15 cm at the lateral entrance surface of the beam. The response curves remained the same, as when the beam was perpendicular to the films.

Three Dimensional Gel Dosimetry by use of Nuclear Magnetic Resonance Imaging (MRI)

Y. De Deene², C. De Wagter², J. De Poorter¹, B. Van Duyse², E. Achten¹ and W. De Neve²

¹Dept. of Magnetic Resonance - University Hospital of Gent

²Dept. of Radiotherapy and Nuclear Medicine - University Hospital of Gent

As comonomers are found to polymerize by radiation, they are eligible for constructing a three dimensional dosimeter. Another kind of three dimensional dosimeter, based on the radiation sensitivity of the ferrous ions in a Fricke solution, was tested in a previous study. However, a major problem that occurs in this kind of gel dosimeters is the diffusion of the ferric and ferrous ions.

The comonomer gels demonstrate a more stable character.

The degree of polymerisation is visualised with a clinical MRI system.

Acrylamide and N,N'-methylene-bis-acrylamide are dissolved in a gel composed of gelatine and water. By irradiation the comonomers are polymerized to polyacrylamide.

The gel is casted in humanoid forms. As such, a simulation of the irradiation of the patient can be performed. Magnetic resonance relaxivity images of the irradiated gel display the irradiation dose. The images of the gel are fused with the radiological images of the patient.

Quantitation of the dose response of the comonomer gel is obtained through calibration by test tubes.

Limits of dose escalation in lung cancer : a dose-volume histogram analysis comparing coplanar and non-coplanar techniques

Derycke, S., Van Duyse, B., Schelfhout, J., and De Neve, W.

Department of Radiotherapy, Nuclear Medicine and Experimental Cancerology, University Hospital, Gent, BELGIUM.

To evaluate the feasibility of dose escalation in radiotherapy of inoperable lung cancer, a dose-volume histogram analysis was performed comparing standard coplanar (2D) with non-coplanar (3D) beam arrangements on a non-selected group of 20 patients planned by Sherouse's GRATIS™ 3D-planning system. Serial CT-scanning was performed and 2 Target Volumes (TVs) were defined. Gross Tumor Volume (GTV) defined a high-dose Target Volume (TV-1). GTV plus the locations of node stations with > 10 % probability of invasion (Minet et al.) defined an intermediate-dose Target Volume (TV-2). However, nodal regions which are incompatible with cure were excluded from TV-2. These are ATS-regions 1, 8, 9 and 14 all left and right as well as heterolateral regions. This definition is different from the ICRU guidelines since the subjective parts defined within the Clinical Target Volume (ICRU) are not drawn. However, they are taken into consideration by adding 2 cm to Sherouse's auto-beam tool (generates beam outlines conformal to the target's projection) and by clinical evaluation of the dose distribution.

2D-plans consisted of APPA and oblique beams. For 3D-planning, Beam's Eye View selected (by an experienced planner) beam arrangements were optimised using Superdot, a method of target dose-gradient annihilation developed by Sherouse.

A second 3D-planning was performed using 4 beam incidences with maximal angular separation. The linac's isocenter for the optimal arrangement was located at the geometrical center of gravity of a tetraheder, the tetraheder's corners being the consecutive positions of the virtual source. This ideal beam arrangement was approximated as close as possible, taking into account technical limitations (patient-couch-gantry collisions).

Criteria for tolerance were met if no points inside the spinal cord exceeded 50 Gy and if at least 50 % of the lung volume received less than 20 Gy. If dose regions below 50 Gy were judged acceptable at TV-2, 2D- as well as 3D-plans allow safe escalation to 80 Gy at TV-1. When TV-2 needed to be encompassed by isodose surfaces exceeding 50 Gy, 3D-plans were necessary to limit dose at the spinal cord below tolerance. For large TV's dose is limited by lung tolerance for 3D-plans. An analysis (including NTCP-TCP as cost functions) of rival 3D-plans is ongoing.

Acknowledgements :

S. Derycke is a recipient of a grant of the "Sportvereniging tegen Kanker". The "UZG project Conformal Radiotherapy" is sponsored by the "Vereniging voor Kankerbestrijding" and the "Centrum voor Gezwellziekten, University Gent".



SPECTROMETRIC METHODS USED IN THE CALIBRATION OF RADIODIAGNOSTIC MEASURING INSTRUMENTS

W. de Vries

Nederlands Meetinstituut, Utrecht, The Netherlands

Recently a set of radiation qualities for use in diagnostic radiology was established at the calibration facility of Nederlands Meetinstituut (NMI). The establishment of these radiation qualities required re-evaluation of the correction factors for the primary air-kerma standards. Free-air ionisation chambers require several correction factors to measure air-kerma according to its definition. These correction factors were calculated for the NMI free-air chamber by Monte Carlo simulations for monoenergetic photons in the energy range from 10 keV to 320 keV. The actual correction factors follow from weighting these mono-energetic correction factors with the air-kerma spectrum of the photon beam. This paper describes the determination of the photon spectra of the X-ray qualities used for the calibration of dosimetric instruments used in radiodiagnostics. The detector used for these measurements is a planar HPGe-detector, placed in the direct beam of the X-ray machine. To convert the measured pulse height spectrum to the actual photon spectrum corrections must be made for fluorescent photon escape, single and multiple Compton scattering inside the detector, and detector efficiency.

From the calculated photon spectra a number of parameters of the X-ray beam can be calculated. The calculated 1st and 2nd half value layer in aluminum and copper are compared with the measured values of these parameters to validate the method of spectrum reconstruction.

Moreover the spectrum measurements offer the possibility to calibrate the X-ray generator in terms of maximum high voltage. The maximum photon energy in the spectrum is used as a standard for calibration of kVp-meters.

In vivo dosimetry of high-dose fractionated irradiation in an experimental set-up with rats.

Fortan, L. (*), Van Hecke, H. (*), Van Duyse, B. (*), Pattyn, P. (†), De Meerleer, G. (*), Van Renthergem, K. (†), and De Neve, W. (*). (*) Department of Radiotherapy, Nuclear Medicine and Experimental Cancerology, and (†) Department of Surgery, University Hospital, Gent, BELGIUM.

Purpose :

With further experiments in mind, we wanted to find out the feasibility to irradiate a limited section of a rat abdomen with well-defined edges. Because of the relative small volume, *in vivo* dosimetry with TLDs was necessary in providing us information about the accuracy of the irradiation method.

Methods and Material :

Three to five days prior to the start of the radiotherapy treatment, 2 plastic strips - each containing a TLD-dosimeter (Harshaw TLD100 Li⁷F rods, 1 mm dia x 6 mm) sealed in polyethylene tubing, and a lead bean - were implanted in the rat abdomen. The plastic strips made a closed loop around the bowel, through the mesentery, and were fixed with a single stitch on the inner abdominal wall. One loop was made in the hepatic area; another was made in the lower abdomen, around the rectosigmoid. Conscious animals were irradiated using a purpose-built plexi-holder, with rear legs immobilised to avoid longitudinal movements. The implanted lead beans enabled us to simulate the rat prior to each radiation session. This way, the radiation field could be set up individually for each rat, in such way that the rectosigmoid area received full dose and the hepatic area received no irradiation dose at all. Irradiation was carried out, using 5 MV photons of a linear accelerator. Fifteen animals per group were irradiated according a conventional (2.0 Gy / fraction; 5 fractions / week) or a hyperfractionated (1.6 Gy / fraction; 2 daily fractions; 5 days / week) schedule, with different total doses (see table below). Prior to implantation, TLDs were individually calibrated and checked for stability. After removal from the abdomen, TLDs were tested again for accuracy. TLDs with an unacceptable read-out curve were rejected (about 2 to 4 TLDs per group of 15).

Results and Conclusions :

The accumulated doses (Gy) in the rat-abdomen, in- and outside the radiation field, are compared with the theoretical doses :

Conventional Irradiation				Hyperfractionated Irradiation			
Hepatic area		Rectosigmoid area		Hepatic area		Rectosigmoid area	
Wanted	Obtained	Wanted	Obtained	Wanted	Obtained	Wanted	Obtained
0.00	1.83 ± 0.36	40.00	41.43 ± 2.83	0.00	0.88 ± 0.08	41.60	39.32 ± 1.24
0.00	1.13 ± 0.09	60.00	56.69 ± 3.87	0.00	2.08 ± 0.29	60.80	67.00 ± 2.76
0.00	1.94 ± 0.35	80.00	82.93 ± 5.06	0.00	2.11 ± 0.66	80.00	73.96 ± 5.51

The obtained accumulated doses - as determined by TLD read-outs - were comparable to the theoretical doses, indicating that fractionated radiation of small fields, with well defined mark off, in rats is feasible.

Acknowledgements : This research was made possible thanks to financial support from "Pharmacia"; suture material was kindly provided by "Ethicon".

Evaluation of ion chamber dependent correction factors for ionisation chamber dosimetry in proton beams using a Monte Carlo method

H. Palmans and F. Verhaegen

Standard Dosimetry Laboratory, Department of Biomedical Physics
University of Gent, BELGIUM

BE9700038

In the last decade several clinical proton beam therapy facilities have been established. To satisfy the demand for uniformity in clinical (routine) proton beam dosimetry two dosimetry protocols (ECHED and AAPM) have been published. Both protocols neglect the influence of ion chamber dependent parameters on dose determination in proton beams because of the scatter properties of these beams, although the problem has not been studied thoroughly yet. A comparison between water calorimetry and ionisation chamber dosimetry showed a discrepancy of 2.6 % between the former method and ionometry following the ECHED protocol. Possibly, a small part of this difference can be attributed to chamber dependent correction factors. Indications for this possibility are found in ionometry measurements. To allow the simulation of complex geometries with different media necessary for the study of those corrections, an existing proton Monte Carlo code (PTRAN, Berger) has been modified. The original code, that applies Mollière's multiple scattering theory and Vavilov's energy straggling theory, calculates depth dose profiles, energy distributions and radial distributions for pencil beams in water. Comparisons with measurements and calculations reported in the literature are done to test the program's accuracy. Preliminary results of the influence of chamber design and chamber materials on dose to water determination will be presented.

Human calf muscular metabolism study with a home-made ergometer using ^{31}P NMR spectroscopy

J. Peynsaert¹, E. Achten¹, E. Claeys¹, M. Rousseaux²

¹ MR Department, Gent University Hospital, Belgium

² Department of Sport Medicine, Gent University Hospital, Belgium

I. Introduction and Purpose

^{31}P NMR measurements were performed to examine the variations in the concentration of phosphate metabolites in calf muscle during exercise. Therefore, volunteers, installed in the supine position, were asked to push repetitively on the pedal of a home-made ergometer. The produced work and the changes in phosphorus containing metabolites were measured continuously. Correlations were made between the inorganic phosphate/phosphocreatine ratio and the cumulative work and between the intracellular pH and the cumulative work. The exercise protocol could be changed interactively with respect to the imposed initial pressure, the maximum pressure, the pressure increase per level and the time a certain level was held. The whole experiment could be graphically followed on-line.

II. Concept ergometer

The whole device globally consists of a pedal, a pressurized air cylinder, air tubings, a table and data collecting equipment, allowing the patient to perform a force in the supine position by pushing the pedal with his foot using his calf muscles. The movements are carried out at a regular frequency conform the rhythm of sound signals produced by a metronome. The pedal has a rotation axis situated at the calcaneus level. By applying a force onto the pedal, the feedback pressure (P_{feedback}) builds up in the air cylinder while the upper pressure (P_{upper}) diminishes. On each moment, P_{upper} and P_{feedback} are measured by the pressure sensors and continuously sent together with the signal from the displacement sensor to an acquisition system DT2812 (Data Translation™) via a junction box after amplification. This system communicates with an interactive input-output program written in a graphical icon-based language (DTVEE, HP™). Using the mechanical data (the upper pressure, the feedback pressure and the displacement), the work, the cumulative work and effective power developed during each bending movement were calculated repetitively and written to a spreadsheet file at the end of the exercise. It was possible to follow the course of the exercise by visualizing the displacement on-line.

III. Results and Discussion

In the first stadium, the in vitro reproducibility of the ergometer was tested for different protocols. These tests revealed that, though the deviation in produced work was markedly the highest at high working pressures, the relative error never exceeded 3%. Consequently, the ex vitro reproducibility of the data was examined with the equipment placed in the scanner. Generally, same conclusions could be derived. In a next stage, the work will be synchronized with the biomechanical data. Extreme precautions will be taken to examine each volunteer every time under the same physical and psychological conditions.



BE9700039

Daily check of the electron beams with a diode system

P. PILETTE

Centre Commun de Radiothérapie
Hôpital Civil de CHARLEROI
Hôpital Saint-Joseph GILLY
BELGIUM



BE9700040

BE9700039

The necessity to check, on a daily basis, all the accelerator beams has driven us to develop fast systems.

A cheap home-made detector, based on non medical diodes (type 1N5408), is used in our department since July 1992 to verify all the electron beams every day.

The idea is to evaluate the relative energy and Top-cGy correspondance with one single irradiation of less than 1 minute by 6 diodes fixed in a polystyrene phantom.

The principle of construction, software implementation and results are presented.

BE9700040

QUALITY ASSURANCE AND ACCURACY IN Co-60 RADIOTHERAPY

F. Scarlat, F. Rebigan

Institute of Atomic Physics, Bucharest, Romania

The characteristics of a set of 88 Co-60 sources ONCOBALT, are described in this paper. This set of radioactive sources is an original choice of a variety of cobalt sources in point of physical size and activity. It includes 5 activity groups of cells (stainless steel) among 2 and 12 mCi, 5 ± 15 mm active length and 2, 2.5 and 3 mm external diameter, 4 activity groups of needle activities between 1.3 ± 3.4 mCi, 15 ± 20 mm active length, 1.8 mm external diameter. By an appropriate choice of activities, dimensions and geometry of irradiation we can get an error of max. 5% as to the receive dose. The radioactive purity of cobalt is 99.9%. To meet the requirements in practical radiotherapy we checked the Co-60 sources by tests: tight test, mechanical test, corrosion test and contamination test that gave us full satisfaction.

TREATMENT PLANNING IN RADIOSURGERY : PARALLEL MONTECARLO SIMULATION SOFTWARE.

Scielzo G.* , Grillo Ruggieri F.** , Modesti M.°, Felici R.°, SurrIDGE M.°°

*Hospital Physics, **Radiation Therapy, Galliera Hospitals, Genova, Italy.

°EDS, Roma, Italy, °°Parallel Communication, Southampton, UK.

Purpose: To evaluate the possibility of direct Montecarlo simulation for accurate dosimetry with short computation time.

Materials and Methods: the Montecarlo EGS4 code was parallelized and tested on clusters of workstations in a UNIX environment (employing Power-PC and other high performance processors) to achieve short computation time. We made use of: graphics workstation, linear accelerator, water, PMMA and anthropomorphic phantoms, for validation purposes; ionometric,

film and thermo-luminescent techniques, for dosimetry; treatment planning system for comparison.

Results and conclusions: benchmarking results suggest that short computing times can be obtained with use of the parallel version of EGS4 we have developed. Parallelism was obtained assigning simulation incident photons to separate processors, and the development of a parallel random number generator was necessary. Validation consisted in: phantom irradiation, comparison of predicted and measured values with good agreement in PDD and dose profiles. Experiments on anthropomorphic phantoms (with inhomogeneities) were carried out, and these values are being compared with results obtained with the conventional treatment planning system.

This work was made possible by full grant from the European Community ESPRIT Project 8863.

PULSED DOSE RATE BRACHYTHERAPY (PDR) : AN ANALYSIS OF THE TECHNIQUE AT 2 YEARS.

Thienpont M., van Eijkeren M., Van Hecke H., Boterberg T., De Neve W.

Department of Radiotherapy and Nuclear Medicine, University Hospital, Gent, Belgium.

Introduction : We analysed 154 applications using a pulsed dose brachytherapy technique in 138 patients over a 2 year period with emphasis on technical aspects influencing the overall treatment time.

Material and Methods : Vaginal ovoids were used in 59 cases, plastic tubes in 52, a Fletcher-type in 18, vaginal cylinders in 14 and a perineal template in 11 cases. Pulses were given at hourly intervals with a median dose rate of 0.6 Gy per pulse (range 0.4 to 3 Gy). The number of pulses per application varied from 3 to 134 (median 32). The number of dwell positions varied from 1 to 542 over 1 to 18 catheters.

Results and Discussion : Patient related problems were few. The room was entered almost every 77 minutes. We noted 561 status codes in 147 applications. Of the 25 different codes, the most frequent one was due to the door left open when a pulse had to be given (35%) or due to constriction of the plastic catheters at the transfer tube junction (26%). However, the median total treatment time was increased by only 5 minutes.

Conclusion : With pulsed dose rate brachytherapy at hourly pulses we can treat our patients within the planned time despite frequent room entrance and occurrence of an appreciable number of status codes. This technique seems to fulfill its promise to replace low dose rate brachytherapy.

Three dimensional conformal radiation therapy may improve the therapeutic ratio of radiation therapy after pneumonectomy for lung cancer.

R.Trouette, N.Causse, M.Elkhadri, M.Caudry, J.Ph.Maire, J.P.Houlard, L.Recaldini and H.Demeaux.

Purpose : Three dimensional conformal radiation therapy would allow to decrease the normal tissue dose while maintaining the same target dose as standard treatment. To evaluate the feasibility of normal tissue dose reduction for ten patients with pneumonectomy for lung cancer, we determined the dose distribution to the normal tissue with 3-dimensional conformal radiation therapy (3-DCRT) and conventional treatment planning (CTP).

Methods and materials : Dose-volume histograms for target and normal tissue (lung, heart) were used for comparison of the different treatment planning.

Results : The mean percentages of lung and heart volumes which received 40 Gy with 3-DCRT were respectively 63 % and 37 % of the mean percentage of lung and volumes which received the same dose with CTP.

Conclusion : These preliminary results suggest that conformal therapy may improve the therapeutic ratio by reducing risk to normal tissue.

MEASUREMENT OF THE PRIMARY AND SCATTER DOSE IN HIGH ENERGY PHOTON BEAMS

P.M. van der Linden, T.B. Tiourina, W. Dries
Radiotherapy Dept. Catharina Hospital, Eindhoven, The Netherlands

Many dose planning systems employ the Cunningham model to separate scatter and primary components for dose calculations. The required data are commonly derived from PDD measurements performed under full scatter conditions for different field sizes. The primary component for the field size zero is interpolated from data for other field sizes. However, the way this interpolation is performed is not clear.

A method is presented to measure the primary and scatter components separately in a watertank using a small cylindrical absorber. Results from this experiment are compared with Monte Carlo calculations.

The measurement setup consists of a small cylindrical absorber placed on a central axis of the beam a few centimeters above the radiation detector. Both absorber and detector move along the central axis while absorbed dose is registered. As the primary radiation is fully blocked, only scatter component is measured when a cylindrical absorber is used. Measurements in open fields result in the total absorbed dose being the sum of primary and scatter components. By subtraction the primary dose component can be derived.

Absorbers with different diameters are used. With decreasing dimensions the relative contribution of the dose due to scatter radiation increases. A steep increase is observed when the range of laterally scattered electrons becomes comparable with the radius of the absorber.

Two different Monte Carlo simulations have been performed : with and without secondary electron transport. The data obtained for the former case perfectly agrees with experiment. The situation where the secondary electron range is assumed zero (i.e. local energy deposition) simulates the Cunningham model. Our results show that the Cunningham model predicts lower scatter component under the block edge which can be important for these applications.

Compton Scatter Correction for Planar Scintigraphic Imaging.



BE970045

Van Steelandt E., Dobbeleir A., Vanregemorter J.
Departments of Nuclear Medicine and Radiotherapy
Middelheim General Hospital, Lindendreef 1, B2020 Antwerp, Belgium.

A major problem in nuclear medicine is the image degradation due to Compton scatter in the patient. Photons emitted by the radioactive tracer scatter in collision with electrons of the surrounding tissue. Due to the resulting loss of energy and change in direction, the scattered photons induce an object dependant background on the images. This results in a degradation of the contrast of warm and cold lesions.

Several techniques have been recently proposed in literature. Although theoretically interesting, most of them like the use of symmetrical photopeaks can not be implemented on the commonly used gamma camera due to the energy/linearity/sensitivity corrections applied in the detector.

We propose a method for a single energy isotope based on existing methods with adjustments towards daily practice and clinical situations. We assume that the scatter image recorded from photons collected within a scatter window adjacent to the photo peak is a reasonably close approximation of the true scatter component of the image reconstructed from the photo peak window. A fraction 'k' of the image using the scatter window is subtracted from the image recorded in the photo peak window to produce the compensated image.

The principal matter of the method is the right value for the factor 'k', which is determined in a mathematical way and confirmed by experiments. To determine 'k', different kinds of scatter media are used and are positioned in different ways in order to simulate a clinical situation. For a secondary energy window from 100 to 124 keV below a photo peak window from 126 to 154 keV, a value of 0.7 is found. This value has been verified using both an antropomorph thyroid phantom and the Rollo contrast phantom

BE970045

10/2/85



Conformal Three Dimensional Radiotherapy Treatment Planning in Lund

Tommy Knöös¹, Per Nilsson¹, Anders Ask², Dept. Radiation Physics¹ and Oncology², Univ. Hosp. S-221 85 Lund, SWEDEN

Introduction

The use of conformal therapy is based on 3D treatment planning as well as methods and routines for 3D patient mapping, 3D virtual simulation, etc. This paper presents the management of patients using commercially available state-of-the-art equipment in the treatment chain. The University Hospital in Lund accepts patients for radiotherapy from the Southern region of Sweden with a population of about 1.5 million people within a distance of 250 km. About 2,100 new patients are treated annually with external radiotherapy on seven linear accelerators and one ⁶⁰Co unit. Three of the accelerators have dual photon energies and electron treatment facilities. One accelerator is equipped with a multi-leaf collimator as well as an electronic portal imaging device. A 3D treatment planning system (TPS), two simulators and an in-house CT-scanner are used for treatment planning. The treatment verification is mainly done the conventional way using film. Today approximately 4,400 patients have received a highly individualised 3D conformal treatment. This report will present the 3D process in Lund.

The Treatment Planning Process

The flow of patients through the radiation therapy department is schematically outlined in Figure 1. Approximately 2,100 new patients are treated annually and about 850 (≈40 %) of these have a pre-planning examination at the CT-scanner of the department. For the rest of the available time, it is used for diagnostics and follow-up of oncological patients. A typical CT-examination for radiotherapy planning includes about 30 abutting slices, 10 mm thick, covering the expected planning target volume, PTV, in both cranial and caudal direction with sufficient margins for allowing non-coplanar beam entrances. In regions with large density gradients, e.g. in the head and neck area, thinner slices are often used (5 mm). The set of CT slices is transferred to

the treatment planning system, TPS via the radiotherapy network (c.f. Figure 2). A superficial reference point is always defined during the CT examination using a small radio-opaque marker placed at an unambiguous position on the patient's skin. The patient position on the CT table is also marked using laser lines to facilitate the positioning. High accuracy in patient positioning is accomplished with several immobilisation techniques, e. g. net-masks for head and neck treatments, polyurethane-foam casts or vacuum-formed pillows.

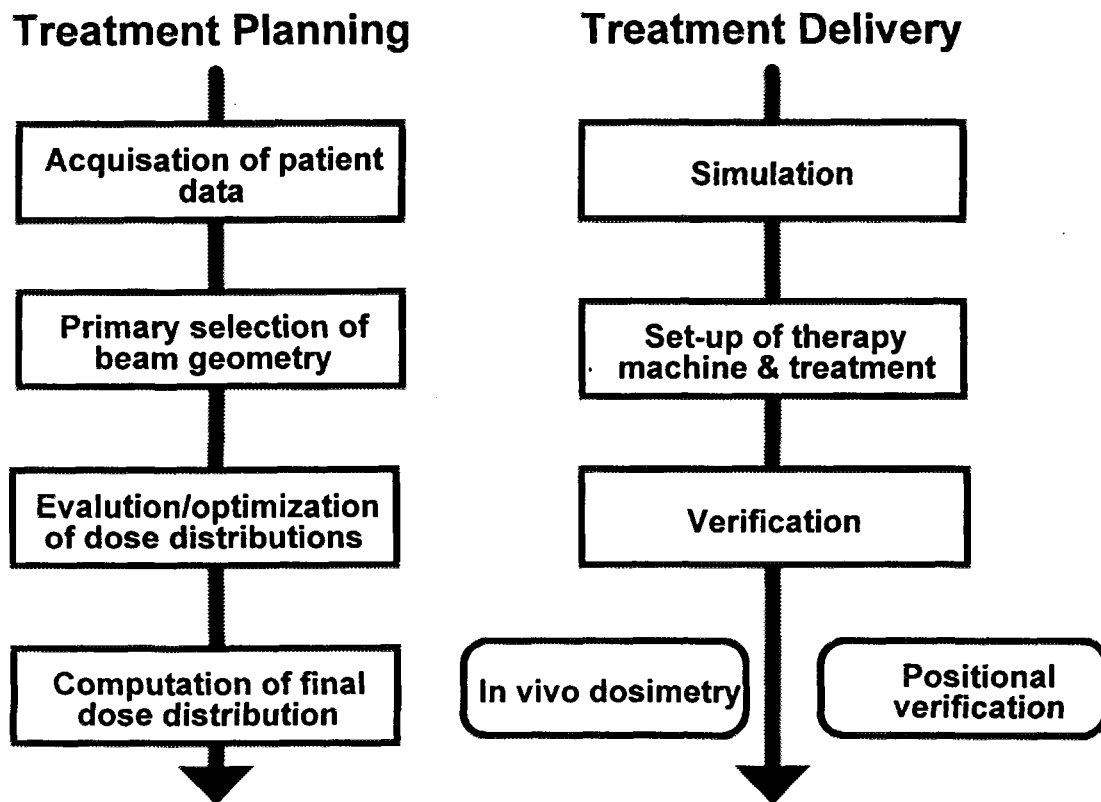


Figure 1: The treatment process divided into a *planning* and a *delivery* part. For 3D radiotherapy, all steps in the planning chain must be performed in 3D.

The treatment planning system (TMS from HELAX AB, Uppsala, Sweden) is used for the virtual simulation where the outlining of the target volume(s) and organs at risk in three dimensions are established. The TMS system handles up to 70 images per patient. The images can be CT images as well as MRI, ultrasound, scintigrams, digitised planar x-rays, etc. Transformations can be defined between different image sets. For example, two different CT studies with and without contrast in the bladder, facilitates the determination of the extension of the tumour. Additional organs and

anatomical landmarks (e. g. the vertebrae) are also outlined during the virtual simulation which facilitates the positioning of the patient at the simulator. This is also of highest importance during the check of verification port films.

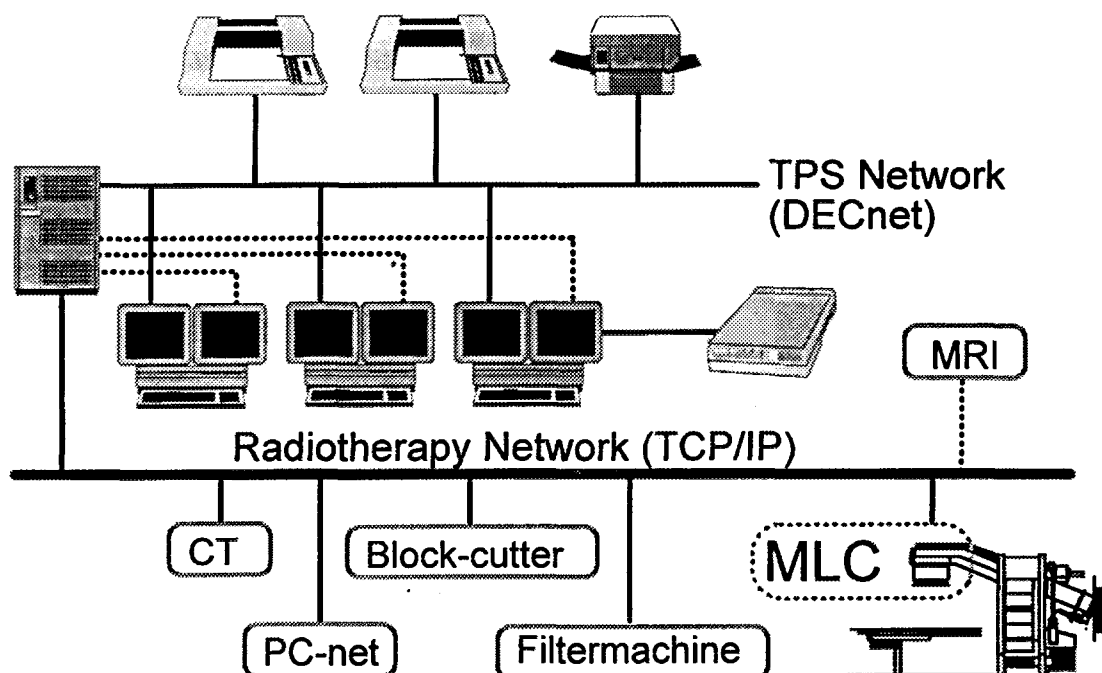


Figure 2: The treatment planning network. Three TPS work-stations with dual monitors are networked with a DEC VAX 4500 server. Each graphic monitor is connected to a Koala graphic processor with 24 Mbytes of memory. A mouse is used for most commands and including all drawing, beam positioning, field shaping etc. CT-information is imported directly using the network. Documentation is presented on laser printer, colour printer and pen plotters. Block shapes, compensators and MLC settings are exported to the appropriate receiver.

The treatment planning system is based on the *dose-to-energy-fluence* concept of Ahnesjö (Ahnesjö *et al*, 1992). This model has extensively been verified (Knöös *et al*, 1994, Hurkmans *et al*, 1995, Knöös *et al*, 1995, Weber *et al*, 1995). The calculations are based on accelerator specific energy fluence spectra which are used to compile a pencil beam from Monte Carlo generated energy absorption kernels. These pencil beams are analytically convolved with the patient modulated energy fluence distribution impinging on the patient surface. The total energy fluence is separated into a primary and a scattered energy fluence from the flattening filter and from the collimator blocks (Ahnesjö 1994, Ahnesjö 1995). Scatter from modulators i. e. wedge filters is under implementation at the moment and will be the subject for further

evaluation. Heterogeneity corrections are performed and gives results close to more conventional dose calculations algorithms (Knöös *et al*, 1995).

The calculations allows irregular fields, either from standard or individual blocks and from multi-leaf collimators. The field shape is determined conveniently using the beam's eye view, BEV. For MLC-shaped fields, a help contour is drawn manually around the target volume indicating the closest position for the leaves and, if no wedge or other modulator is used, the system determines the collimator rotation that results in the smallest area of irradiated normal tissue between the leaves and the help contour. If the operator is not satisfied with the solution, each leaf can be moved individually using the mouse. The final field shape is exported via the network to the MLC control computer at the Philips SL 15 accelerator. This machine is equipped with a MLC with two leaf banks, each having 40 leaves, with a projected width of 1 cm at isocenter. An over travel of 12 cm is possible. Back-up collimators are used to reduce the transmission between the leaves. The design of the MLC is such that all fields always use the leaves even for standard rectangular shapes.

The TPS calculated output factors for MLC shaped fields have been checked for 71 different geometries. Both energies (6 and 10 MV) and open as well as wedged beams were included. The average calculated-to-measured ratio of output factors did not show any deviation (mean 0.0 %, SD - 0.02 %).

For the accelerators without MLC, blocked fields are defined in the TPS and exported to a block-cutting machine (Par Scientific, Denmark). Approximately 2,000 individual blocks have been produced during 1994. If each field is treated at 20 sessions on average, a total of 40,000 conformal blocked fields are handled annually. On the MLC accelerator a total of 14,099 fields was treated 1994. A milling machine for manufacturing compensators is also available and work on beam-intensity modulation using filters is in progress.

The final treatment plans are presented as dose distributions overlaid on the CT-slices. Previously for 2D and semi 3D plans with a limited number of cross sections this was often sufficient. However, in the case with a full three dimensional dose distribution with about 50 slices, a compilation of the distribution into a dose-volume histogram is necessary. Several different treatment plans can be analysed simultaneously and the

most optimal can be chosen. A review session is performed daily with all involved personal categories i. e. radiotherapists, physicists and nurses (incl. dosimetrists) using a video projector for display of treatment plans on a 3x2 m² screen.

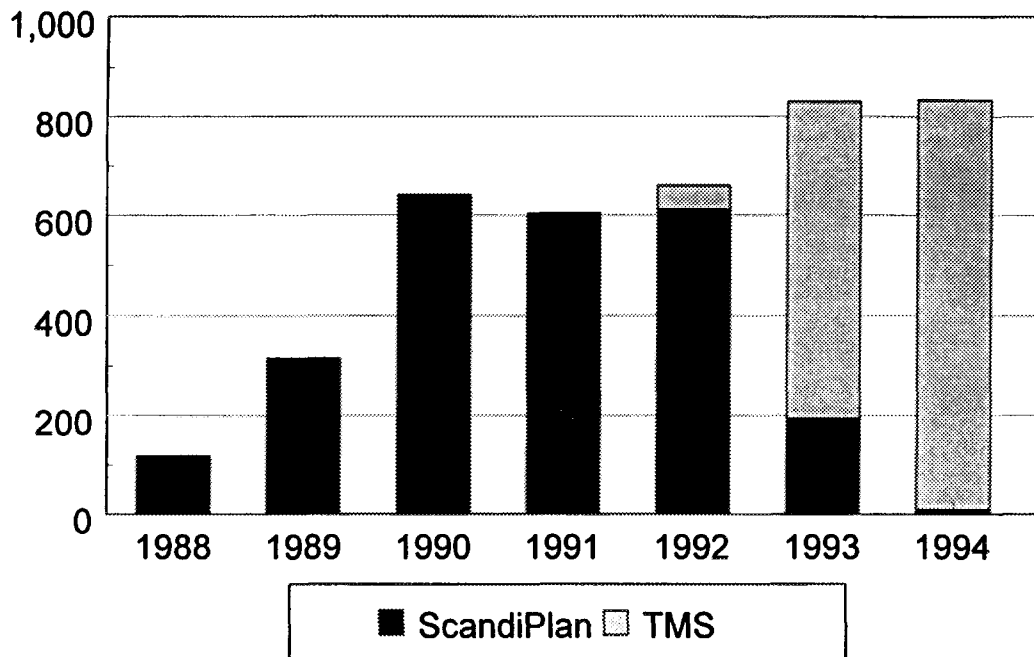


Figure 3: The number of three-dimensional dose plans created at the radiation therapy department in Lund. All these plans are based on CT-scans covering the whole volume to be treated.

The process of simulation is more or less reduced to the identification of the superficial reference point or if this point is replaced by an internal more unambiguous reference point. This position is also checked by orthogonal fluoroscopic views before the individual fields are positioned and verified on planar x-rays. For positioning, digital reconstructed radiographs, DRR and BEVs are used. The BEV for each field is always printed at a scale identical to the magnification factor of the x-ray film. A system for transferring DDRs directly to the simulator would allow a direct comparison with fluoroscopy image using e. g. overlay techniques. This would increase the accuracy of field positioning and also the positioning of the isocentre if orthogonal DDRs have been produced. An important task at the simulator is the estimation of the planning target volume (the clinical target volume with margins for e. g. respiration and patient movements) which can not always be determined accurately using only a CT-simulator or virtual simulation.

Today, approximately 850 three-dimensional dose plans are produced annually (Figure 3). The dominating group is breast cancer after conservatory surgery with about 200 patients for the first 10 month of 1995.

Conclusions

Three dimensional conformal therapy has been in use for the several years in Lund. A large amount of efforts have made this possible in clinical routine. For the 2,100 new patients, more than 50,000 conformal fields are given annually. To accomplish this, the following is required:

- Full-time access to CT
- A 3D TPS that handles all types of fields available on the accelerators
- Verification of dosimetry, set-up of the accelerator and positioning of the patient during treatment

References

1. Ahnesjö A, Saxner M, Trepp A, A pencil beam model for photon dose calculation, *Med Phys*, 19, 263-273, 1992.
2. Hurkmans C, Knöös T, Nilsson P, Svahn-Tapper G, Danielsson H, Limitations of a pencil beam approach to photon dose calculations in the head & neck region, *Radioth Oncol*, 37, 74-80, 1995.
3. Knöös T, Ceberg C, Weber L, Nilsson P, Dosimetric verification of a pencil beam based treatment planning system, *Phys Med Biol*, 39, 1609-1628, 1994.
4. Knöös T, Wittgren L, Which depth dose data should be used for dose planning when wedge filters are used to modify the photon beam?, *Phys Med Biol*, 36, 255-267, 1991.
5. Knöös T, Ahnesjö A, Nilsson P, Weber L, Limitations of a Pencil Beam Approach to Photon Dose Calculations in Lung Tissue, *Phys Med Biol*, 40, 1411-1420, 1995.
6. Weber L, Ahnesjö A, Nilsson P, Saxner M, Knöös T, Verification and implementation of dynamic wedge calculations in a treatment planning system based on a dose to energy fluence formalism, submitted to *Med Phys*, 1995.



Evaluation of penumbras of a Philips multileaf collimator

F.LAFAY*, C.MALET*, C.MOMBARD*, C.GINESTET*
E.BLONDEL**, Y.DESFARGES***, G.DUPIN***

BE9700005

* Radiophysics Unit - Radiotherapy Department - Centre Léon Berard - 28 Rue Laënnec - Lyon

** Isotec - Saint Quentin

*** Philips Medical System- Lyon

INTRODUCTION

Since January 1995, we have been using a Philips SL20 Linac equipped with a multileaf collimator. This installation allows to practice conformal therapy [1]. This new technique consists of creating easily irregular fields according to the shape of the tumour and so to increase the dose delivered to the tumoral volume by increasing the number of fields and to protect in the same time the safe tissues. An other advantage of a multileaf collimator is to use no more conventional shield blocks [2],[3]. This kind of treatment requires a good accuracy and strictness in the realization of each part of the treatment.

First, we realize a system of immobilization of the patient (polyurethane foam for pelvis and thoracic tumours, masks and dental print for brain tumours); After, the patient has a scanner exam and the acquisition of several slices allows the physician to draw the planning target volume. With the beam's eye view function of the new dosimetry system Philips SL-Plan, it's possible to conform the shape of the collimator to the planning target volume. Because of the penumbra of the collimator, we need to take account of an additional margin to choose the field size which is defined by the 50% isodose relative to the beam axis (internal penumbra). When the edge of the field is next to a critical organ, a second security margin can be taken in order to limit the dose (external penumbra)

The aim of this work is to evaluate the penumbras according to their origins and the different margins required when we realize a treatment planning.

A similar work has been done about other collimators [4].

METHODS AND MATERIALS

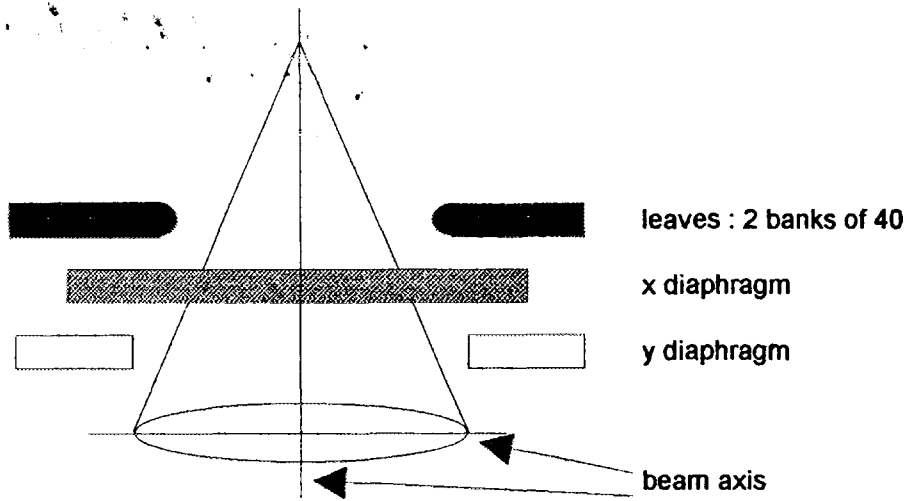
Multileaf collimator

Measures have been done with a linear accelerator Philips SL20 equipped with a multileaf collimator which delivered 6MV and 18MV photons.

The collimation system is located in the head of the linac and, from the base to the source, it can be described this way :

- leaves in tungsten with a size of 1 cm in the isocentric plane, for Y direction
- some classical diaphragm for X direction
- a pair of additional diaphragm in the Y direction to limit the leakage radiation between the leaves.

Fig. 1: Simplified schematic of the Philips multileaf collimator



Multileaf collimator is composed of 2 opposing banks of 40 leaves. Each leaf is driven by a individual motor and is separated from its neighbour with a space required to minimized the rubbing. Their sections with a form of bayonet are useful to reduce the leakage radiation between themselves. The X-Rays run always across a same thickness of leaves. The lateral side of the leaves follows the divergence of the beam and the more they are far away from the center of the beam, the more they are tilted.

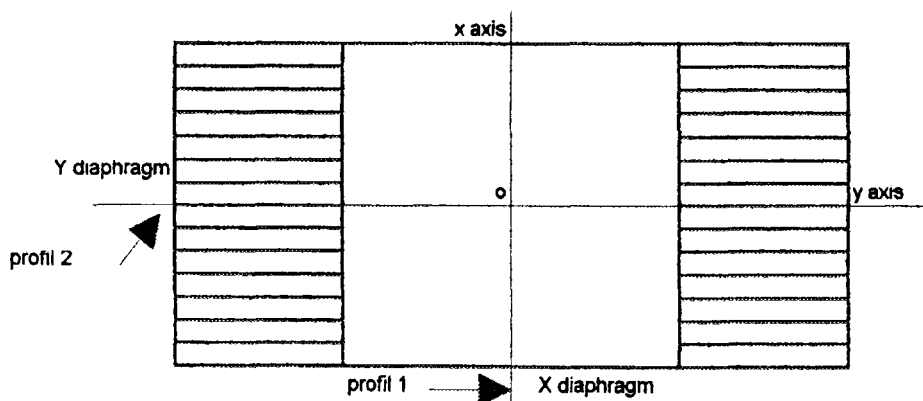
A more detailed description has already been published [5].

We have realized beam profiles for different fields shapes. Measures have been done for two energies: 6 and 18 MV, respectively at 5 and 10 cm of depth in a Wellhöffer water phantom. All the profiles have been normalized on the beam axis. We have measured the distance perpendicular to the axis of the point 95%, 90%, 80%, 50% and 20% and calculated the distance between the 80% and 20 %, 95% and 50%, 90% and 50%, 50% and 20% isodoses relative to the beam axis.

Penumbra measures for square fields

Seven fields sizes have been studied : 4x4, 10x10, 14x14, 20x20, 24x24, 30x30, 35x35. Beam profiles have been realized for the two directions X and Y.

This measures allow to evaluate the influence of the x diaphragm (X dimension) and of the couple (y diaphragm + leaves) for the Y dimension.

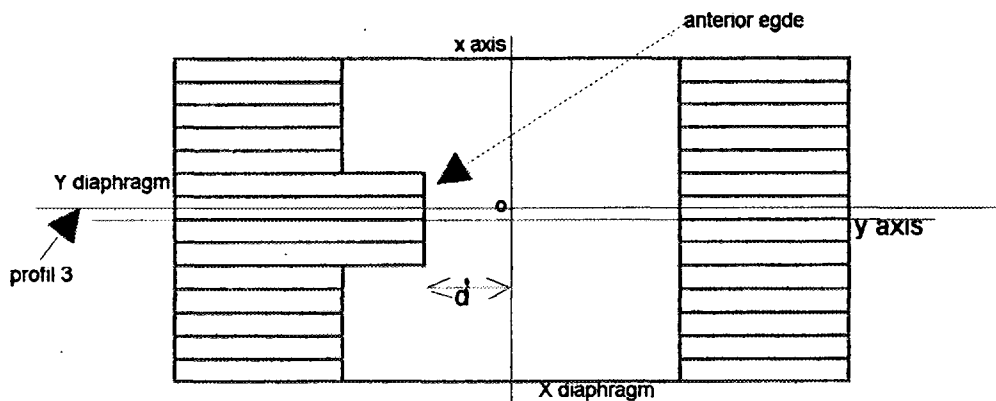


Penumbra measures in the direction of leaves moving (Y direction)

We have set several joining leaves in the irradiation field. In order to be in the center of a leaf and not between two leaves, we realize a profil beam parallel to the leaves with a shift of 5 mm relative to the field axis.

Distances between the leaves anterior edge and the collimator axis are : -12, -10, -7, -5, 2, 5, 7, 10, 12, 15 cm.

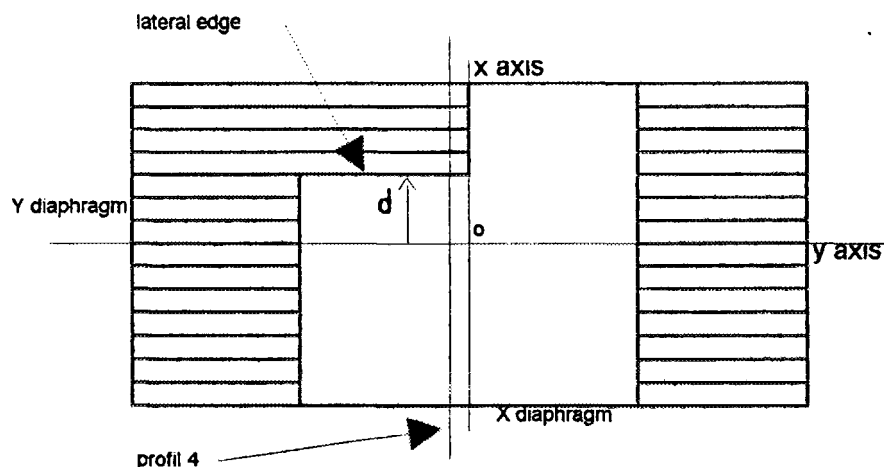
This measures allow to evaluate the influence of the anterior edge of leaves.



Penumbra measures perpendicular in the direction of leaves moving (X direction)

We have used several joining leaves in the irradiation field and realized a profil beam perpendicular to the leaves with a variable distance between the lateral edge of the leaf and the collimator axis.

This distance is : -12, -10, -7, -5, -2, 0, 2, 5, 7, 10, 12.



The different measures have been realized in a Wellhöffer water phantom with a dosimetric system WP 700 and an Wellhöffer ionization chamber IC10 connecting to a WP5007 electrometer.

A comparison between first measures realized with different kind of chamber and with radiographic films shows us that our system sensibility is sufficient to determine the variation of the different penumbras.

RESULTS

The different results are recapitulated by energy and by kind of penumbra in the table not joined in this text. **All penumbras are given in millimeters.**

For each table, there is a graph.

d(I1-I2) is the distance between I1 and I2 isodoses relative to the beam axis.

d is the distance between the edge of the collimator and the collimator axis.

The X colum is for the x collimator, the Y colum the y collimator. "ant edge", "lateral edge>0" and "lateral edge <0" is for leaves in according to the moving direction of the blocks.

x collimator represents the diaphragm x and y collimator the couple (y diaphragm + leaves).

DISCUSSION

The classical penumbra is defined by the distance between the 80% and the 20% isodoses relative to the beam axis.

Graphs for two energies show a distinguished action of x and y collimator with regard to the leaves. It's clear that leaves penumbras are more important than collimators penumbras: For 18 MV photons, 8.2 to 8.6 mm for x and y collimator versus 10.4 and 11.6 mm for leaves.

It seems interesting to compare penumbras in a same direction but with a different origin : x collimator versus lateral edge leaves and y collimator versus anterior edge leaves.

For the two energies, results show that the different penumbras are a little dependant on the distance between the edge and the collimator axis. We can consider a mean penumbra for each kind of penumbra and each energy. (table 1)

Table 1 : Mean, max and min values of penumbras for 6 and 18 MV photons

Photons X6	x collimator	lateral edge	y collimator	anterior edge
80%-20%	6.4 (+0.4)(-0.7)	8.1 (+0.4) (-0.3)	7.2 (+0.6) (-1)	9.5 (+0.6) (-0.7)
50%-20%	3.4 (+0.2)(-0.5)	4.5 (+0.2) (-0.1)	3.9 (+0.4) (-0.7)	5.9 (+0.6) (-0.6)
95%-50%	6.5 (+0.6) (-0.9)	8 (+1.2) (-0.8)	7.6 (+1.1) (-1.4)	7.6 (+1.3) (-1.2)
90%-50%	4.6 (+0.2) (-0.3)	5.4 (+0.7) (-0.4)	5.2 (+0.3) (-0.6)	5.4 (+0.5) (-0.5)

Photons X18	x collimator	lateral edge	y collimator	anterior edge
80%-20%	8.2 (+0.6) (-1.2)	10.4 (+0.6)(-0.5)	8.6 (+0.7) (-1.3)	11.6 (+0.6) (-1)
50%-20%	4.5 (+0.5) (-0.9)	6.4 (+0.5)(-0.4)	4.7 (+0.6) (-0.9)	7.5 (+0.7) (-0.7)
95%-50%	10.3 (+1.1) (-2.1)	10.7 (+1.4)(-1.2)	10.5 (+1.4) (-2.3)	10.1 (+1.4) (-1.2)
90%-50%	6.6 (+0.5) (-0.9)	6.9 (+0.7)(-0.4)	6.7 (+0.6) (-1)	6.7 (+0.5) (-0.4)

The penumbra of the lateral edge is more important than the x collimator penumbra, in the same way that penumbra of the anterior edge is bigger than the y collimator penumbra.

Penumbras of only leaves is superior than x and y collimator penumbras.

6 MV photons : 80%-20% x collimator : 6.4mm
 anterior leaf edge : 9.5mm

18 MV photons : 80%-20% x collimator : 8.2 mm
 anterior leaf edge : 11.6 mm

The mean values for x and y collimator are very closed, like those of the two edges of a leaf: So, we can consider a **overall mean penumbra** for collimators (x,y) and for the leaves.
 For the treatment dosimetric study, we have chosen like **useful penumbra value**, the maximum value. (table 2)

Table 2 : Useful penumbras for (x,y) collimators and leaves

X6 photon	x,y collimator	leaves
80%-20%	7.8	10.1
50%-20%	4.3	6.5
95%-50%	8.7	8.9
90%-50%	5.5	5.9

X18 photon	x,y collimator	leaves
80%-20%	9.3	12.2
50%-20%	5.3	8.2
95%-50%	11.9	11.5
90%-50%	7.3	7.2

If we consider the internal (95%-50%) or (90%-50%) penumbra, the useful penumbra value is the same for the collimators and the leaves. But the external penumbra defined by the distance (50%-20%) is more important for the leaves than for the collimators.

During the dosimetry by computer, the choice of the physicist is to have the target volume surrounding with the 95 % (or sometimes the 90% isodose).

The knowledge of the distance between the 95% (or 90%) and 50% isodose relative to the beam axis is useful to determine the supplementary margins required to fit the target volume.

The first aim of a collimator is to reduce the irradiation field to protect the surrounding healthy tissues. The study of the distance between 50% and 20% isodoses relative to the beam axis is interesting.

Results confirm that it's better to protect critical organs with one collimator than with leaves.

CONCLUSION

The goal of this work is to measure the penumbra given by the different parts of the Philips multileaf collimator and to evaluate margins required to fit the target and critical volumes during the realization of dosimetric treatment plan with a computer.

Results show that using leaves introduce more important external penumbra.

Finally, we can associate for each energy a penumbra value to the part of the collimator independent of the distance between axis and edge of the collimator.

This work want to be a supplementary decisive tool for physician and physicist in the choice (size and shape) of the irradiation fields diuring a dosimetric treatment planning.

The integration of results into a software of leaves positionning (Philips MLP system for example) [6] can be considered.

It's sure that it's interesting and important to know what become penumbras when several leaves are closed to each other (for example when they are put in stairs). This is the continuation of this study.

REFERENCES

1. Radiothérapie Conformationnelle. Fédération nationale des Centres de Lutte Contre le Cancer
Bull Cancer 82 (1995) 325-330
C.Carrie and All
2. Multileaf collimation versus alloy blocks: Analysis of geometric accuracy
Radiation Oncology Biol. Phys 32 (1995) 499-506
3. The acceptability of a multileaf collimator as a replacement for conventional blocks
E.M.Fernandez, G.S.Shentall, W.P.M. Mayles, D.P.Dearnaley
Radiotherapy & Oncology 36 (1995) 65-74
4. Clinical dosimetry for implementation of a multileaf collimator.
Arthur L.Boyer, Timothy G.Ochran, Carl E.Nyerick and Timothy J.Waldron
Calvin J.Huntzinger
Med.Phys 19 (1992) 1255-1261
5. The design and performance characteristics of a multileaf collimator.
Med. Phys. Biol. 39 (1994) 231-251
6. A multileaf collimator field prescription preparation system for conventional therapy
M.N.DU and all
Radiation Oncology Biol. Phys 32 (1995) 513-520

**NEXT PAGE(S)
left BLANK**



BE 97 0000 6

Modification of a 3D-planning system for use with a multileaf collimator.

Van Duyse, B., Colle, C., De Wagter, C., and De Neve, W.

Department of Radiotherapy, Nuclear Medicine and Experimental Cancerology, University Hospital, Gent, BELGIUM.

Introduction

Recent technological developments such as 3D planning and modern linear accelerators make it possible to treat more patients with conformal radiotherapy. This can be done using traditional Cerrobend blocks to shape the beam. This method however is time consuming since a block has to be made for each individual beam. During the treatment, the room has to be entered between different beams to replace the block. Therefore, a multileaf collimator (MLC) was retrofitted on our Philips SL25 linear accelerator. This MLC has 3 major advantages :

- 1/ There is no need to make Cerrobend blocks.
- 2/ There is no need to enter the treatment room between different beams.
- 3/ There is more freedom of movement, since there is no tray hanging under the machine head.

One great disadvantage was that all leaf settings had to be derived manually from simulator films. Once known they had to be fed into the MLC computer using the keyboard. This method takes a lot of time and introduces potential errors during the data transfer.

A much more efficient way is to determine the leaf settings on the planning system and to send them over a network to the MLC computer.

At our department, conventional 2D treatment planning is done on a Philips Oncology Support System (OSS). There is no way to plan the leaves on this system, so we bought a commercially available program that determines the leaf settings from the digitized field shape and creates a binary file which can be imported directly into the MLC computer.

For the 3D treatment planning on the other hand, we use the GRATIS(tm) software package by Prof. G. W. Sherouse. As the source code is freely available, we were able to write an extension to plan the leaf settings. A link was made between the planning computer and the MLC computer, allowing data transfer and avoiding manual data handling.

Methods and materials

The GRATIS(tm) 3D planning system runs under a UNIX environment. The program is completely written in the C programming language and uses the X Window System.

The source code is freely available for the users. At our department the software runs on a Digital Alpha Station 3300X.

Our goal was to write an extension for the MLC, changing as little as possible for the

GRATIS(tm) users. This was realized by adding the leaves in the Beam's Eye View (BEV) if a machine with MLC is selected. The leaves can be set automatically or by hand. This is the only change that has been made for the users.

First of all a distinction had to be made between a machine with and one without an MLC. Each machine used in the planning system has 5 files which determine its characteristics : "unit", "time_calc", "sar", "tray" and "filter". A field called "mlc" was added to the "unit" machine file. The value of "mlc" is set to 1 if an MLC is present and is set to 0 if a traditional collimator head is used.

The main change was made in the Virtual Simulator(tm). The BEV window was made sensitive for mouse movements with the right mouse button pressed. In that way, the leaf closest to the pointer can be selected and dragged to the desired position.

Every time the beam outline is changed, an array called "Collimated Beam Outline" (CBO) is written that contains all points which determine the beam contour at isocentric distance. When an MLC is used, these points are the corners of the leaves. Since the program uses this CBO to calculate the intersection of a beam with CT slices, no further adjustments had to be made to get the right shape of the beam in these slices or in the XVIEW and YVIEW windows. Even when a Digitally Reconstructed Radiograph (DRR) is calculated, the beam shape created by the leaves is superimposed on the image without any further adjustments.

The numerical values of the leafsettings are displayed in the BEV.

In Release 5 there is a tool, called autobeam, which draws a beam outline around a specified anatomical structure (anastruct) with respect to a user-defined margin. The result of this calculation is a Beam Outline (BO). For normal blocks, this BO is combined with the diaphragms to produce the CBO. When a machine with MLC is used however, just after the BO is calculated, the leaf settings are determined by placing the middle of the leaf on the BO. For the upper leaf pair used to determine the beamshape, the lower corner of the leaves is placed on the BO, avoiding problems when the top of the BO lies under the middle of the leaf. For the lowest leaf pair used, the top corners are set at the BO. The CBO is then written with the corners of the leaves, just as with manual leaf placement. If this shape does not satisfy the radiotherapist each leaf can be adjusted manually.

The Y backup jaws are positioned at the largest opening of the leaves. All leaves lying under the X diaphragms are closed. In this way, the setup of the leaves and the diaphragms is the same as on the real linear accelerator.

When leaving the Virtual Simulator(tm), a file containing all beam characteristics is created for each beam. If a machine with MLC is used, a second file is generated with data needed by the MLC computer to make a beam description. This is an ASCII file containing the patients name, energy, diaphragm positions, accessory fitment and, of course, the leafsettings. This file has to be converted to a binary file which can be read by the MLC computer. The conversion is done on the planning computer and the data is transferred over a local ethernet network using the TCP/IP protocol.

Results

An important benefit of the MLC extension is the opportunity to enhance the ease of quality control.

The beam outline, formed by the leaves can be plotted at any desired Target Film Distance (TFD). This plot can then be compared with the light field of the linac to check the leaf settings.

The generated DRR's can be compared directly with the portal films or images.

With the leafs drawn on this DRR, a lot of reference points can be used to find possible discrepancies.

To check the relative dose calculation, a plane perpendicular to the beam axis was scanned in a PTW water phantom for both photon energies (6MV and 25 MV). The SSD used was 95 cm and the depth 5 cm. The step size of the matrix was 2.5 mm. Isodoses were calculated using MEPHYSTO, the software package from PTW that controls the water phantom. The comparison of the measured and the calculated 50% and the 90% isodoses are drawn in Fig. 1 and Fig 2. The dashed line is the measured isodose. Each tick on the axes represents one cm.

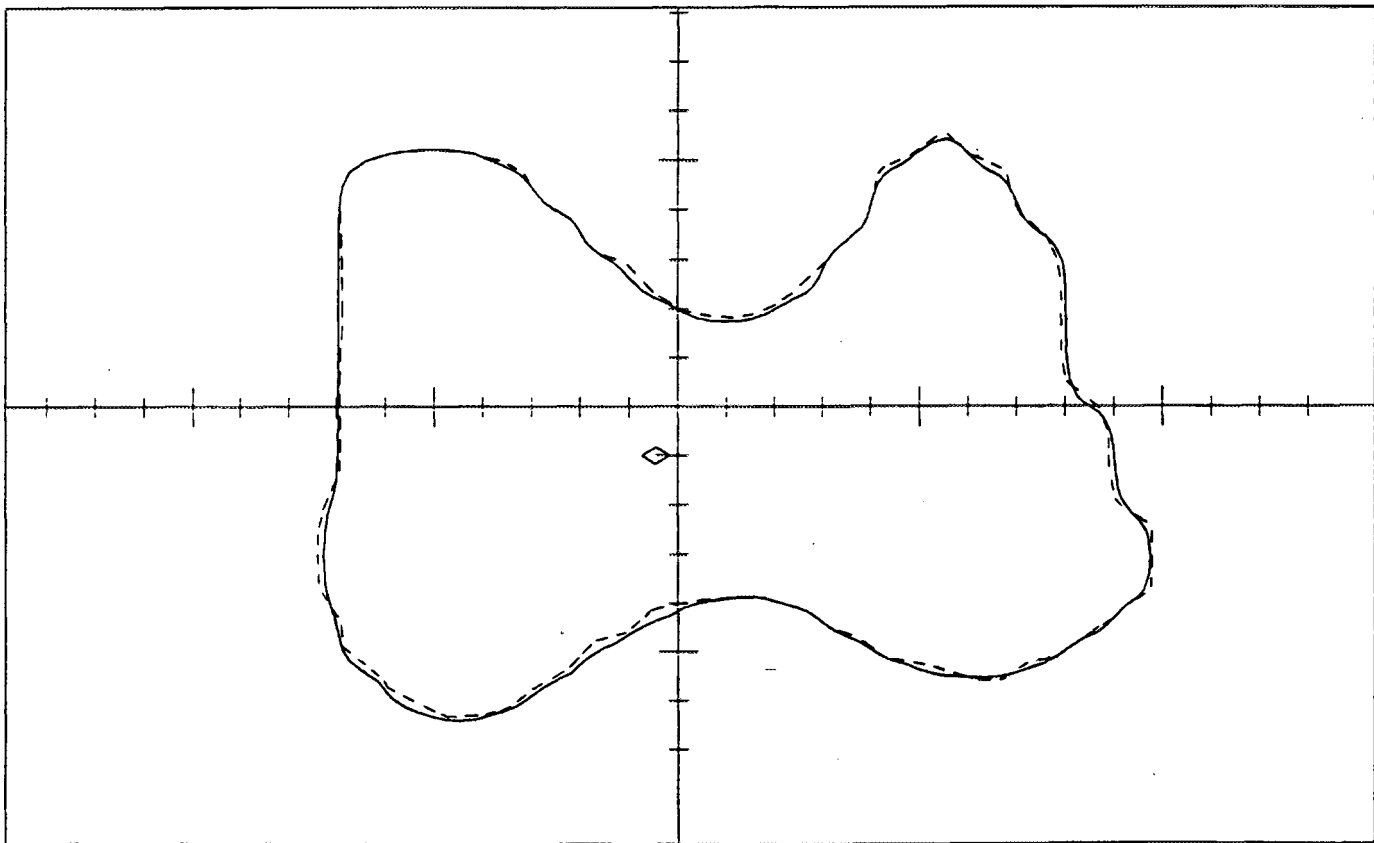


Fig 1.a : 50 % isodose (6 MV photons)

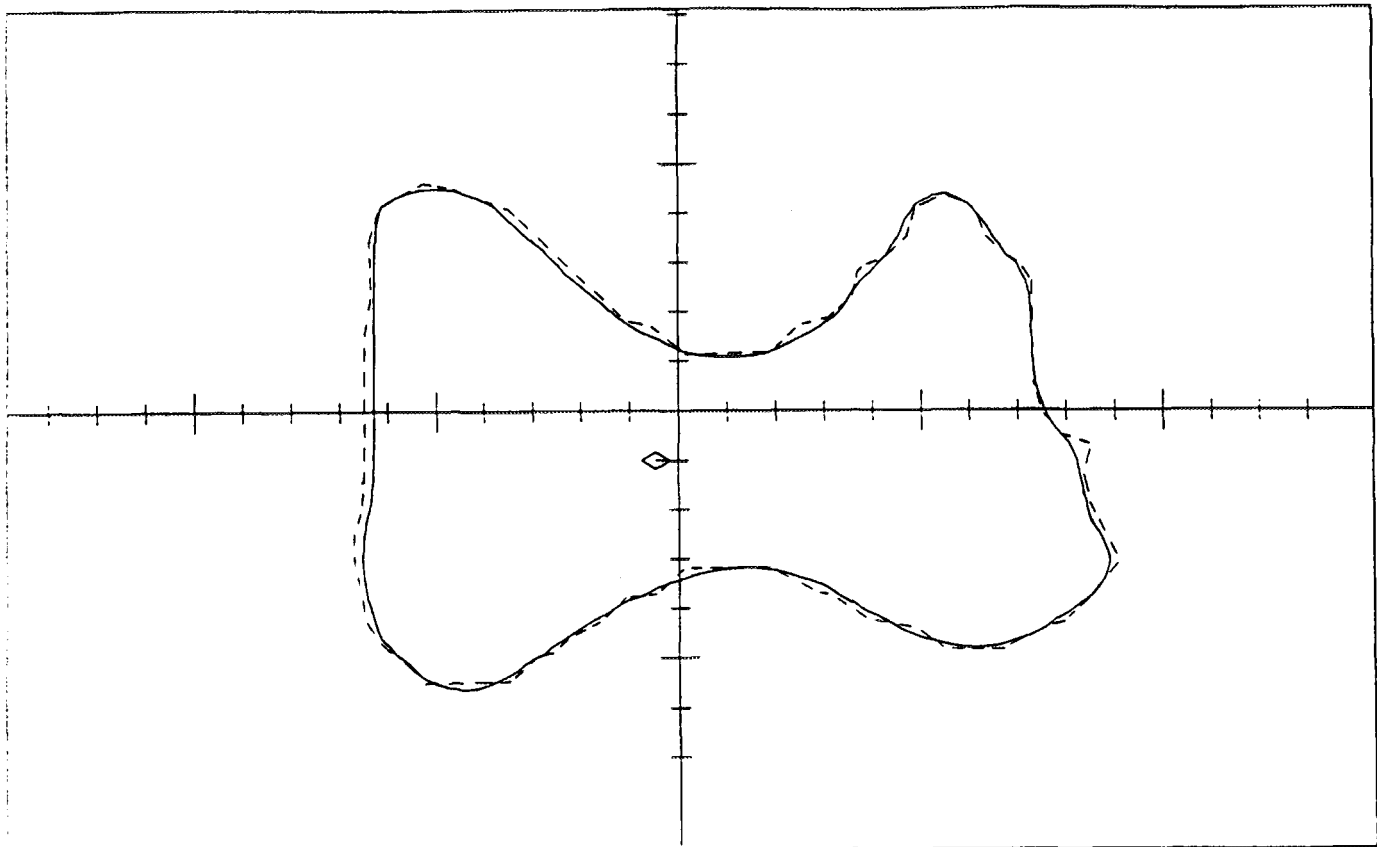


Fig 1.b : 90 % isodose (6 MV photons)

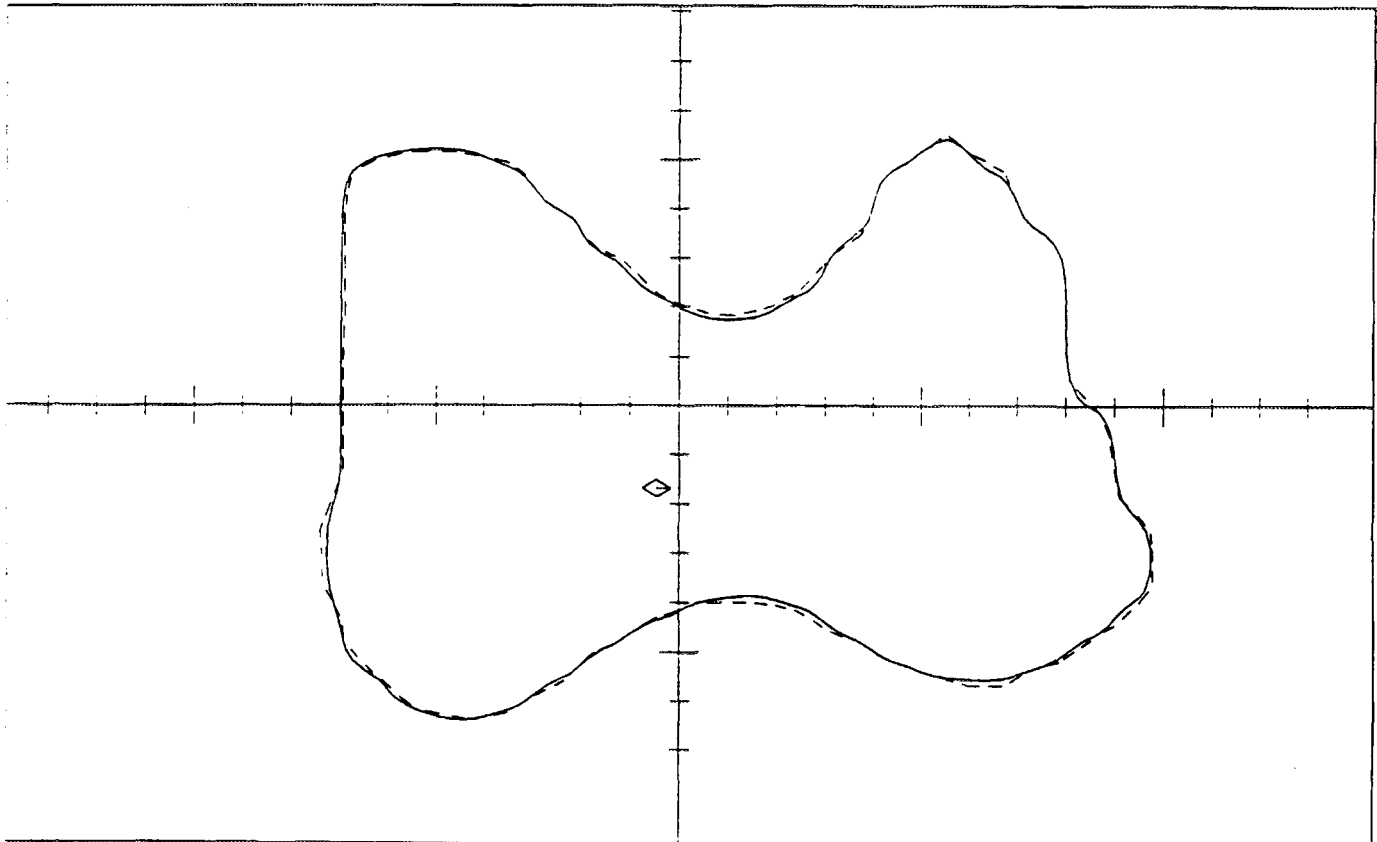


Fig 2.a : 50 % isodose (25 MV photons)

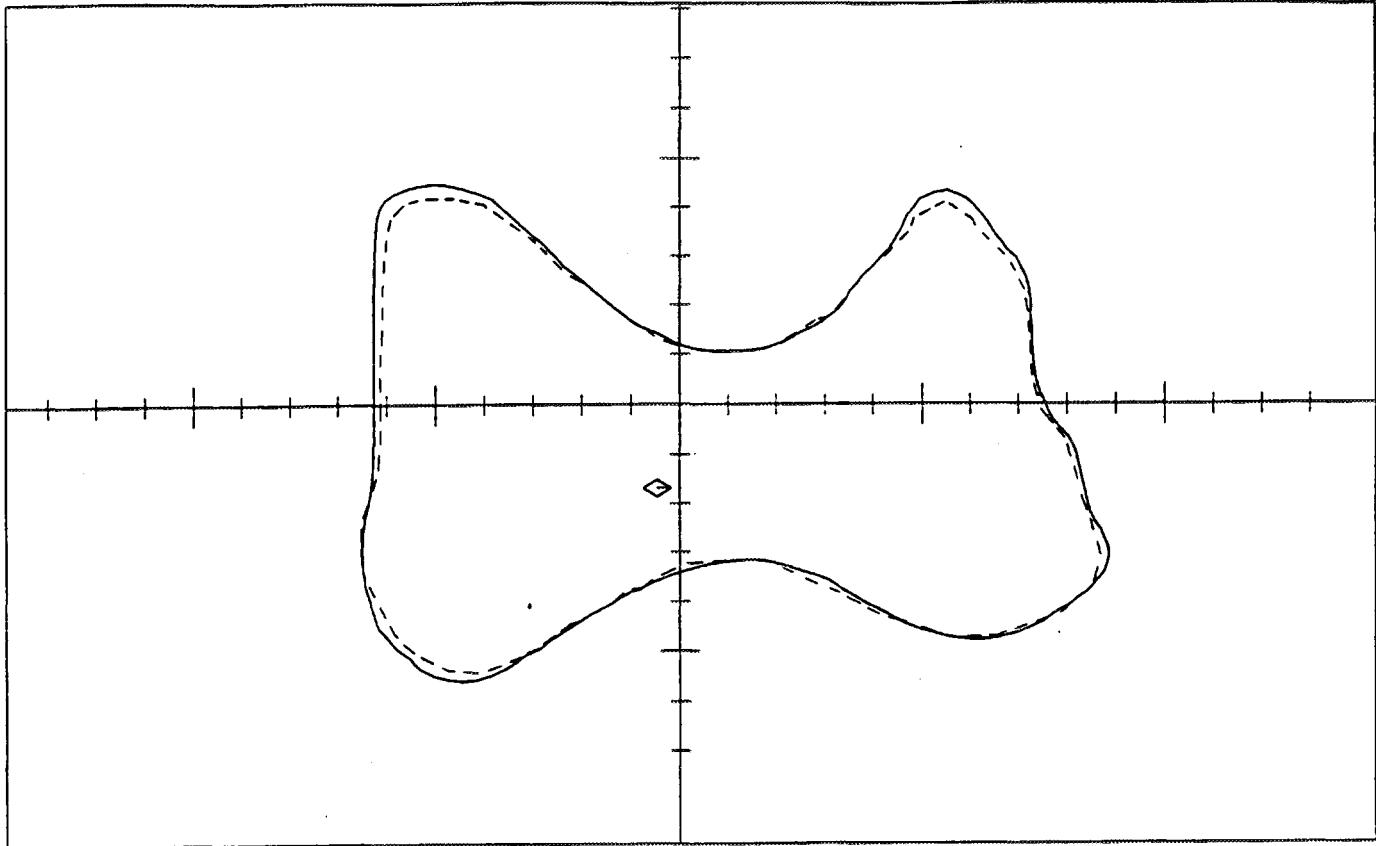


Fig 2.b : 90 % isodose (25 MV photons)

The calculation of the absolute dose in water however needed some modifications. For a few fields, the output factors were measured and compared with the results of the planning system. (Table 1 & 2)

The field called irreg is the shape used for the relative measurements.

fieldname	measured output factor	calculated output factor without adjustment	error	calculated output factor after adjustment	error
5x5	94.76 %	94.70 %	0.06 %	94.67 %	0.09 %
10x10	100.00 %	100.00 %	0.00 %	100.00 %	0.00 %
15x15	102.84 %	102.85 %	0.01 %	102.84 %	0.00 %
20x20	104.92 %	104.90 %	0.02 %	104.90 %	0.02 %
Ø 5 cm	92.22 %	94.85 %	2.85 %	93.35 %	1.22 %
Ø 10 cm	98.54 %	100.30 %	1.78 %	98.88 %	0.35 %
Ø 15 cm	101.63 %	103.00 %	1.35 %	101.69 %	0.06 %
Ø 20 cm	103.90 %	105.02 %	1.08 %	103.84 %	0.06 %
irreg	99.35 %	102.84 %	3.51 %	100.27 %	0.93 %

Table 1 : Output factors for 6 MV photons

fieldname	measured output factor	calculated output factor without adjustment	error	calculated output factor after adjustment	error
5x5	90.92 %	91.98 %	1.17 %	91.95 %	1.01 %
10x10	100.00 %	100.00 %	0.00 %	100.00 %	0.00 %
15x15	103.50 %	102.89 %	0.59 %	102.90 %	0.58 %
20x20	105.82 %	105.10 %	0.68 %	105.11 %	0.67 %
Ø 5 cm	87.90 %	91.87 %	4.51 %	90.24 %	2.66 %
Ø 10 cm	98.20 %	100.00 %	1.83 %	98.20 %	0.00 %
Ø 15 cm	102.12 %	102.89 %	0.75 %	101.71 %	0.40 %
Ø 20 cm	104.50 %	105.10 %	0.57 %	103.83 %	0.64 %
irreg	98.83 %	101.81 %	3.02 %	99.30 %	0.48 %

Table 2 : Output factors for 25 MV photons

Especially for small and irregular fields there was a quite important difference between the measured and the calculated dose. The reason for this is the determination of the collimator scatter factor (Sc). Without adjustment, the Sc is taken which matches the backup diaphragm settings. The part of the beam that is determined by the leaves only is not taken into account, so the calculated Sc is too large.

This problem was solved by calculating the total area between the leaves and using the Sc of the equivalent rectangular field with the same area and height. The results of this modification can be found in Table 2. The function `lookup_Sc` was changed so that a distinction is made between a machine with an MLC and one without. If no MLC is present, nothing is changed, but when the MLC is used, the Sc is recalculated in the way described.

Conclusions

Most of the advantages of an MLC are lost if no proper planning system is used to plan the leaf settings. A library of standard shapes is available, but mostly these shapes do not meet the needs of conformal radiotherapy. One is almost obligated to buy a new planning system with an MLC to work efficiently. With our extension we have overcome these problems : we no longer have manual data transfer of the leaf settings and in that way the chance of introducing errors is minimized.

Some more fine tuning of the determination of the collimator scatter factor (Sc) is desirable.

References

- Jordan T. J. and Williams P.C., The design and performance characteristics of a multileaf collimator, *Phys. Med. Biol.* 39: 231-251, 1994.
- Perez C.A., Purdy J.A., Harms W., Gerber R., Graham M.V., Matthews J. W., Bosch W., Drzymala R., Emami B., Fox S., Klein E., Lee H.K., Michalski J.M. and Simpson J.R., Three-dimensional treatment planning and conformal radiation therapy: preliminary evaluation, *Radiotherapy and Oncology* 36: 32-43, 1995.
- Zhou S. and Verhey L.J., A robust method of multileaf collimator (MLC) leaf-configuration verification, *Phys. Med. Biol.* 39: 1929-1947, 1994.
- Stein J., Bortfeld T., Dorschel B. and Schlegel W., Dynamic X-ray compensation for conformal radiotherapy by means of multi-leaf collimation, *Radiotherapy and Oncology* 32: 163-173, 1994.
- Fernandez E.M, Shentall G.S., Mayles W.P.M. and Dearnaley D.P., The acceptability of a multileaf collimator as a replacement for conventional blocks, *Radiotherapy and Oncology* 36: 65-74, 1995.
- Boesecke R., Becker G., Alandt K., Pastyr O., Doll J., Schlegel W. and Lorenz W.J., Modification of a three-dimensional treatment planning system for the use of multi-leaf collimators in conformation radiotherapy, *Radiotherapy and Oncology* 21: 261-268, 1991.
- Huq M.S., Yu Y., Chen Z. and Suntharalingam N., Dosimetric characteristics of a commercial multileaf collimator, *Med. Phys.* 22 (2): 241-247, 1995.
- Philips Medical Systems, Service Manual: System, SL Series Linear Accelerator with Multileaf Collimator, Customer Acceptance Test Schedule, Publication Nr. 4513 370 35585, Philips Electronics U.K. Limited, 1994.
- Philips Medical Systems, Multileaf Collimator (MLC) Operator's Manual for MLCsa1 Version, Operator's Manual, Publication Nr. 4522 984 40891/764, Philips Electronics U.K. Limited, 1994.
- Philips Medical Systems, Multileaf Collimator (MLC) Operator's Manual for MLCsa1 Version, Operator's Manual, Publication Nr. 4522 984 40891/764, Philips Electronics U.K. Limited, 1994.
- Philips Medical Systems, Multileaf Collimator (MLC) Geometric Prescription Limits & Constraints, Publication Nr. 4522 984 12101/764, Philips Electronics U.K. Limited, 1994.
- Philips Medical Systems, User Manual for Interfacing External Computer Systems to The MLC, Publication Nr. 4522 984 40851/764, Philips Electronics U.K. Limited, 1994.
- Philips Medical Systems, Service Manual: Subsystem, Linac Assembly, Publication Nr. 9811 731 60005, Philips Electronics U.K. Limited, 1985.
- Griffiths S. and Short C., *Radiotherapy: Principles to Practice*, A manual for quality in treatment delivery, Churchill Livingstone, 1994.
- Khan F.M., *The Physics of Radiation Therapy*, Williams & Wilkins, Baltimore, USA, 1984.



APPLICATIONS OF THREE-DIMENSIONAL IMAGE CORRELATION IN CONFORMAL RADIOTHERAPY.

M van Herk, KGA Gilhuijs, H Kooy^{*}, S Kwa, JV Lebesque, S Muller, JC de Munck, A. Touw, Radiotherapy department, The Netherlands Cancer Institute, Amsterdam, The Netherlands
^{*}Joint Center for Radiation Therapy, Harvard Medical School, Boston, MA

Note: this paper contains parts from: van Herk, M.; Kooy, H.M. Automatic three-dimensional correlation of CT-CT, CT-MRI, and CT-SPECT using chamfer matching. Med. Phys. 21: 1163-1178; 1994 and van Herk, M., Bruce, A., Kroes, G., Shouman, T., Touw, A., and Lebesque, J.V., Quantification of organ motion during conformal radiotherapy of the prostate by three-dimensional image registration, Int. J. Radiat. Oncol. Biol. Phys., 33: 1311-1320; 1995.

ABSTRACT

The development of techniques for the registration of CT, MRI and SPECT has created new possibilities for improved target volume definition and quantitative image analysis which are particularly useful for conformal radiotherapy. Our technique, based on chamfer matching, is suitable for automatic 3-D matching of CT with CT, CT with MRI, CT with SPECT and MRI with SPECT. The following applications will be discussed:

Target volume definition. By integrating CT with MRI, the diagnostic qualities of MRI are combined with geometric accuracy of the planning CT. Significant differences in the delineation of the target volume for brain, head and neck and prostate tumors have been demonstrated when using integrated CT and MRI compared with using CT alone. In addition, integration of the post-operative planning CT with pre-operative scans improves knowledge of possible tumor extents.

Quantification of organ motion. By first matching scans based on the bony anatomy and subsequently matching on an organ of study, relative motion of the organ is quantified accurately. In a study with 4 CT scans of 11 patients, magnitude and causes of prostate motion have been analysed. The most important motion of the prostate is a forward-backward rotation around a point near the apex caused by rectal volume differences. Surprisingly, significant correlations were also found between leg and prostate motion and legs and bladder filling.

Follow-up studies. By integrating functional lung images made before and after radiotherapy with the planning CT, the local relation between change of function and delivered dose can be quantified accurately. The technique of chamfer matching is a convenient and more accurate alternative for the use of external markers on CT and SPECT. In some cases, late damage visible in diagnostic scans can be related to local radiation dose, improving follow-up diagnostics.

Conclusion. 3-D image integration plays an important role in assessing and improving the accuracy of radiotherapy and is therefore indispensable for conformal therapy. However, user-friendly implementation of these techniques remains required to facilitate clinical applications on a large scale.

INTRODUCTION

Improvements in the accuracy of radiation therapy delivery, such as achieved through verification using electronic portal imaging [e.g., Bel et al, 1993], have led to the possibility of applying more accurate treatment techniques. However, before reducing treatment margins, other uncertainties should be analysed as well. We have applied our experience in the field of image processing derived from our electronic portal imaging work to develop a new technique for 3-D image registration based on chamfer matching. With this technique, different scans from the same patient can be placed automatically in the same coordinate system derived from a specified part of the anatomy, e.g., the skull or the pelvis. Previous methods for this purpose were often based on landmarks or interactively delineated contours [Kessler et al., 1991]. There are a number of applications of 3-D matching in the field of conformal radiotherapy. A first application is the pixel by pixel combination of CT and MRI to combine the diagnostic quality of MRI with the geometric accuracy and density information of CT for delineating the tumor and planning the treatment. Other applications are based on the accurate comparison of repeated scans of the same patient to analyse organ motion or follow-up on tumor control or normal tissue damage. The objective of this paper is to provide a brief overview of these applications.

MATERIAL AND METHODS

2-D chamfer matching

The technique of chamfer matching [Borgefors, 1988] was originally applied in the field of aerial photography, e.g., to overlay images made with radar and using infrared imaging equipment. In this technique, a set of contour points is first derived from one image. Next, the corresponding structure in the other image is segmented. A distance transform [Borgefors, 1986] is next applied to this segmented image, i.e., all pixels on the structure will be set to zero and the value of all other pixels is set to the smallest distance of this pixel to the segmented structure. This image can then be used as a lookup table to quickly measure the distance of an arbitrary point to the segmented structure. By overlaying the set of contour points on the distance transform a cost function that describes the goodness of fit can be derived easily, e.g., the average pixel value under all contour points describes the average distance between both structures. Just as simple, RMS or other distances can be evaluated quickly. By numerical optimization of this cost function matching takes place (Fig. 1). Because the distance transform can be computed recursively and only the set of contour points (instead of the whole volume) needs to be transformed (translated, rotated, scaled) during the optimization, chamfer matching is a very fast procedure. For example, matching of 2-D structures such as portal field edges takes less than a second on a modern PC. In addition, the method is quite robust against noise and small shape errors, making it an ideal solution for the latter application [Gilhuijs et al, 1993].

An important finding from our work in the field of electronic portal imaging is that chamfer matching still converges to the visually preferred solution if the segmentation of the second image is extremely poor [Gilhuijs et al, 1993]. For that reason, matching of the anatomy can be achieved automatically. The anatomy in the reference image (simulator image, DRR) is described in the set of contour points and segmentation of the portal image is performed using a simple top-hat filter. This filter detects most of the bone ridges, but parts of the anatomical structures are often missed due to insufficient contrast and artifacts are often introduced in the segmented image due to noise.

Still, with this filter, reliabilities up to 98% have been achieved for matching AP pelvic images. Improved filters, such as the multiscale medial axis transform [Fritsch et al, 1994], further improve the reliability, making the method also more suitable for lateral pelvic fields and many other treatment sites [Gilhuijs, 1995].

3-D chamfer matching

Extension of chamfer matching to 3-D is relatively straightforward [van Herk et al, 1993]. Contour points derived by autotracing each CT slice at suitable threshold for bone are stacked to form a 3-D description of the anatomy in the CT scan (Fig. 2). Because a poor segmentation of the other image is expected to be adequate we have first used a simple grey-value segmentation technique for the MRI. In this technique, the average grey value of the brain is derived by analysis of the histogram of pixel value of the MRI scan. Next, two thresholds are chosen at fixed percentages from this average value and segmentation takes place by selecting all pixels with a value between these two thresholds (Fig. 3). For the distance transform and contour point description it has been taken into account that the slice distances applied for medical scans are often non-uniform. For optimization of the cost function, the simplex method is used [Nelder and Mead, 1965]. At least 6 parameters are optimized: 3 translation values and 3 rotation values. However, also scaling factors along 3 axes can be taken along in order to provide a first order correction for MRI distortions. To improve the reliability of CT-MRI matching, a pre-match is performed using chamfer matching on the patient outlines. The reliability and reproducibility of the method were estimated using a perturbation method. Matching was restarted thousands of times from a random starting position according to a clinically observed distribution of orientation differences. Failures to converge to the visually preferred match were counted to obtain a figure for the reliability, while small differences in the final match parameters were used to estimate the reproducibility. The capture range is defined as the initial displacement of one scan to another (defined as the average vector length of the displacement of all contour points under an arbitrary rotation and translation) at which 90% of the optimizations converge.

Hardware and software environment

The correlation software was implemented in the AVS (Application Visualization System) software system (AVS Inc, Waltham MA). This processing and visualization tool allows users to construct their own visualization applications, by combining software components into executable flow networks. The software components, called modules, implement specific functions in the application such as filtering, mapping and rendering. An advantage of using AVS for prototype software development is that new modules can be easily added, while there exists a sufficient base of software modules to test newly developed components independently. The flow networks are created using a graphical development tool, the network editor. For the image correlation application that is described in this study many additional software modules were written in C. Many of these modules will not be used in the final application but have been written to supply a suitable test environment. In a later stage, the same code base has been integrated in our software environment used for portal image analysis, QUIRT (quality assurance and imaging for radiation therapy) which has been extended with a windows NT user interface.

Fig. 1. Schematic representation of 2-D chamfer matching. The contour points (white) are aligned with the segmented structure (black) by iteratively minimizing the average gray value of the distance transform image under the contour points.

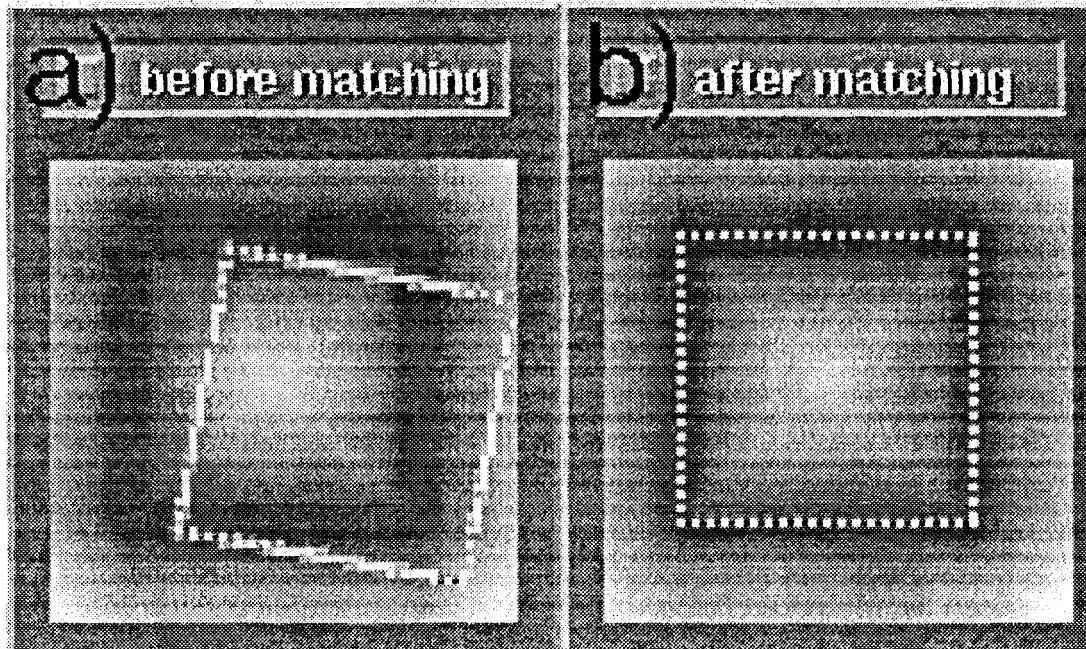
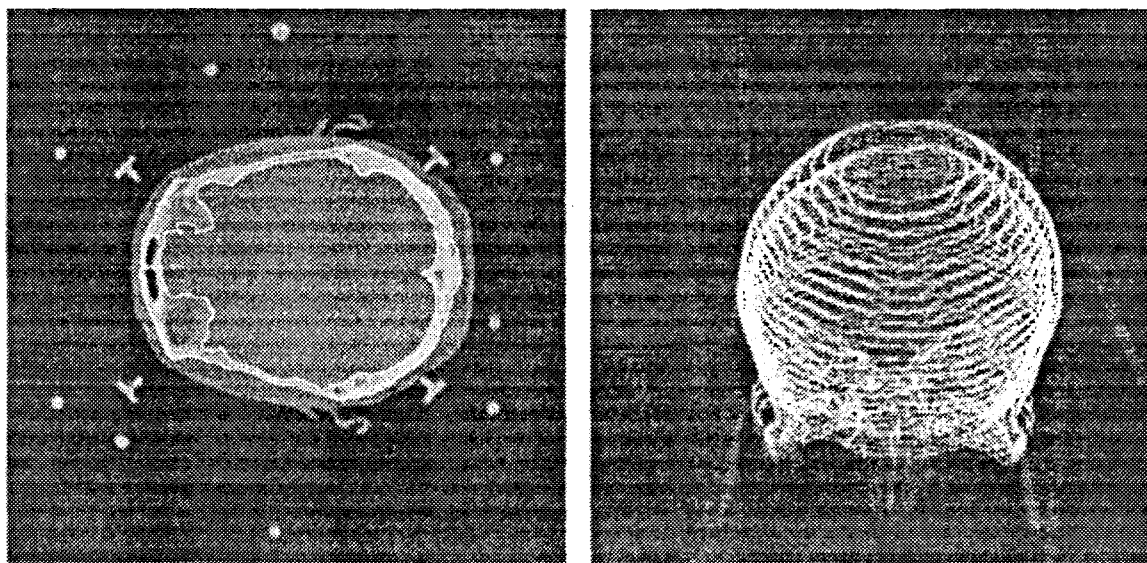


Fig. 2. Selection of contour points from a CT scan. First all contours are autotraced at a suitable threshold value for bone. Next, contours smaller than a given size are deleted and the remaining contours are stacked.



Traced and classified

Ring stack

Image material

In this study we have applied CT scans from a Siemens Somatom Plus. Typically slice distances are 3 mm in the region of the tumor and 5 mm for the rest of the scan. The number of pixels per slice is either 512 x 512 or 256 x 256 and typically 30 to 60 slices are used. The MRI scans are obtained from a Siemens Magnetom 63SP. Typical sequences that are applied are T2 (resulting also in a proton density (PD) image), T1 with and without contrast and a flash 3-D sequence. For matching, we apply most often the PD or a T1 scan. Because the PD and T2 scans are in by definition in the same coordinate system, the match of CT with the PD scan can be used directly to fuse CT and T2 images.

Visualization

We implemented several visualization techniques for the qualitative assessment of the match quality. Comparison is based on the resampling of a single, arbitrarily oriented slice, from volume B and the spatially corresponding slice (after matching) from volume A using trilinear interpolation. Selection of the displayed slice is interactive (resampling of a new slice takes less than a second). The two corresponding slices are mixed using various color schemes or image garbling procedures which produce checkerboard-like alternations between, e.g., CT and MRI. For three-dimensional visualization of the correlated volumes, Digital Reconstructed Radiographs (DRR) are created either by ray tracing through the three-dimensional data, or by perspective projection of selected surface points. The latter option, even when using several ten thousands of points, is fast enough for interactive adjustment and is useful for obtaining the initial guess for matching or for visual feedback when clipping mobile anatomy. In practice, an initial guess of 0 degrees or 180 degrees rotation is often sufficient.

Organ motion studies

Four CT scans were made during the course of conformal treatment of 11 patients with prostate cancer. With the use of a three-dimensional treatment planning system (UM-Plan), the prostate and seminal vesicles were contoured interactively. In addition, bladder and rectum were contoured and the volume computed. Next, the bony anatomy of subsequent scans was segmented and matched automatically on the first scan. Femora and the pelvic bone were matched separately to quantify motion of the legs. Prostate (and seminal vesicle) contours from the subsequent scans were matched on the corresponding contours of the first scan, resulting in the 3D rotations and translations which describe the motion of the prostate and seminal vesicles relative to the pelvic bone. The method measures relative organ motion between two scans, e.g., differences in prostate position. From the four scans made for each patient (A, B, C and D) six parameter differences can be derived: A-B, A-C, A-D, B-C, B-D and C-D. Overall standard deviations of each motion parameter were computed from these differences combined for all patients. Because the difference between two samples from one distribution has $\sqrt{2}$ times the standard deviation of the original distribution, the resulting standard deviations are divided by $\sqrt{2}$ to estimate the standard deviation of each motion parameter of the organ. Correlation coefficients have been computed for most combinations of the different motion parameters and the volume differences of rectum and bladder. In addition, the contribution of each parameter to the standard deviation of each other parameter was

Fig. 3. A simple segmentation scheme for bones in MRI data. (a) One slice of a T1 weighted MRI scan. Due to the lack of water in bone, the skull shows up dark gray. (b) A histogram is derived from all slices and the location of the rightmost peak (corresponding to the brain) is found. Two segmentation thresholds are chosen at fixed fractions of this pixel value. (c) Pixels between the selected thresholds are segmented. A distance transform will be applied to this image.

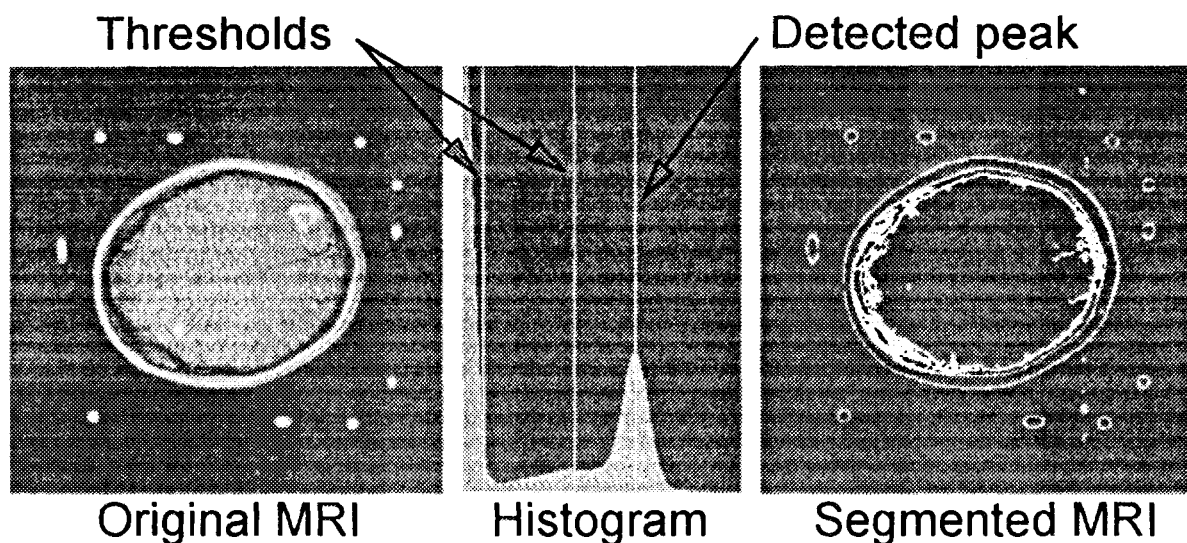
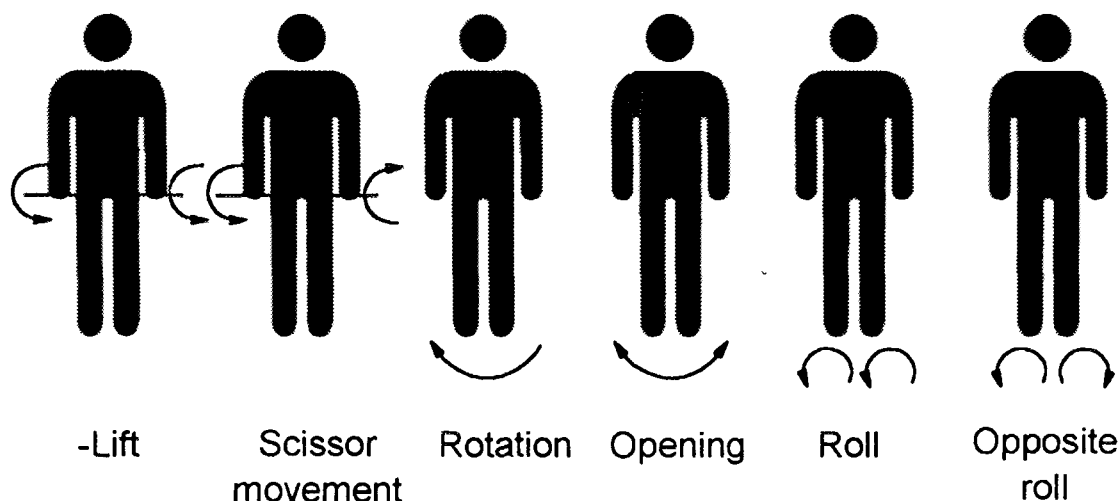


Fig. 4. The following combinations of rotations of the femurs have been considered in our organ motion study.



computed. This contribution, e.g., from parameter A on parameter B, is computed as the standard deviation of B times the correlation coefficient of A and B. This value is equal to the product of the slope of a linear function fitted through B versus A times the standard deviation of A.

Due to the symmetry it can be expected that both legs (femora) have the same influence on movement of organs in the pelvis. However, depending on the type of motion, the motion of left and right leg either have the same or an opposite influence on the organ movement. For this reason, both the sum and the difference of rotation angles of both legs have been used for statistical computation. Six types of leg motion have been considered (Fig. 4).

Follow-up studies

Good visualization of changes in tumour or normal tissue is obtained by matching a follow-up scan with, e.g., the planning CT scan. Because 3-D dose computation is based on the planning CT scan, this match can directly be used to relate visual changes on any anatomical location to the planned dose on that location. By applying functional images for the follow-up scan, measurable changes in function can directly be related to dose on a voxel by voxel bases [Boersma et al, 1993].

RESULTS

CT-MRI matching for target volume delineation

The matching process requires no user interaction and takes about 100 s on an HP715/50 workstation. Tests on clinical data with cost functions based on mean, root-mean-square (RMS) and maximum distances in combination with two general purpose optimization procedures have been performed. The performance of the methods has been quantified in terms of accuracy and capture range (reliability). The best results on clinical data are obtained with the cost function based on the mean distance and the simplex optimization method. The accuracy is 0.3 mm for CT-CT, 1.3 mm for CT-MRI and 1.4 mm for CT-SPECT correlation of the head. The accuracy is usually at sub-pixel level but is limited by geometric distortions, e.g., for CT-MRI correlation. Both for CT-CT and CT-MRI correlation the capture range is about 6 cm, which is higher than normal differences in patient setup on the scanners (less than 4 cm). This means that the correlation procedure seldom fails and user interaction is unnecessary. For CT-SPECT matching the capture range is about 3 cm, and must be further improved. The method has already been introduced in clinical practice: matching of CT and MRI for target volume delineation in radiotherapy treatment planning has been applied routinely since 1992 at Harvard Medical School, Boston [Kooy et al, 1993] and since 1993 at the Netherlands Cancer Institute. The reliability of the method depends for a large deal on the pre-match on skin and is excellent when the whole head is scanned on CT and MRI. However, mobile anatomy, such as the lower jaw, must be clipped interactively. Otherwise, a local minimum is created for a good match of the lower jaw, which influences both the reliability and accuracy of the method. Typically, the complete matching procedure takes only a few minutes. In previous perturbation studies we have found that the reproducibility of the method is on the order of 1 mm translation and 1 degree rotation. These data are in agreement with the accuracy observed by visual evaluation. Recently, we have started studying the use of MRI in the pelvic region. For successful matching in that region, mobile anatomy (legs) and MRI artifacts must be clipped as well. The accuracy of the latter method has not yet been studied in great detail but seems somewhat poorer

Fig. 5. a) Checkerboard visualization of matched CT and MRI. The contrast has been optimized for visualization of the eyes and internal structures of the brain. Due to the partial volume effect, the skull in CT appears to be much broader than in MRI. b) Often very large differences occur in appearance of the tumor in MRI (top) and CT (bottom).

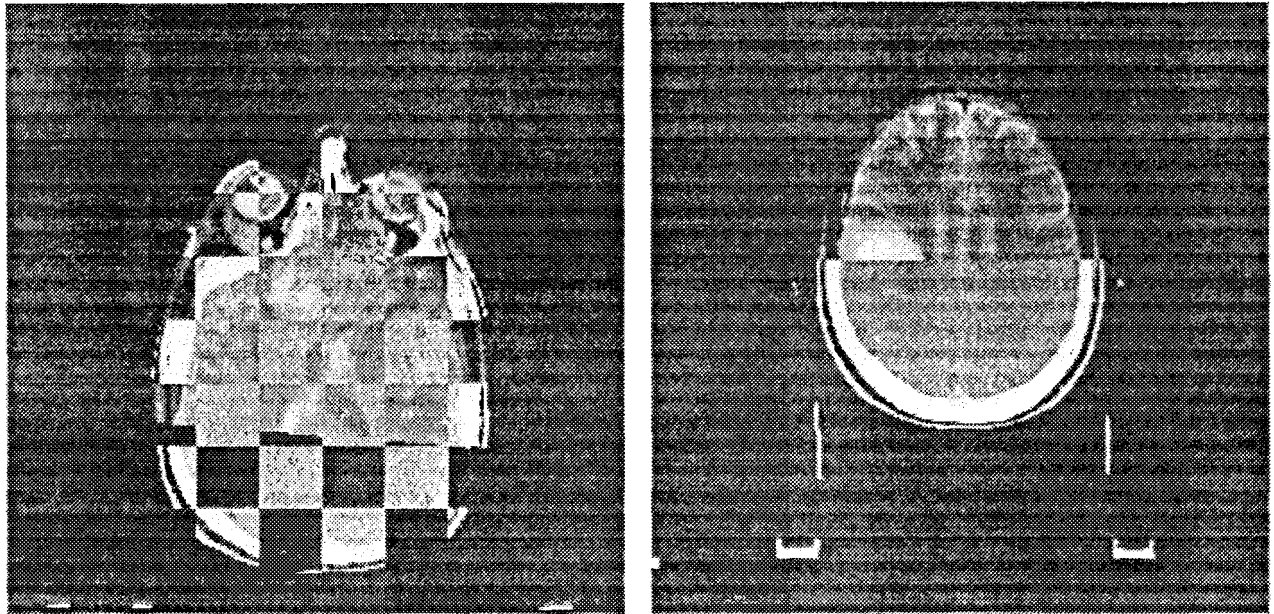
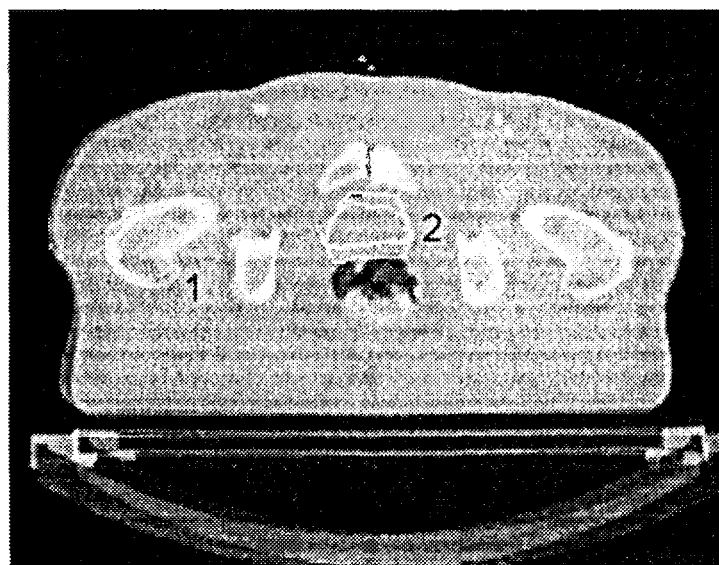


Fig. 6. Visualization of the match between two pelvic CT scans. Part of the intensity in this image has been derived from each scan. Double images are visible where the match is poor due to organ motion, e.g., at the skin surface, left femur (1) and prostate contour (2).



than in the head region. Often, large differences are found in visualization of the tumor in CT and MRI (Fig. 5).

Organ motion studies

Bone matching of two scans with about 50 slices of 256 x 256 pixels takes about 2 minutes on an HP715/50 and achieves sub-pixel registration accuracy (Fig. 6). Matching of the organ contours takes about 30 s. The accuracy in determining the relative movement of the prostate is 0.5 to 0.9 mm for translations (depending on the axis) and 1 degree for rotations (standard deviations) (table I). Because all organ contours are used for matching, small differences in delineation of the prostate, missing slices or differences in slice distance have only a limited influence on the accuracy. Rotations of femora and pelvic bone are quantified with about 0.4 degree accuracy. A strong correlation was found between rectal volume and anterior-posterior translation and rotation around the left-right axis of the prostate (Fig. 7, Table III). Because the rectum volume varies significantly, these parameters had the largest standard deviations of 2.7 mm and 4.0 degrees (Table II). Bladder filling had much less influence. Less significant correlations were found between various leg rotations and pelvic and prostate motion and bladder filling (Fig. 8, Table III). Standard deviations of the rotation angles of the pelvic bone were less than 1 degree in all directions (Table II).

Organ	Parallel to slice	Perpendicular to slice	Rotation
Pelvic bone	0.25 mm	0.5 mm	0.15 degree
Femora	0.25 mm	0.5 mm	0.15 degree
Prostate	0.4 mm	0.7 mm	1.0 degree

Table I. Translational and rotational accuracy of chamfer matching in the pelvic area, specified as one standard deviation in each parameter. The accuracies for matching of the pelvic bone and the femora were estimated from upper error limits determined by visual inspection.

Relative motion	Translation (mm) along axis:			Rotation (degrees) around:		
	L-R	A-P	C-C	L-R	A-P	C-C
Pelvic bone-table	3.9	2.3	8.8	0.9	0.5	0.7
Femora-pelvic bone	1.0	5.4	3.3	2.7	2.0	3.7
Prostate-pelvic bone	0.9	2.7	1.7	4.0	1.3	2.1

Table II. Magnitude of relative organ motion in the pelvic area specified as one standard deviation. These values are quantified from differences in position between pairs of scans by dividing the standard deviation of the differences by $\sqrt{2}$. The values for motion of the pelvic bone relative to the table indicate the setup deviations on the scanner. The statistics for left and right femora have been combined. Because rotations are described around the center of gravity of the applied leg contours, rotations around the joint induce translations as well. The prostate is fairly stable, except for translations in the A-P direction and rotations around the L-R axis. For most parameters, measurement errors are well below the observed variations.

Fig. 7. Correlation between rectal volume differences (measured with the U-Mplan system) and rotation and translation of the prostate (measured using chamfer matching). Increasing rectal filling tends to rotate the prostate around a left-right axis of the patient near the apex of the prostate. The translations are measured because our reference point is the center of gravity of the prostate.

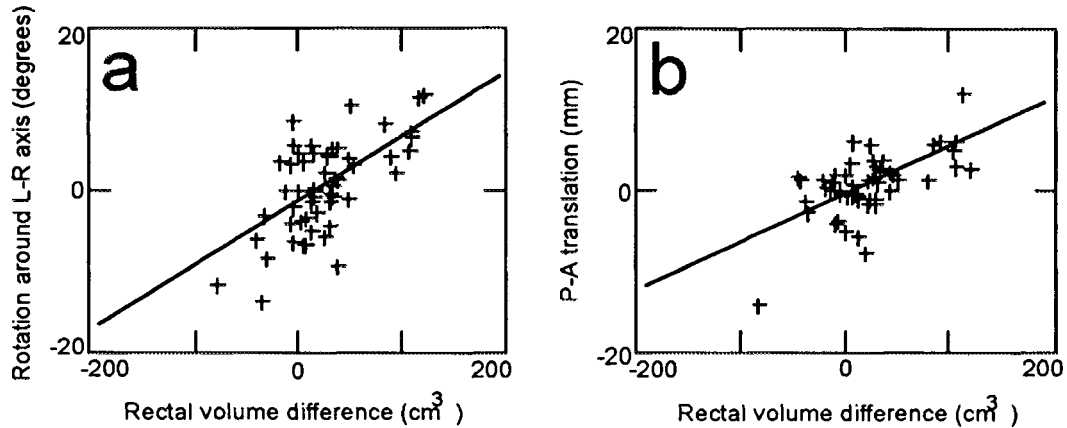
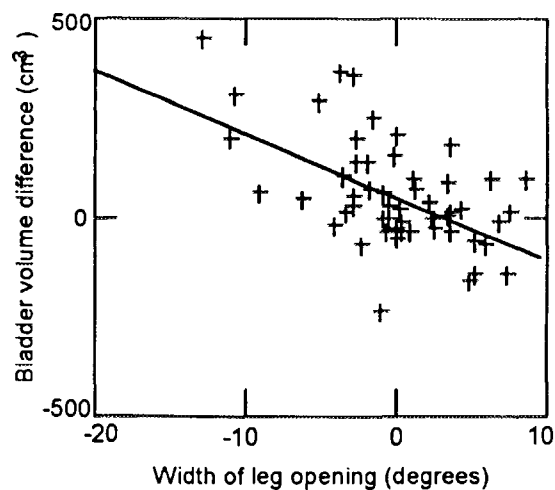


Fig. 8. Correlation of differences in bladder filling and differences in the width of leg opening (averaged over 60 scans of 11 patients). Patients with a full bladder tend to reduce the width of leg opening.



Parameter pair		corr(A,B)	stdev(A)	stdev(B)	slope(A,B)
A	B				
Rectum (cm ³)	Prostate R(L-R) (dg)	0.65	29.8	4.0	0.085
Rectum (cm ³)	Prostate T(A-P) (mm)	0.62	29.8	2.7	0.06
Leg opening(dg)	Pelvis R(L-R) (dg)	0.56	3.3	0.9	0.15
Bladder (cm ³)	Leg opening (dg)	0.52	95.2	3.3	0.02
Leg scissor (dg)	Prostate R(C-C) (dg)	0.47	1.6	2.1	0.6
Leg roll (dg)	Prostate R(C-C) (dg)	0.46	3.7	2.1	0.3
Bladder (cm ³)	Prostate T(A-P) (mm)	0.26	95.2	2.7	0.008
Combination (*)	Prostate R(C-C) (dg)	0.54	3.0	2.1	0.4

Table III. The most significant relations between pairs of measured parameters of organ motion in the pelvic area. Slope(A,B) indicates the slope of a straight line fitted through a scatter plot of B as function of A. Only those relations are included for which the correlation coefficient {corr(A,B)} exceeds 0.325 ($p < 0.01$) and for which the contribution of A to the standard deviation of B {slope(A,B) * stdev(A)} is clinically relevant. An exception is the influence of the bladder on prostate translation which is shown, even though it is non-significant. The slope values {slope(A,B)} can be used to predict the influence of variations in parameter A on parameter B. (*) This combination is computed as follows: $0.5 * \text{leg roll (dg)} - \text{leg scissor (dg)}$.

Follow-up studies

By integrating functional lung images made before and after radiotherapy with the planning CT, the local relation between change of function and delivered dose can be quantified accurately. The technique of chamfer matching is a convenient and more accurate alternative for the use of external markers on CT and SPECT. In some cases, late damage visible in diagnostic scans can be related to local radiation dose, improving follow-up diagnostics. Fig. 9 shows an example of tumor regression over a period of three months in a patient which was treated stereotactically twice at Harvard Medical School. Fig. 10 shows CT scans of a patient with a lung reaction half a year after receiving a mantle field treatment. By correlating the planning CT with the follow-up CT based on the lung tops (the scans were made with the arms in different orientations) the given dose at the point of the lung reaction could be estimated. These data were important for the subsequent clinical decision, because it showed that the lung damage was most likely related to the high local radiation dose.

Fig. 9. Example of tumor regression. Two CT scans of the same patient with three months in-between have been matched based on the skull. The outer enhancement ring is from the first scan, the inner ring is from the second scan.

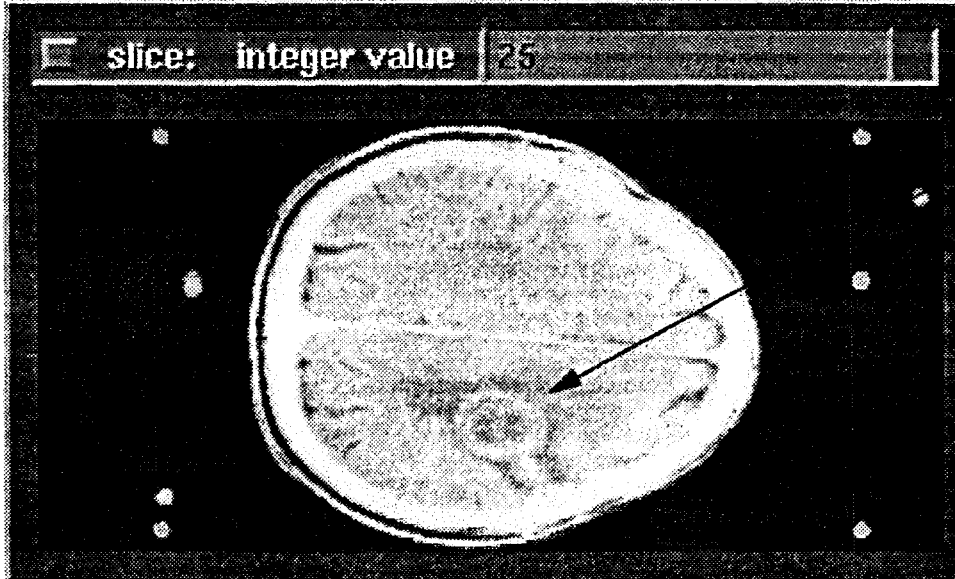
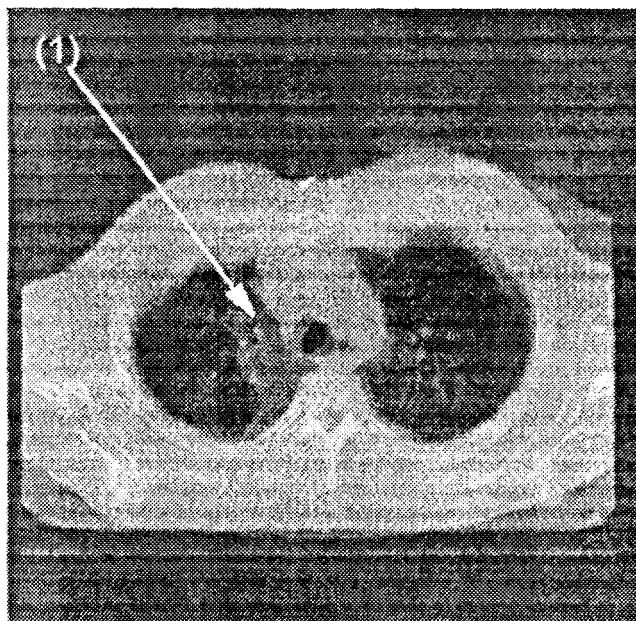
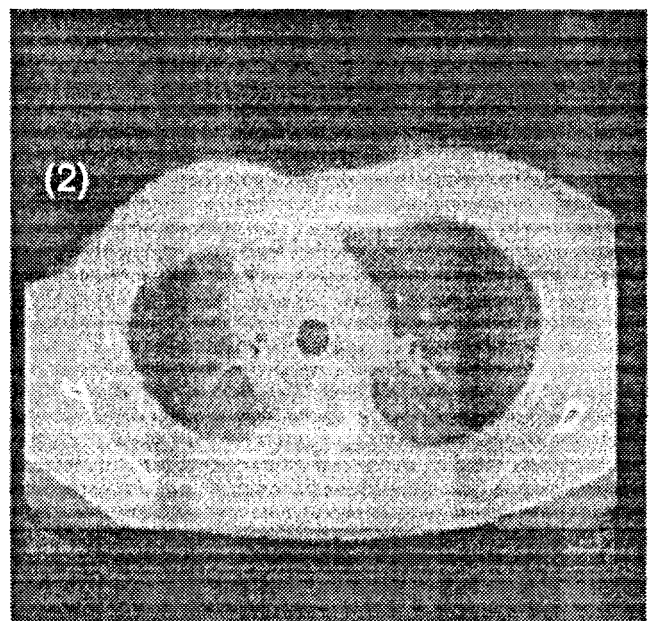


Fig. 10. (1) lung damage visible in a follow-up scan. (2) By overlaying the dose distribution (defined on the planning CT) on the follow-up scan, the given dose at the area of damage can be estimated. A complicating factor for this match was that the scans were made with the arms in a different orientation. Consequently, only the lung tops were used for matching.



Planning CT + follow-up CT)



Follow-up CT + planned dose

DISCUSSION AND CONCLUSIONS

3-D matching

We have developed a general purpose 3D image correlation method based on chamfer matching that does not rely on interactively delineated landmarks or external markers. The method works completely automatically and does not require user interaction for the definition of contours or other tasks, except when mobile anatomy must be excluded for matching. A correlation on routine clinical data, e.g., with non-equidistant slices is performed accurately and reliably in less than two minutes. The result of the correlation is verified by using simple colorwash or garbling schemes in which a slice from one dataset is compared with a resampled slice of the correlated dataset. Since the end of 1992, the method is applied in routine clinical practice at Harvard Medical School.

Using automatic segmentation schemes based on histogram driven thresholding, successful correlation has been demonstrated between CT-CT, CT-MRI and CT-SPECT of the head. In a perturbation study with clinical data, reliability and accuracy of the matching method has been quantified for these three applications with various combinations of cost function, optimization procedures and number of contour points. In general, the cost function based on mean absolute distances outperforms the RMS cost function which is used by most other authors. For this application, the simplex optimization method works better than Powell's method [Brent, 1973]. In general, 1000 or more contour points are required for reliable and accurate correlation.

In the absence of distortions, an accuracy of sub-pixel level is obtained, which is the case for CT-CT and CT-SPECT matching. The accuracy for CT-MRI matching is limited by distortions, but is still about 1 mm. The reliability of the method depends most on the presence of artifacts in the segmented images and is 100% for CT-CT correlation. The reliability can be improved when a good initial guess of the matching transformation is available. For CT-MRI correlation this first guess has been obtained by first matching on the skin, resulting in a reliability of about 98%. For other applications, interactive matching techniques can be applied. Without such an interactive pre-match, the reliability of CT-SPECT matching is about 80%.

In future work, distortions should be considered in the matching procedure. A possible approach is to model the distortions and to include the parameters of the distortion model for optimization during the chamfer matching process. By taking distortions into account, e.g., those introduced by object-induced inhomogeneities of the magnetic field, CT-MRI correlation should become more accurate. To improve the reliability of the correlation method (especially required for CT-SPECT matching) better segmentation methods must be developed. Finally, more work is required for testing the method for other combinations of modalities and for other anatomical sites.

Organ motion

Using three-dimensional image correlation, the motion of organs relative to bony anatomy can be quantified accurately. The accuracy is better than 1 degree rotation and 1 mm translation for measuring prostate position and around 0.2 degrees for measurement of motion of bony anatomy. Uncertainties in contouring and visual interpretation of the scans have a much smaller influence on the measurement of organ displacement with our new method than with conventional methods for

quantifying organ motion. However, a disadvantage of our method is that it only quantifies motion, and no shape variations. Therefore, the organ under study must have a relatively constant shape. Shape variations of the prostate appear, however, to be acceptably low to allow accurate measurements.

From the measurements in the pelvic region of this group of patients the following conclusions can be drawn. Prostate motion is small, except for A-P translation (3.2 mm standard deviation) and rotation around the L-R axis (4.5 degrees). Most prostate motion can be attributed to rectal filling differences, but leg rotation and bladder filling also contribute. Rotations of the pelvic bone are very small, less than 1 degree standard deviation in all directions, but pelvic rotation around the L-R axis is influenced by the width of leg opening. Finally, an interesting correlation has been observed between bladder filling and the width of leg opening.

Using three-dimensional image registration, the motion of organs relative to bony anatomy has been quantified accurately. Uncertainties in contouring and visual interpretation of the scans have a much smaller influence on the measurement of organ displacement with our method than with conventional methods. We have quantified correlations between rectal filling, leg motion and prostate motion.

In general, 3-D image integration plays an important role in assessing and improving the accuracy of radiotherapy and is therefore indispensable for conformal therapy. However, user-friendly implementation of these techniques remains required to facilitate clinical applications on a large scale.

REFERENCES

Bel, A.; van Herk, M.; Bartelink, H.; Lebesque, J.V. A verification procedure to improve patient set-up accuracy using portal images. *Radiother. Oncol.* 29: 253-260; 1993.

Boersma, L.J., Damen, E.M.F., de Boer, R.W., Muller, S.H., Valdes Omos, R.A., Hoefnagel, C.A., Roos, C.M., van Zandwijk, N., Lebesque, J.V., A new method to determine dose-effect relations for local lung-function changes using correlated SPECT and CT data, *Radioth. Oncol.* 29: 110-116, 1993

Borgefors, G. Distance transformations on digital images, *Comput. Vision, Graphics. Image Processing* 34: 344-371, 1986.

Borgefors, G. Hierarchical chamfer matching: A parametrical edge matching algorithm. *IEEE Trans. Pattern Recognition and Machine Intelligence*, 10: 849-865; 1988.

Gilhuijs, K.G.A., van Herk, M., Automatic on-line inspection of patient set-up in radiation therapy using digital portal images, *Med. Phys.* 20: 667-677, 1993.

Gilhuijs, K.G.A., Automatic verification of radiation treatment geometry, reconstruction of patient setup in two and three dimensions using portal images, PhD Thesis, University of Amsterdam, 1995

Fritsch, D.S., Pizer, S.M., Morse, B.S., Eberly, D.H., Liu, A., The multiscale medial axis and its applications in image registration, *Pattern recognition letters* 15: 445-452, 1994.

Kooy, H.M.; van Herk, M.; Barnes, P.D.; Dunbar, S.F.; Tarbell, N.J.; Mulkern, R.V.; Holupka, E.J.; Loeffler, J.S. Image fusion in stereotactic radiotherapy and radiosurgery. *Int. J. Radiat. Oncol. Biol. Phys.* 28: 1229-1234; 1994.

van Herk, M.; Kooy, H.M. Automatic three-dimensional correlation of CT-CT, CT-MRI, and CT-SPECT using chamfer matching. *Med. Phys.* 21: 1163-1178; 1994.

Kessler, M.L., Pitluck, S., Petti, P., and Castro, J.R., Integration of multimodality imaging data for radiotherapy treatment planning, *Int. J. Radiat. Oncol. Biol. Phys.* 21, 1653-1667, 1991.

Nelder J.A., Mead, R., A simplex method for function minimization, *Computer Journal* 7, 308-313, 1965.

Brent, R.P., Algorithms for minimization without derivatives, Englewood Cliffs, N.J.: Prentice-Hall, chapter 7, 1973.

**NEXT PAGE(S)
left BLANK**



BE9700010

Reprinted from "International Radiotherapy Review", Vol. 1, based on "The Philips 1995 International Radiotherapy Users' Meeting", Ed. R.F. Mould, pp. 21-32, 1995.

Irradiation of Target Volumes with Concave Outlines

W. De Neve, L. Fortan, S. Derycke, B. Van Duyse, and C. De Wagter

Department of Radiotherapy and Nuclear Medicine,

University Hospital, De Pintelaan 185, 9000 Gent, Belgium

BE 9700010

Introduction

For target volumes with convex shapes, it is often not difficult to find beam incidences that isolate the target volumes from the tissues at risk. Using these beam incidences a dose distribution that conforms to the 3D shape of the target (sometimes called a 3D conformal dose distribution) can generally be obtained by dose optimisation involving human trial and error. When the target volume has concavities, it may be impossible to find beam incidences for which the target volume is isolated from the tissues at risk.

In these situations, beam intensity modulation may be required to obtain a 3D conformal dose distribution. The determination of the beam intensity profiles by human trial and error is very time consuming but practical solutions to this problem have been described by several authors and often involve a solution of the *inverse problem*.

Within this *inverse problem*, a given target volume is considered to represent the prescribed dose distribution. Several investigators have described methods to compute the beam intensity profiles (Brahme 1988), simulated annealing (Webb 1991), back projection (Bortfeld *et al* 1990). All of these methods involve the use of dedicated planning systems and none of them is easily portable to other institutions.

We are investigating a heuristic planning procedure that allows us to obtain a 3D conformal dose distribution for target volumes with concavities. This procedure divides the planning problem into a number of sub-problems each solvable by known methods. By patching together the solutions to the sub-problems a solution with a predictable dosimetric outcome can be obtained. Our procedure can be applied on most 3D planning systems and the aim of this chapter is to describe this procedure and its application in the irradiation of the macular degenerations.

1 Methods & Materials

1.1 Macular Degeneration

Macular degeneration is a vascular disease of the retina and a common cause of progressive blindness in the elderly. Treatment of subfoveal macular degeneration by laser photocoagulation (Study Group 1991), results in severe visual impairment.

It has recently been shown that radiotherapy can stop and even reverse this degenerative process (Chakravarthy *et al* 1993). Although the optimal dose is unknown, fractionated radiotherapy to total doses of 10 to 20 Gy was shown to be efficient.

These doses are above tolerance of the lens so that shielding of the lens is required. Such shielding limits the dose to the anterior parts of the retina. For these reasons irradiation is used in the treatment of subfoveal (posteriorly located) macular degenerations while laser coagulation is the treatment of choice for more anteriorly located disease.

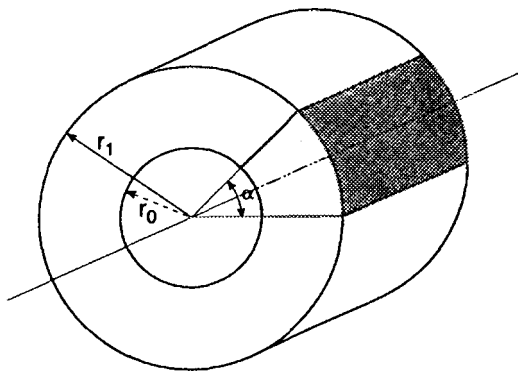


Figure 1. Drawing of a cylindrical shell. The darkened region of this cylindrical shell is called a cylindrical shell section. r_0 is called the internal radius.

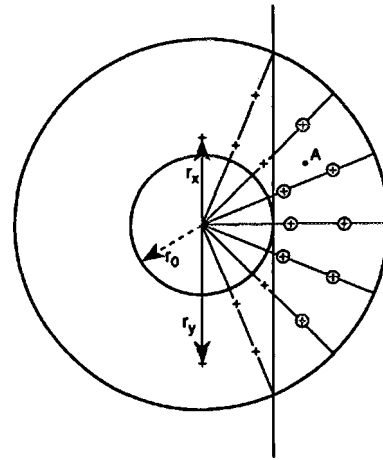


Figure 2 (above right). Analogy of arc therapy with therapy using many static fields. In arc therapy, the dose delivered to points at distance r_x or r_y from the centre of rotation is proportional to their arc of rotation through the "ideal" beam (see Appendix). Assuming, instead of arc therapy, the use of a large number of equally weighted beams placed at equi-angular steps, then the dose delivered to points at distance r_x or r_y from the centre of rotation is proportional to the number of times that these points are hit by the beam (frequency of exposure). This frequency of exposure is in turn proportional to the arc of rotation through the beam. The same reasoning can be followed for beam segments. The frequency of exposure to a beam segment using static beams is proportional to the arc of rotation through the beam segment in rotation therapy. Therefore the field segmentation and segment intensities calculated for rotation therapy can also be applied with many static fields. Decreasing the number of beam incidences will decrease the analogy with rotation therapy and thus the efficacy of the gradient filters to homogenise the dose distribution.

Using beam intensity modulation, a dose distribution was obtained that allows us to use radiotherapy irrespective of the location or extent of the disease without exceeding the tolerance of the lens. The intensity profiles of the means were computed using a heuristic method applicable to other problems involving 3D concave targets.

1.2 Planning Procedure Philosophy

The aim of our method is to reduce the planning to a problem with a known solution, namely, the deposition by arc therapy of a homogeneous dose distribution with the shape of a cylindrical shell. This reduction process is carried out in sequential steps and it is obvious that a homogeneous dose distribution, shaped as a part of a cylindrical shell (section), can be created in incomplete rotation.

Finally, the arc therapy is emulated by multiple static fields and the desired dose distribution is obtained by patching units shaped as cylindrical shell sections. Such a cylindrical shell section is drawn in **Figure 1**. Targets with a single concave region can be irradiated by stacking such cylindrical shell sections.

A dose distribution with the shape of a cylindrical shell section can be irradiated homogeneously and with distinctive edges and Brahme *et al* (1982) described an analytical solution using arc therapy. The beam intensity profile to obtain such dose distributions assumed an idealised beam profile (no divergence, no dose gradients, no penumbra).

We used a step function to approximate the intensity profiles required to homogeneously irradiate a cylindrical shell-shaped dose distribution. The nature of this step function is described in the **Appendix**. Extensions of this step function are used to irradiate a section, and allow its use with less ideal beam profiles: divergent beams and depth dose gradients.

Using arc therapy homogeneous dose distributions can be obtained by means of a beam fluence profile defined by this step-function. However, a cylindrical shell-shaped target with a centrally located cylindrically shaped tissue at risk is rarely encountered. Most deviations from this ideal situation would require continuous adaptations of the basic fluence profile to adjust for arc dependent variation in missing tissue, radiological path length and beam's-eye-view projections of target and tissue at risk.

Such continuous modulation of the beam's fluence profile is presently only feasible with the system described by Carol (1993), since beam shaping and dose intensity modulation would have to change continuously while the gantry and/or couch are rotating; with the present state of technology, such treatment, as well as its quality control, is hardly possible with conventional equipment.

It is clear that arc therapy can be emulated by a treatment with many static fields separated by equal angles. In this case, **Figure 2** shows that the basic fluence profile of the static fields is identical to that of the beam used for arc therapy.

Let us consider a point A at a distance r from the axis of rotation. Using arc therapy, the point A travels at constant angular speed through the beam while it jumps with constant angular separation through each beam segment. Using arc therapy, the dose accumulated in point A is proportional to the magnitude of the arc that it describes through each beam segment.

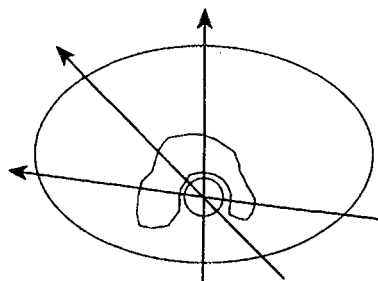
Using static fields separated by equal angles, the dose accumulated in point A is proportional to the number of times that it resides in each beam segment and this is again proportional to the arc spanned by each beam segment. Therefore, the basic fluence profiles for static and arc therapy are similar.

1.3 Heuristic Procedure for Planning

The planning procedure is modular and the goal of this modular process is to obtain the basic fluence profile in planes through the axis of rotation and orthogonal to the axes of the different beams. Initially, flat profiles of equal fluence are created for all beams. By adding the gradient filter, the basic fluence profile is obtained for all beams. The optimal procedure is as follows, [1] to [6].

- [1] An axis of rotation was chosen. Although any axis of rotation can be used, we try to use an axis in the X, Y or Z direction of the treatment room. In this way, the transition from one field to the next can be performed with rotation around a single axis.

Step 1 :



Step 2 :

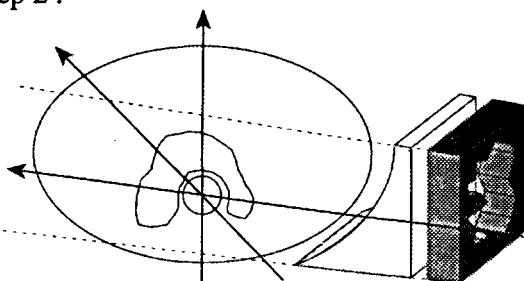


Figure 3. Horseshoe-shaped target surrounding tissue at risk. Step 1 (**top**) The common isocentre of the equi-angularly separated beams is at the geometrical centre of gravity of the tissue at risk. Step 2 (**bottom**) Computation of missing tissue compensation and determination of the geometry of the open beam.

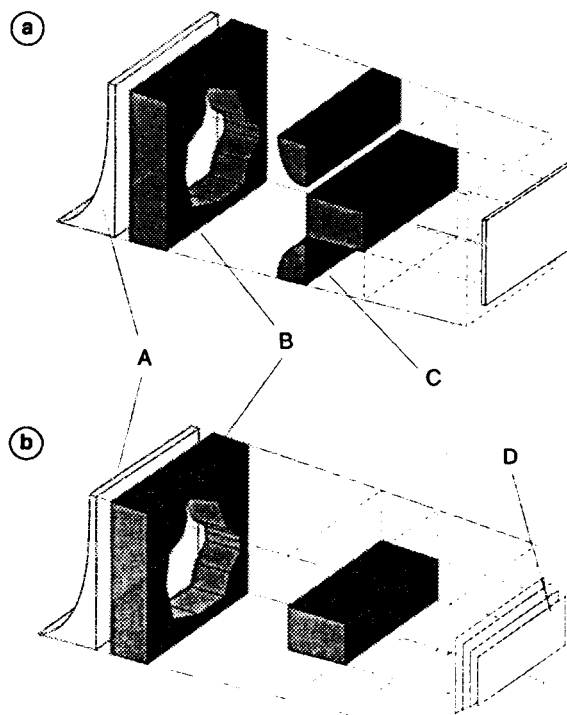


Figure 4. (**top**) Blocking radiation to the tissue at risk and adding gradient filtering (C) to missing tissue compensation (A) and beam's-eye-view conformation (B). (**bottom**) Emulation of the physical gradient filter by field segmentation (D).

A rotation of the gantry is required if the X or Y direction is used, and an isocentric rotation of the couch for the Z axis. This axis of rotation is generally located at the centre of the target's concavity, (**Figure 3** step 1).

- [2] A number of equi-angularly separated beam incidences were chosen, (**Figure 3** step 1).
- [3] Missing tissue was calculated in the plane described by the axes of the beams and was compensated using standard wedges or other devices, (**Figure 3** step 2). The aim of this compensation is to obtain a flat dose profile at the target.
- [4] Angle dependent differences in radiological path length were calculated at the axes of the beams. By adjusting the beam weights, the contributions of (open) beams to their point of intersection were equalised. The aim is to equalise the fluence rates between all beams.
- [5] Adding gradient filtering is the last step. The physical gradient filter (**Figure 4 top**) can be emulated by field segmentation (**Figure 4 bottom**). With the latter procedure, the basic fluence profile is obtained by replacing the open beams by a number of beam segments. The relative intensities of the first segments are identical to the relative intensities of the open beams.
- [6] In the irradiation of macular degeneration, rotational symmetry of the beam incidences could not be obtained and the dose gradient vectors were eliminated by wedges. A two-by-two field dose gradient vector annihilation was made. In these cases, the gradient filters were added to a distorted fluence profile.

1.4 Planning System

Virtual simulation and planning was performed using the GRATIS system developed by Sherouse *et al* (1989).

2 Results & Discussion

2.1 Application to Macular Degeneration

The aim of the planning was to irradiate the largest possible fraction of retina, while at the same time to limit the dose to the lens below tolerance. Six co-planar beams in the sagittal plane (with respect to the patient) were used. Gantry positions were 0°, 30°, 60°, 90°, 120° and 330° and the couch isocentre rotation was 90°.

All beams had their isocentre at the centre of gravity of the lens. For each incidence, two field segments were used. The width of the internal segment was proportional to the radius of the protected region. In this case, it can be shown that a flat fluence profile across this segment will homogenise dose at the edge between the first and the second segment.

The computation of the relative intensity of the second to the first segment is described in the **Appendix**. A dose-volume histogram of the lens is shown in **Figure 5**. The dose distributions in a transverse and a sagittal plane through the geometric centre of the lens are shown in **Figure 6**.

3 General Applications & Conclusions

A heuristic model has been developed and was investigated to obtain 3D concave dose distributions. Its range of application is more general than the treatment of macular degeneration.

It was found applicable to the irradiation of ethmoid carcinoma and vertebral metastases in the vicinity of previously irradiated spinal cord: two cases have been treated. It is now under investigation for the irradiation of targets with more than one concavity such as cervical carcinoma and prostatic carcinoma.

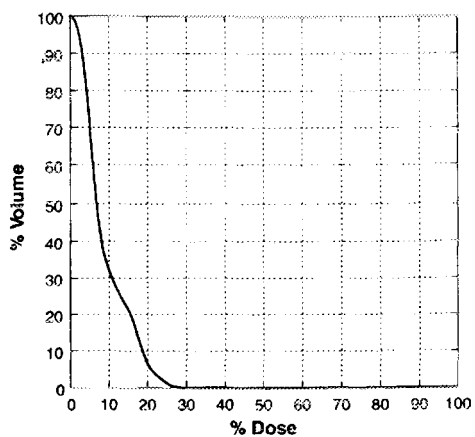


Figure 5. Dose-volume histogram of the lens



Figure 6. Dose distributions in the transverse (top) and sagittal (bottom) planes.

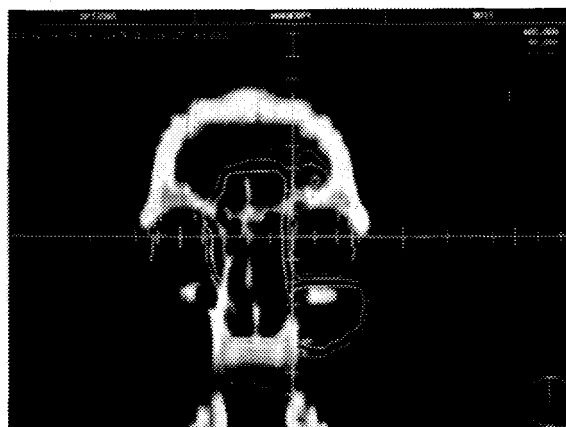
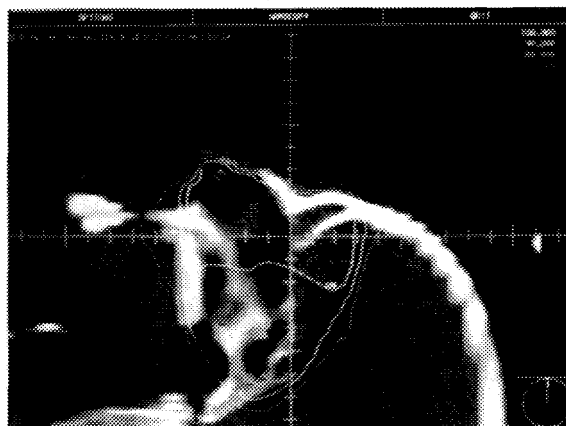


Figure 7. Transverse, sagittal and coronal view of a dose distribution for ethmoid carcinoma with invasion of orbit, maxillary and frontal sinus.

Appendix

1 Homogeneous Irradiation of a Cylindrical Shell

The attempt is to achieve a homogeneous irradiation of a structure with the shape of a cylindrical shell. The dose should be minimal over a radius r_0 around the axis of the cylinder and homogeneous over the thickness $r_1 - r_0$ of the shell, **Figure 1**.

1.1 Assumptions Regarding the Beam

Non-divergent

No dose gradient

No penumbra

No scatter

1.2 Technique

360° arc around the axis of the cylinder. Beam segments of width Δx .

1.3 Homogenising the Dose

Consider a beam segment of width Δx travelling around the axis at distance r_0 at constant speed. This beam segment will cause a dose distribution that increases centrifugally for points located at distances between r_0 and $r_0 + \Delta x$ from the axis and decreases centrifugally for points located at distances further than $r_0 + \Delta x$.

Under the conditions described above the dose delivered by the beam Δx to any point at a distance r from the axis is proportional to the time that the point is exposed to the beam and this is, in turn, proportional to the angle d over which the point is irradiated by the beam Δx . Therefore the dose at any point at a distance r larger than r_0 but smaller than or equal to $r_0 + \Delta x$ from the axis is given by

$$D = c_1 \cdot \text{acos} \left(\frac{r_0}{r} \right)$$

where c_1 is a constant, representing the dose rate (and thus the beam intensity) of the first beam segment while the dose at any point at a distance larger than $r_0 + \Delta x$ is given by

$$D = c_1 \cdot \left(\text{acos} \left(\frac{r_0}{r} \right) - \text{acos} \left(\frac{r_0 + \Delta x}{r} \right) \right)$$

The aim is to homogenise the cylindrical zone outside the circumference $r_0 + \Delta x$. Therefore additional beam segments of the same width Δx are added, each beam segment abutting with the previous. The dose intensity of the second beam segment is chosen so that the dose at the distance $r_0 + 2\Delta x$ is equal to the dose at the distance $r_0 + \Delta x$. By adding the third beam segment, the dose at the distance $r_0 + 3\Delta x$ is equalised with the doses at distances $r_0 + \Delta x$ and $r_0 + 2\Delta x$. By adding further beam segments, the dose is homogenised over the entire thickness of the cylindrical shell.

1.4 Computation of the Dose Intensity of the Second Beam Segment

The dose D_1 and the distance $r_0 + \Delta x$ is generated only by the first beam segment and is given by

$$D_1 = c_1 \cdot \text{acos} \left(\frac{r_0}{r_0 + \Delta x} \right) \quad [1]$$

The dose D_2 at the distance $r_0 + 2\Delta x$ results from a contribution from the first and second beam segments. The contribution D_{2a} from the first beam segment is

$$D_{2a} = c_1 \cdot \left(\text{acos} \left(\frac{r_0}{r_0 + 2\Delta x} \right) - \text{acos} \left(\frac{r_0 + \Delta x}{r_0 + 2\Delta x} \right) \right) \quad [2]$$

The contribution D_{2b} from the second beam segment is

$$D_{2b} = c_2 \cdot \left(\text{acos} \left(\frac{r_0 + \Delta x}{r_0 + 2\Delta x} \right) \right) \quad [3]$$

To meet the dose homogeneity requirements

$$D_1 = D_{2a} + D_{2b} \quad [4]$$

From equations [1] to [4], the relative dose intensities of the second and the first beam segments (c_2/c_1) can be computed

$$\frac{c_2}{c_1} = \frac{\text{acos} \left(\frac{r_0}{r_0 + \Delta x} \right) - \text{acos} \left(\frac{r_0}{r_0 + 2\Delta x} \right) + \text{acos} \left(\frac{r_0 + \Delta x}{r_0 + 2\Delta x} \right)}{\text{acos} \left(\frac{r_0 + \Delta x}{r_0 + 2\Delta x} \right)}$$

1.5 Generalisation: Relative Dose Intensity of the Beam Segment

Define $F_{n,1}$ as the relative dose intensity of the n^{th} beam segment with regard to the first beam segment.

$$F_{n,1} = \frac{c_n}{c_1}$$

By definition $F_{1,1} = 1$. $F_{0,1}$, and the relative dose intensity of the shielded region to the first segment is 0.

Define two terms $A_{i,n}$ and $B_{i,n}$ where

$$A_{i,n} = \text{acos} \left(\frac{r_0 + (i-1)\Delta x}{r_0 + n\Delta x} \right)$$

and

$$B_{i,n} = \text{acos} \left(\frac{r_0 + i\Delta x}{r_0 + n\Delta x} \right)$$

Now, the dose at distance $r_0 + n\Delta x$ results from the contribution of n beam segments and can be tabulated as follows.

Beam segment	Dose contributed at distance $r_0 + n\Delta x$	Remark
1	$c_1(A_{1,n} - B_{1,n})$	$F_{1,1} = 1$
2	$c_2(A_{2,n} - B_{2,n})$	$c_2 = c_1 F_{2,1}$
3	$c_3(A_{3,n} - B_{3,n})$	$c_3 = c_1 F_{3,1}$
↓	↓	↓
n	$c_n(A_{n,n})$	$B_{n,n} = 0$

The sum of the doses contributed by the different segments can be written as follows:

$$c_1 \cdot \sum_{i=0}^{i=n-1} (F_{i,1} \cdot (A_{i,n} - B_{i,n})) + c_n \cdot A_{n,n} \quad [5]$$

and for dose homogeneity, this sum is equal to $c_1 A_{1,1}$ [6], the dose at distance $r_0 + Dx$.

From equations [5] and [6] we can calculate $F_{n,1}$

$$F_{n,1} = \frac{A_{1,1} - \sum_{i=0}^{i=n-1} (F_{i,1} \cdot (A_{i,n} - B_{i,n}))}{A_{n,n}}$$

2 The Homogeneous Irradiation of a Sector of a Cylindrical Shell

Assume that we want to irradiate homogeneously a part of a cylindrical shell and consider the arc of the cylindrical shell to be α degrees (α -sector), the internal radius being r_0 and the thickness being $r_1 - r_0$ (**Figure 1**). The total arc therapy angle ϕ required to irradiate an α -sector is given by

$$\phi = \alpha + 2 \cdot \arccos\left(\frac{r_0}{r_1}\right)$$

Note that this solution results in a generous irradiation of structures at both sides of the α -sector.

Decreasing the internal radius of rotation at the radial edges sharpens the dose fall-off at the radial edges of an α -sector. The penalty is irradiation inside the r_0 radius and induction of more dose inhomogeneity inside the α -sector.

2.1 Beam Divergence & Dose Gradients

Divergence and dose gradients have been included in the model and are the subject of another publication. In extreme cases the dose cannot be homogenised. In clinically relevant situations, the segment intensities computed with or without taking divergence and dose gradients into account are very similar.

References

Bortfeld T., Buerkelbach J., Boesecke R. & Schlegel W., *Methods of Image Reconstruction from Projections Applied to Conformation Radiotherapy*, *Physics in Medicine & Biology*, **35**, 1423-1434, 1990.

Brahme A., Roos J. E. & Lax I., *Solution of an Integral Equation Encountered in Rotation Therapy*, *Physics in Medicine Biology*, **27**, 1221-1229, 1982.

Brahme A., *Optimisation of Stationary & Moving Beam Radiation Therapy Techniques*, *Radiotherapy & Oncology*, **12**, 129-140, 1988.

Carol M. P., *Integrated 3D Conformal Planning/Multivane Intensity Modulating Delivery System for Radiotherapy*, in *Proceedings of the 3D Radiation Treatment Planning & Conformal Therapy Symposium, Session 6*, Washington University, St. Louis, 1993.

Chakravarthy U., Houston R. F. & Archer D. B., *Treatment of Age-Related Subfoveal Neovascular Membranes by Teletherapy*, *Brit. J. Ophthalmology*, **77**, 265-273, 1993.

Sherouse G. W., Thorn J., Novins K., Margolese-Malin L. & Mosher C., *A Portable 3D Radiotherapy Treatment Design System*, *Medical Physics*, **16**, 466, 1989.

Study Group on Macular Photocoagulation, *Laser Photocoagulation of Subfoveal Neovascular Lesions in Age-Related Macular Degeneration*, *Archives Ophthalmology*, **109**, 1220-1231, 1991.

Webb S., *Optimisation by Simulated Annealing of 3D Conformal Treatment Planning for Radiation Fields Defined by a Multileaf Collimator*, *Physics in Medicine & Biology*, **36**, 1201-1226, 1991.



BE9700046

**An analytic solution for calculating the beam intensity profiles
useful to irradiate target volumes with bi-concave outlines.**

BE9700046

W. De Neve, S. Derycke and C. De Wagter.

**Department of Radiotherapy and Nuclear Medicine,
University Hospital Gent (U.Z.G.), Belgium**

Acknowledgement: The project "Conformal Radiotherapy U.Z. Gent" is funded by the Vereniging voor Kankerbestrijding. This work was supported by grants of the Centrum voor Studie en Behandeling van Gezwelziekten and the Sportvereniging tegen Kanker. J. Schelfhout is acknowledged for logistic support.

1. Introduction

We have described previously a heuristic planning procedure that allowed us to obtain dose distribution for concave target volumes [2]. This procedure allowed us to solve planning problems related to tumors in the head and neck region wrapping around the spinal cord or other radiation sensitive structures [2, 3]. Typically 20-25 beam segments were required to obtain a dose distribution that was highly conformal to these targets. The unifying property of these targets was the presence of a single concavity.

The aim of this technical note is to extend the previously described method to allow the irradiation of bi-concave or even multi-concave targets. As proof of principle, the "Brahme pelvic target" was planned on a phantom.

2. Methods, Materials and Results

2.1. The Brahme pelvic target and the Proimos phantom

The pelvic target described by A. Brahme and coworkers [1] is anatomically relevant for advanced cervix cancer with involved regional lymph nodes (Fig. 1). The target is butterfly shaped and thereby bi-concave. The organs at risk are rectum, posteriorly; the bladder anteriorly and, to a lesser extent, the femoral heads, laterally, left and right.

In the margin of the European Dynarad project, B. Proimos (Patras, Greece), distributed a water-equivalent density wooden phantom (Fig. 2a). The phantom consists of 2, mirror-image halves and can be assembled with a film for transverse plane dosimetry. We slightly modified the phantom by drilling holes 1 mm diameter; 10 mm deep in one of the halves. These holes follow the delineations of target, rectum, bladder and femoral heads; they are visible on CT-scan and are suitable for TLD-rod dosimetry. For dosimetry and reference reasons, additional holes were drilled at the cornerpoints of a predefined raster. Fig. 2b shows a CT-image (slice thickness: 1.0 cm) through these holes. This CT-slice was multiplied 10 times to

span a 10 cm thickness and was flanked on both sides by CT-slices without visible drill-holes. In this way, the phantom was transferred to the virtual world of Sherouse's GRATIS® planning system [4]. The holes were used as markers to contour the target and the critical organs and structures.

2.2. Philosophy of the planning procedure

The planning procedure was divided in 2 steps. During the first step, the gantry angles and beam segments were defined to obtain the best possible conformal dose distribution, considering only the rectum as critical structure and thus neglecting the bladder (rectum-sparing subplan). During the second step, the opposite was done; i. e. only the bladder was considered a critical structure (bladder-sparing subplan). Each of the subplans resulted in a concave dose distribution, sparing respectively the rectum (fig. 3a) or the bladder (fig. 3b). The final plan consists of a weighted sum of both dose distributions with predictable dose levels at bladder and rectum (fig. 3c). Both subplans were generated as described previously [2, 3]. The rectum-sparing subplan was generated using 6 gantry angles and 28 beam segments. The bladder-sparing subplan used 7 gantry angles and 30 beam segments. Segment intensities were calculated using the step function described before [2, 3]. A correction for variation in radiological pathlengths for different segments was performed (10% increase in segment intensity per 2.5 cm increase in radiological pathlength). Radiological pathlengths were defined as the distances between the phantom's surface and the plane of angulation [2] of the respective segments, measured along the source to segment-center-of-gravity axis. Radiological pathlengths were measured by a ruler on the phantom. The resulting plan is shown in fig. 4.

3. Conclusion:

An analytical method was found useful to develop plans relevant for conformal radiotherapy of targets featuring a concave surface. The method can be extended to more complex targets with more than one concavity.

Legends to the figures

Figure 1: The Brahme pelvic target as it is drawn on the Proimos phantom.

Figure 2:

- a. View of the water-equivalent phantom developed by B. Proimos.
- b. Additional drill holes in one half of the phantom. as visible by CT-scan.

Figure 3: drawing of the planning procedure.

- a. Step 1: rectum-sparing subplan. The dose distribution is homogenized to a level D_1 maximally avoiding the irradiation of the rectum.
- b. Step 2: bladder-sparing subplan. The dose distribution is homogenized to a level D_2 maximally avoiding the irradiation of the bladder.
- c. Summing grids of both subplans. The resulting dose at the target is $D_1 + D_2$. D_1 is limited to a dose level below tolerance of the bladder; D_2 is kept below the tolerance level of the rectum.

Figure 4: dose-distribution as computed by GRATIS®. Dose contributions by the rectum-sparing and the bladder-sparing subplans were equally weighted.

Figure 1

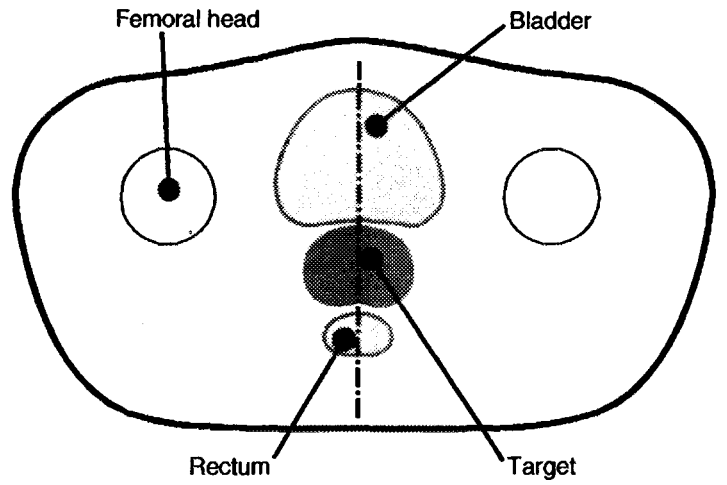


Figure 2a

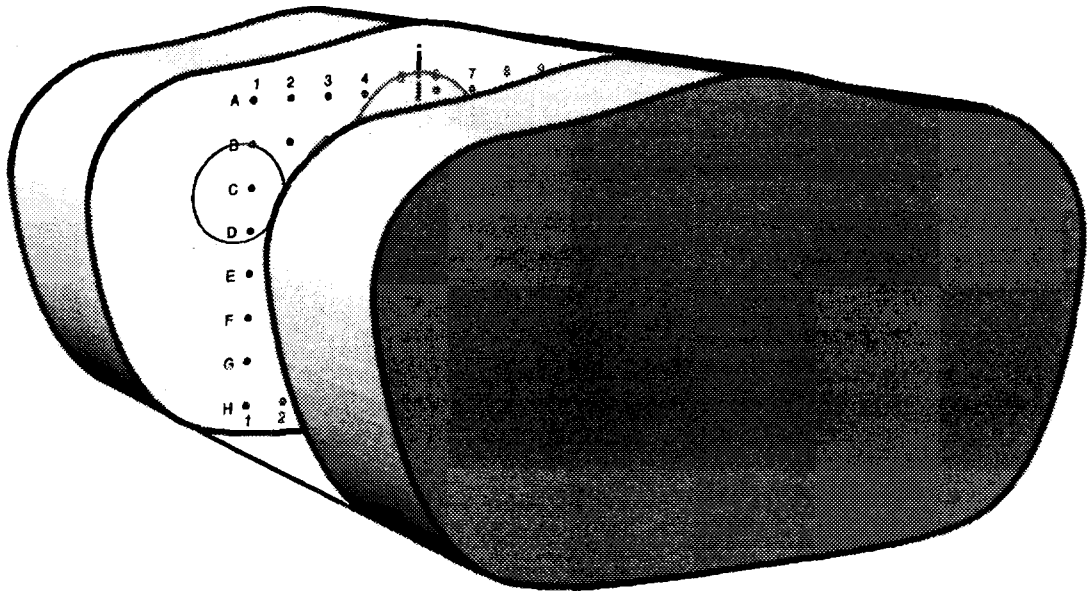
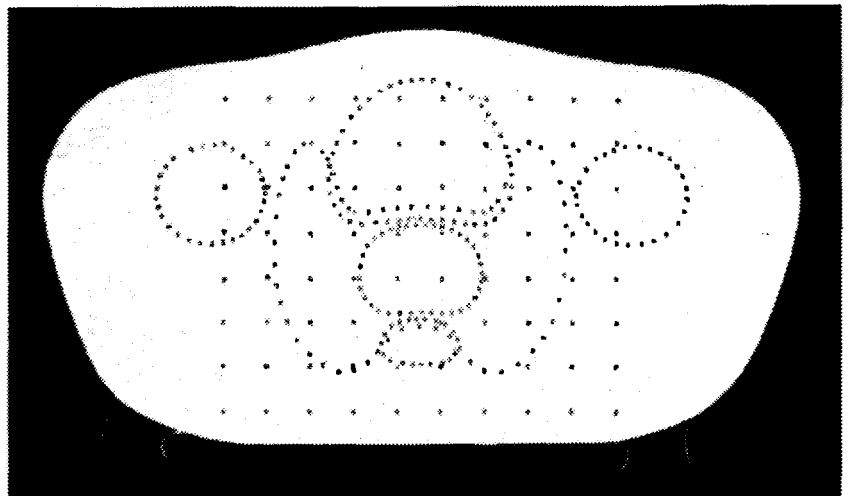


Figure 2b



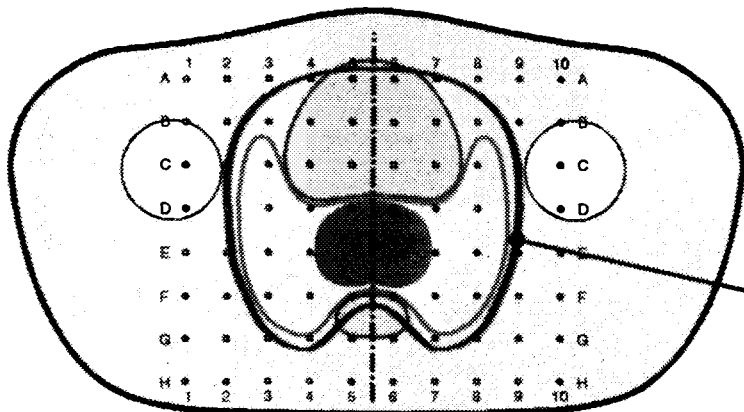


Figure 3a

Reference Dose D1

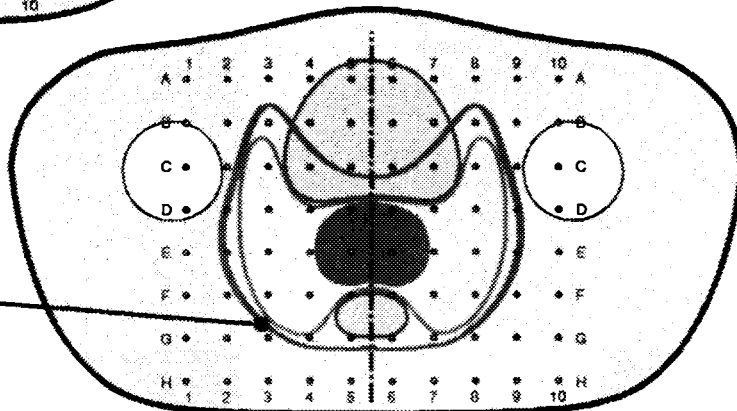


Figure 3b

Reference Dose D2

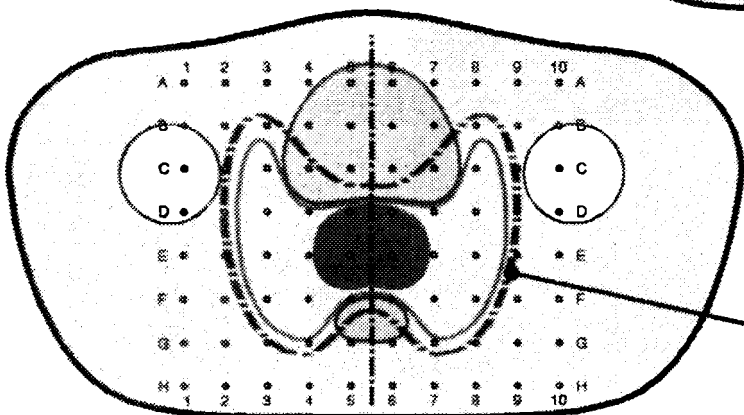
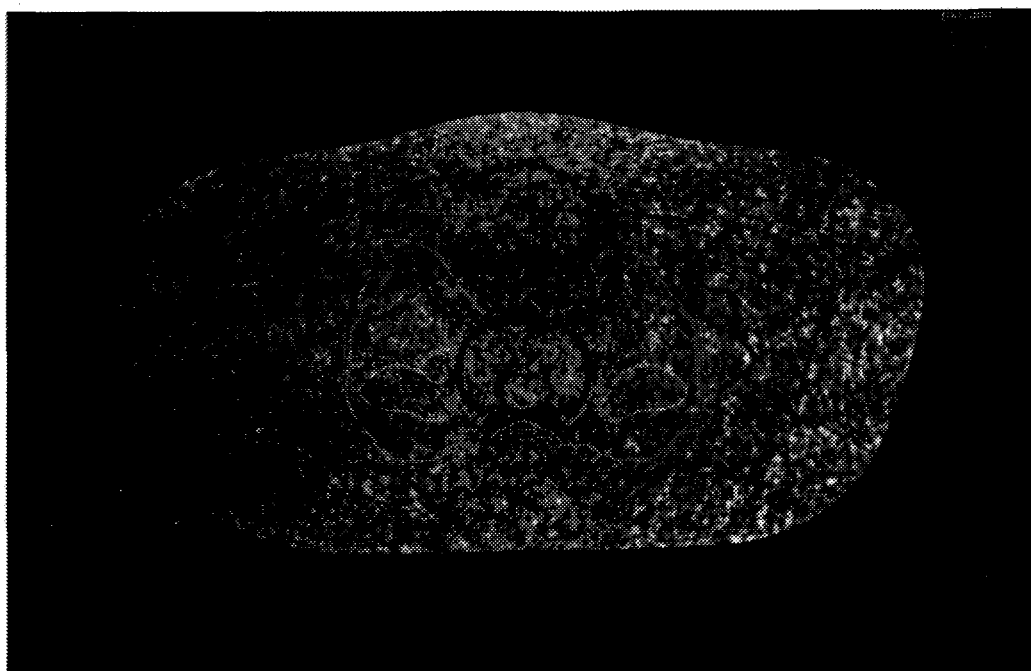


Figure 3c

Reference Dose D1 + D2

Figure 4



References

1. Brahme, A., "Optimization of stationary and moving beam radiation therapy techniques," *Radiotherapy and Oncology*, vol. 12, pp. 129-140, 1988.
2. De Neve, W., De Wagter, C., De Jaeger, K., Thienpont, M., Colle, C., Derycke, S., and Schelfhout, J., "Planning and delivering high doses to targets surrounding the spinal cord at the lower neck and upper mediastinal levels: static beam-segmentation technique executed by a multileaf collimator," *Radiotherapy and Oncology*, vol. (submitted), 1995.
3. De Neve, W., Fortan, L., Derycke, S., Van Duyse, B., and De Wagter, C., "The irradiation of target volumes with concave outlines: a heuristic approach to the calculation of beam intensity profiles and its application in the treatment of macular degenerations," *In: International Radiotherapy Review*, vol. Chapter 3, pp. 21-31, Philips, Crawley, U.K., 1995. Ed: R.F. Mould
4. Sherouse, G. W., Thorn, J., Novins, K., Margolese-Malin, L., and Mosher, C., "A portable 3D radiotherapy treatment design system," *Medical Physics*, vol. 16, pp. 466-, 1989.

**NEXT PAGE(S)
left BLANK**



Planning and delivering high doses to targets surrounding the spinal cord at the lower neck and upper mediastinal levels : static beam segmentation technique executed by a multileaf collimator.

Schelfhout J., Derycke S., Fortan L., Van Duyse B. Colle C., De Wagter C., and De Neve W..

The estimated number of new head and neck cancer cases represents no less than 4% of the yearly total new cancer cases. For carcinoma arising in head and neck, surgery and radiation therapy are the only curative treatments. Thyroid carcinoma is a relatively rare disease, where for certain subgroups of patients external-beam radiotherapy is indicated and beneficial.

Typically, radiation therapy on this location implies portals shaped to include the involved lymph nodes. In our hospital we use the standard one-point set-up technique where the anterior-posterior beam used for the lower neck has a common junction line with the upper neck portals (4).

Problem definition

When in head and neck or thyroid cancer the planning volume reaches to a level below the shoulder, one of the technical challenges is to limit the dose delivered to the spinal cord below tolerance. Indeed, no standard solution exists allowing for the delivery of a homogeneous dose to the target without exceeding spinal cord tolerance (2). This clinical situation belongs to a class of problems in conformal radiotherapy involving the design of 3D-conformal dose distributions for targets with concave outlines. For these targets it is impossible to use beam incidences for which the target volume can be isolated from the tissues at risk. Indeed, if such beam incidences would exist, they would pass through the shoulders or the vertex !

We investigated the possibility to plan and deliver beam intensity modulated radiotherapy using a general purpose 3D-planning system, GRATIS® by G. Sherouse (3) and a linear accelerator equipped with a standard multileaf collimator (Philips MLC). Planning and dosimetry were performed on the RANDO phantom.

Planning procedure

An axis of angulation was chosen in the cranio-caudal direction. We selected five beam incidences, equi-angularly separated by 30°, sharing a single isocenter - the isocenter used in the standard one-point set-up technique. See figure 1.

Using the beam's eye view tool, we drew outlines conformal to the target's projection, further dividing the outlines in segments. Segments were named S₀ and S₁ to S₄. See figure 2. The medial edges of all segments were located tangential to the spinal cord, so that in effect the segments were tiled, this is they are partially underlying. The segment intensities were

computed using an internal radius of 1.0 cm and a segment width of 1.0 cm for the smallest segment (1). See table.

These initial five beams generated a dose gradient in the posterior-anterior direction. In order to compensate for this dose gradient vector, two wedged open beams were used at incidences of -60° and $+60^\circ$. See figure 3. Their relative weights were set by trial and error. The dose distribution showed also the dose gradient between spinal cord and target to be much shallower in the PA direction than in the latero-lateral direction. See figure 4.

Dosimetric optimization

In order to increase the dose difference between spinal cord and target, the optimization steps described below were performed:

The medial edges were separated further from the spinal cord, in order to decrease dose on the spinal cord coming from penumbra and scatter.

By offsetting the gantry angles the dose homogeneity was increased: the dose 'hills' and 'valleys', typical of the segment arrangement were levelled off.

The shallow dose gradient between spinal cord and target was improved by increasing the weights of the first two anterior segments of the beams at the $\pm 60^\circ$ incidence (now offset to $\pm 65^\circ$).

Technical optimization

At this point of optimization, the treatment plan contained no less than 40 segments spread over 10 gantry angles. To make the treatment technically feasible, we investigated if some gantry positions beams and/or segments could be omitted without deteriorating the target's dose volume histogram. Indeed, all segments at gantry angles $\pm 7.5^\circ$ could be deleted and also all S2 and S4 segments could be deleted.

In this way we reduced the plan to 20 segments spread over 8 gantry angles plus both open beams. See figure 5.

The effects of the optimization are well illustrated by the dose-volume histogram for target and spinal cord. See figure 6.

Film and TLD dosimetry were performed on the RANDO-phantom. The mean measured (TLD) dose was 5 % ($\pm 2.6\%$) lower than the dose computed by the GRATIS[®]-program.

The shortest time of execution of a similar treatment (22 segments) on a patient (unpublished) was 32 minutes. During the treatment, the shortest possible beam-off time between 2 segments was 48 seconds.

Conclusion

A heuristic model has been developed and investigated to obtain a 3D concave dose distribution applicable to irradiate targets in the lower neck and upper mediastinal regions. The solution to the key problem of long execution times lays in synchronising the linear accelerator with the multileaf collimator or ultimately in dynamic leaf control.

Figure 1

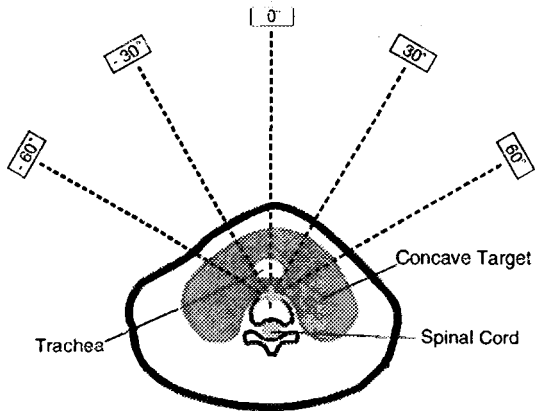


Figure 2

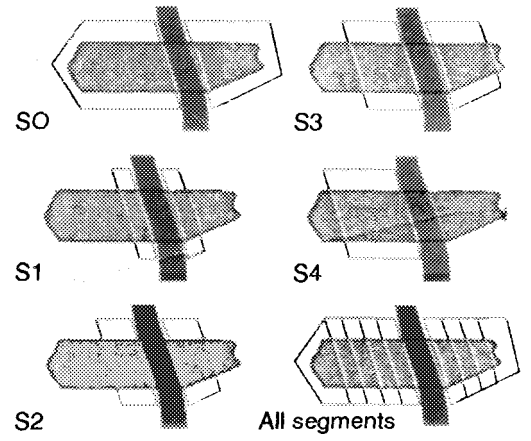


Figure 3

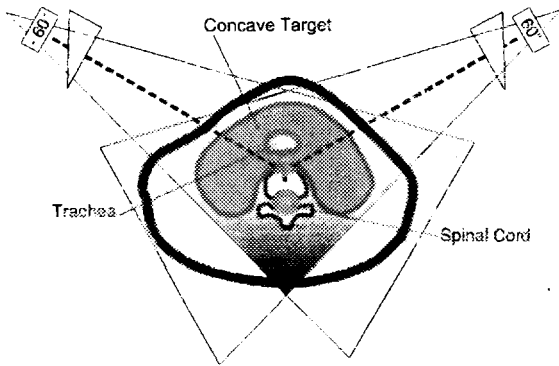


Figure 4

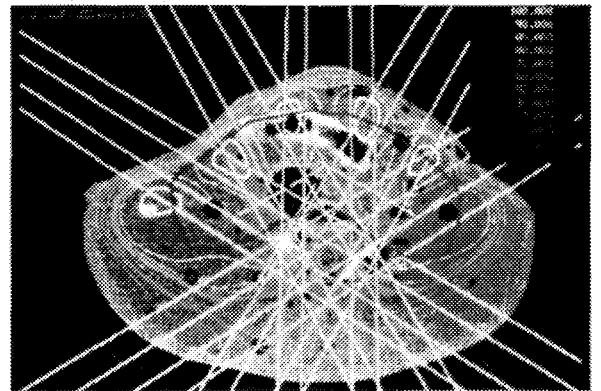


Figure 5

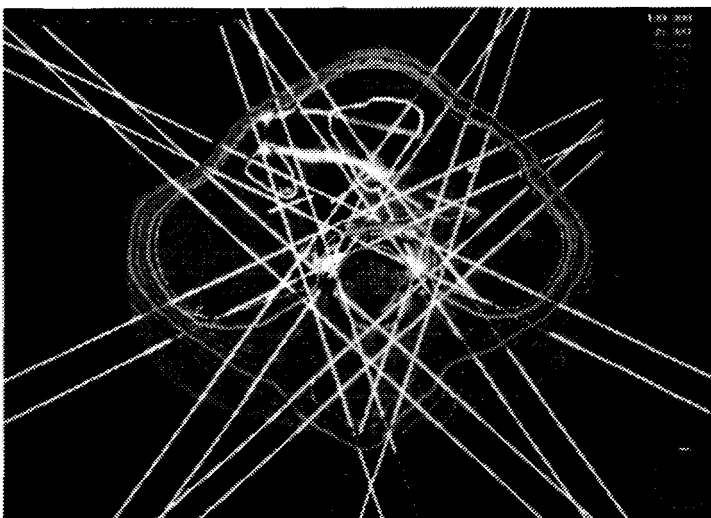
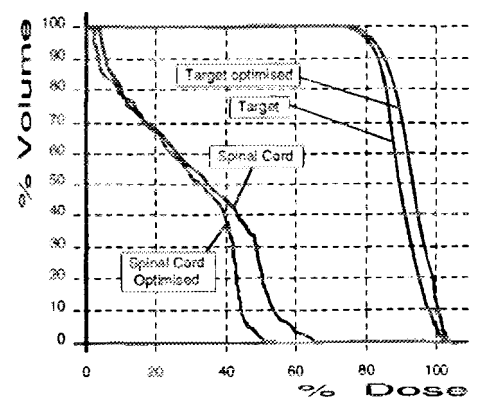


Figure 6



References

- (1) De Neve, Fortan, L., Derycke, S., Van Duyse, B., and De Wagter, C., "The irradiation of target volumes with concave outlines: a heuristic approach to the calculation of beam intensity profiles and its application in the treatment of macular degenerations" *International Radiotherapy Review*, vol. Chapter 3, pp. 21-31, Philips, Crawley, U.K. 1995. Ed. R.F.Mould.
- (2) Sailer, S. L., Sherouse, G. W., Chaney, E. L., Rosenman, J. G., and Tepper, J. E., "A comparison of postoperative techniques for carcinomas of the larynx and hypopharynx using 3D-distributions" *Int. J. Radiat. Oncology Biol. Phys.* vol. 21, pp. 767-777, 1991.
- (3) Sherouse, G. W., Thorn, J., Novins, K., Margoiese-Malin, L., and Mosher, C., "A portable 3D radiotherapy treatment design system" *Medical Physics*, vol. 16, pp. 466-1989.
- (4) Sohn, J. W., Suh, J. H., and Pohar, S., "A method for delivering accurate and uniform radiation dosages to the head and neck with asymmetric collimators and a single isocenter," *Int. J. Radiat. Oncology Biol. Phys.*, vol. 32, pp. 809-813, 1995.

Table

Gantry Angle		- 60		- 30		0		30		60	
Group		ant	post	ant	post	left	right	ant	post	ant	post
	SO	0.69	0.72	0.70	0.72	0.70	0.70	0.70	0.72	0.69	0.72
	S1	0.22	0.22	0.22	0.22	0.22	0.22	0.22	0.22	0.22	0.22
	S2	0.06	0.06	0.06	0.06	0.06	0.06	0.06	0.06	0.06	0.06
	S3	0.02	/	0.02	/	0.02	0.02	0.02	/	0.02	/
	S4	0.01	/	/	/	/	/	/	/	0.01	/

Legends to the figures

Figure 1

Definition of gantry positions: 5 beams equi-angularly separated.

Figure 2

Definition of beam segments: example of the lay-out of the drawn the segments as visualised with the beams eye view at the -30° incidence.

Figure 3

Wedge beams at +/- 60°. compensating for the PA gradient.

Figures 4 and 5

Dose distributions computed by GRATIS® in transverse planes projected on CT-images of the RANDO-phantom at the level of the lower neck before (fig.4) and after (fig.5) optimization.

Figure 6

Dose-volume Histograms of target and spinal cord before and after optimization.



BE9700012

Optimization of radiotherapy to target volumes with concave outlines : target-dose homogeneization and selective sparing of critical structures by constrained matrix inversion

C. Colle, D. Van den Berge, C. De Wagter, L. Fortan,
B. Van Duyse, and W. De Neve.

1 Introduction

A class of problems in conformal radiotherapy involves the design of 3D-conformal dose distributions for targets with concave outlines. For these targets, it is impossible to find beam incidences for which the target volume can be isolated from the tissues at risk. Commonly occurring examples are most thyroid cancers and targets located at the lower neck and upper mediastinal levels related to some head and neck. We recently developed a solution to this problem, using beam intensity modulation executed with a multileaf collimator by applying a static shape as well as the calculation of segment weights. Tests on Prof. Dr. G. Sherouse's *GRATISTM* planning system [1] allowed to escalate the dose to these targets to 65 - 70 Gy without exceeding spinal cord tolerance. Further optimization by quadratic optimization with constrained matrix inversion was investigated to explore the possibility of further dose escalation.

2 Methods and materials

2.1 Dose calculations

The dose due to a beam configuration is calculated using the 3D-SAR/SMR algorithm [2]. This highly accurate algorithm uses complex 3D-computations and is time consuming. By calculating the dose contribution for a segment with unity intensity, a relative dose contribution for each segment is obtained. By applying weight factors to each of the segment intensities the absolute dose distribution is calculated. This is a simple multiplication of all relative doses to each voxels by the weight factors and does not require recalculation of the dose deposition in the 3D-space. The absolute dose distribution is obtained by summation of the weighted contributions of all segments. The dose is a linear function in the segment weights, as shown in equation 1.

$$D_i = \sum_{\text{segment } j} x_j \cdot \alpha_{i,j} \quad (1)$$

where

- D_i : absolute total dose in voxel i
- x_j : weight factor for segment j
- $\alpha_{i,j}$: relative dose in voxel i due to segment j

2.2 The objective function

The objective function to be minimized

$$\sum_i (D_I - d_i)^2 + w \sum_j D_j \quad (2)$$

is a weighted sum of 2 categories of terms.

$\sum_i (D_i - d_i)^2$, where D_i and d_i are the calculated and the desired constant dose at the i -th voxel inside the target, expresses the homogeneity of the dose in the target volume. In $\sum_j D_j$, D_j is the calculated dose at the j -th voxel inside the organs at risk. The weight factor w defines the importance of dose limitation in the organs at risk to dose homogeneity at the target. A small w -value means that a high degree of homogeneity is to be achieved. A high w -value indicates that high doses are to be eliminated in the organs at risk, at the expense of dose homogeneity in the target volume. w is determined empirically based upon clinical bases. The geometrical layout of the segments is proposed by radiotherapists.

2.3 Quadratic optimization using constrained matrix inversion

Minimizing the objective function 2 is done by requiring that

$$\begin{aligned} \frac{dW}{dx_k} &= 0 \\ \Leftrightarrow \frac{\partial W}{\partial x_k} &= 0 \end{aligned} \quad (3)$$

Calculating these parital derivatives using formula 1 for each segment k

$$\begin{aligned} \frac{\partial W}{\partial x_k} &= \frac{\partial}{\partial x_k} \left(\sum_{\forall i} \left(\sum_{\forall l} \alpha_{i,l} \cdot x_l - d_i \right)^2 + w \cdot \sum_{\forall j} \sum_{\forall l} \alpha_{j,l} \cdot x_l \right) \\ &= \sum_{\forall i} 2 \cdot \alpha_{i,k} \cdot \left(\sum_{\forall l} \alpha_{i,l} \cdot x_l - d_i \right) + w \cdot \sum_{\forall j} \alpha_{j,k} \\ &= 2 \sum_{\forall l} \sum_{\forall i} \alpha_{i,k} \cdot \alpha_{i,l} \cdot x_l \left(\sum_{\forall i} \alpha_{i,k} \cdot d_i - w \cdot \sum_{\forall j} \alpha_{j,k} \right) \\ &= \sum_{\forall l} a_{k,l} \cdot x_l - b_k \end{aligned}$$

results in a set of n linear equations, given in matrix form by

$$\begin{pmatrix} a_{1,1} & a_{1,2} & \dots & a_{1,n} \\ a_{2,1} & a_{2,2} & \dots & a_{2,n} \\ \dots & \dots & \dots & \dots \\ a_{n,1} & a_{n,2} & \dots & a_{n,n} \end{pmatrix} \cdot \begin{pmatrix} x_1 \\ x_2 \\ \dots \\ x_n \end{pmatrix} = \begin{pmatrix} b_1 \\ b_2 \\ \dots \\ b_n \end{pmatrix}$$

This linear system is solved using the constrained matrix inversion [3] under the condition that the n segment weights x_k are positive. The constrained matrix inversion is based on the following iteration formula:

$$\hat{x}_i = x_i + \frac{b_i - \sum_j a_{i,j} \cdot x_j}{a_{i,i}}$$

in which \hat{x}_i is the updated value for x_i .

2.4 Optimization steps

First the skin contours, the target volume contours and the contours of organs at risk are determined. The voxels used in (2) are randomly selected in the volume at risk and the organs at risk. Typically a 1000 different voxels are selected in each of these volumes. After calculating the relative dose contribution of each segment in these voxels the first optimization is done with a fixed weight factor w . Then an evaluation is done based on the dose volume histograms in the organs at risk and the target volume. A few other iterations are done with new weight factors w , which are chosen depending on the evaluation. The weight factor w is decreased if more homogeneity is needed and when the dose in the organs at risk is allowed to increase more. On the other hand, the weight factor w is increased if the dose in the organs at risk is unacceptable high.

case number	MANUAL			OPTIMIZED		
	max dose ¹ in OAR	homogeneity ¹ in target	nr. of segments	max dose ¹ in OAR	homogeneity ¹ in target	nr. of segments
1	65	30	41	43	20	25
2 ²	70	30	30	70	40	4
				70	20	16
3	70	40	30	65	25	20
4	60	40	24	30	40	20

Table 1: Comparison between manual and optimized plans.

3 Results and discussion

In the last 2 months, a limited number of patients were planned using the quadratic optimization algorithm. For each of these patients not more than 10 iterations were needed to obtain a proper weight factor w that meets the clinical limitations. One optimization with a fixed weight factor takes only a few seconds on an Alpha 3000. This implies that 10 optimizations and 10 evaluations of the corresponding dose volume histograms resulting in an acceptable planning takes less than 5 minutes.

Table 1 shows that that the optimized plans improve the dose homogeneity in the target volume and/or decrease the dose in the organs at risk with regard to plans generated by human planners. The same table shows also that optimized plans tend to have more segments with a 0 or very small weight with regard to plans generated by human planners. These beams can be ignored at execution time and will decrease the treatment time.

The following optimization steps to plan a tumor in the lower neck region show how dose escalation is obtained using the quadratic optimization with the constrained matrix inversion algorithm. We started from an initial plan with 41 segments. Fig 1 show how the dose homogeneity in the target decreases when limiting the maximum dose in the myelum, by increasing the weight factor w . Figure 2 shows how the maximum dose in the myelum was decreased by almost a factor 2 with the same homogeneity in the target volume using the quadratic optimization algorithm. This indicates the importance of optimization of treatment plans with computer.

Figure 3 shows the final dose distribution which conforms to a horse shoe shape.

4 Conclusions

The dose distributions produced by the quadratic optimization algorithm were compared with those of human planners by examining the dose volume histograms. The runs on the example considered and on other patients have shown that the optimization algorithm achieves a more homogeneous dose in the target volume while keeping the dose at acceptable dose levels in the organs at risk, which are surrounded by the target volume. This indicates that the quadratic optimizations offer a therapeutic benefit.

A second advantage of this algorithm is the time savings induced. Only a few seconds are needed to optimize the segment weights for a fixed weight factor w . In practice 5-10 different weight

¹This table is normalised to convert the average dose in the target volume to 100.

²This patients has been optimized twice. The first optimization resulted in a plan with only 4 segments, but with a poor homogeneity. This was due to the fact that there was a small part of the tumor, which wasn't irradiated at high doses. The second time more voxels were chosen in the least irradiated part of the target, which resulted in a more homogeneous irradiation of the target volume. This plan needs 16 beams. One can ask if it is worth treating the patient with 16 segments compared to the fairly good result obtained with only 4 segments.

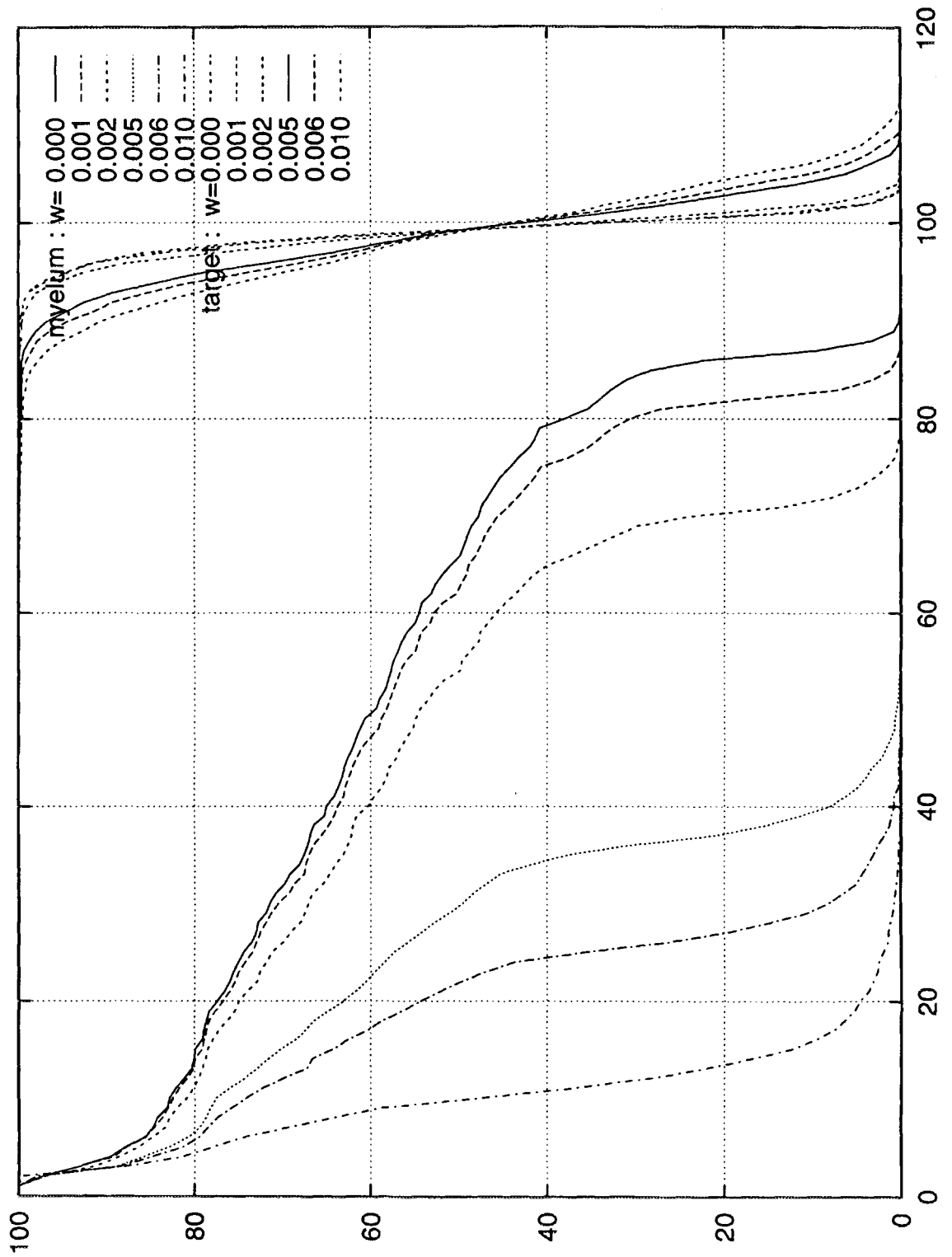


Figure 1: Dose volume histograms in function of different wightfactors w .

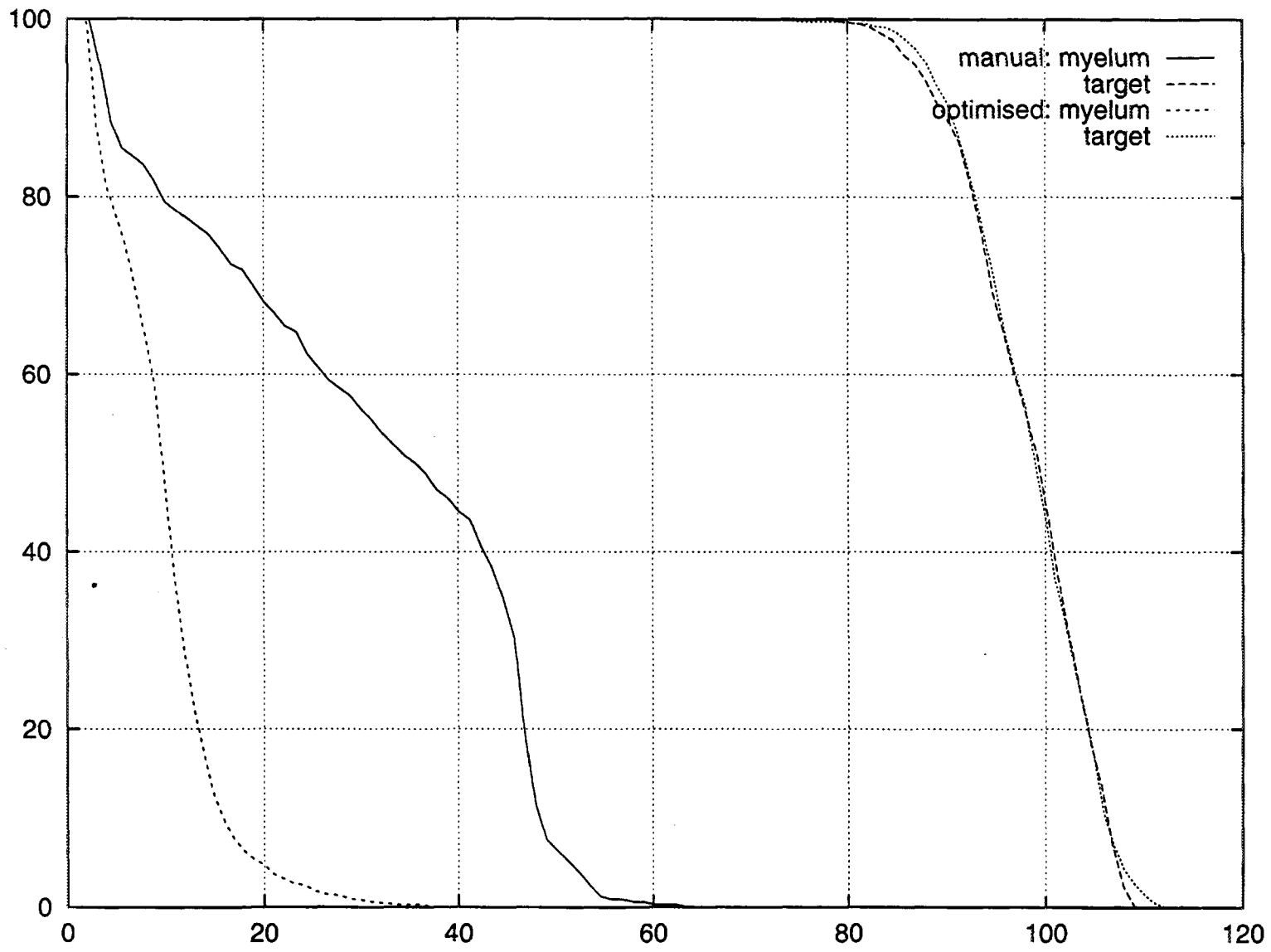


Figure 2: Dose volume histograms for a manual and an optimized plan.

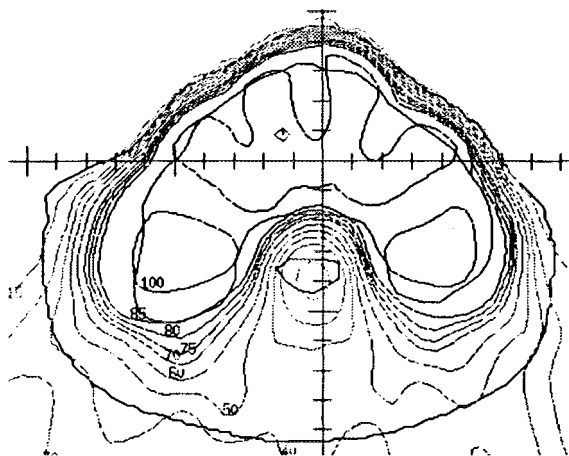


Figure 3: Dose volume profile conforming a horseshoe.

factors had to be tested and evaluated, making optimization a less-than-five-minutes procedure. This reduction in time allows more patients to be planned on the same dose planning system.

Optimized treatment plans tend to have more zero-weighted segments which allows to obtain shorter execution time. This indicates that more patients can be treated on the same treatment machine.

Both time savings will result in a reduction of costs.

Aknowledgements

This work is supported by a grant of the "Centrum Gezwelziekten, Univeristy Gent". The "Comprehensive Project Conformal Radiotherapy, UZG" is funded by the "Vereniging voor Kankerbestrijding".

References

- [1] G. W. Sherouse, J. Thorn, K. Novins, L. Margolese-Malin en C. Mosher, "A portable 3D radiotherapy design system", Medical Physiscs, vol. 16 p 466, 1989.
- [2] Kahn, F. M., "A system of dosimetric calculations", In: The Physics of Radiation Therapy (Williams and Wilkins, Baltimore), pp 182-204, 1984.
- [3] Thomas B. Chriss, Michael G. Herman, Moody D. Wharam, Nai-Chuen Yang, Scott R. Simons, Juan F. Jackson, Jefferey A. Williams, "Rapid Optimization of Stereotactic Radiosurgery Using Constrained Matrix Inversion", 2nd Congress of the International Stereotactic Radiosurgery Society, June 14-17,1995, Boston, USA.



TOMODENSITOMETRY IMAGES : INTEGRATION IN RADIOTHERAPY.

F. Dessy¹, M.T. Hoornaert¹, F. Malchair².

Abstract

With a view to utilisation of CT scan images in radiotherapy, we have measured the effective energy and the linearity of four different scanners (Siemens somatom CR, HiQS, Plus and Picker PQ 2000) and two "non standard scanners", simulators with CT option (Webb 1990) (Varian Ximatron and Oldelft Simulx CT) using the method described by White and Speller in 1980. When the linearity relation is presented using the density or the electron density as the abscissa, we obtain a "blurred area" where two different components of equal density or electron density can have two different Hounsfield's numbers. Using the linearity relation, we determined the "density" of Rando's lung heterogeneity. We calculated a treatment planning (T.P.) using this value and made a comparison between the T.P. and the real absorbed dose which was measured using diodes. The comparison between the TP and the relative absorbed doses showed a difference of up to 4 %. We only made one measurement. This will be explored in a near future.

INTRODUCTION :

In order to use CT images in radiotherapy, we have set up a quality assurance program on CT scanners. This program includes a control of the electromechanical parameters (alignment of table to the gantry, angle of the gantry, light localisation, position of the slice, slice sensitive profiles), the quality of the images (noise, uniformity, resolution, modulation transfer function). With the purpose of comparing scanners from different types and/or manufacturers, these measurements have been carried out on four different scanners and two "non standard scanners" (Webb 1990) i.e. conventional simulators with a CT option. We most particularly have turned our attention to the measurement of the effective energy (the emitted X rays of scanners are distributed over a large spectrum) and the linearity of those scanners as well as the relation between the Hounsfield's unit (HU) and the density or electronic density (ED). Those last relations are used to obtain the density or the ED of an heterogeneity from the mean value of HU of a given area or pixel by pixel by a treatment planing system. In this work, we will compare the relation obtained on different scanners and simulator scanners with the relation proposed as standard by the treatment planing ISIS II used in our institution.

We have used, for the determination of the effective energy, the method described by White and Speller in 1980. This method is based on comparison of the Hounsfield's unit of different solutions containing Carbon tetrachloride (CCl₄) and Ethanol (C₂H₅OH) in different proportion, which have for a given energy the same lineic attenuation coefficient as water for

¹ Hopital de Jolimont, Service d'oncologie et de médecine nucléaire, Haine St Paul, chef de service Dr M. Beauduin.

² Biomed Engineering, Bonnelles..

this specific energy, and on the other hand water scanned sequentially at the same position in the phantom.

Once the effective energy of the scanners is known, we have tested the linearity with other solutions using the same phantom as the one used for the determination of the effective energy, but the used were different.

MATERIAL AND METHODS :

Measurements were carried on four scanners and two “non standard scanners” (Webb 1990). The principal characteristics of the standard scanners are summarised in table 1.

	Somatom CR (Jolimont)	Somatom HiQS (Jolimont)	Somatom Plus (VUB)	Picker PQ 2000 (CHU Liège)
kV	80 et 125 kV	80 et 133 kV	80 et 137 kV	80 à 140 kV
mA(s)	500 et 670 mAs	de 120 à 475 mAs	220 mA	30 à 200 mA
Matrix	256 pixels	512 Pixels	340, 512 Pixels	340, 512 Pixels
Detectors	Gas	Gas	Gas	Semi-conductors
Channel's diameter	800 mm	800 mm	700 mm	700 mm

Table 1 : Characteristics of the different standard scanners.

The “non standard scanners” were

	Varian Ximatron (Institut Curie)	Oldelft SimulX CT (KUL)
kV	125 kV	125 kV
mA(s)	600 mA	500 mA
Matrix	256 Pixels	256 Pixels
Detectors	Brilliance amplifier and CCD	Brilliance amplifier
Channel's diameter	800 mm	900 mm

Table 2 : Characteristics of the different simulator scanners.

For the determination of the effective energy of each scanner, we have used the method and the phantom described by White and Speller (1980). This phantom is made of plexiglas and has an external diameter of 20 cm. It could hold eight inserts containing vials with different solutions.

This method is based on the sequentially evaluation of the HU of water and a mixture of Carbon tetrachloride (CCl_4) and Ethanol ($\text{C}_2\text{H}_5\text{OH}$) of high purity in different proportion. This mixture shows, for a specific concentration, the same linear attenuation coefficient as water for a given energy of X ray. These solutions are called : "energy mixture". Using this method, White and Speller (1980) obtained the effective energy with an accuracy better than 2 keV.

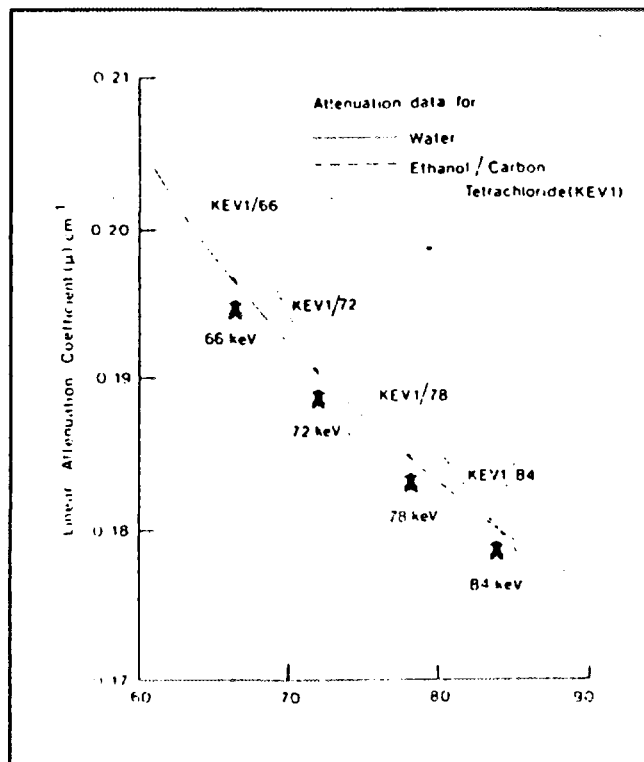


Figure 1 : Variation of the linear attenuation coefficient of water and of energy mixture with the energy of the radiation (White and Speller 1980).

Vial n°	“energy” of the mixture	%/vol. of ethanol	%/vol. of CCl ₄
1	60 keV	90,68	9,32
2	64 keV	89,68	10,32
3	68 keV	88,67	11,33
4	72 keV	87,64	12,36
5	76 keV	86,61	13,39
6	80 keV	85,58	14,42
7	84 keV	84,58	15,42
8	88 keV	83,60	16,40

Table 3 : Composition of the energy mixture.

Once the effective energy of each scanner was known, we could determine the “linearity” i.e. the relation between the HU and the linear attenuation coefficient for the effective energy of the scanner. In fact, the Hounsfield’s unit depend of the effective energy of the X ray :

$$HU = \frac{\mu_{tissue}(E) - \mu_{water}(E)}{\mu_{water}(E)} \cdot 1000$$

where μ_{tissue} and μ_{water} respectively are the linear attenuation coefficients for tissue and for water, E is the energy.

For this purpose, we used the AAPM¹ phantom and the same phantom as the one used for the determination of the effective energy but the inserts contained different solutions of high purity of polyethylene ((C₂H₄)_n), polystyrene ((C₈H₈)_n), nylon (C₆H₁₁NO), polycarbonate ((C₁₆H₁₄O₃)_n), acrylic (C₂H₅O₂), dichloromethane (CH₂Cl₂), dimethylsulfoxyde (C₂H₆OS), dimethylformamide (C₃H₇NO), formaldehyde (HCHO), glycerol (C₃H₈O₃), carbon tetrachloride (CCl₄), ethanol (C₂H₆O) and of hexane (C₆H₁₄).

The values of the linear attenuation coefficient of the different solutions are taken from the work of White and Speller (1980), AAPM N° 39 report (Quality control in computed tomography) or ICRU n°44 report (Tissue substitutes in radiation dosimetry and

¹American Association of Physicist in Medicine

measurement). Comparison with different bibliographic sources give the same values for the lineic attenuation coefficients.

The electron density of each solution were calculated using the relation :

$$\rho_{e-} = \rho \cdot N_A \cdot \sum_i \rho_i \frac{Z_i}{A_i}$$

where ρ_{e-} is the electronic density in e^-/cm^3 , ρ the density in g/cm^3 , N_A the Avogadro number, ρ_i the percentage in mass of the element i^{th} in the composition and Z_i and A_i respectively the atomic number and the mass number of the i element. The treatment planning ISIS II needs, for the calculation of the relative absorbed doses in heterogeneity, the density or the electron density of this heterogeneity.

RESULTS :

The results of the determination of the effective energy of the four standard scanners and the two "non standard scanners" are summarised in table 4 and table 5 and demonstrate that :

STANDARD SCANNERS :

	Somatom CR			Somatom plus	Somatom HiQS	Picker		
Date	11/5/1995	29/5/1995	26/6/1995	7/8/1995	12/7/1995	10/6/1995	10/6/1995	10/6/1995
Nominal energy	125 kV	125 kV	125 kV	120 kV	133 kV	120 kV	130 kV	140 kV
Effective energy	70 keV	70 keV	70 keV	70 keV	72 keV	66 keV	70 keV	72 keV

Table 4 : Obtained effective energies of the standard scanners.

- the solutions are stable within the duration of our measurements: we obtained the same result for a period of one month and a half for the Somatom CR.

- the effective energies of the four scanners are quite similar

NON STANDARD SCANNERS :

	Varian Ximatron	Oldelft SimulX CT	
Date	19/5/1995	12/6/11995	25/8/1995
Nominal energy	Unknown	120 kV	120 kV
Effective energy	63 keV	72 keV	78 keV

Table 5 : Obtained effective energies of the non standard scanners.

An unexplained variation of 6 keV during a period of two month and a half was observed for the Oldelft simulator.

The most critical point for the determination of the effective energy is the “purity” of the “energy mixture”. To verify the accuracy of the mixture, we made this solution tree times. For the three different sets of “energy mixture”, we obtained exactly the same HU. Therefore, we concluded that the solutions were the same and respond to the description made above.

THE LINEARITY : RELATION BETWEEN THE HOUNSFIELD'S UNIT AND THE LINEAR ATTENUATION COEFFICIENT :

The linearity (relation between the HU and the linear attenuation coefficient) of the different scanners is expressed on the figures 2, 3 and 4. We also presented the relation between the Hounsfield's unit and the density in figures 5 and 6.

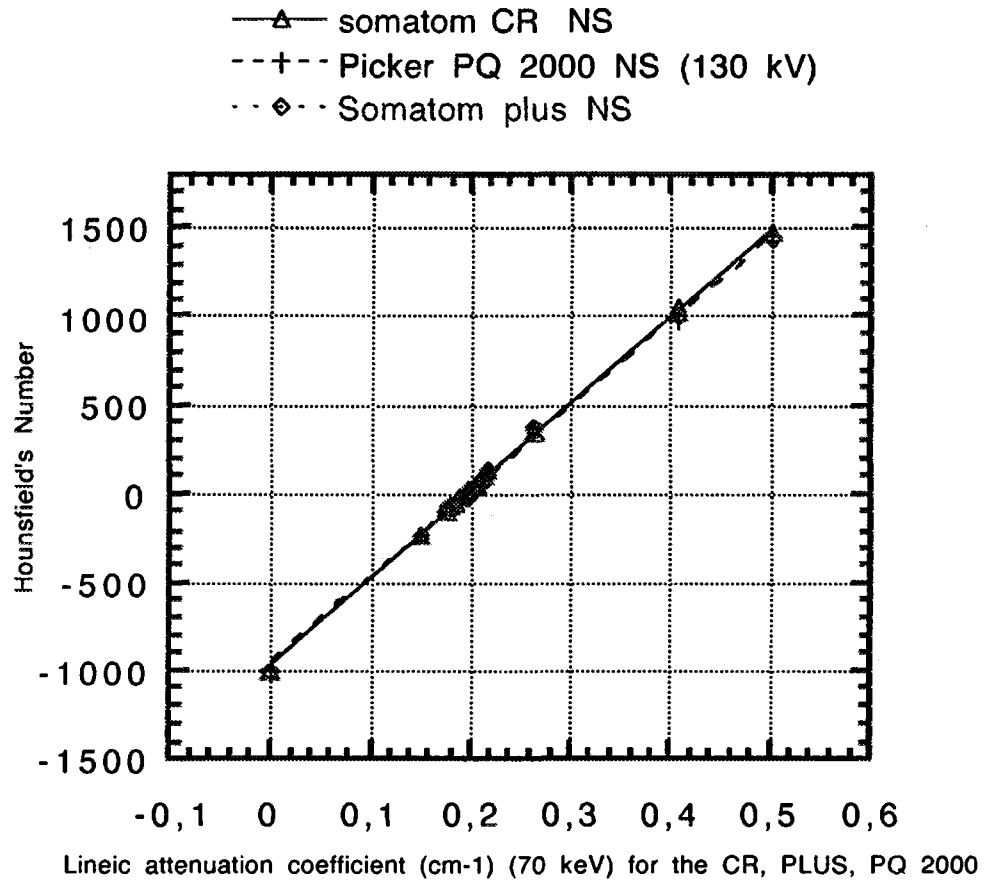


Figure 2 : Linear attenuation coefficient at 70 keV and the associated Hounsfield's number.

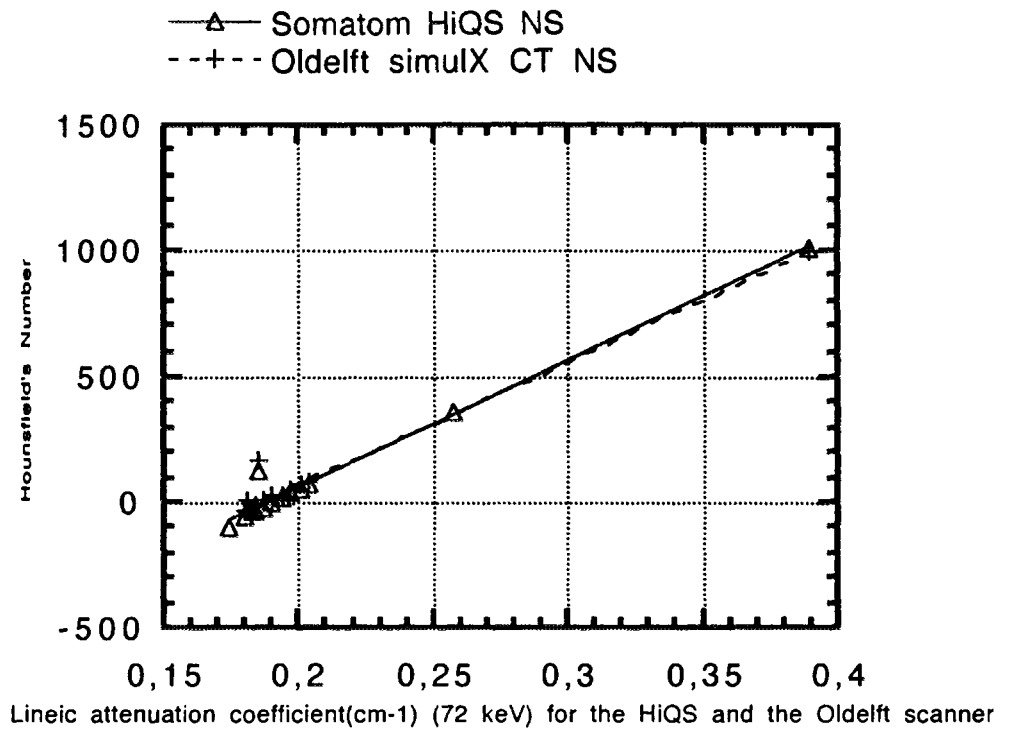


Figure 3 : Linear attenuation coefficient at 72 keV and the associated Hounsfield's number.

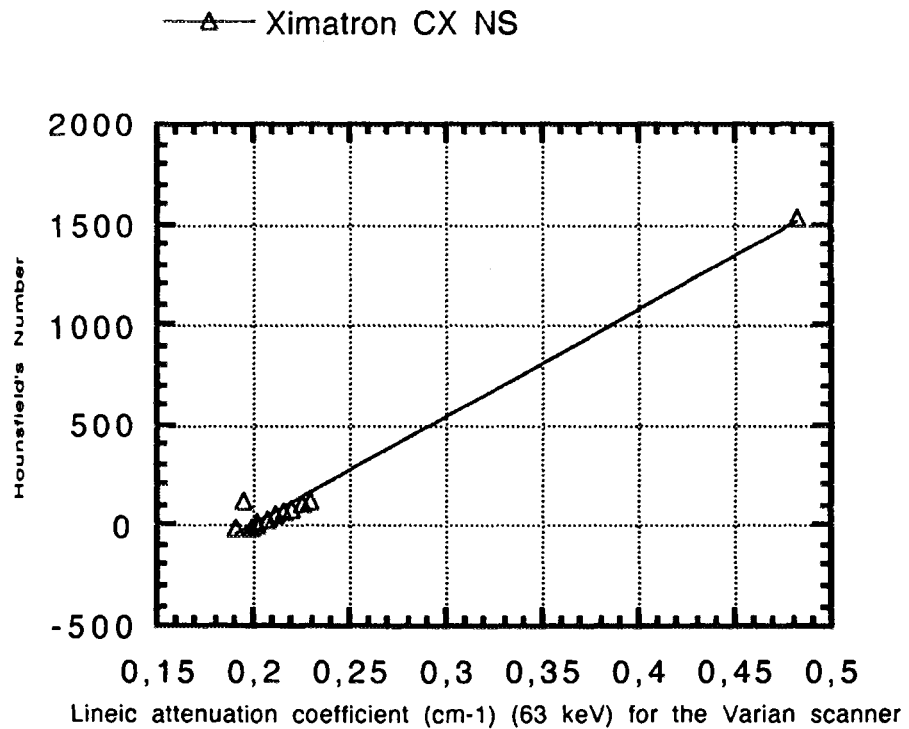


Figure 4 : Linear attenuation coefficient at 63 keV and the associated Hounsfield's number. This result must be taken with great care because we have no measurement between the lineic attenuation coefficient of 0,25 and 0,45 cm⁻¹.

These results show that the relation between the Hounsfield's unit and the linear attenuation coefficients of the different inserts is perfectly linear. This means that all the scanners tested are linear

RELATION BETWEEN THE HOUNSFIELD'S UNIT AND THE DENSITY:

THE STANDARD SCANNERS

The results are summarised in figure 5 and demonstrate that :

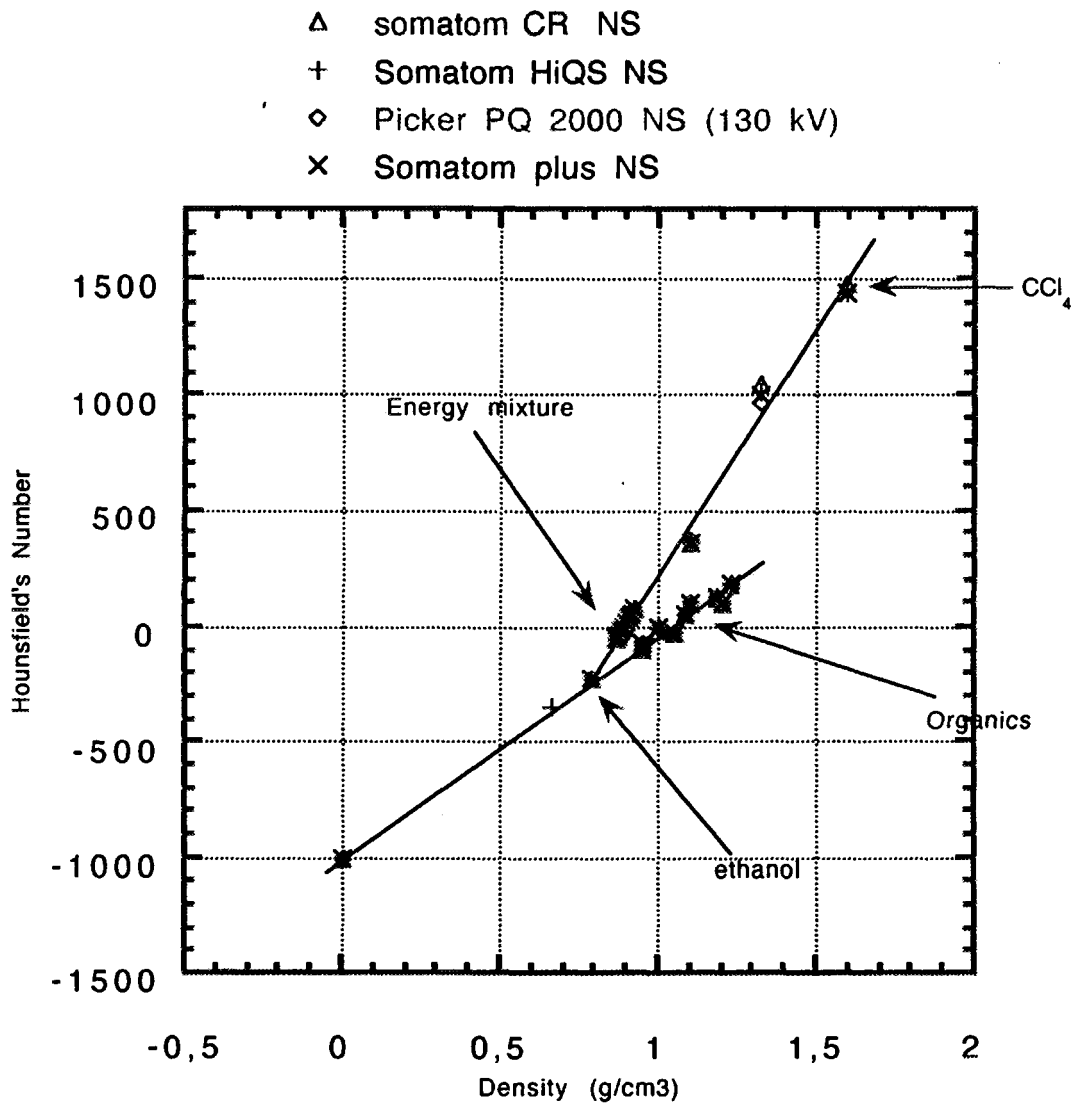


Figure 5 : Density and the associated Hounsfield's number.

- the Hounsfield's units of every insert are similar for the different scanners
- the different components are distributed along two straight line. The point of intersection of these two lines is exactly situated at the position of the ethanol (the diluant of

the energy mixtures). The lowest line is the one which intercepted all the organic compounds without high Z. The other one runs through the ethanol, the different energy mixtures and the carbon tetrachloride (CCl₄). The difference is explained by the composition of the different scanned inserts. On the lowest line, they contain low Z elements (C, H, N, O), at the effective energy of the scanner, these elements show a low photoelectric effect. The others, situated on the highest line, contain in different proportions an element of high Z (Cl), for which, at the effective energy of the scanner, the photoelectric effect is important. These differences of composition explain the two relations observed above.

- This two lines determine a “blurred area” where two materials of the same density but different compositions have two different values of Hounsfield’s unit for a given scanner.

THE NON STANDARD SCANNERS.:

The results obtained for the non standard scanners are summarised in figure 6.

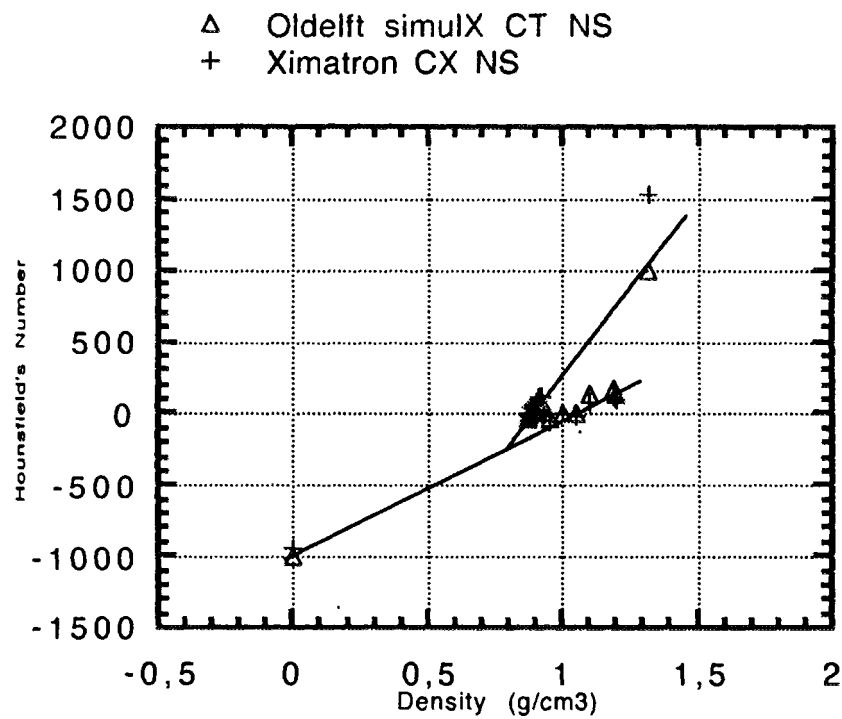


Figure 6 : Density and the associated Hounsfield's number.

And shows similar results as those obtained with the standard scanners.

COMPARISONS BETWEEN THE MEASURED RELATION HOUNSFIELD'S UNIT-ELECTRONIC DENSITY REPORTED TO WATER AND THE STANDARD RELATION USED BY ISIS II :

The ISIS II treatment planning proposes as standard, for the determination of the electronic density of the heterogeneity contained in the different scanned object, a relation between the Hounsfield's unit and the electronic density reported to water. In order to verify the validity of this relation, we have made a comparison between this relation and the one we obtained for the different tested scanners.

The figure 5 shows that the values of the HU of the different inserts are the same for the different scanners so, for the clarity of the graph in figure 7, the results obtained for one scanner, the Somatom HiQS, are presented.

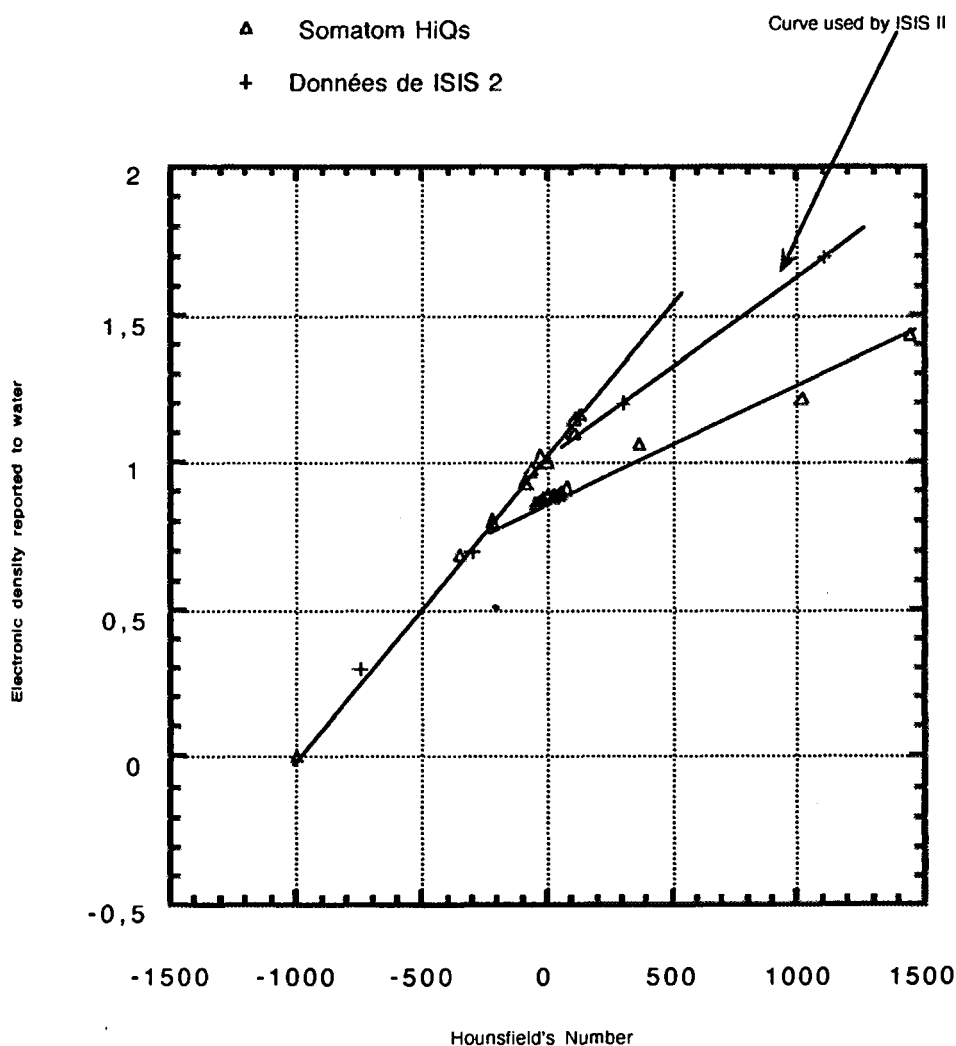


Figure 7 : Comparison of the relation used by ISIS II for the determination of the electronic density of the different scanned objects and the relation we obtained.

This graph shows that the “low” part of the relation used by ISIS II fits the relation obtained for the Somatom HiQS. The highest part of the relation used by ISIS II is situated in the “blurred area” described above.

This means that the standard relation used by ISIS II takes well into account the lung heterogeneity which through its large dimension has the biggest influences in the calculation of the absorbed doses. Concerning the bones (small heterogeneity), situated in the blurred area, we need a more elaborate study. The relation given by ISIS II is established, in that area, from two points of measurement only which are tainted with a big error (Kappas, 1986). Furthermore, for the determination of the relation HU-density and/or electronic density, we used a solution containing an element of higher Z than the one contained in the bone. The measurement should be carried with bone equivalent materials.

CONCLUSION :

From this first experience we can conclude that :

- the Hounsfield's unit of the inserts are the same for the different scanners.
- the effective energies of the different scanners are similar.
- all the scanners are linear.
- below a value of Hounsfield's unit of -200, the relation between the HU and the density or the electron density is well described by the one used by ISIS II for the calculation. The influences of the largest heterogeneity are therefore well taken into account. For the highest density, the relation is different, a careful study must be taken with bone equivalent solutions.

BIBLIOGRAPHY:

AAPM : "Specification and acceptance testing of computed tomography scanners", *AAPM report* , n°39, 1993.

Alderson S.W., Lanzl L.H., Rollins M., Spira J. : "An instrumented phantom system for analog computation of treatment plans", *Am J. Roentgenol.*, 87, 185, 1962.

Hounsfield G.N. : "Computerised transverse axial scanning (tomography). Part 1 : Description of the system." *Br. J. Radiol.*, 46, 1016-1022, 1973.

ICRU 44 : " Tissue substitutes in radiation dosimetry an measurement".

- Kappas K. : "Les hétérogénéités dans les faisceaux de photons de haute énergie employés en radiothérapie, recherches expérimentales et théoriques." Thèse de doctorat, 1986.
- Webb S. : "Non-standard CT scanners : their role in radiotherapy", *Int. J. Radiation Oncology Biol. Phys.*, 9, 1589-1607, 1990.
- White D.R., Speller R.D. : "The measurement of effective photon energy and "linearity" in computerised tomography", *Brit. J. Radiol.*, 53, 5-11, 1980.
- White D.R., Speller R.D., Taylor P.M. : "Evaluating performance characteristics in computerised tomography", *Brit. J. Radiol.*, 54, 221-231, 1981.

**NEXT PAGE(S)
left BLANK**



BE9700016

Impact of immobilization procedures on the efficiency of radiation therapy treatment in the pelvic region

*F. Van den Heuvel (†), M. De Beukeleer, P. Bijdekerke, M. Robberechts,
R. Van Cauwenbergh and G. Storme*

Dept. Radiotherapy
Academic Hospital, Free University Brussels

1. Introduction

Accuracy of positioning in the pelvic region for purposes of radiation treatment has been shown to be a difficult task. A number of groups have been studying this problem (2-7, 16). When all pathologies are pooled, an overall standard deviation of about 5 mm seems to be a common size for detected in-plane setup errors. The size of these setup errors forces the physician to choose fairly large fields to take movement into account, thereby increasing the probability of normal tissue complications (NTCP).

A number of solutions have been proposed to alleviate this problem. Several groups try to minimize errors by monitoring the setup errors for a given time and introduce action levels in order to minimize systematic errors (1, 13). Other groups propose on-line correction, where the treatment of a fraction is interrupted for a short time allowing an objective algorithm to determine the setup error after which correction can be done using a given action level. (3, 16). These methods have been studied for their effectiveness as well as for their cost-benefit. A more traditional method like immobilization has not been looked at with the same methods. It is taken for granted that they are less costly because they are an established part of the radiation therapy procedure.

It is the goal of this paper to study the impact (effectiveness and cost) of an immobilization method based on the same principle as head immobilization using a cast made from Orfit® material, as well as determining possible improvements to the design of the casts. The survey is carried out in an analogue manner as a recent survey on the effectiveness of on-line repositioning (16). Indeed an Electronic Portal Imaging Device (EPID) was used to determine the possible setup errors. This device

combined with an adjustment protocol ensured the correct treatment of the patients enlisted in the study.

2. Methods and Materials

2.1. Equipment

2.1.1. Immobilization Cast

A prototype of an Orfit® cast for the pelvic region was delivered to us with kind permission of the manufacturer(*). The cast consists of orfit material which is mouldable when heated to a temperature of 60°C. After cooling the cast becomes rigid and keeps the moulded form. The fixation plate, which is positioned on the treatment table, was made of radio-transparent carbon.

2.1.2. Electronic Portal imaging device

The fluoroscopic EPID system (Beamview Plus®) developed by Siemens (Concord, CA, USA) was used. Fluorescence, generated by ionizing radiation of a metal-phosphor screen was reflected by a 45° mirror to a video camera mounted in the gantry of a Siemens KDS-2 linear accelerator, dual photon energy; 6 or 18 MV. The system design is described by Leszczynski et al. (9, 12).

2.1.3. Couch controller

In order to make fast adjustments of the couch position, one of the four controllers was removed from the couch (Siemens ZIV, digital read-out couch) and installed outside the treatment room near the control table. A digital read-out panel was also installed outside. This digital read-out served to make, interactively, adjustments of the couch position. The precision was 1 mm.

(*). Orfit Industries n.v. Vosveld 9a B-2110 Wij-negem, Belgium

(†) For Correspondence

2.2. Measuring localization errors using OPIDUM

OPIDUM is an acronym for On line Portal Imaging with Distant User Manipulation. It compares two images by comparing the position of a set of soft rulers in an image. OPIDUM and its validation are the subject of a separate publication (15). OPIDUM proved to be very efficient and accurate on pelvic AP-PA fields.

2.3. Patient Inclusion and Treatment Procedure

Thirteen patients were treated using a diamond shaped AP-PA field with a beam of 18MV photons. All patients were treated using an isocentric technique with a Source to Axis Distance (SAD) of 100 cm. A total of 169 fractions were imaged and available for analysis. The patient is positioned on the table using the cast. The treatment starts by giving the minimum dose necessary to obtain a portal image, after the treatment is paused. With the patient remaining on the table the portal image is compared to a simulator image using the OPIDUM system. If the discrepancy measured for translations is larger than 5 mm in either transversal or longitudinal direction, a correction is applied using the couch controller. After correction if any the treatment is resumed. Setup errors were measured for 169 fields. A similar on-line correction procedure has been clinically applied with a smaller action level (2 mm) is described in a previous paper (16).

2.4. Reporting overall errors

Information on overall setup errors consists of the spread in the distribution of all errors of all patients for each group separately. The measure for this spread is the standard deviation (SD).

Graphical representation

In the further treatment of overall errors we will represent the in-plane translational errors as a scatter plot in longitudinal and transversal directions. On such a scatter plot the confidence limit of 95% is calculated and drawn on the graph as an ellipse (10). All scatter plots are constructed following the methods described by Lebesque and colleagues (8).

2.5. Reporting individual setup errors

Geometric setup errors in patient position are traditionally subdivided as systematic errors and random errors. The systematic error in a certain direction will be defined as the mean of the errors

in that direction, again assuming independency, summing over all fractions. The random error will be defined as the SD of the distribution of every patients setup error calculated over all the fractions measured. The SD will be denoted as σ_i with i the order in which the patient was entered in the study. To report this distribution the mean of the systematic error was calculated. This gives an overall value which can be considered as the systematic errors introduced by the treatment chain which is specific for the procedure used. Another interesting value is the spread of the systematic error estimated by calculating the standard deviation of the systematic errors.

2.6. Estimating extra time in the treatment procedure

The use of an immobilization device in pelvic treatment is likely to increase the overall treatment time per fraction. Due to the large number of factors involved in the procedure we can only estimate the increase of treatment time by comparing with a study where on-line correction was also applied. For this purpose absolute times will be considered for the treatment of the first field, data which is also available in the comparison study (16).

2.7. Correlations

A possible selection criterium for the use of on-line correction is the obesity of the patient (14). A measure for the obesity is the Body Mass Index (BMI), defined by:

$$BMI = \frac{\text{weight in kilogram}}{(\text{length in meters})^2} \quad (1)$$

The BMI was correlated to the random error as well as the absolute value of the systematic error per patient. The correlation is quantified using the Spearman Rank-Order-Correlation Coefficient r_s (11).

3. Results

3.1. Adjustments

Of the 169 fields were the on-line correction protocol was performed 55.7% were corrected. Table 1 shows the results for the detected setup errors. Given are the overall mean, overall Standard Deviation (SD), the mean of the and SD of the systematic errors and the mean and SD of the random errors both in the transversal and longitudinal direction.

	transversal	longitudinal
Overall mean	0.04 mm	0.32 mm
Overall SD	3.14 mm	8.99 mm
Mean random error	2.48 mm	5.44 mm
SD_{sys}	1.80 mm	7.20 mm

The rotational error for setup was -0.06° whereas the overall SD for rotation was 1.25° .

3.2. Graphical representation

Figure 1 shows the translational errors as a scatter plot of the transversal and the longitudinal errors. The ellipse shows the 95% confidence region for this distribution. Noteworthy is the large excentricity of the ellipse in the longitudinal direction.

Figure 2 shows a histogram of the distribution of the rotational errors.

Figure 3 shows the distributions of time for the treatment of one field. The histogram in overlay shows the same data from a study using an on-line correction algorithm without immobilization and a tighter action level (2 mm) (16).

Correlations calculated for the BMI with respect to the absolute values of the systematic errors are highly significant in the longitudinal direction. A $r_s = 0.93$ was obtained with $p < 0.001$. In the transversal direction no correlation was found ($p = 0.12$). This means that errors in the longitudinal direction were more important as the BMI (or obesity) of the patient increased.

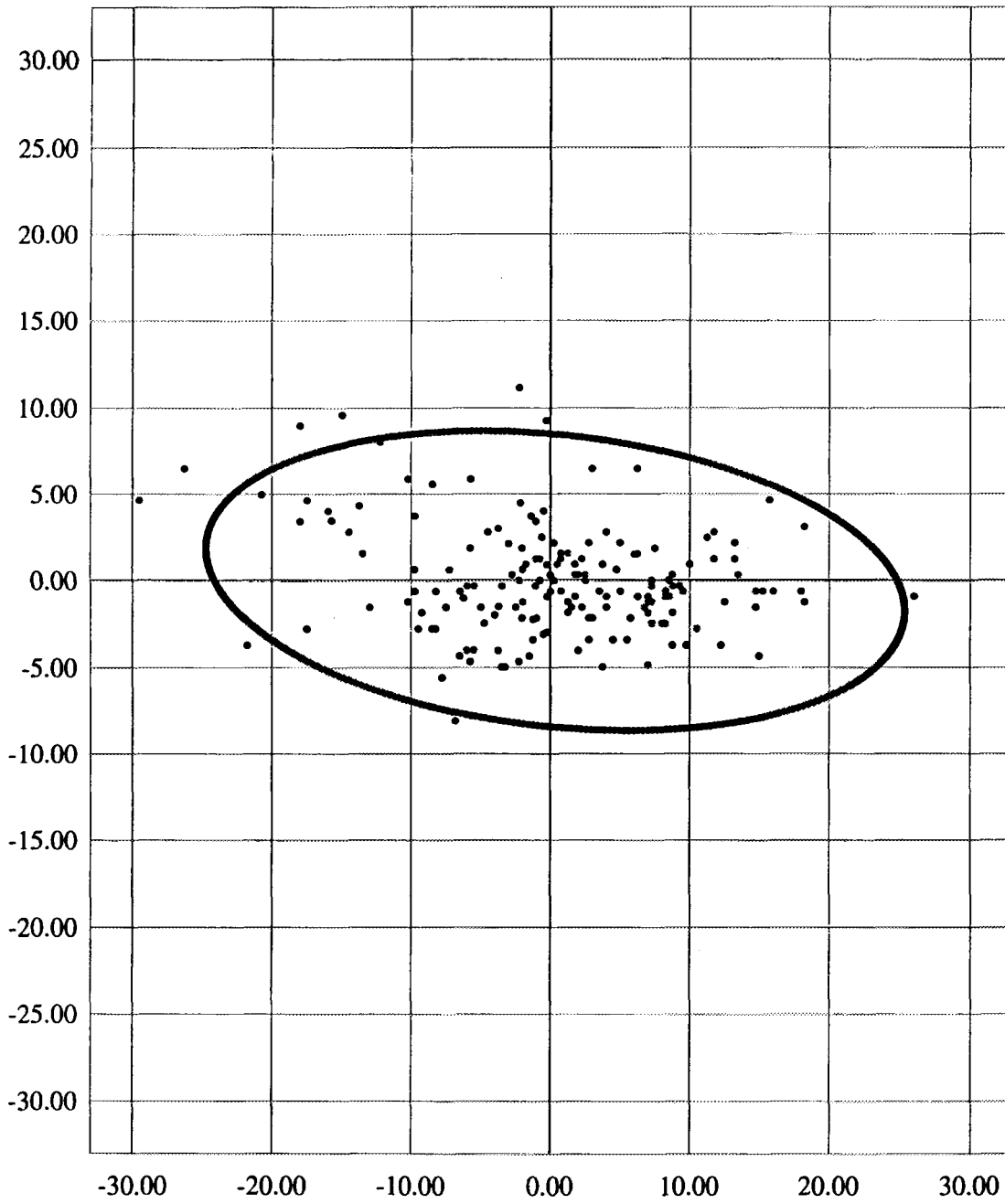
References

1. Bel, A., Herk, M. Van, Bartelink, H., and Lebesque, J.V., "A Verification Procedure to Improve Patient Setup Accuracy using Portal Images," *Radiother. Oncol.*, 29, pp. 253-260 (1993).
2. Bel, A., Vos, P.H., Rodrigus, P.T.R., Creutzberg, C.L., Visser, A.G., Stroom, J.C., and Lebesque, J.V., "High-precision prostate cancer irradiation by clinical application of an offline patient setup verification procedure, using portal imaging.," *Int. J. Radiation Oncology Biol. Phys.* (In Press).
3. De Neve, W., Van den Heuvel, F., De Beukeleer, M., Coghe, M., Verellen, D., Thon, L., De Roover, P., Roelstraete, A., and Storme, G., "Interactive use of on-line portal imaging in pelvic radiation," *Int. J. Radiation Oncology Biol. Phys.*, 25, pp. 517-524 (1993).
4. Dunscombe, P., Loose, S., and Leszczynski, K., "Sizes and Sources of Field Placement Error in Routine Irradiation of Prostate Cancer," *Radiother. Oncol.*, 26, pp. 174-176 (1993).
5. Ezz, A., Munro, P., Porter, A.T., Battista, J., Jaffray, D.A., Fenster, A., and Osborne, S., "Daily Monitoring and Correction of Radiation Field Placement using a Video-Based Portal Imaging System: A Pilot Study.," *Int. J. Radiation Oncology Biol. Phys.*, 22, pp. 159-165 (1991).
6. Herman, M.G., Abrams, R.A., and Mayer, R.R., "Clinical use of on-line portal imaging for daily treatment verification," *Int. J. Radiation Oncology Biol. Phys.*, 28 (4), pp. 1017-1023 (1994).
7. Hunt, M.A., Schultheiss, T.E., Desobry, G.E., Hakki, M., and Hanks, G.E., "An evaluation of setup uncertainties for patients treated to pelvic sites.," *Int. J. Radiation Oncology Biol. Phys.*, 32(1), pp. 227-233 (1995).
8. Lebesque, J.V., Bel, A., Bijhold, J., and Hart, A.A.M., "Detection of systematic patient setup errors by portal film analysis," *Radiother. Oncol.*, 23, p. 198 (1992).
9. Leszczynski, K.W., Shalev, S., and Cosby, S., "A digital video system for on-line portal verification," *Medical Imaging IV: Image Formation*, SPIE 1231, pp. 401-405, The International Society for Optical Engineering, Box 10, Bellingham, Washington 98227 (1990).
10. Press, W.H., Teukolsky, S.A., Vetterling, W.T., and Flannery, B.P., "Modeling of Data" in *Numerical Recipes: The art of scientific Computing*, Cambridge University Press (1993).
11. Press, W.H., Teukolsky, S.A., Vetterling, W.T., and Flannery, B.P., "Statistical Description of Data" in *Numerical Recipes: The art of scientific Computing*, Cambridge University Press (1993).
12. Shalev, S., Leszczynski, K., Cosby, S., and Chu, T., "Static and dynamic portal imaging," *Proceedings of the 7th annual meeting of the European Society for Therapeutic Radiology and Oncology*, p. 425, Den Haag (September 5-8, 1988).
13. Shalev, S. and Glutchev, G., "Decision Rules for the Correction of Field Setup Parameters (Abstract).," *Med. Phys.*, 21 (6), p. 952

- (1994).
14. Van den Heuvel, F., De Neve, W., Coghe, M., Verellen, D., and Storme, G., "Relations of image quality in on-line portal images and patient individual parameters for pelvic field radiotherapy," *European Radiology*, 2, pp. 433-438 (1992).
 15. Van den Heuvel, F., De Neve, W., Verellen, D., and Storme, G., "OPIDUM: On line Portal Imaging with Distant User Manipulation - A way to detect in plane setup errors quickly" in *Proceedings Book: Medical Physics '93*, pp. 469-471, Puerto de la Cruz, Spain (Sept.22-24 1993).
 16. Van den Heuvel, F., De Neve, W., Verellen, D., Coghe, M., Coen, V., and Storme, G., "Clinical implementation of an objective computer-aided protocol for intervention in intra-treatment correction using electronic portal imaging.," *Radiother. Oncol.*, 35, pp. 232-239 (1995).

SETUP ERROR

Transversal (mm)

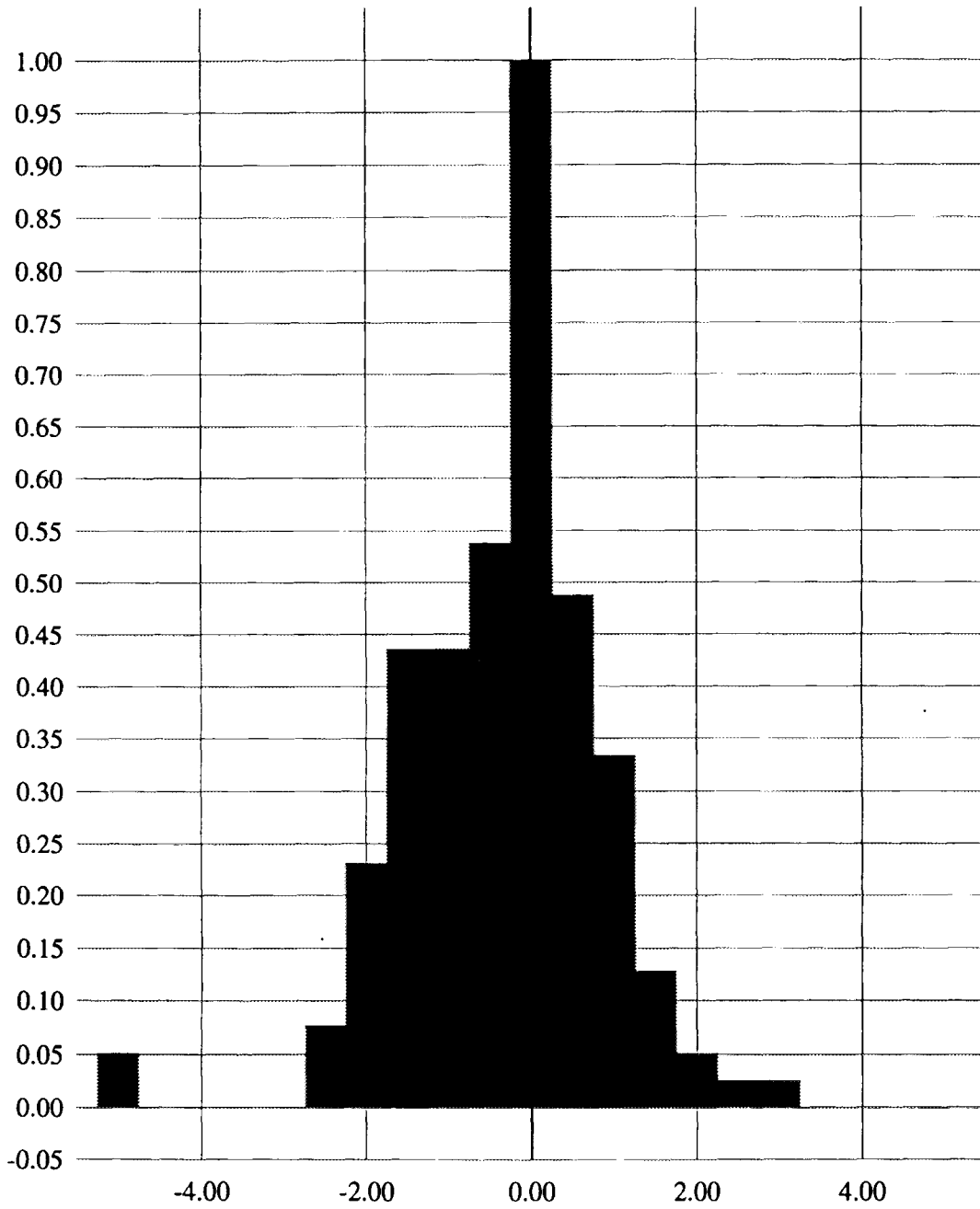


N = 169

Longitudinal (mm)

Rotational error

Relative Frequency (mm)'

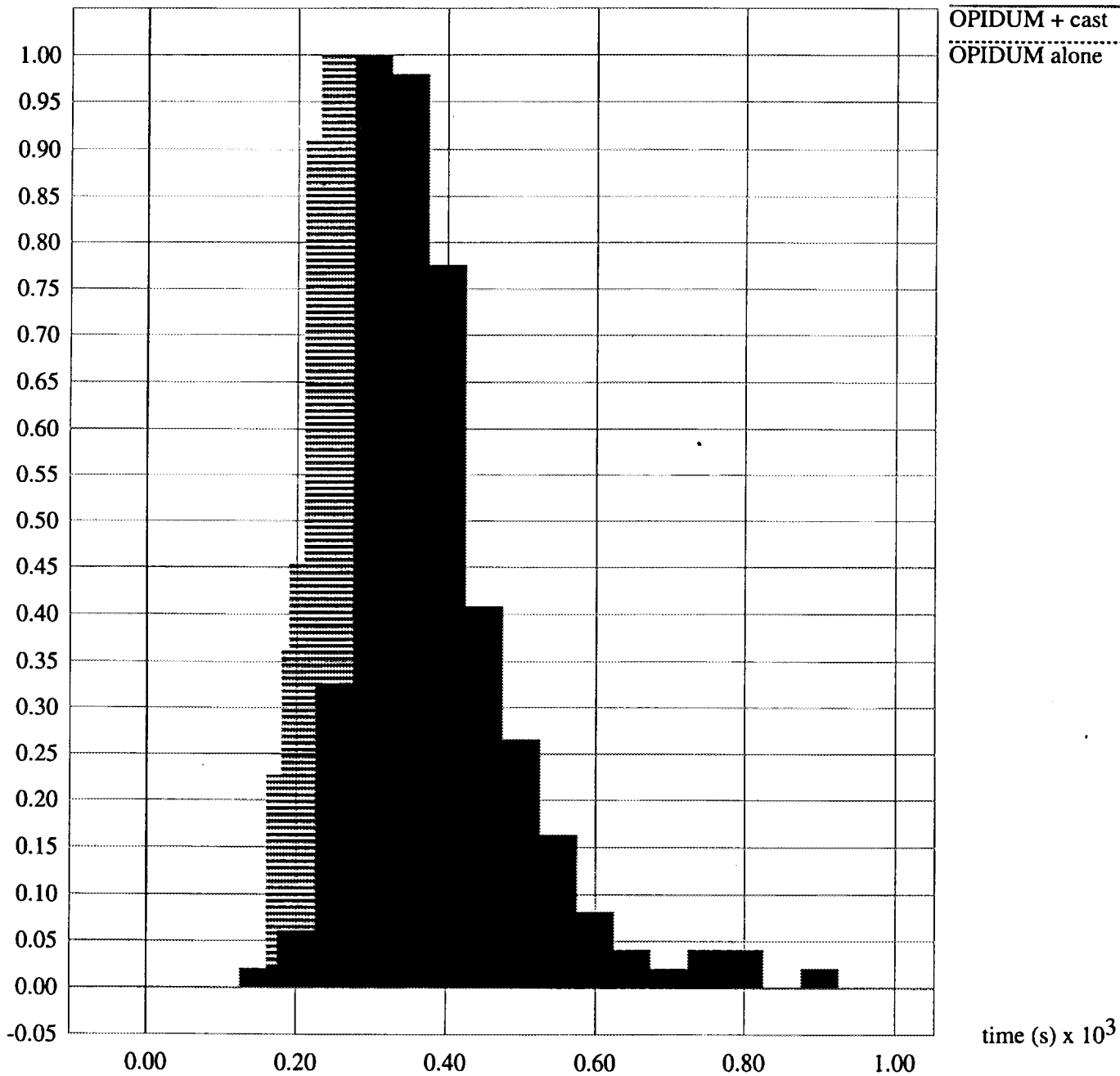


Rotation (degrees)

Time first field

Relative frequency

OPIDUM + cast
OPIDUM alone



NEXT PAGE(S)
left BLANK



Application of an EPID for fast daily *dosimetric* quality control of a fully computer-controlled dual gantry treatment unit ¹

M.L.P. Dirkx, M. Kroonwijk, J.C.J. de Boer and B.J.M. Heijmen

Dr. Daniel den Hoed Cancer Center, Groene Hilledijk 301, 3075 EA Rotterdam, The Netherlands

Abstract

The MM50 Racetrack Microtron, suited for sophisticated three-dimensional computer-controlled conformal radiotherapy techniques, is a complex dual gantry system. Therefore, for both gantries, *daily* quality control of the absolute output and the 2D fluence profile of the scanned photon beams is performed for a number of gantry angles. A fast method for these daily checks, based on *dosimetric* measurements with the Philips SRI-100 Electronic Portal Imaging Device (EPID), has been developed and tested. Open beams are checked for four different gantry angles; for gantry angle 0, a wedged field is checked as well. The fields are set up one after another under full computer control. Performing and analyzing the measurements takes about ten minutes.

Characteristics of the EPID relevant for dosimetric quality control

The SRI-100 is a fluoroscopic system: radiation incident on a fluorescent screen (at a distance of 150 cm from the focus) is converted into an optical image which is digitized using a CCD camera [3]. For dosimetric quality control measurements with the EPID the gain and offset of the CCD camera have been set to fixed values and a fixed data acquisition time, which is longer than the beam on time, has been used. In addition, the images have only been corrected for dark current, which is measured just before irradiation starts.

A fixed field size of 18 x 18 cm² has been used for all measurements in this study. For data reduction, average grey scale values have been calculated for 49 areas of 15 x 15 mm² inside a measured EPID-image, yielding dosimetric data for the beam axis and for 48 off-axis points.

The reproducibility, stability and linearity of the EPIDs have been assessed by comparing measured grey scale values with absolute dose measurements at the beam axis using an ionisation chamber.

Both for the on-axis and off-axis points the EPID-measurements show a short term reproducibility of the measured grey scale values of 0.5% (1 SD). A significant correlation exists between on-axis and off-axis fluctuations: after correcting the grey scale values in the off-axis points for the observed on-axis fluctuations, the remaining image-to-image variation for off-axis points decreases to only 0.2% (1 SD).

The day-to-day sensitivity stability of an SRI-100 over a period of several weeks is 0.6% (1 SD). Measured grey scale values are within 0.2% linear with the applied dose.

It may be concluded that the applied EPID has favourable characteristics for daily dosimetric quality control measurements. No adverse interference effects related to the combined use of the MM50 scanning photon beams and the slow scan mode of the CCD-camera have been observed. For at least a period of several weeks it is possible to derive the output at the beam axis from a *single* EPID-measurement with an accuracy of 0.6% (1 SD), while the relative 2D fluence profile can be determined even more accurately.

¹ This paper is an extension of the work described in reference 1.

Daily quality control measurements

For the open 25 MV scanning photon beam, EPID images have been obtained on a daily basis for four different gantry angles (0, 90, 180 and 270 degrees). For gantry angle 0, a 60° wedged field image has been measured as well to verify the position of the motorized wedge and to check the beam penetrative quality. All images have been acquired using a fixed dose of 150 Monitor Units. The five fields (four open fields and one wedged field) have been set up under computer control using the MM50 multi-segment treatment mode [1,2].

To determine deviations in the absolute beam output and in the relative 2D fluence profile, each image has been compared with a corresponding reference image. This reference image reflects the *absolute* 2D fluence profile at the time of beam commissioning for a fixed dose of 150 MU and a cGy/MU value of 1 for the 10 x 10 cm² field.

For each of the 49 areas defined in the measured images, the percentual difference in measured grey scale value compared to the corresponding area in the related reference image has been determined. Observed differences at the beam axis relate to deviations in the *absolute* output of the photon beam. Deviations in the *relative* 2D fluence profile have been determined by correcting the 49 percentual differences for the observed deviation in absolute output at the beam axis.

The observed deviations in absolute on-axis output for gantry angle 0, measured with the EPID during a period of 300 days for one of the gantries, are depicted in figure 1. Table 1 summarizes the results of 1300 measured images, equally spread over the five different fields and both gantries.

Once an output deviation of about 6% was detected for each field (this value has not been included in figure 1). This deviation was confirmed by measurements with an ionisation chamber. Only because of the performed morning quality control checks with the EPID, erroneous dose delivery to patients could be avoided; there is no interlock in the MM50-system that would have prevented patient treatment in this case.

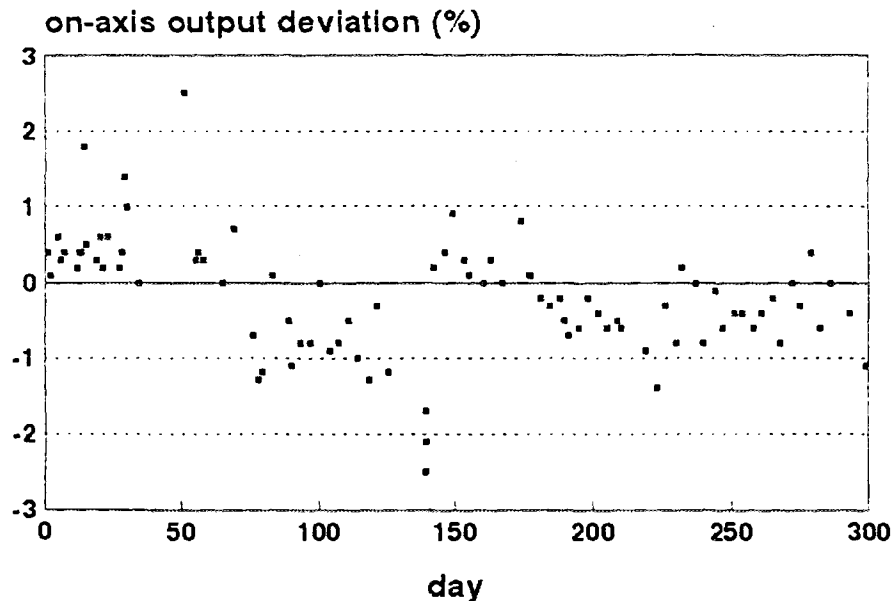


Figure 1 Deviations in absolute on-axis output of the 25 MV photon beam for one of the gantries, measured with the EPID for gantry angle 0.

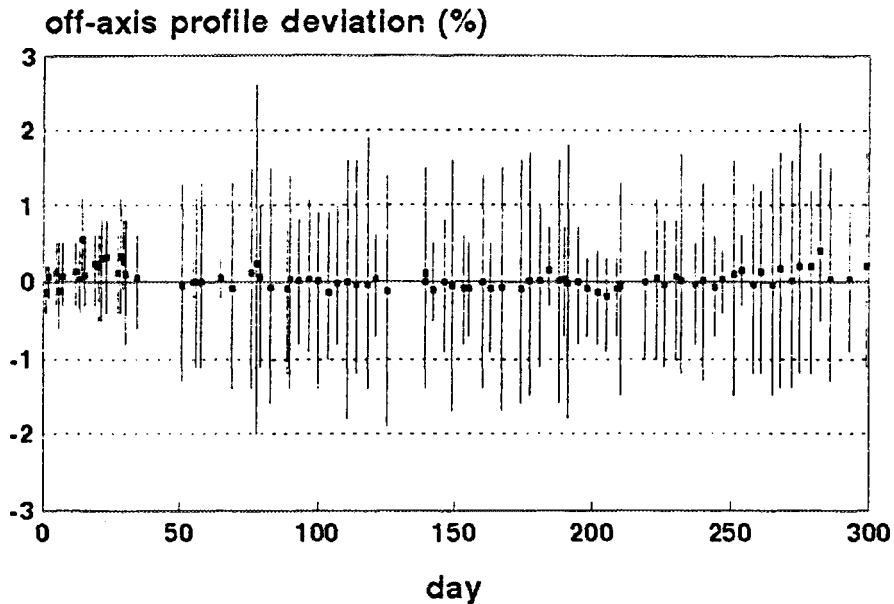


Figure 2 Off-axis deviations in the relative 2D beam profiles for gantry angle 0. The dots indicate the average off-axis deviations for the 48 off-axis points, the bars indicate the maximum deviations.

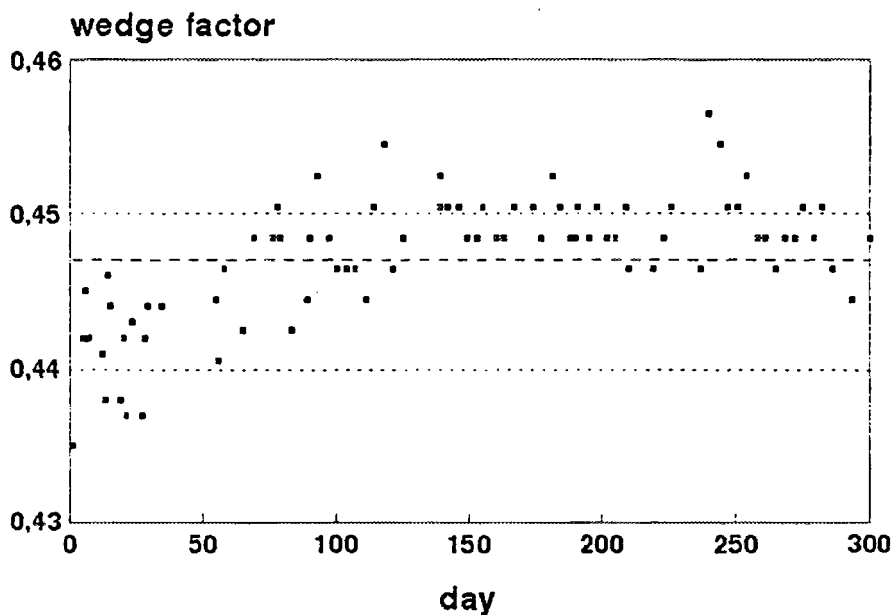


Figure 3 Wedge factors, calculated from measured grey scale values at the beam axis for the open and the wedged field at gantry angle 0.

The observed average and maximum deviations in the relative 2D beam profile, determined from the measurements in the 48 off-axis points, are depicted in figure 2 for gantry angle 0 and summarized in table 1 for all fields. Because the average off-axis deviation was always less than 0.6% and the maximum observed off-axis deviation was 2.6%, it may be concluded that the relative 2D fluence profile is very stable. Wedge factors have been calculated from measured grey scale values at the beam axis for the open and the wedged field at gantry angle 0. The results, depicted in figure 3 for one of the gantries, show a constancy of 0.7% (1 SD).

Table 1 Overview of observed deviations from corresponding reference images. The incidence rates indicate the percentage of the total number of analyzed fields (N = 1300) in which a certain deviation occurred.

	deviations	incidence rate
absolute on-axis output deviations	< ± 2.0 %	94 %
	$\pm (2.0 - 3.0)$ %	5 %
	> ± 3.0 %	1 %
average off-axis profile deviations	< ± 0.3 %	94.7 %
	$\pm (0.3 - 0.5)$ %	5 %
	> ± 0.5 %	0.3 %
maximum off-axis profile deviations	< ± 1.5 %	89 %
	$\pm (1.5 - 2.0)$ %	10 %
	> ± 2.0 %	1 %

Conclusion

Because of its characteristics, the Philips SRI-100 Electronic Portal Imaging Device, is suitable for *fast* and *accurate* daily dosimetric quality control of photon beams under different gantry angles. Deviations in the absolute output and in the relative 2D fluence profiles are determined within 10 minutes for five fields.

Despite the complexity of the MM50, the 2D fluence profile of the 25 MV scanned photon beam has been very stable for all gantry angles during a period of one year: a maximum profile deviation of 2.6% was observed. Once, a deviation in the cGy/MU-value of 6% has been detected. Only because of the performed morning quality control checks, erroneous dose delivery to patients could be avoided. Based on our experiences and on clinical requirements regarding the acceptability of deviations of beam characteristics, a protocol has been developed including action levels for additional investigations [1].

In the near future the quality control measurements will be extended to the 10 MV photon beam and geometric checks on multileaf collimator defined fields will be added as well. Studies on the application of the SRI-100 for in-vivo dosimetry on the MM50 have been started.

References

- 1 Dirkx, M.L.P., Kroonwijk, M., de Boer, J.C.J. and Heijmen B.J.M.
Daily quality control of the MM50 Racetrack Microtron using an Electronic Portal Imaging Device *Radiotherapy and Oncology* 37: 55-60, 1995
- 2 Mageras, G.S., Fuks, Z., O'Brien, J., Brewster, L.J., Burman, C., Chui, C.S., Leibel, S.A., Ling, C.C., Masterson, M.E., Mohan, R. and Kutcher, G.J.
Initial clinical experience with computer-controlled conformal radiotherapy of the prostate using a 50 MeV Medical Microtron
Int. J. Radiation Oncology Biol. Phys. 30: 971-978, 1994
- 3 Visser, A.G., Huizenga, H., Althof, V.G.M. and Swanenburg, B.N.
Performance of a prototype fluoroscopic radiotherapy imaging system
Int. J. Radiation Oncology Biol. Phys. 18: 41-50, 1990

BE9700021



BE9700021

QC in MRI : useful or superfluous ?

S. Infantino & F. Malchair (Biomed Engineering, Boncelles)

A European task group has developed a protocol of quality controls (QC) in MRI. It essentially relates on control of image properties (uniformity of the signal, signal-to-noise ratio (SNR), resolution, distortion,...).

We applied this protocol to the Magnetom SP (Siemens) of the CHU in Liège. We had to use the Siemens multipurpose phantom that doesn't permit a QC as complete and accurate as the Test Objects used in the protocol. The phantom simulates the magnetic properties of the body. We tested the body and head coils with and without a loading annulus that simulates the body conductivity and we obtained interesting results :

- body coil : the signal, SNR, uniformity and artifacts were satisfactory just after a maintenance but had changed significantly and became unacceptable two weeks later.
- head coil : the uniformity of the signal and SNR were satisfactory without the annulus. With the annulus the signal increased from the right to the left of the phantom of nearly 20 % ! This came from a lack of correction of uniformity in the static field.

Other parameters (slice width and spacing, resolution and distortion) were satisfactory.

Since the head coil problem didn't appear during the maintenance we suggest Siemens' QC should include observation of intensity profiles. The images obtained should be archived so that the evolution of performances of the scanner is known.

Introduction

We have controlled the MRI scanner of the CHU in Liège, the Magnetom SP 63 (Siemens) installed in 1989. In particular we checked the body coil and the head coil. Its main static field intensity is 1,5 T so the resonance frequency of ^1H in water molecules is ≈ 63 MHz. In this paper we will describe the phantoms used, then quote the QC's that can be made (reference), we will present our results and we will conclude.

1. Phantoms

They are made of an acrylic resin that gives no MR signal. They contain a solution whose concentration and composition allow the simulation of :

- magnetic properties of human body. Solution's characteristics :

- $100 \text{ ms} < T_1 < 1200 \text{ ms}$.
- $50 \text{ ms} < T_2 < 400 \text{ ms}$.
- proton density \approx water's proton density.

The phantoms used contained a solution at $1,25 \text{ g NiSO}_4 \cdot 6\text{H}_2\text{O per dm}^3$ water. They were the head phantom (spherical, inner \varnothing 170 mm), the body phantom (spherical, inner \varnothing 240 mm) and Siemens' multipurpose phantom (cylindrical, \varnothing 190 mm, length 175 mm). We will describe the last one later.

- body's conductivity :

- T_1 and T_2 very short (a few ms) so it does not appear on the images.
- solution's composition : 3 g $MnCl_2 \cdot 4H_2O$ and 5 g NaCl per dm^3 water.

These phantoms are the "loading annulus" : they are hollow cylinders whose double wall contains the conductive solution. In this annulus we can lay a phantom simulating the magnetic properties. Field gradients induce eddy currents in the solution that shield the magnetic field and so increase the image's noise.

Here's a brief description of the Siemens multipurpose phantom we used. We already said it is cylindrical. It can be subdivided in three sections :

- a uniformity section.
- a section containing parallel cylindrical rods of increasing diameters (1, 2, ..., 12,5 mm). These rods form a "resolution pattern". They produce no signal.
- a section containing several structures producing no signal :
 - four cylindrical rods \varnothing 5 mm whose centres form a 100 mm square ("position markers").
 - two pairs of parallel ramps 1 and 2 mm thick with a 45° slope.
 - two 45° wedges and a $\approx 26,5^\circ$ wedge.

We couldn't use an annulus with this phantom because of their dimensions.

2. Quality controls

Ideally they should be made on a slice (or group of slices) centred on the "isocentre" of the magnet and in offset positions. The isocentre is the centre of the sphere where the static field is the most homogeneous ($\approx \varnothing$ 50 cm). They also should be made in the three "main" planes, that means transversal, coronal and sagittal. On the figure 1 is represented the set of axis used in imaging. The z axis is also the magnet's axis.

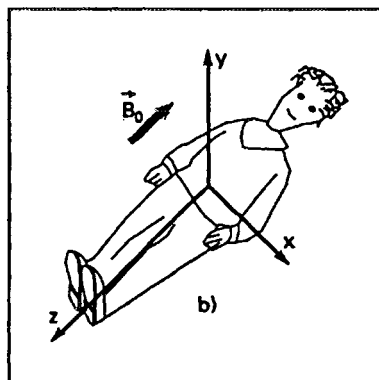


Figure 1 : Imaging's set of axis (Guinet & Grellet, 1992).

In such a system, the transversal plane is parallel to the xy plane, the coronal plane is parallel to the xz plane and the sagittal plane is parallel to yz plane.

In this paper we will only quote the QC's that we have made. For further information the reader should refer to the EEC Concerted Research Project (1988), Lerski et al. (1988) and to Lerski (1993) :

- *signal uniformity* : we simply take an horizontal or vertical intensity profile on the image of the uniformity section (each direction corresponds to one of the x, y or z axis). This function "profile" is already implemented on the Magnetom. The European Protocol gives no tolerance about signal uniformity so the user must evaluate this parameter himself.
- *signal to noise ratio (SNR)* : the device calculates it on a region of interest (ROI) that we have selected on the image of the uniformity section. The SNR is defined as the mean pixels' intensity on the ROI divided by the standard deviation of pixels' intensity on the same ROI. The ROI must contain at least 100 pixels.
- *artifacts* : they are defined by the following formula :

$$\frac{G}{T} \cdot 100 \text{ in } \%$$

where G is the mean pixel intensity on a ROI of the ghost image and T is the mean pixel intensity on the true image (we chose a ROI at the centre of the image).

We also used the uniformity section. Artifacts must be the lowest and ideally they should be less than 5 % (Price et al, 1990).

- *geometric distortion* : we simply measure distances on the images and compare them to the real one. For this QC we used the section containing the position markers. Unknown tolerances.
- *slice width* : the slice profile is identical to the radiofrequency pulse shape. The slice width is the full width at half maximum height of the slice profile. In practice we measure the full width at half maximum height (FWHM) on an intensity profile of the ramps. If their slope is θ° , then the slice width SW is given by the formula :

$$SW = FWHM \cdot \tan \theta$$

Ideally we should use crossed ramps (see figure 2) so an eventual misalignment is compensated, the Siemens phantom contains parallel ramps thus this error cannot be corrected. Tolerance : $\pm 1 \text{ mm}$ for $SW \geq 5 \text{ mm}$ (Price et al., 1990).

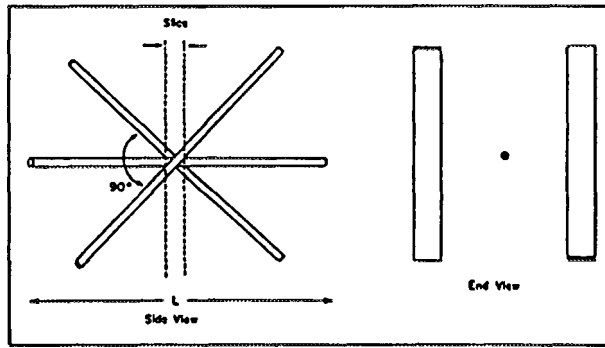


Figure 2 : Crossed ramps with alignment rod (Price, 1988).

- *slice spacing* : it is the spacing between the centres of the FWHM's of a group of slices. Tolerance : ± 1 mm or 20 % of the theoretical spacing, whichever is greater (Price et al., 1990).
- *resolution* : we use the resolution pattern. The rods whose diameter is greater or equal to the theoretical resolution must be visually resolved.

We have acquired all our images with a spin echo sequence using a 1000 ms repetition time (TR) and a 40 ms echo time (TE). The slice width was 5 mm. The matrix was $256 * 256$ and the FOV (field of view) was 256 mm, so the theoretical resolution is 1 mm. We had two signal acquisitions for slice width and spacing and a single acquisition for all other QC's. Signal uniformity and SNR are checked with and without loading annulus. All other QC's are made without annulus so we know the intrinsic performances of the device.

3. Results

Body coil

We have controlled the three "principal planes" : transversal (T), coronal (C) and sagittal (S). Distortion was very low (< 3 %), slice width and spacing were satisfactory.

The T and C planes have been controlled just after a Siemens' maintenance and then two weeks later. During the maintenance the technician corrected a gradient instability that led to a lack of signal uniformity and high artifacts. About the signal we will expose the most interesting results obtained with the multipurpose phantom without annulus (intrinsic performances). If we compare the intensity profiles obtained at the isocentre we note that the signal has an acceptable uniformity (for MRI images) just after the maintenance in both planes but later, we observe a serious degradation of the performances (figures 3, 4, 5 and 6). The SNR shows the same evolution. We estimated the artifacts' intensity on these images :

- T plane : $\approx 3,3$ and $2,7$ % just after the maintenance, and two weeks later we obtained 6 and $8,3$ %. So in two weeks the artifacts became unacceptable.
- C plane : $\approx 3,1$ and $3,6$ % after the maintenance and two weeks later we have artifacts of the order of $13,9$ and $15,1$ %. The degradation is quite clear.

The S plane has been controlled two weeks after the maintenance. The signal is not uniform (concave profiles) and so is the SNR. The artifacts are unacceptable : $10,8$ and $6,3$ %.

Resolution : on some images all the rods were not separated (1 or 2 rods did not appear clearly). To conclude about this problem we must exclude the presence of artifacts.

Head coil

With the multipurpose phantom we observed that distortion, slice width and spacing and resolution were satisfactory. We could only control the T plane because of the dimensions of the multipurpose phantom.

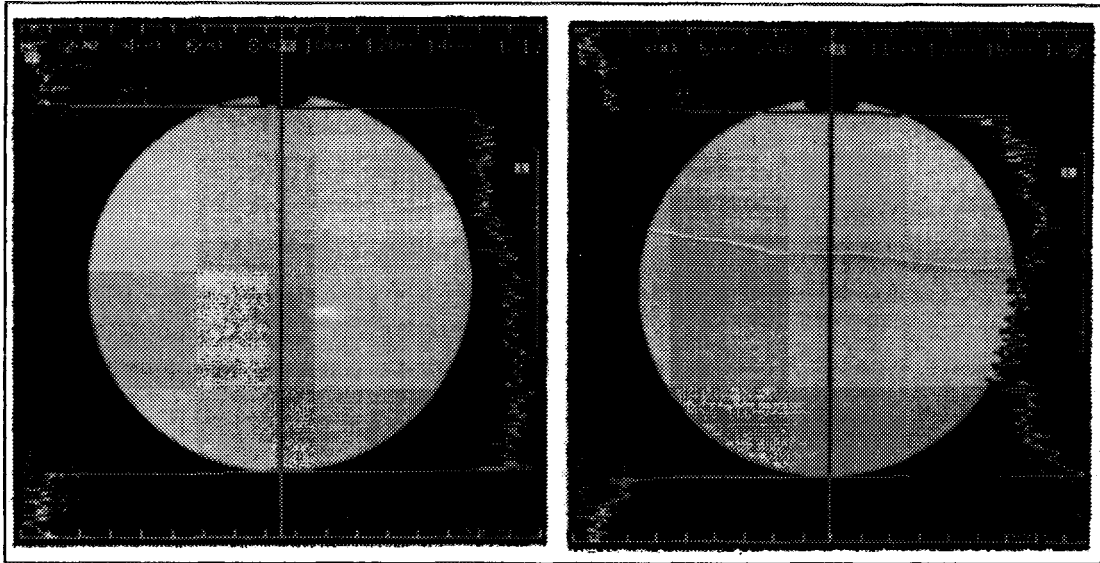
Head phantom alone : signal uniformity (figure 7) and SNR are quite OK in the T plane. Artifacts are very low (< 3 %).

Head phantom and loading annulus : the signal is no longer uniform but increasing ! (see figure 8). The intensity increases from ≈ 1800 (right side of the phantom) to ≈ 2200 (left side) on a phantom diameter (170 mm). This corresponds to a ≈ 20 % higher signal on the left side than on the right side. This direction is the x axis of the magnet. In order to verify that this increase is not due to the phantom but to the scanner, it must also appear in another plane that contains the x axis : the C plane. The figure 9 shows a coronal image of the head phantom. We can see that the signal also increases in the same direction than in the T plane. It is due to a lack of correction of the static field inhomogeneity in presence of conductivity (simulated by the annulus) in other words, in presence of a human body ! This phenomenon appeared clearly on the screen and also on the films.

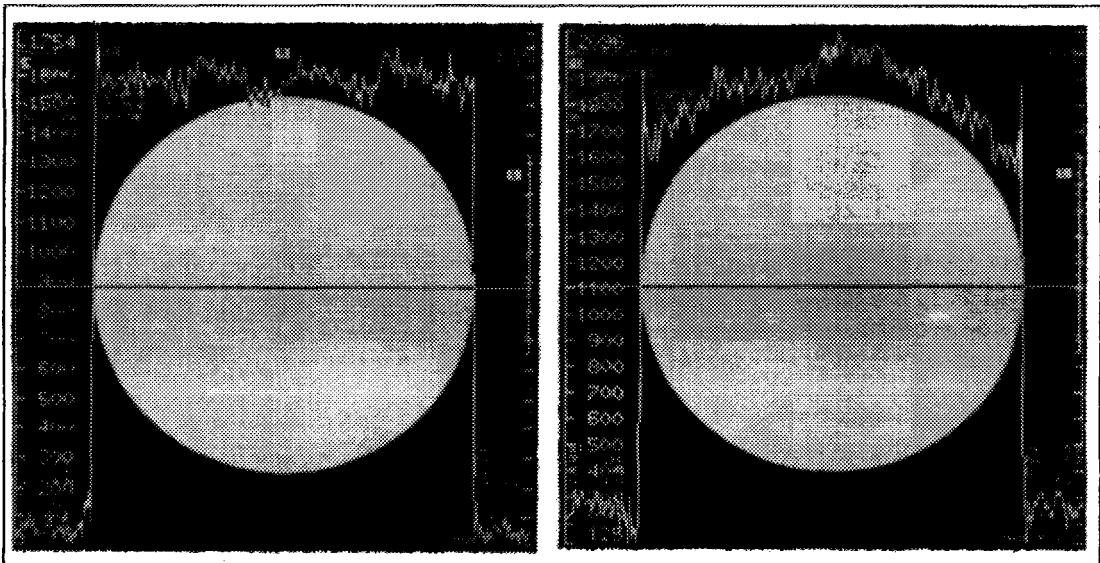
Profiles taken along the z direction are concave (figure 10). It is due to :

- the inhomogeneity of the static field along that axis (unavoidable by construction).
- the variation of the response of the coil along this axis.

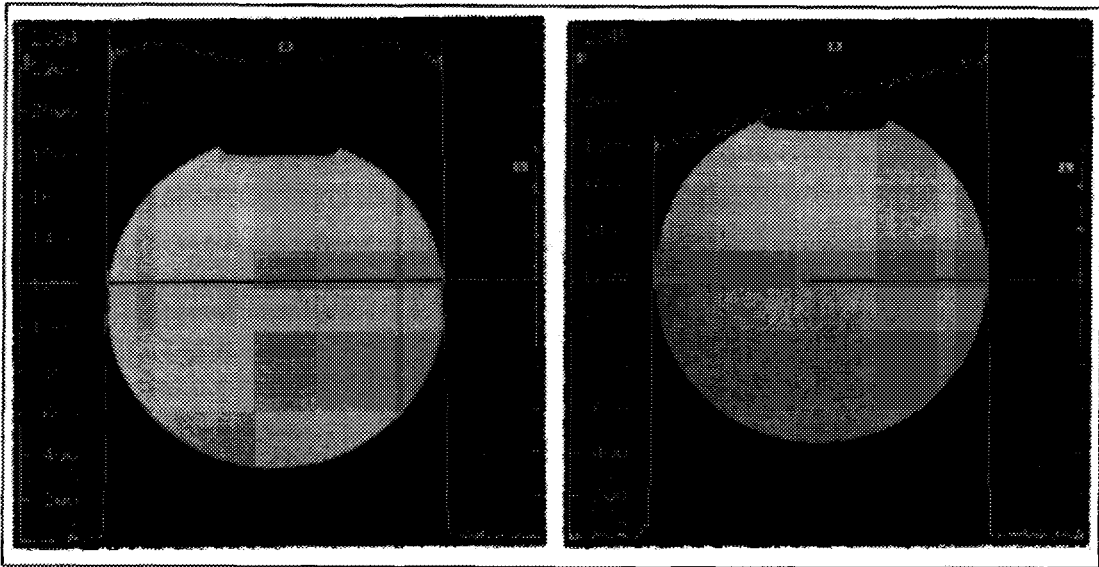
This phenomenon appears on coronal and sagittal images.



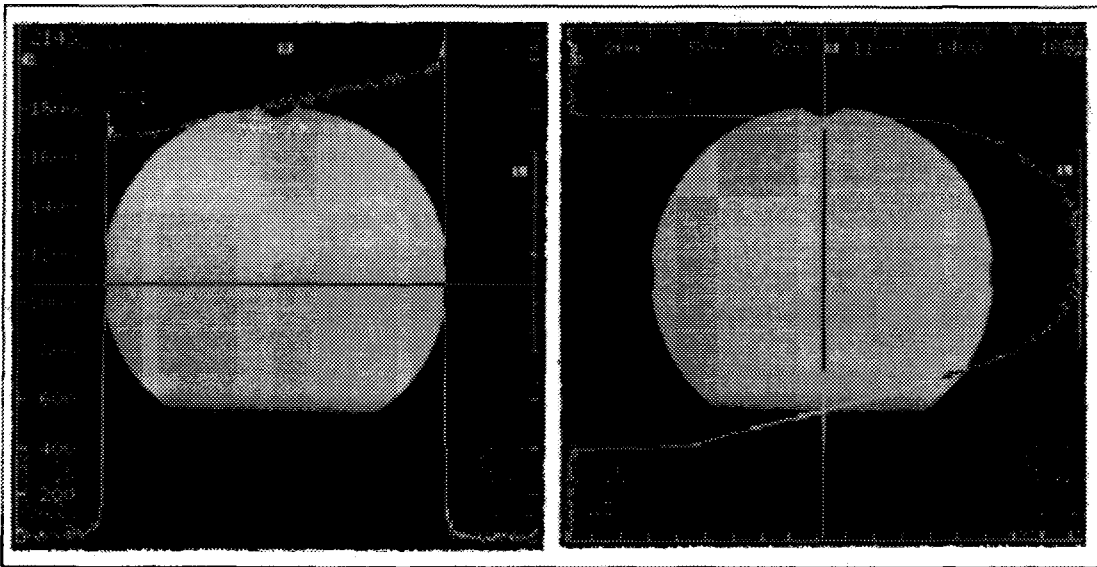
Figures 3 (left) and 4 (right) : Intensity profiles taken just after the maintenance (3) and two weeks later (4) on a transversal image in the body coil.



Figures 5 (left) and 6 (right) : Intensity profiles taken just after the maintenance (5) and two weeks later (6) on a coronal image in the body coil.



Figures 7 (left) and 8 (right) : Intensity profiles without the loading annulus (7) and with the annulus (8) on a transversal image in the head coil.



Figures 9 (left) and 10 (right) : Intensity profiles taken on a coronal image in the head coil along the x axis (9) and along the z axis (10).

Conclusions

With the body coil we noted a degradation of the device's performances in two weeks that is probably due a gradient instability (lack of signal uniformity and increased artifacts). With the head coil we observed a 20 % increase of the signal along the x axis (right - left direction) in presence of conductivity that means in presence of a human body. This is due to a lack of correction of the inhomogeneity of the static field. All other parameters were satisfactory for both coils.

During the Siemens' maintenances the technicians measure SNR at the centre of the images obtained in the three principal planes with the head and body coils (maintenances' frequency : two weeks). They also measure the diameter of the phantom on the images. From the QC we made, we note that an intensity profile is not negligible and, especially, it doesn't take a long time. The images acquired should be archived so the evolution of the device's performances are known. Our results show that QC's in MRI are not superfluous and that they should include intensity profiles. We propose a two weeks frequency for the control of signal and SNR (current frequency). A complete QC should be done every month or every two months. In UK, this complete QC occurs with a 3 months frequency and the company that carries them out is external to the hospital.

Acknowledgements

We wish to thank Pr Dondelinger who allowed us the access to the scanner and the nurses for their collaboration. We also thank Mr. Steve Hill and Mr. Peter Cole for their reception, explanations and for the references they gave to us.

Bibliography

EEC Concerted Research Project (1988). Protocols and test objects for the assessment of MRI equipment. *Magnetic Resonance Imaging*, **6**, pp. 195 - 199.

Guinet C. & Grellet J. (1992). "Introduction à l'IRM. De la théorie à la pratique". Éditions Masson (collection Abrégés).

Lerski R.A., McRobbie D.W., Straughan K., Walker P.M., de Certaines J.D. & Bernard A.M. (1988). Multi-center trial with protocols and prototype test objects for the assessment of MRI equipment. *Magnetic Resonance Imaging*, **6**, pp. 201 - 214.

Lerski R.A. (1993). Trial of modifications to Eurospin MRI test objects. *Magnetic Resonance Imaging*, **11**, pp. 835 - 839.

Price R.R. (1988). Spatial resolution and spatial linearity. In : "MRI : Acceptance testing and quality control. The role of the clinical medical physicist" (proceedings of an AAPM Symposium in Winston-Salem, 6-8 April 1988), pp. 18 - 32. Editor : Dixon R.L., éditions Medical Physics Publishing Company (Madison, Wisconsin).

Price R.R., Axel L., Morgan T., Perman W., Schneiders N., Selikson M., Wood M. & Thomas S.R. (1990). Quality assurance methods and phantoms for magnetic resonance imaging : Report of AAPM nuclear magnetic resonance Task Group n°1. *Medical Physics*, **17** (2), pp. 287 - 295.

**NEXT PAGE(S)
left BLANK**

Noninvasive MRI Thermometry with the Proton Resonance Frequency (PRF) Method: *In Vivo* Results in Human Muscle

John De Poorter, Carlos De Wagter, Yves De Deene, Carsten Thomsen, Freddy Ståhlberg, Eric Achten

The noninvasive thermometry method is based on the temperature dependence of the proton resonance frequency (PRF). High-quality temperature images can be obtained from phase information of standard gradient-echo sequences with an accuracy of 0.2°C in phantoms. This work was focused on the *in vivo* capabilities of this method. An experimental setup was designed that allows a qualitative *in vivo* verification. The lower-leg muscles of a volunteer were cooled and afterwards reheated with an external water bolus. The temperature of the bolus water varied between 17°C and 37°C. The *in vivo* temperature images can be used to extract the temperature in muscle tissue. The data in the fat tissue are difficult to interpret because of the predominance of susceptibility effects. The results confirm the method's potential for hyperthermia control.

Key words: noninvasive thermometry; proton resonance frequency; lower-leg muscles; hyperthermia control.

INTRODUCTION

MRI based noninvasive thermometry methods exploit the temperature dependence of a physical property whose spatial distribution can be visualized. Two physical tissue properties have been suggested as good candidates, namely the spin-lattice decay time, T_1 , (1, 2) and the molecular diffusion coefficient of the water molecules, D , which quantifies the thermal Brownian motion (3). *In vivo* thermometry based on T_1 proved to be difficult because of the thermo-regulative perfusion changes during cooling or heating (4). Also, hysteresis effects between signal intensity and temperature can occur for specific dynamic measurement protocols (5). Perfusion changes can be quantified with the diffusion-based thermometry technique (6) but *in vivo* implementations suffer from an extremely high sensitivity to tissue motion. The motion sensitivity of the diffusion method can be reduced by applying a line-scanning technique (6, 7).

MRM 33:74-81 (1995)

From the MR Department (J.D.P., C.D.W., Y.D.D., E.A.) and Radiotherapy and Nuclear Medicine (C.D.W.), University Hospital, De Pintelaan, Gent, Belgium; Danish Research Center of Magnetic Resonance, Hvidovre University Hospital, Kettegård Alle, Hvidovre, Denmark (C.T., F.S.), and the Department of Radiation Physics, Lund University Hospital, Lund, Sweden (F.S.).

Address correspondence to: John De Poorter, M.Sc., University Hospital (MR Department (-1/K12)), De Pintelaan 185, B-9000 Gent, Belgium.

Received March 11, 1994; revised July 14, 1994; accepted September 13, 1994.

This research was supported by a grant from the IWONL to J.D.P. and the Belgian Science Foundation, and COMAC-BME for supporting our cooperation with the Scandinavian Flow Group.

0740-3194/95 \$3.00

Copyright © 1995 by Williams & Wilkins

All rights of reproduction in any form reserved.

Reliable *in vivo* thermometry results in human muscle have been obtained. The signal to noise was improved by employing big voxel sizes and several acquisitions decreasing the spatial and temporal resolution of the technique. Single-shot techniques like echo-planar imaging (EPI) will reduce the motion sensitivity of the diffusion measurements but also give rise to special hardware demands and a reduced signal to noise ratio (8).

We considered a third method based on the temperature dependence of the proton resonance frequency (PRF). This method provides a significantly better accuracy during *in vitro* experiments than the diffusion-based method (9, 10). Its attractive, spatial, and temporal resolution indicates the possible application for the control and dosimetry of a hyperthermia treatment. Those treatments are based on the sterilizing or killing effect of tumor tissue heated above a threshold temperature of around 42°C (11). Phase transitions of the heated tissue may occur above 42°C. This will compromise thermometry methods that are based on specific properties of the tissue, including the PRF method. The effects of phase transitions were not investigated in this study.

The exploration of the temperature dependence of the PRF for thermometry is not new (12). The method has been used in spectroscopy to monitor temperature in cell cultures (13). It gained importance for imaging purposes when the idea was introduced by Ishihara *et al.* to measure the temperature-related frequency shifts from the phase images of gradient-echo sequences (14). The mean phase in a voxel that was built up during the echo time is proportional to the frequency shift. The advantages of this method are clear. No special hardware is necessary, a standard gradient-echo sequence can be used and short acquisition times lie within the possibilities. However, the method puts high demands on the temporal stability of the external magnetic flux density. The drift of this external field during the thermal process will enhance the temperature related changes. Our previous work demonstrated that the mean drift can be corrected by using external reference phantoms that remain at a fixed temperature (9). In this paper, we propose a further improvement, namely the correction for the first-order spatial variations of the external field drift during the thermal experiment. Further, *in vivo* results in the human lower leg muscles will be presented. The obtained temperature distributions will only be verified on a qualitative basis. A quantitative analysis of the *in vivo* temperature distributions will be the subject of future studies.

MATERIALS AND METHODS

Theoretical Considerations

An object with a volume susceptibility χ_o is placed in a uniform external magnetic-flux-density field B_{ext} . The macroscopic magnetic flux density B_{mac} can be determined in and outside the object from Maxwell's equations in matter. This field is a function of the external field, the geometry and the volume susceptibility of the object. The PRF of that object is proportional to the magnitude of the local magnetic flux density B_{loc} . This is the field at the protons of the molecules in the object. The screening constant σ_{is} of the molecules in interaction with its neighbors relates the local field with the macroscopic field. An approximated relation between these fields is given by (15)

$$B_{loc}(r) \cong B_{mac}(r) - \frac{2\chi_o(T(r))}{3} B_{ext} - \sigma_{is}(T(r)) B_{ext} \quad [1]$$

where $T(r)$ is the temperature at position r inside the object. Hydrogen bonds distort the electronic configuration of the molecules (16) resulting in a less effective electronic screening. Because the fraction and the nature of the hydrogen bonds in water vary with temperature (17), the screening constant and the nuclear magnetic resonance frequency will also change. The screening constant of pure water has a linear temperature dependence over a broad range (18). This range includes the temperature region of interest for hyperthermia, namely from 37 to 45°C. As a result, the magnitude of the local magnetic flux density decreases with 0.01 ppm/degree Celsius temperature elevation.

An important complication is the fact that the local magnetic flux density will also change with temperature due to the temperature dependence of the susceptibility constant (Eq. [1]). The temperature sensitivity of the susceptibility is dependent on the tissue type. We have examined these effects quantitatively in muscle and fat tissue and compared them with the temperature dependence of the tissue screening constant. A detailed discussion of these measurements is published elsewhere (19), and we will only summarize the results. The muscle tissue behaves like water, so its screening constant has the same temperature dependence as water and the susceptibility-related changes of the local field can be neglected in a first approximation. The screening constant of fat tissue, however, does not change significantly over the temperature range of interest for hyperthermia. Shifts in the magnitude of the local field in fat are therefore mainly related to the temperature dependence of the susceptibility. This dependence proved to be of the same order of magnitude as that induced by the change of the muscle screening constant. This makes temperature changes in fat tissue difficult to examine with the PRF method. Another important result of our study of susceptibility effects is that strong paramagnetic substances should be used with great care. They effect the macroscopic magnetic flux density significantly in a region around the objects. Therefore the cooling water of the *in vivo* experiment was not doped with a paramagnetic salt, a measure generally taken to avoid motion artifacts in the images.

A gradient-echo sequence with an echo time TE allows measurement of the phase distribution, altered by field differences, relative to a reference phase distribution. The thermally induced phase difference $\Delta\varphi(r)$ will be proportional to the temperature difference $\Delta T(r)$, ignoring temperature related susceptibility effects (9). If α is the proportionality constant of the linear temperature dependence of $\sigma_{is}(T)$, the temperature dependence of the phase ($\Delta\varphi/\Delta T$) is given by

$$\frac{\Delta\varphi(r)}{\Delta T(r)} = \gamma B_{ext} \alpha TE, \quad [2]$$

where γ is the gyromagnetic ratio of hydrogen and B_{ext} the amplitude of the external magnetic flux density vector. This relation assumes that the amplitude of the external field in the voxel did not vary during the thermal experiment. For pure water in a 1.5 T system and for a TE of 30 ms, the temperature dependence of the phase has the value $6.9^\circ(\text{C})^{-1}$.

Drift of the external-field strength will induce a shift in the amplitude of the local field which in a good approximation is material and temperature insensitive. This gives rise to an extra phase shift, that we will call the phase drift. This phase drift can be measured with a reference phantom that remains at a constant temperature if the external field drift is uniform over the image plane. For our scanner this is not the case. Experiments prove that the phase drift varies linearly over a transversal image. We used three reference phantoms to reconstruct this first-order space-dependent phase drift.

Experimental Procedures

The experiments were conducted on a Siemens 1.5 T SP scanner, using the built-in gradient system and the standard circularly polarized head coil. The gel phantoms consisted of 1.5% agarose gel (Sigma, type V, high gelling

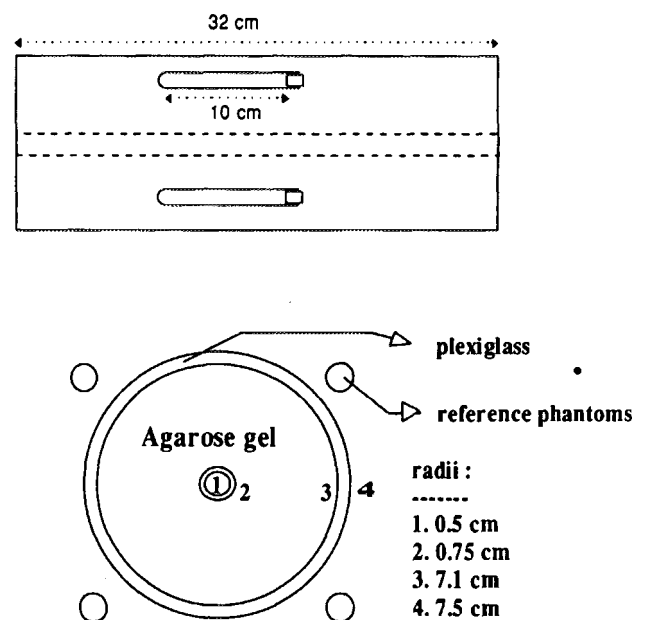


FIG. 1. A horizontal and vertical projections of the experimental setup used in the phantom experiment.

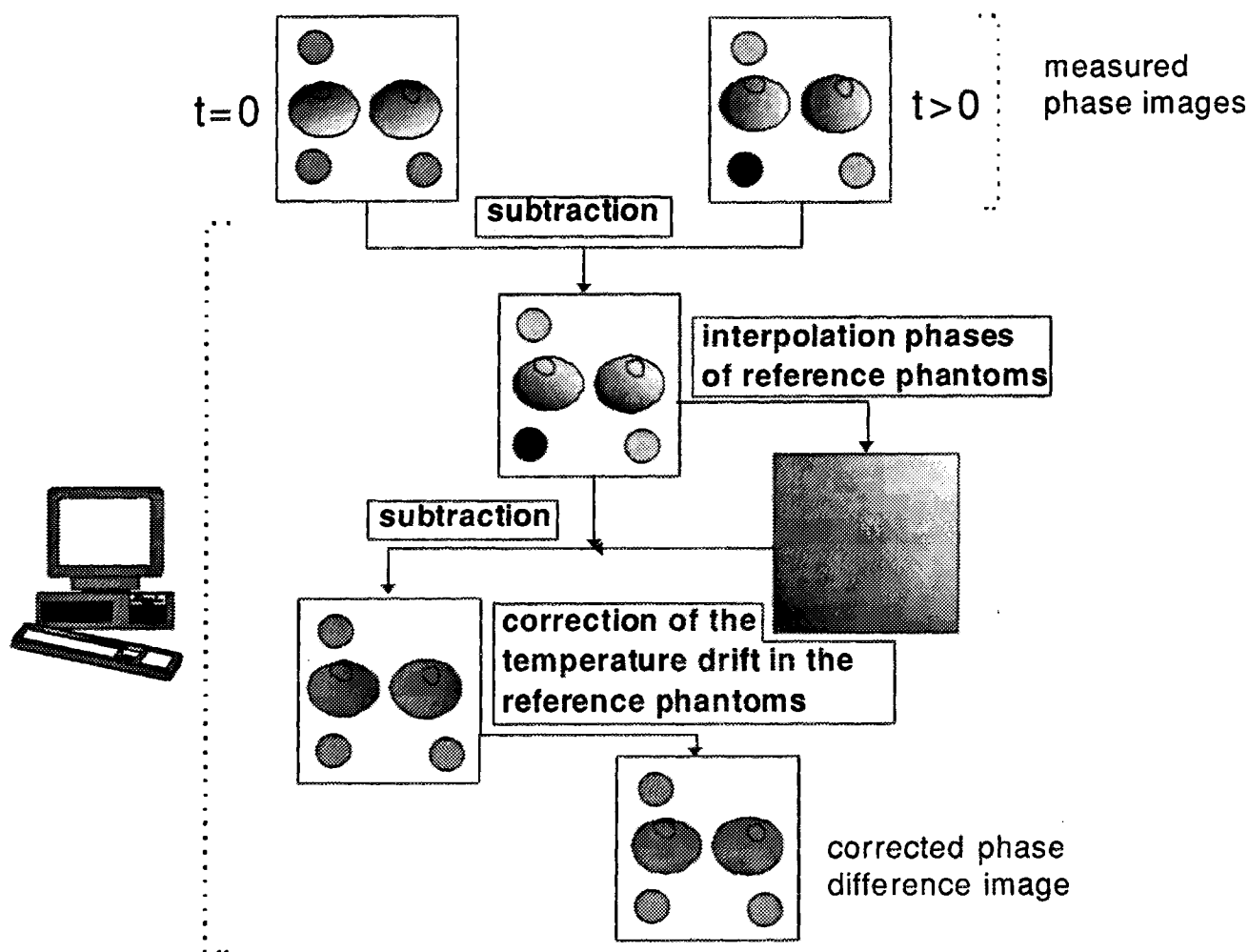


FIG. 2. Scheme of the postprocessing algorithm that calculates temperature images from the phase images.

temperature) doped with 0.2 g/liter CuSO_4 (Aldrich, 98%). Invasive temperature measurements were performed by means of fiber optic probes of a Luxtron fluoroptic 8 channel system (model 3000). The Luxtron thermal probes are single point, type MPM, and have a diameter of 0.5 mm. The experiments were realized by use of a gradient-echo sequence with the following imaging parameters: repetition time $TR = 250$ ms, echo time $TE = 27$ ms, flip angle $FA = 40^\circ$, orientation transverse, resolution 256×256 , field of view $FOV = 220$ mm, and slice thickness $= 10$ mm. A reduction of the blood flow motion artifacts was obtained by using two saturation bands of 5 cm, on both sides of the image plane. The distance between the center of the image plane and the saturation bands was 3.2 cm. The resonance frequency during the measurements was 63.60903 MHz. The magnetization was brought into a steady-state regime by performing measurements without data acquisition during 5 s. The total measurement time became 69 s. Image postprocessing was done on a DIGITAL DECstation 5000/200.

A phantom experiment and an *in vivo* experiment are described. The phantom experiment illustrates the devel-

oped correction mechanism for the phase drift while the *in vivo* experiment demonstrates the method's relevance for *in vivo* thermometry.

For the phantom experiment, a cylindrical phantom with a small central tube was placed horizontally in the head coil (Fig. 1). This phantom will be referred to as the central phantom. Its small central tube is not relevant for this experiment. It was of use in previous experiments. The central phantom was surrounded by four small cylindrical reference phantoms (inner diameter $= 1.4$ cm, length $= 10$ cm). Before starting the measurements, the whole setup was placed in the scanner tunnel for 10 h to obtain a thermal equilibrium. A set of 127 measurements were performed during this thermal equilibrium. The measurements were separated with 51 s of waiting time, which results in one measurement every 2 min. In combination with the air temperature in the scanner tunnel, the temperature in the reference phantoms and the central phantom was monitored during the experiment. This was done to verify the thermal steady state.

The first phase image of the set was subtracted from each of the subsequent phase image. All the values that were under a threshold value in the first amplitude image

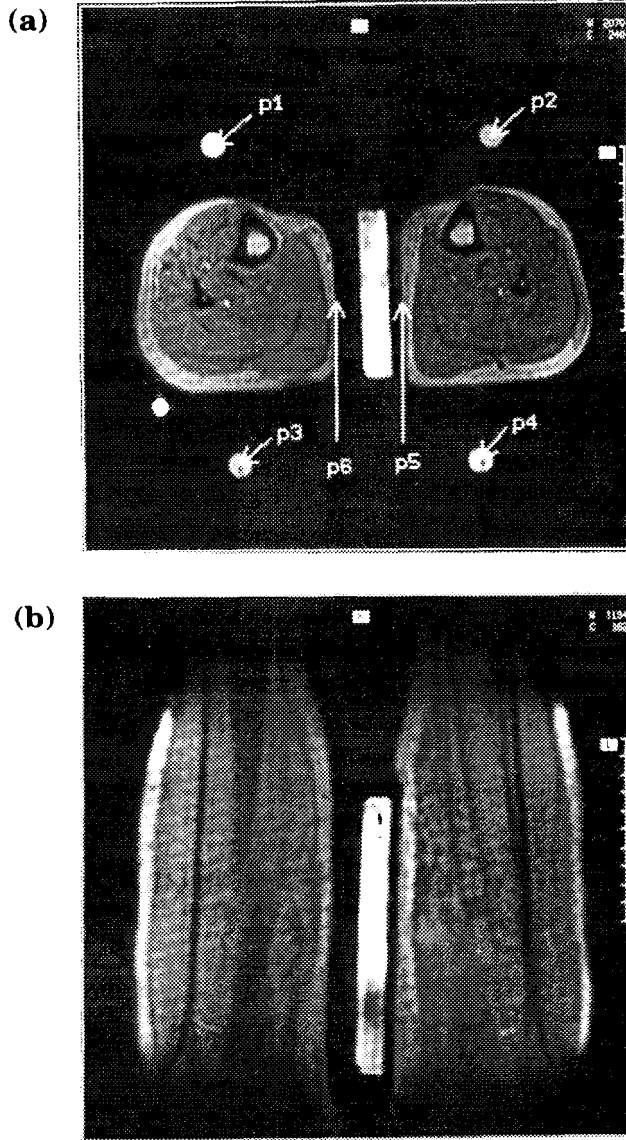


FIG. 3. (a) Transverse and (b) coronal amplitude images of the *in vivo* experimental setup. The position of the temperature probes (p1-p6) is also indicated.

were set to zero in every difference image. The subtraction algorithm was constructed to filter out the phase aliasing of the original phase images (20). For every measurement, a map of the magnetic field drift relative to the first measurement was obtained by extrapolating the phase differences of three of the four reference phantoms linearly over the whole image. The fourth reference phantom is only employed for the control of the correction algorithm. The mean value $\langle \Delta \varphi \rangle$ and the standard deviation $s_{\Delta \varphi}$ of the phase differences in the central phantom pixels were calculated, according to the following definitions.

$$\langle \Delta \varphi \rangle = \frac{1}{N} \sum_{i=1}^N \Delta \varphi(i) \quad [3]$$

and

$$s_{\Delta \varphi} = \sqrt{\frac{1}{N} \sum_{i=1}^N [\Delta \varphi(i) - \langle \Delta \varphi \rangle]^2} \quad [4]$$

The number N corresponds with the number of pixels within the central phantom. Three different post-processing schemes were examined. In the first case, we calculated the difference images without any further correction. Secondly, the mean phase drift of the reference phantoms was subtracted from the difference images. In the third case, the first-order-phase-drift map was subtracted from the difference image implying a correction for the spatial variation of the drift. The third correction procedure was used in the further experiments. The algorithm is shown schematically in Fig. 2. An extra step allows a correction for possible temperature changes in the reference phantoms. For *in vivo* experiments this step is necessary as the temperature inside the scanner tunnel can increase due to the body temperature.

During the *in vivo* experiment, we monitored the cooling and reheating of the lower leg muscles of a volunteer. The positioning of the legs, the reference phantoms, the cooling element and the thermal probes (p1-p6) are visualized in Fig. 3. The cooling element was placed close to the right leg. Extra insulation material was placed between the left leg and the cooling element. The extra circle under the left leg in Fig. 3a is a section of the tube through which water flows to the cooling element. Two different circulation pumps were used to provide pure water at the controlled temperatures of 5°C and 37°C, respectively. The cooling element was made of a polymer with a high thermal conductivity, namely Epramid 6.6 KC (Eriks). A rigid cooling element was preferred because classical bolus elements moved when the water was switched between the different pump systems. Initially, water of 37°C was pumped through the cooling element. At time 0, a series of measurements was started.

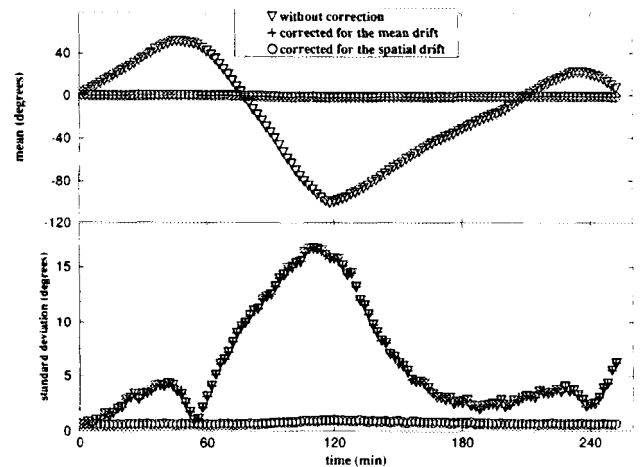


FIG. 4. The mean value and the standard deviation of the phase over the central phantom during the stability experiment. Different correction schemes are applied to the images. Apparently, the correction for the spatial drift, with the help of three reference phantoms, results in a temporally stable and uniform phase distribution.

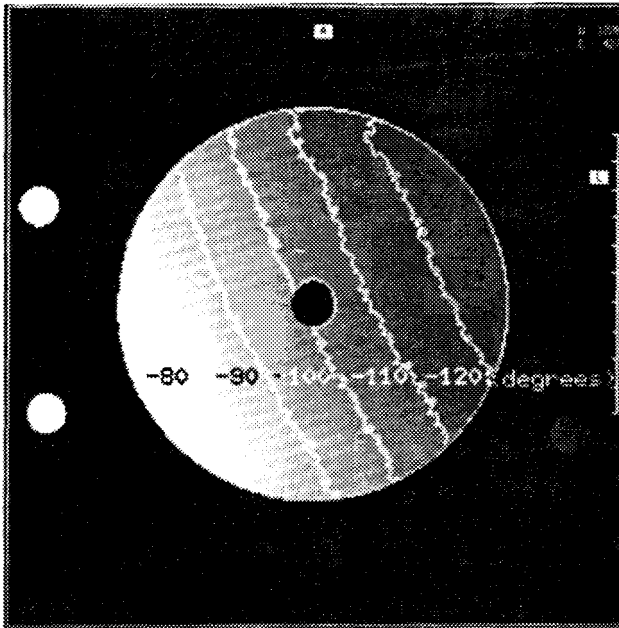


FIG. 5. A phase difference image with a standard deviation of 16 degrees that was measured at $t = 120$ min. The iso-phase contours of -80° , -90° , -100° , -110° , -120° are drawn. The contour configuration supports the assumption that the spatial phase drift is linear over the image.

spaced 2 min in time. After the second measurement ($t = 3$ min), the cooling was switched on and after the 12th measurement ($t = 23$ min), warm water was pumped through the cooling element again. We stopped the protocol after the 29th measurement.

RESULTS

During the whole phantom experiment, the temperature changes measured invasively remained below 0.2°C to

0.3°C . The mean and the standard deviation of the distribution of phase differences in the central phantom are drawn in Fig. 4 (∇ : without correction). The phase differences are relative to the first phase image measured at $t = 0$. The cause of the phase shifts measured are the changes in the amplitude of the external magnetic flux density. The mean phase in the central phantom changed more than 100° during the 127 measurements and had an oscillating behavior. A positive phase shift corresponds to a decrease of the amplitude of the external field and vice versa. The phase shifts of a measurement vary also spatially, and this has been expressed by the standard deviation of the set of pixels within the central phantom. These standard deviations also vary between the consecutive measurements. The phase-difference image measured at $t = 120$ min with a high standard deviation of 16 degrees is shown in Fig. 5. The iso-phase contours of -80° , -90° , -100° , -110° , -120° are drawn in the same figure. The appearance suggests that the spatial variation of the phase difference can be described by a two-dimensional linear function.

The results for the two different correction schemes are also plotted in Fig. 4. In the first scheme the mean phase drift in the reference phantoms is subtracted from the difference images ($+$: corrected for the mean drift). The mean phase shift in the central phantom remains almost zero after this correction, but the spatial variations and the corresponding standard deviation remain unaltered. It is only when three reference phantoms are used to calculate the spatial distribution of the phase drift and when this map is subtracted from the phase-difference images that the correction is satisfactory (Fig. 4, \circ : corrected for the spatial drift). In this case the phase in the central phantom remains constant over the different experiments.

The temperatures measured by thermal probes at the skin surfaces and in the upper left reference phantom during the *in vivo* experiment are plotted in Fig. 6a. The

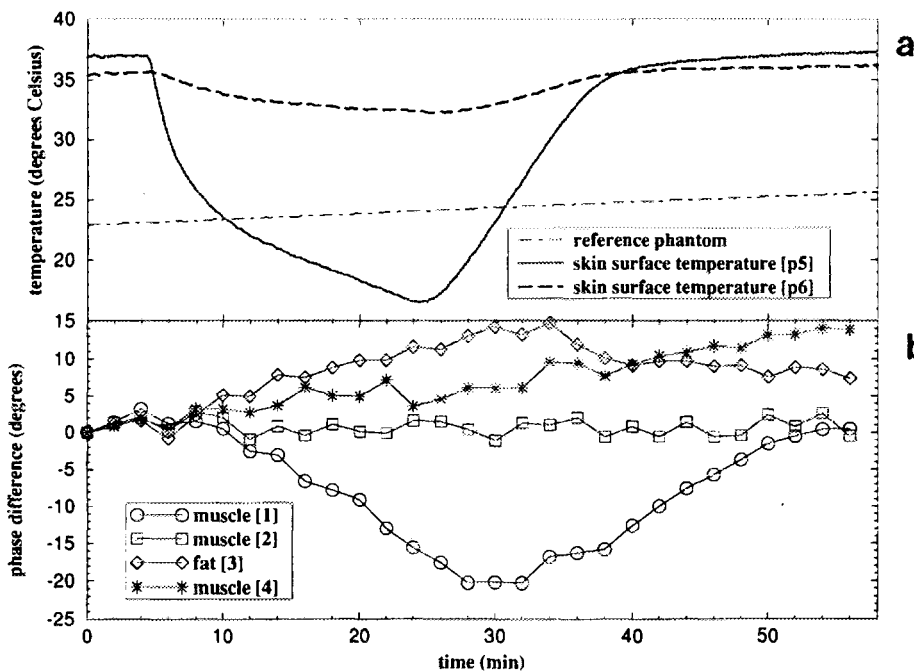


FIG. 6. (a) Probe measurements during the *in vivo* experiment. (b) Time evolution of the mean phase calculated over specific regions in the PRF-images. The regions are indicated in Fig. 7a, their surface is 16 mm^2 .

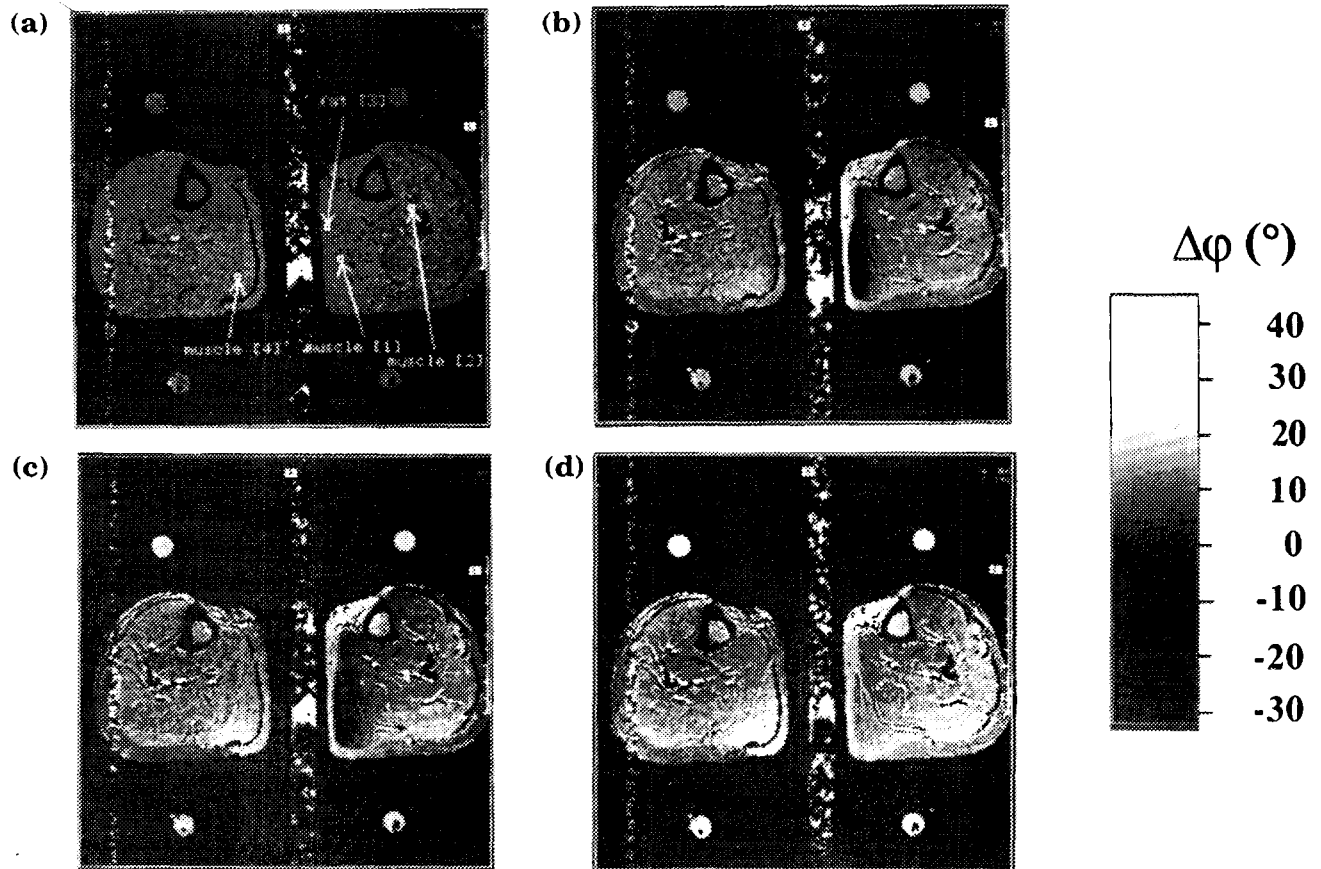


FIG. 7. Corrected phase-difference images at (a) $t = 2$ min, (b) $t = 22$ min, (c) $t = 40$ min, and (d) $t = 56$ min after the starting of the cooling process. The vertical bands in the images are motion artifacts due to the flow of the cooling water.

exact position of the probes is indicated in Fig. 2. Over the whole time range, there is an increase of around 2°C of the temperature in the reference phantoms. These changes correspond with phase differences of 13.8° , so it is necessary to correct for them (Fig. 3). The skin surface temperature at the cooling element decreased with 20°C by the cooling process. There is also a smaller temperature decrease of 2° to 3°C at the skin surface of the left leg.

The corrected phase-difference images are visualized in Fig. 7. All these images display motion artifacts due to the flow of the cooling liquid. Initially, before cooling (Fig. 7a), the phase-difference distribution in the fat and muscles is uniform. After a cooling period of 10 min (Fig. 7b), a decrease of the phase in the muscles is observed near by the cooling element. The phase of the fat layer in between the cooled muscles and the cooling element is increased during the cooling process. The reheating of the muscles close to the fat layer is visible in Fig. 7c. At $t = 56$ min (Fig. 7d), after 32.5 min of reheating, the phase differences near the cooling element are becoming close to zero, indicating that the temperature distribution returns to its initial state. These results are quantitatively illustrated in Fig. 6b, where the time evolution of the mean phase differences at specific regions indicated in Fig. 7a is drawn. These regions have a surface area of 16 mm^2 and contain 16 pixels.

It can be seen that the temperature distribution is not completely homogeneous at the end of the reheating (Fig. 7d). Especially in the musculus gastrocnemius (muscle [4] in Fig. 7a), there is an increase in phase in comparison with the initial phase distribution. The time evolution of the mean phase of a region in those muscles is also drawn in Fig. 6b.

DISCUSSION AND CONCLUSIONS

The phantom experiment illustrates the effectiveness of the proposed correction scheme. No significant temperature changes were measured in the reference phantoms and in the scanner tunnel. Thus, there was no heating because of the MR measurements themselves.

After the spatial correction, the maximum change of the mean phase in the central phantom is 1.5 degrees, and the maximum standard deviation 1 degree. This corresponds to temperature changes of 0.2°C and 0.14°C , respectively, applying the temperature sensitivity of the phase for pure water, i.e., $6.9^{\circ}(\text{C})^{-1}$. These results can be compared with a similar experiment in our earlier work (9). There the correction algorithm was tested in a phantom during 4 h of a cooling process. The experiment described now is in principle the same, only the temperature distribution remains spatially and temporally con-

stant. However, in our earlier work, the correction algorithm loses accuracy after the 60 min of measurement. We found out that the cause of this loss of accuracy was a temperature decrease of 1°C in the scanner tunnel during the measurements. This resulted in temperature variations in the reference phantoms and an imperfect phase drift correction.

The oscillations in the phase drift prove that the origin of the phenomenon is not only the decay of the superconductive current. In previous work (9), the space-dependent phase drift was not that important. There the measurements were more separated in time (10 min). The origin of the drifting processes are not yet understood, only the conclusion that the time constants of the phenomena are in the order of minutes can be made.

The PRF images of the *in vivo* experiment are of a good quality and demonstrate the sensitivity of the method to temperature induced changes of the local magnetic flux density. The phase of the muscle tissue decreases when it is cooled. This corresponds with the behavior of pure water. The lowest temperatures measured in the muscles are 5°C lower than the initial temperature when the α -value of water (Eq. [2]) is used. The PRF images (especially Fig. 7b) illustrate the insulating function of the fat layer. The temperature decrease in the muscle is higher where the fat layer is thinner.

The fact that the phase in the fat layer close to the cooling element increases illustrates that fat tissue does not behave like pure water. This is because the fat structure is not determined by hydrogen bonds. It will be shown in our paper about susceptibility effects that the extraction of the temperature distribution from the phase distribution is not a trivial problem. This has its consequences for the method as a noninvasive thermometry tool.

Most of the phase reductions due to the muscle cooling, disappear after the reheating (Fig. 7). This process is without any hysteresis. But in the final images, there are regions in the muscle and fat tissue with a significant phase difference with respect to their initial phase ($t = 0$ min). For instance, in the musculus gastrocnemius these phase changes are significant with respect to temperature related phase changes in the cooled regions. These "hot" places in the muscles are situated where no cooling took place. A possible explanation can be that the origin of these changes are small deformation of the lower leg during the thermal process. When amplitude images of the beginning and of the end of the experiment are compared, it looks like the legs are a little deformed or displaced. These deformations in the phase images are also seen in Fig. 7. The muscle structure becomes more visible as the experiment progresses. The first PRF image (Fig. 7a) is almost completely homogeneous. The muscle outlines are better visible in Figs. 7b–7d, and this can be explained by small displacements. Other sources of phase variations are perfusion changes and changes in the oxygenation level of the blood. Because the susceptibility of blood is a function of the blood oxygenation level (21), the macroscopic magnetic flux density can vary with this level. The order of magnitude of these

changes is a complex function of the distribution and orientation of the blood vessels in the muscles. Good models are necessary to study these perfusion effects and to determine whether these effect are of any importance to the PRF data.

We conclude that the PRF method is an attractive tool to study time-varying temperature changes in muscle tissue. The temperature images can be explained on a qualitative basis. Because of the good quality of *in vivo* temperature images and the reasonable acquisition times, the application of the method for hyper-thermia control remains feasible. Drawbacks of the method are the difficulties to examine temperature distribution in fat tissue, and the possible sensitivity of the method to parameters other than temperature.

ACKNOWLEDGMENTS

The authors thank Mr. E. Claeys for the realization of the cooling box and for the technical support.

REFERENCES

1. D. L. Parker, Applications of NMR imaging in hyperthermia: an evaluation of the potential for localized tissue heating and noninvasive temperature monitoring. *IEEE Trans. Biomed. Eng. BME-31*, 161–167 (1984).
2. A. S. Hall, M. V. Prior, J. W. Hand, I. R. Young, R. J. Dickinson, Observation by MR imaging of *in vivo* temperature changes induced by radio frequency hyperthermia. *J. Comput. Assist. Tomogr.* **14**, 430–436 (1990).
3. D. Le Bihan, J. Delannoy, R. Levin, Temperature mapping with MR imaging of molecular diffusion: application to hyperthermia. *Radiology* **171**, 853–857 (1989).
4. I. R. Young, J. W. Hand, A. Oatridge, M. V. Prior, N. Saeed, G. R. Forse, Impact of perfusion changes on *in vivo* measurements of temperature with MRI using T_1 changes, in "Proc., 12th Annual Meeting, SMRM, 1993," p. 1279.
5. F. A. Jolesz, A. R. Bleier, P. Jakab, P. W. Ruenzel, K. Huttel, G. J. Jako, MR imaging of laser-tissue interactions. *Radiology* **168**, 249–253 (1988).
6. D. Morvan, A. Leroy-Willig, A. Malgouyres, C. A. Cuenod, P. Jehenson, A. Syrota, Simultaneous temperature and regional blood volume measurements in human muscle using an MRI fast diffusion technique. *Magn. Reson. Med.* **29**, 371–377 (1993).
7. D. Morvan, A. Leroy-Willig, P. Jehenson, C. A. Cuenod, A. Syrota, Temperature changes induced in human muscle by radio-frequency H-1 decoupling: measurement with an MR imaging diffusion technique. *Radiology* **185**, 871–874 (1992).
8. R. Turner, D. Le Bihan, J. Maier, Echo-planar imaging of intravoxel incoherent motion. *Radiology* **177**, 407–414 (1990).
9. J. De Poorter, C. De Wagter, Y. De Deene, C. Thomsen, F. Ståhlberg, E. Achten, The proton resonance frequency shift method compared with molecular diffusion for quantitative measurements of two-dimensional time dependent temperature distributions in a phantom. *J. Magn. Reson. [B]* **103**, 234–241 (1994).
10. R. Stollberger, M. Fan, E. Ebner, P. W. Ascher, Mapping of temperature changes in heterogeneous tissues for the monitoring of hyperthermia, in "Proc., 12th Annual Meeting, SMRM, 1993," p. 156.

11. T. C. Cetas, T. V. Samulski, P. Fessenden, J. C. Bolomey, M. S. Hawley, M. Chive, in "Clinical Thermology-Methods of Hyperthermia Control" (M. Gautherie, Ed.), p. 1, Springer-Verlag, Berlin Heidelberg, 1990.
12. L. D. Hall, S. L. Talagala, Mapping of Ph and temperature distribution using chemical-shift-resolved tomography. *J Magn. Reson.* **65**, 501-505 (1985).
13. N. W. Lutz, A. C. Kuesel, W. E. Hull, A ¹H-NMR method for determining temperature in cell culture perfusion systems. *Magn. Reson. Med.* **29**, 113-118 (1993).
14. Y. Ishihara, A. Calderon, H. Watanabe, K. Mori, K. Okamoto, Y. Suzuki, K. Sato, K. Kuroda, N. Nakagawa, S. Tsutsumi, A precise and fast temperature mapping method using water proton chemical shift, in "Proc., 11th Annual Meeting, SMRM, 1992," p. 4803.
15. N. Yamada, S. Imakita, T. Sakuma, Y. Nishimura, Y. Yamada, H. Naito, T. Nishimura, M. Takamiya, Evaluation of the susceptibility effect on the phase images of a simple gradient echo. *Radiology* **175**, 561-565 (1990).
16. D. Eisenberg, W. Kauzmann, "The Structure and Properties of Water," The Clarendon Press, Oxford, 1969.
17. G. Némethy, H. A. Scheraga, Structure of water and hydrophobic bonding in proteins—I. A model for thermodynamic properties of liquid water. *J. Chem. Phys.* **36**, 3382-3400 (1962).
18. J. C. Hindman, Proton resonance shift of water in the gas and liquid states. *J. Chem. Phys.* **44**, 4582-4592 (1966).
19. J. De Poorter, The proton resonance frequency method for noninvasive MRI thermometry: study of susceptibility effects, in "Proc., 2nd Annual Meeting, SMR, 1994," p. 426.
20. F. Ståhlberg, J. Mogelvang, C. Thomsen, B. Nordell, M. Stubgaard, A. Ericsson, G. Sperber, D. Greitz, H. Larsson, O. Henriksen, B. Persson, A method for MR quantification of flow velocities in blood and CSF using interleaved gradient-echo pulse sequences. *Magn. Reson. Imaging* **7**, 655-667 (1989).
21. R. M. Weisskoff, S. Kiihne, MRI susceptometry: image-based measurement of absolute susceptibility of MR contrast agents and human blood. *Magn. Reson. Med.* **24**, 375-383 (1992).

Dosimetry at the location of secondary tumours after radiotherapy

H.W. Baas, J. Davelaar, J.J. Broerse, E.M. Noordijk

University Hospital, Clinical Oncology, Leiden

BE9700023

Abstract

From 1969 until 1990 468 patients were treated at our hospital for Hodgkin's disease. Treatments included radiotherapy, chemotherapy or a combination of both. In 38 cases a secondary cancer was observed. After an average latency period of 9.9 years the actuarial incidence could be as high as 47% for a total observation period of 20 years and a combined treatment with recurrence. For patients who received radiotherapy alone, dosimetry is mandatory to estimate the risk as a function of dose. We employed a Monte Carlo calculation method and as an illustration of the technical possibilities the dose at the location of the second tumour is calculated for two patients.

I. Introduction

As shown in table 1 the 468 patients have been subjected to radiotherapy, chemotherapy and a combined treatment. The overall incidence and the actuarial risk after 20 years are also shown.

Table 1 Number of treatments for Hodgkin's disease in Leiden University Hospital, 1969-1990, and the incidence of secondary tumours

Therapy	# patients	# sec. tumours	% sec.tum.	% Risk**
Radiotherapy	151	8	5.3	21
Chemotherapy	78	4	5.1	13
Combination RT/CT	171	15	8.8	26
Sequential RT/CT*	68	11	16.2	47

* This group contains the patients with recurrence of the disease.

** Actuarial risk after 20 years.

Reports in the literature indicate an increasing interest in the subject of secondary malignancies after Hodgkin's disease. Van Leeuwen¹ derived a relative risk after radiotherapy of 4.3 for lung cancer and 1.8 for other solid tumours. J.Slanina et. al.² observed for patients treated for Hodgkin's disease with radiotherapy 33 secondary malignancies in a group of 996 patients. Also the location with regard to the radiation field and the dose at that location were estimated. They reported that 33.5% of the secondary malignancies arise on the margin of the field and 36.5% outside: an indication that there is a relation between dose and risk.

For an estimation of the risk for radiotherapy, patient dosimetry is mandatory. The dose is difficult, if not impossible to measure, because the treatments were performed some decades ago, treatment machines are no longer in use and in addition some patients

are no longer alive. Therefore dose estimation has to be done by means of calculations. The systems for treatment planning in our hospital were not in use for planning of mantle fields. Therefore we decided to apply the existing Monte Carlo program EGS4³. The measured data of the actual planning systems are then used for validation of the simulation model.

II. Methods

Monte Carlo Code

EGS4 is a Monte Carlo code, that simulates each step of photons and electrons separately. For our simulation we adapted the program XYZDOS, which requires an input file that describes the incoming photon or electron beam, the irradiated area in orthogonal voxels and the voxels for which the dose is required. It generates an output file describing the dose distribution in the specified voxels. We now describe all the elements in the simulating process.

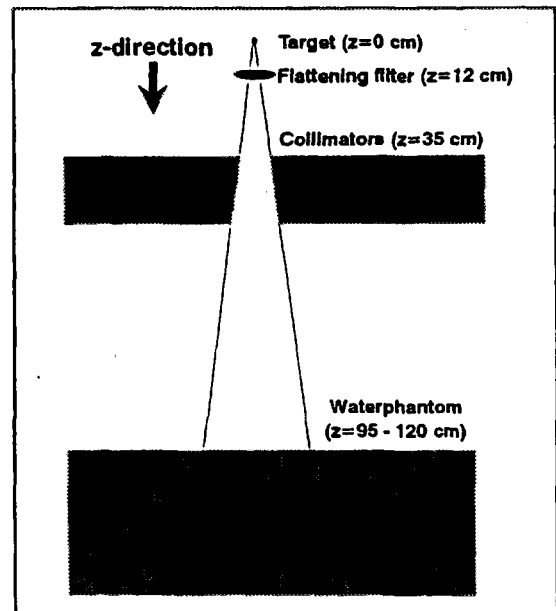


fig 1 Model of LINAC radiation head

II.a. LINAC beam

A number of patients were treated at a LINAC with a 8 MeV bremsstrahlungs spectrum. For our simulation we used the following model: the radiation source is composed of a target (almost point source) and a flattening filter (plane source with a diameter of 3 cm). We changed XYZDOS to incorporate diverging beams with more than one origin. The collimator consists of 10 slabs (see figure 1).

The spectrum is simulated by calculating PDD's for mono-energetic photon beams arising from target and flattening filter with photon energies of 0.5, 1.5, 2.5, 3.5, 4.5, 5.5, 6.5 and 7.5 MeV. The 16 PDD's were fitted on a measured PDD by weighted summation. The weight factors are then considered to represent the spectrum. In the fitting process we also assumed that 90% of the particles arise from the target and 10% from the flattening filter, as based on the results of Chaney et al.⁴

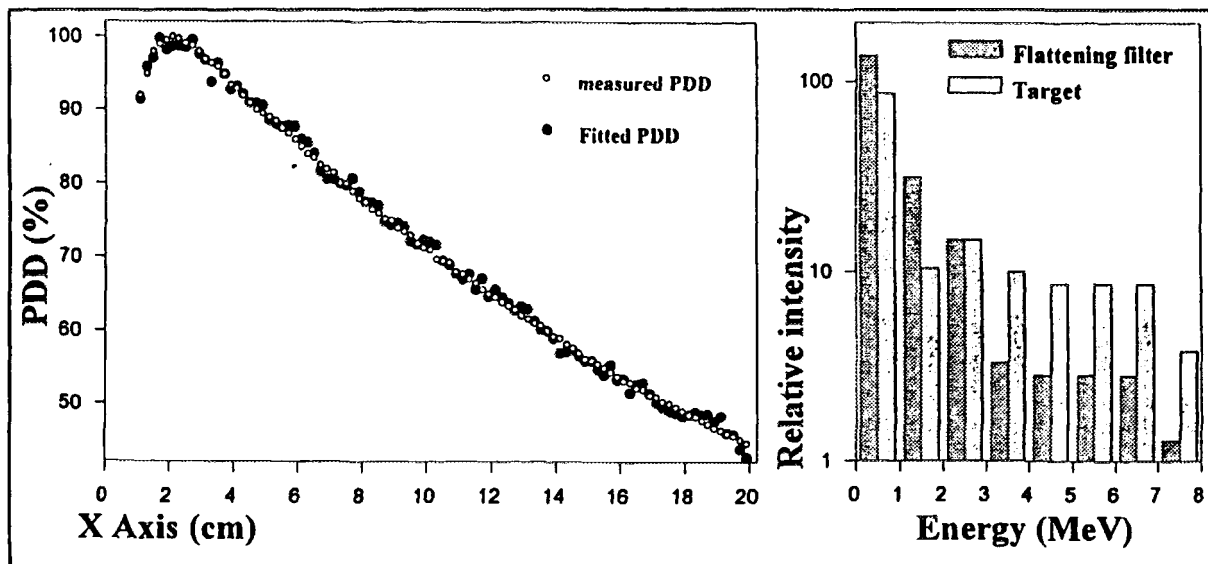


fig 2: Fitted spectrum with target and flattening filter; PDD and spectrum

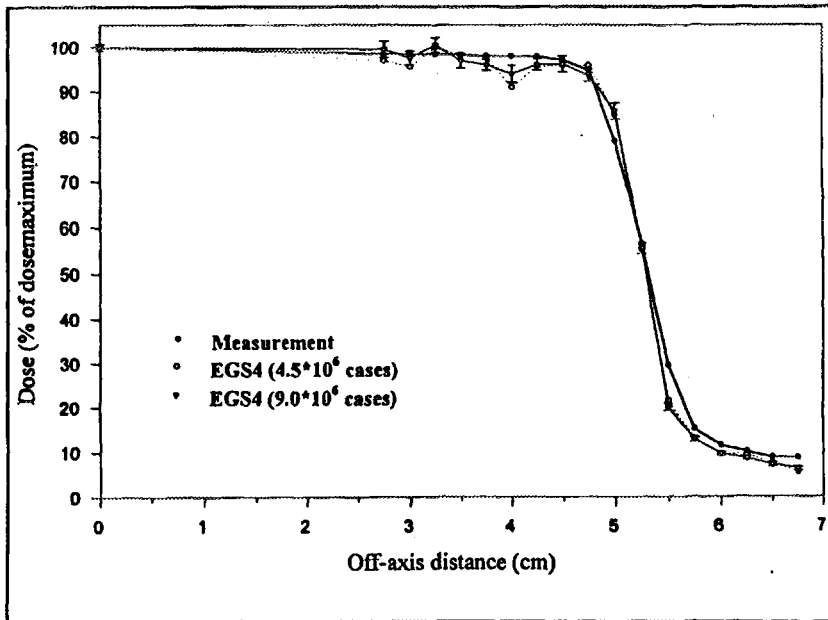


fig 3: Dose profile at 5 cm depth in phantom (8 MV LINAC beam)

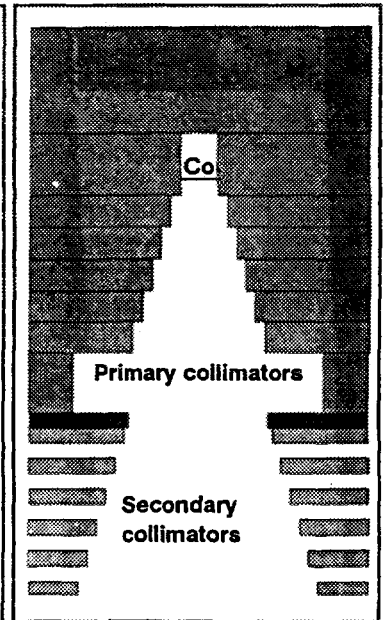


fig 4: Model ^{60}Co radiation head

The spectrum was verified by calculating the dose profile at 5 cm depth in a water phantom at a SSD of 95 cm. Figure 3 shows the results. The simulation fits quite good with the measurement, with large statistical fluctuation, mainly behind the collimator blocks.

II.b. Cobalt beam

Until 1979 patients were treated with ^{60}Co gamma radiation in our hospital. The Cobalt machine consists of the source head, the immovable primary collimators and the movable secondary collimators (see figure 4). We used the known spectrum for ^{60}Co . Because of

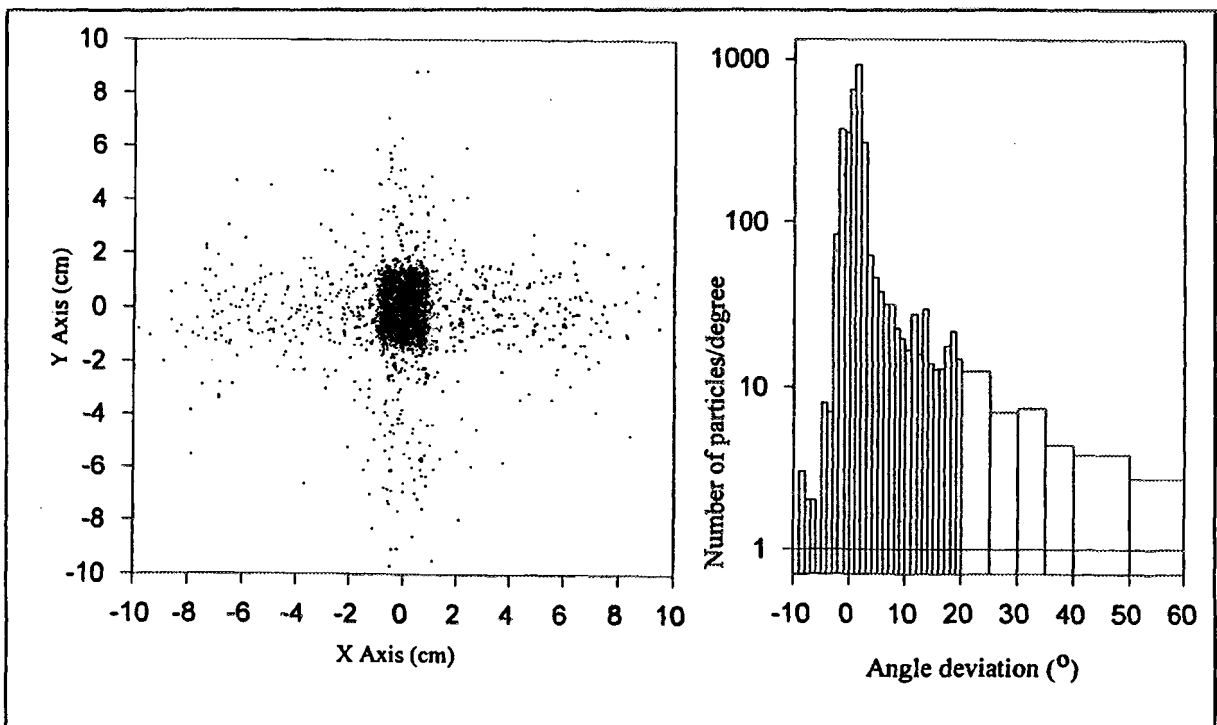


fig 5: XY- and Angular distribution after first part of ^{60}Co simulation.

the many voxels used for head-modelling we had to divide the simulation into two parts. At the end of the first part we created a phase space file, containing the xy-location, charge, energy and direction of the particles that reached the end of the collimators, as illustrated in figure 5. That file was loaded for input values of the particles in the second part. Then we verified the model, for a $6 \times 6 \text{ cm}^2$ field and an SSD of 60 cm, by comparing the dose profile at 5 cm

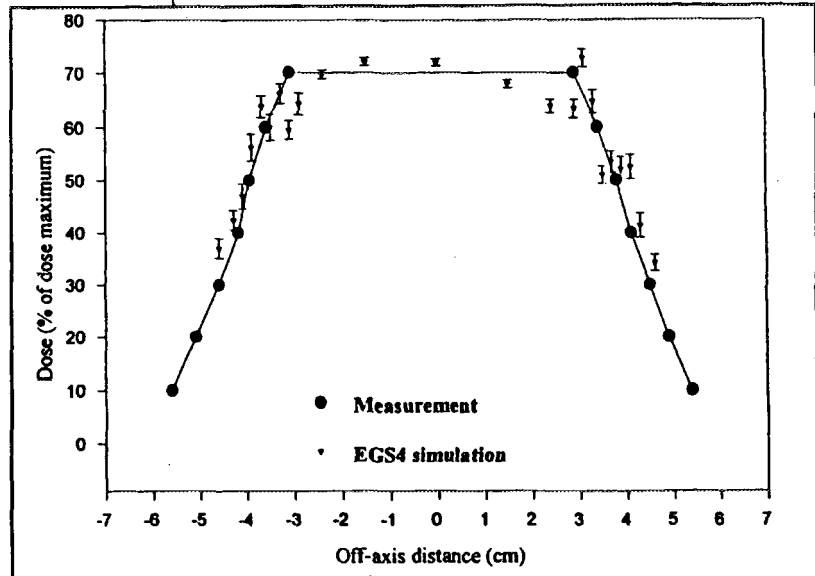


fig 6: Dose profile at 5 cm depth in phantom (^{60}Co beam)

depth with measurements. The measurements were approximate, because we derived our data from an isodose plot. The results are shown in figure 6. The calculations still show fluctuations at the field edge due to statistical uncertainties caused by the small voxels.

II.c. Mantle field and inverted-Y field.

Because XYZDOS requires orthogonal voxels, we had to make some simplifications to shielding blocks and the modelling of the body. We only simulated the lower parts of the fields and kept the block widths constant over the patient's vertical axis. Both fields have lead blocks of 15 cm thickness and an effective ρ of 7.0 g/cm^3 (grain instead of massive lead). The shielding consists of 5 diverging layers each 3 cm thick. The mantle field is simulated by a diverging gap and the inverted-Y field by a diverging block (figure 7).

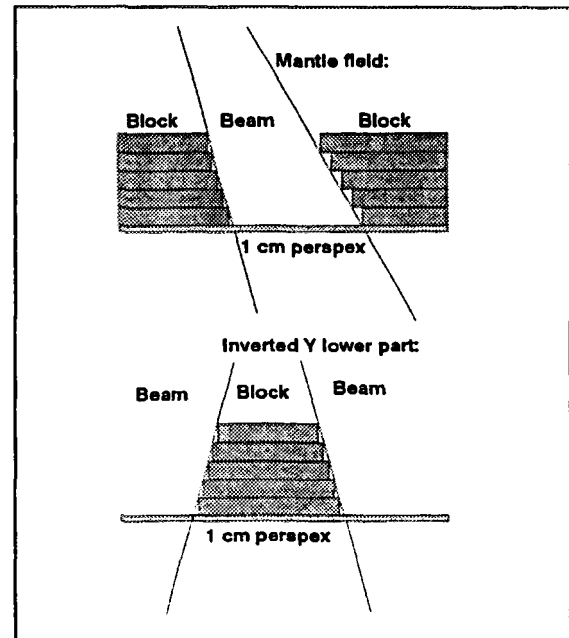


fig 7: Field modelling for Mantle and inverted-Y.

d. The body.

The body was simulated by a slab of water, with the thickness of the individual patient. For the mantle field the lungs are simulated by orthogonal blocks of with an effective of $\rho = 0.25 \text{ g/cm}^3$ and the atomic composition of water.

III. Results

In table 2 the patients are described, that developed a secondary cancer after radiotherapy up to 1993. As an illustration we calculated the dose profiles for 2 patients; one from this table with a bronchus carcinoma and one patient with a very recently observed endometrium carcinoma.

Table 2: Description of secondary tumours: radiation dose, machine, field and fraction

pat. nr	tumour type	dose (Gy)	machine	field	fractional dose(Gy)
1	melanoma ear	35	Co-60	STN	2.0
2	pancreas	35	Co-60	Y	3.5
3	granulosa cell tumour	35	Co-60	STN	3.3
4	basalioma left shoulder	35	Co-60	M	2.3
5	basalioma left eye corner	35	LINAC	STN	2.0
6	bronchus left lower lobe	40	LINAC	M	2.0
7	mult. trunk skin basaliomas	35	Co-60	STN	3.0
8	basalioma right cheek	35	Co-60	STN	1.8

remarks: Y = inverted-Y field, M = mantle field, STN = subtotal nodal.

The patient we regard first, was treated with 2 tailored mantle fields. Therefore we made 2 models for the simulation and afterwards we summed the results. This total dose profile is shown in figure 8. The dose maximum is 40 Gy. The location of the secondary tumour (in figure 8 marked with a grey bar) was at the field margin: 10 cm depth, 3.5 cm off-axis. The local dose at that position was 55(+/-15)%, that is between 16 and 28 Gy.

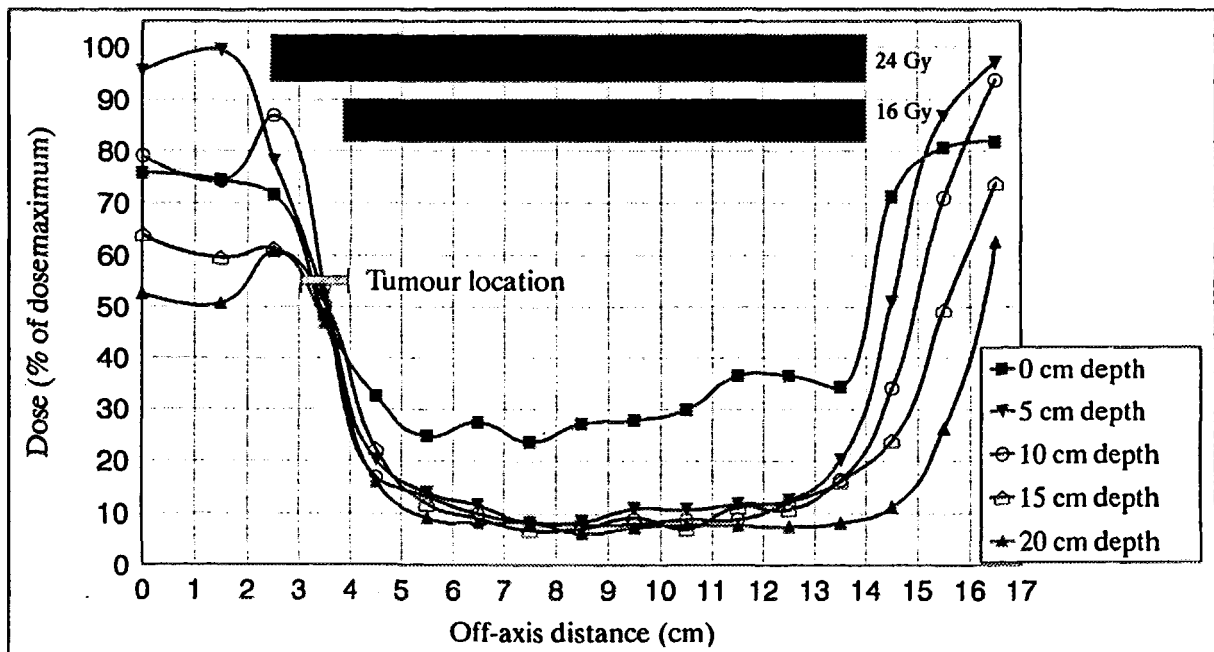


fig 8: Dose profile of mantle field, 8 MV LINAC spectrum, simulation with 9.7×10^6 cases. Sum of 2 fields

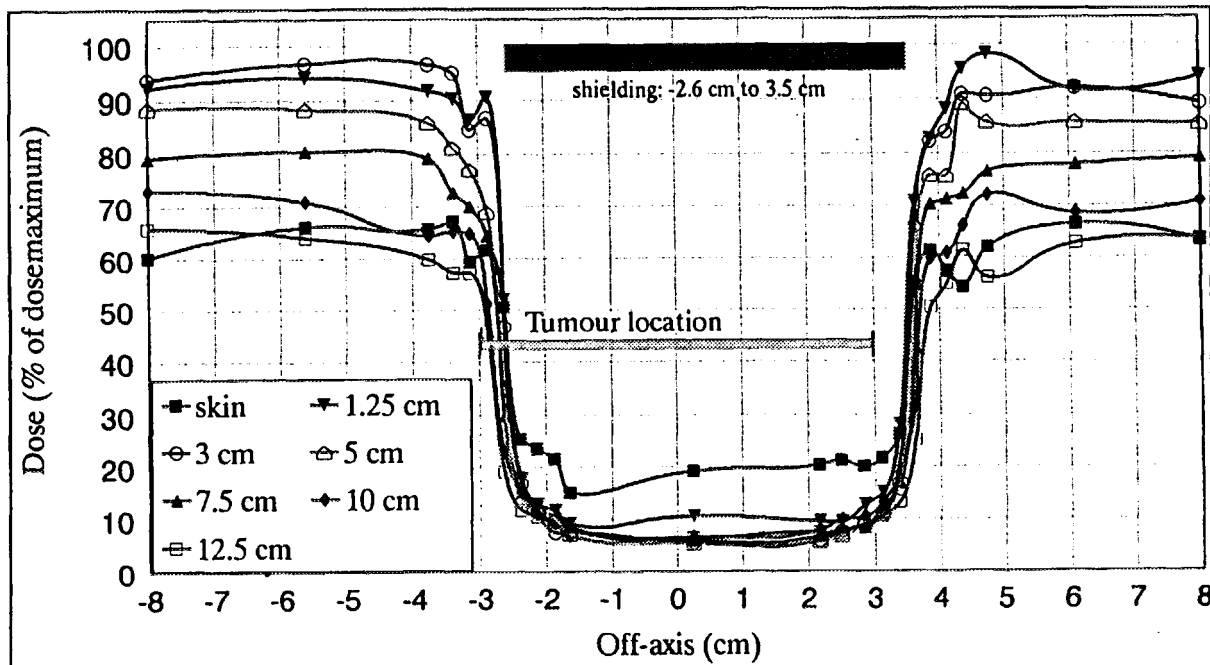


fig 9: Dose profile of Y-field, 8 MV LINAC spectrum, simulation with 1.2×10^7 cases.

In addition we simulated a treatment with an inverted-Y field. In a patient an endometrium carcinoma recently was observed after a treatment in 1976 at the LINAC with an inverted-Y field and a dose maximum of 35 Gy. The calculated dose profile is shown in figure 9. For this case it was very difficult to locate the tumour. The depth is 6-8 cm, but the off-axis value is unknown, between -3 and 3 cm. So the dose estimation is 5-80% of the dose maximum, that is between 1.75 and 28 Gy.

IV. Conclusion

Dosimetry at the location of secondary tumours is feasible with the aid of Monte Carlo calculations, which seems to be the only way to estimate the dose after the long latency period found for the tumour occurrence. Further statistical analysis of all patients with a secondary tumour after radiotherapy is necessary in an attempt to derive a dose effect relationship. The dose was calculated in two patients and has been observed to vary between the low dose of about 2 Gy up to 70% of the maximum dose given in the treatment of Hodgkin's disease (35-40 Gy). This wide range is partly due to statistical fluctuations in the Monte Carlo calculations as well as the uncertainty of the location of the secondary tumour, which was usually found close to the edge of the shielding blocks, leading to a very steep dose gradient.

References:

1. Leeuwen F van, Second malignancy as a sequel to cancer treatment, an assessment of risk. Ph.D. thesis 1994.
2. Slanina J., Henne K., Schäffer G., Hodapp N., Moog G. and Frommhold H., Incidence of Secondary Malignancies in Patients with Hodgkin's Disease: Preliminary Results. RRCR, Vol. 130, 1993, p. 270-277.
3. Nelson W.R., Hirayama H. and Rogers D.W.O., The EGS4 code system, Stanford Linear Accelerator Center Report 265, 1985.
4. Chaney E.L., Cullip T.J. and Gabriel T.A., A Monte Carlo study of accelerator head scatter, Med.Phys. 21 (9), 1994, p.1383-1390.



Conformal Radiotherapy made easy through Gravity-oriented Absorbers : A Solution to the Inverse Problem.

Basil S. Proimos

Department of Medical Physics, University of Patras, 26500 Patras, Greece.

BE9700026

1. Geometrical terms.

The following examples of two ellipses illustrate the meaning and clarify the differences between a few geometrical terms used in this paper.

1.1. Parallel 2D figures.

The large (AB and ab) and the small (DE and de) axes of the two ellipses shown in Fig. 1a, are respectively parallel. These ellipses are two **parallel** 2D figures, which lie either on the same plane

(coplanar) or at two parallel planes. They are not **similar** figures because: $\frac{(AB)}{(ab)} \neq \frac{(DE)}{(de)}$

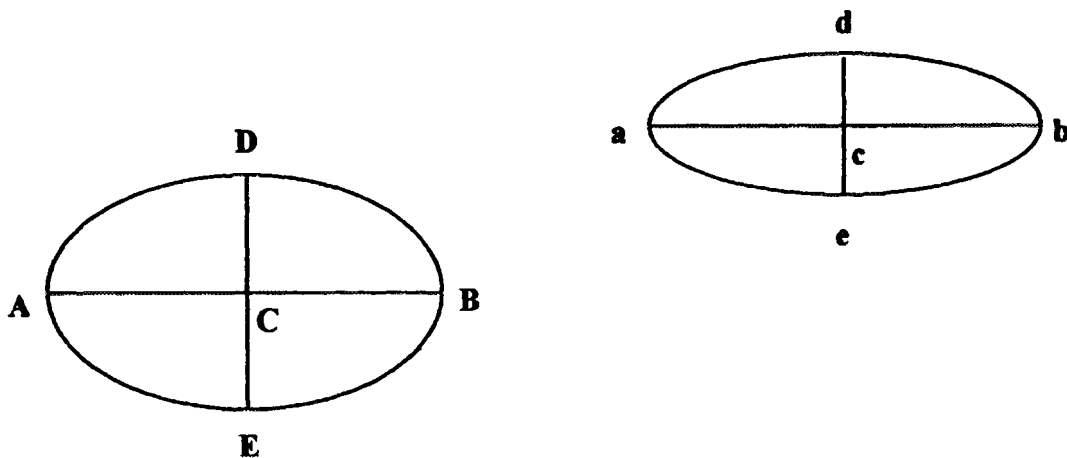


Fig. 1a. Two "parallel" ellipses.

1.2. Similar 2D figures.

The axes of the ellipses shown in Fig. 1b are proportional: $\frac{(AB)}{(ab)} = \frac{(DE)}{(de)}$.

These two ellipses are "**similar**" figures with "**ratio of similarity**" $\frac{(AB)}{(ab)} = \frac{(DE)}{(de)}$.

They are not **parallel** because their large and small axes are not respectively parallel.

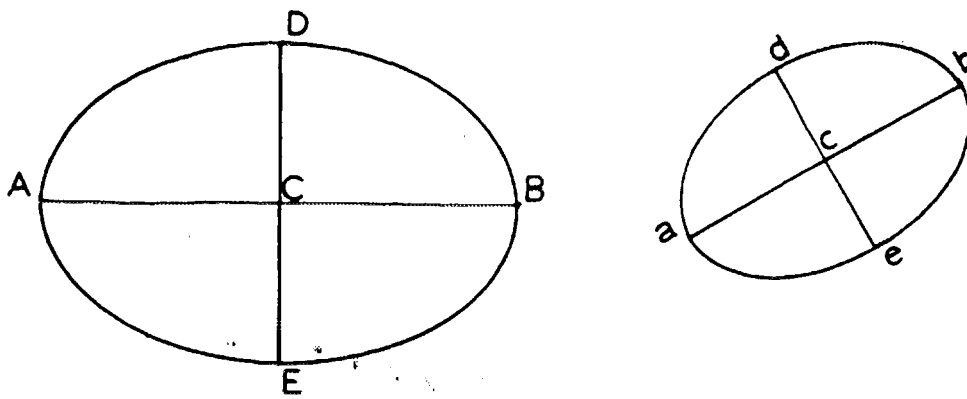


Fig. 1b. Two "similar" ellipses

1.3. Homiotheta 2D figures.

In Greek, "homios" means similar and "thesis" means position.

The two ellipses of Fig. 1c are "parallel" (AB and DE are parallel to ab and de, respectively).

They are also "similar" because : $\frac{(AB)}{(ab)} = \frac{(DE)}{(de)}$.

Consequently, they are "homiotheta" with "center of homiothesis" the point S and "ratio of

homiothesis": $\lambda = \frac{(SC)}{(Sc)} = \frac{(AB)}{(ab)} = \frac{(DE)}{(de)}$.

In the case of "homiotheta" figures, the "ratio of homiothesis", λ , is of course equal to the "ratio of similarity".

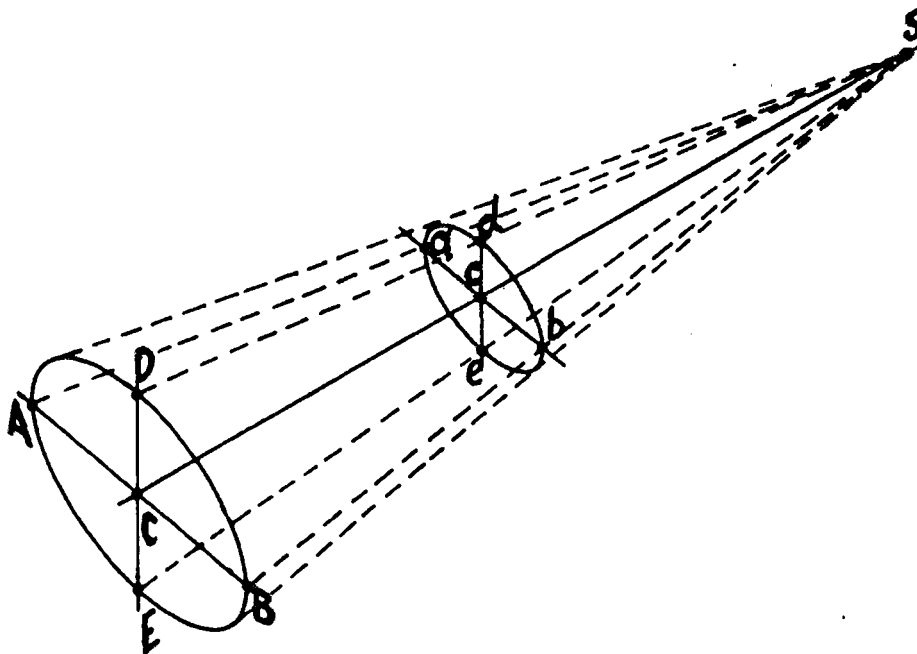


Fig. 1c. Two "homiotheta" (parallel and similar) ellipses.

2. Historical review.

In 1957, at MIT, we had the idea to protect vital organs using rotating radiation absorbers. The photon beam of a 2 MV "Van de Graaff" accelerator was horizontal and immobile, while the patient and the absorber(s) were synchronously rotating, about two vertical axes, lying on the same immobile plane with the source.

In this method of beam modulation by synchronous rotation of absorbers, only the relative motion between the beam, the absorbers and the patient, counts. This relative motion and the result are the same in both of the following cases:

Case (a) : The absorber(s) are rotating synchronously with the rotating vertical patient (immobile, horizontal beam) as in Fig. 2 and Fig. 3.

Case (b) : The gravity oriented absorbers, remain parallel to themselves, rotating with respect to the beam, which is emitted by the rotating about the patient source (immobile, horizontal patient) as in Fig. 3 and Fig. 4.

2.1. Spinal cord protection.

The above idea is applied for the case (a) of spinal cord protection shown in Figure 2 (horizontal section). The cross-sections of the spinal cord, A, and of the lead protector, P, remain always "homiotheta". Their center of "homiothesis" is the source S and their constant ratio of "homiothesis" is $(SC)/(SO)$, for all positions of rotation. Therefore, the protective "shade" of the absorber, as casted by the beam, covers the spinal cord continuously. Any other point B of the neck cross-section is protected during a portion of the irradiation time. That portion (protection time) decreases with the distance of the point B from the center A (Fig. 15).

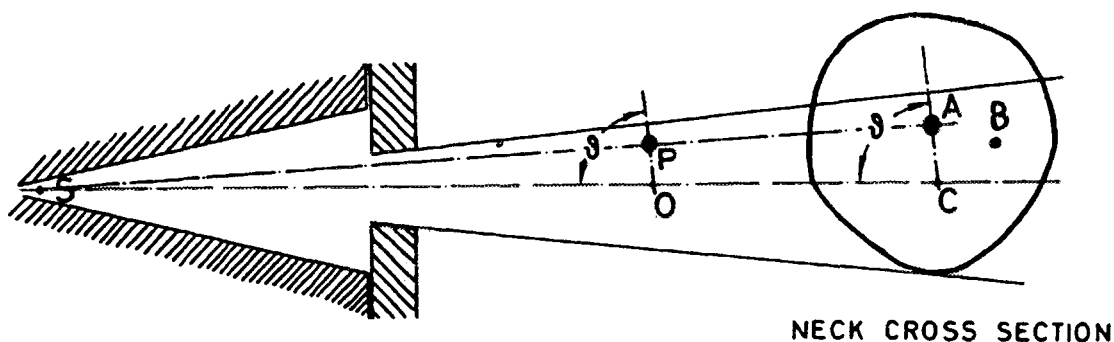


Fig. 2: Central section by the horizontal plane, which passes through the source S. The cross-sections of the spinal cord, A, and of the lead protector, P, rotate synchronously about the centers C and O, respectively, and they remain homiotheta, with center the source S, for all values of angle θ . (Reprinted from "RADIOLOGY", Vol. 77, No. 4, October 1961).

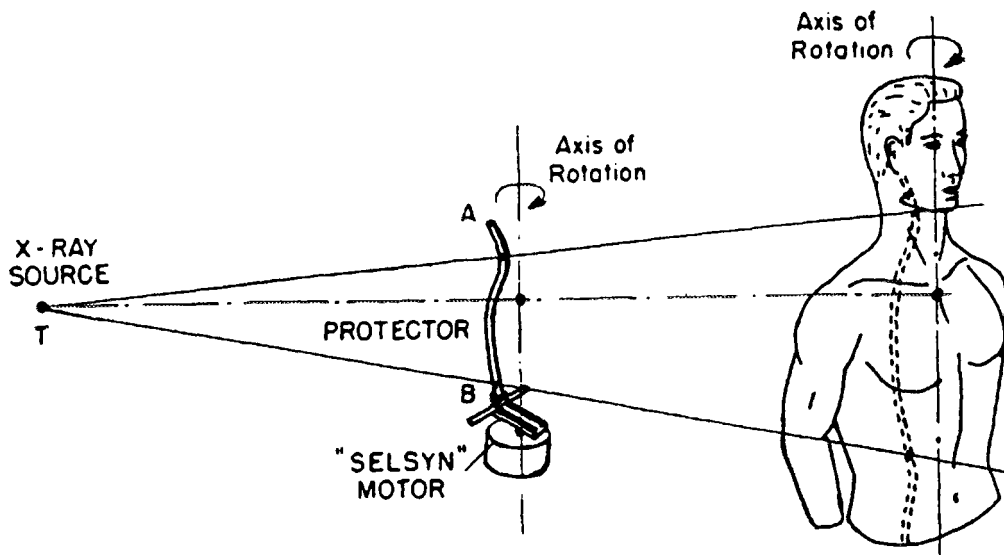


Fig. 3: Three dimensional drawing illustrating the principle of spinal cord protection by a lead rod, which rotates synchronously with the patient. (Reprinted from : " THE SURGICAL CLINICS OF NORTH AMERICA", June 1959, Vol. 39, No. 3)

The same arrangement is shown in the 3D sketch of Figure 3. If a Co-60 beam is used, a lead rod, 2 cm in diameter, reduces the dose to the spinal cord to less than half of the cord dose without protection. This 50% reduction of the dose to the cord is sufficient and optimum for almost all patients, who need spinal cord protection. Overprotection of the cord by a thicker or more dense absorber will cause non uniformity of dose distribution to the tumor, if it is located near the cord.

Therefore, the spinal cord protection can be standardized by using for all patients a lead rod 2 cm in diameter.

In the '60s the above idea of synchronous protection was applied in the usual case (b) , using gravity oriented absorbers. Now, the source is rotating about the immobile horizontal patient and it describes a vertical circle, the center of which is called "isocenter" and it coincides with the center of the tumour.

Fig. 4 and Fig. 5 show the gravity oriented device and the arrangement for the protection of the spinal cord by the same lead rod. During the rotational irradiation, gravity keeps the lead rod homiothetic to the spinal cord, with center of homothesis the source.

In Fig. 5, the axis (AO) of suspension of the device and the axis (CC) of rotation of the source S, are always parallel. The source lies on the "principal plane" defined by those two parallel axes. The front plate of the head of a Co-60 unit and the gravity oriented device are shown for four positions of the source (S_1, S_2, S_3 and S_4). The holder AB of the lead rod always remains vertical because of gravity.

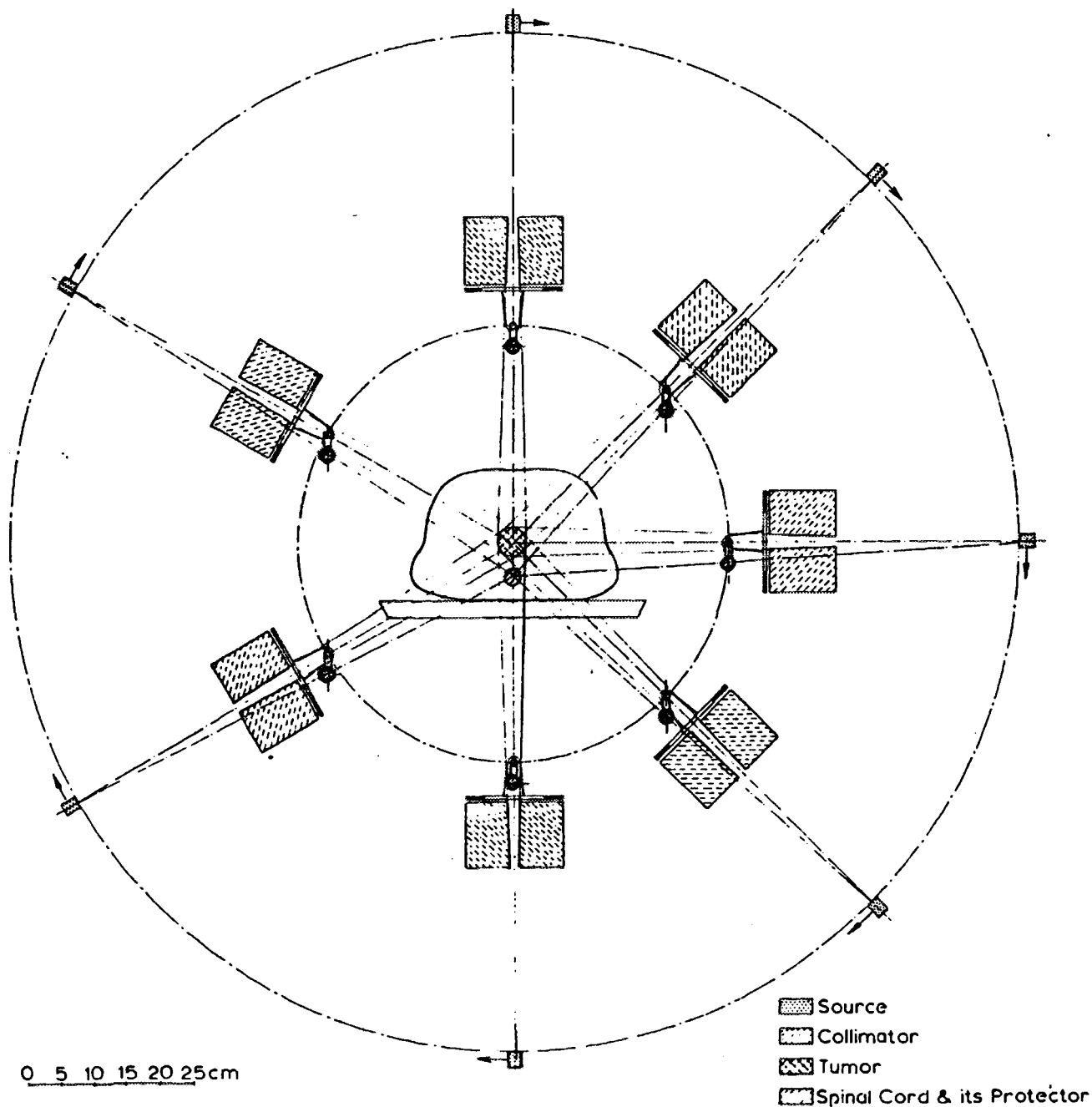


Fig. 4. The Co-60 source, the collimator and the gravity oriented spinal cord protector are shown for seven positions of the source in the vertical cross-section. The protector is homiothetus to the cord with center of homiothesis the source, for all positions of rotation. (Reprinted from RADIOLOGY, Vol. 87, No.5, November 1966).

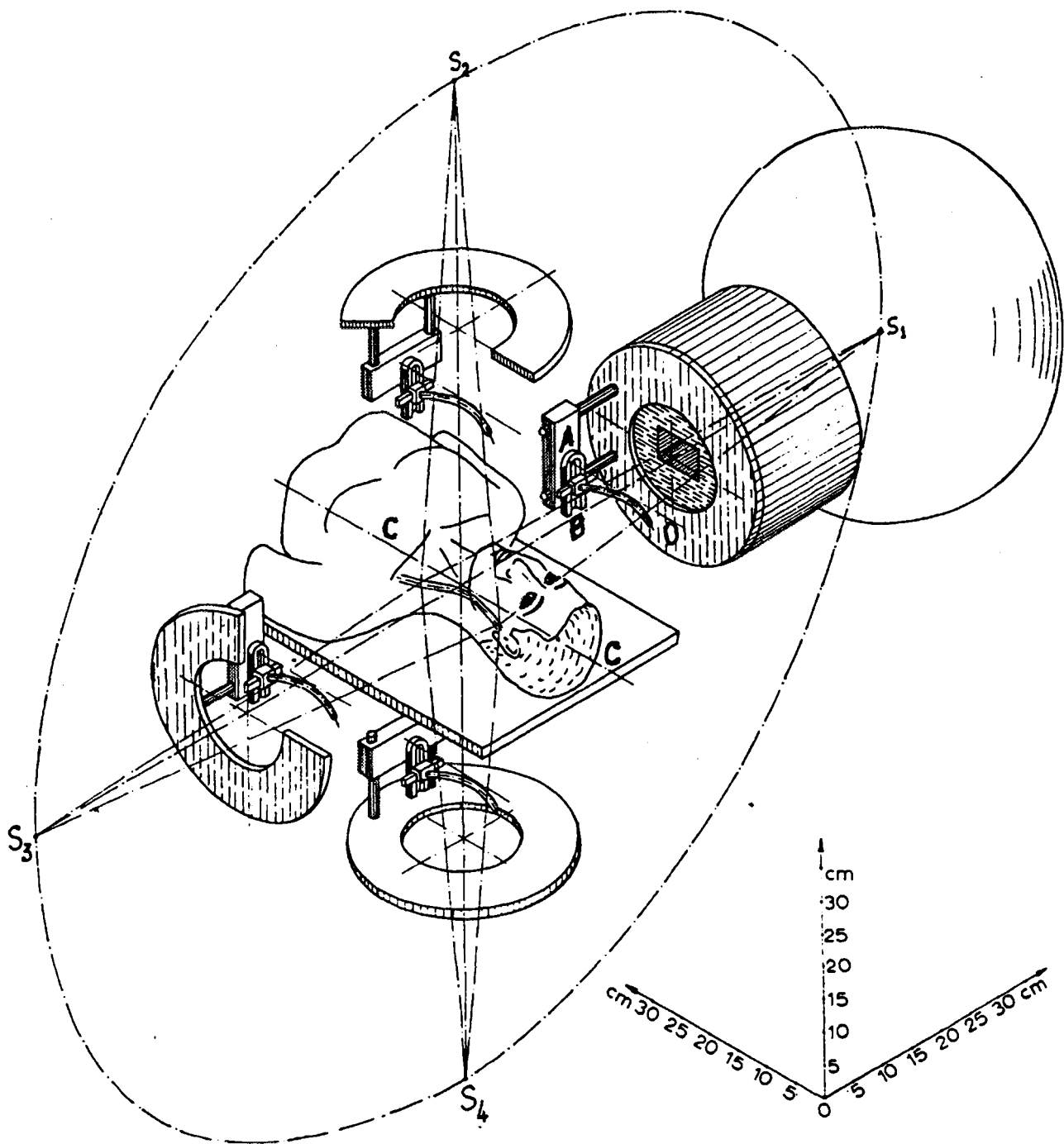


Fig. 5. Three dimensional drawing showing the head of the Co-60 unit, in a horizontal beam position and the face plate with the gravity oriented device in four positions of rotation. The protective "shade" of the lead rod is casted by the beam over the cord for all positions of rotation. (Reprinted from RADIOLOGY, Vol. 77 : 594, October 1961).

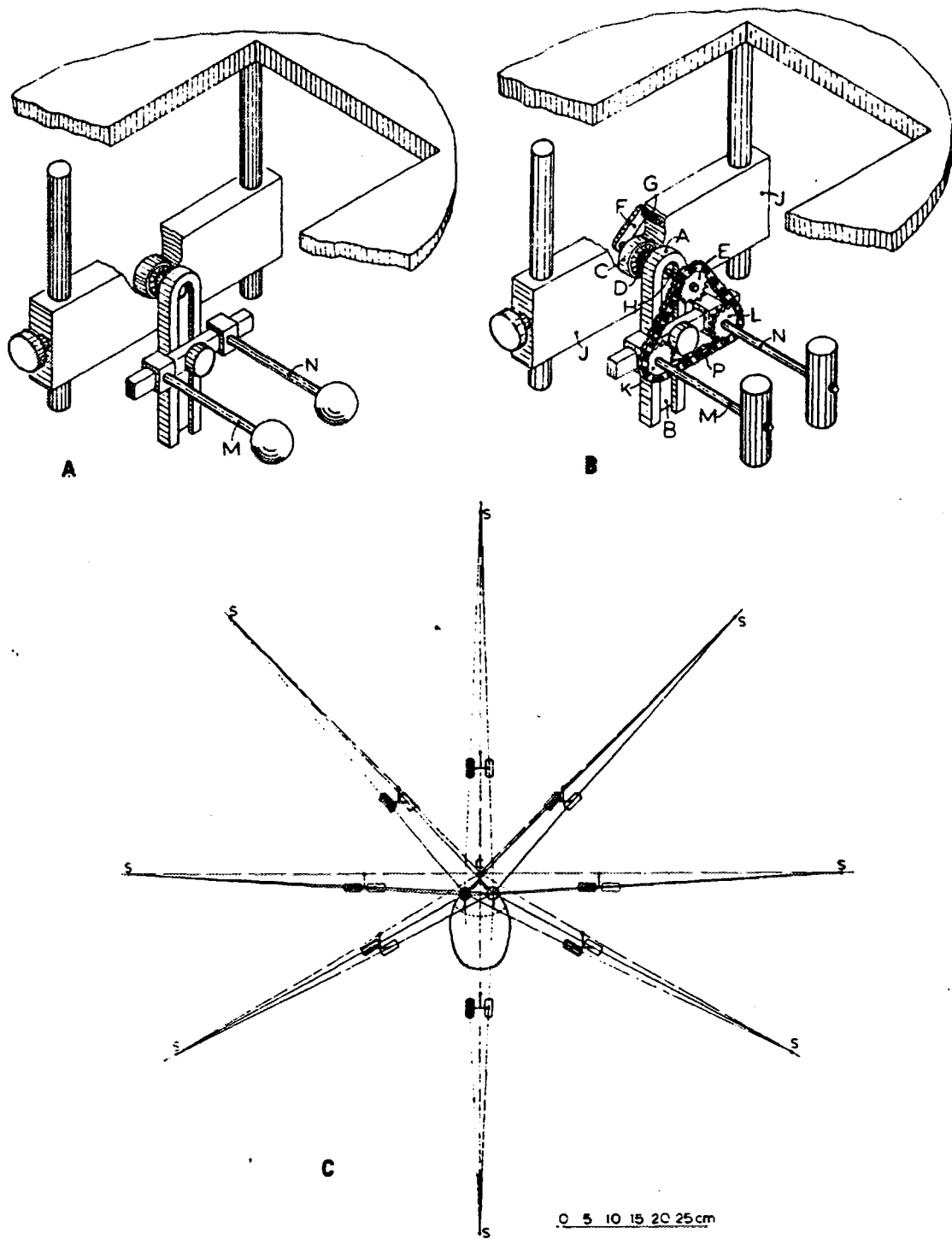


Fig. 6. Protection of both eyes.

A. Device for protection of eyes by two gold spheres.

B. Device for more effective eye protection by two cylinders parallel to the central ray of the beam.

C. Cross section of the eye protection arrangement for a few positions of the rotating source S.

(Reprinted from RADIOLOGY, Vol. 81, No.2, August 1963.)

2.2. Central tumors.

The same technic can be applied to all cases of deep seated tumors, for any shape (convex and/or concave) of the PTV (Planning Target Volume). E.g. the uterus and the parametria, having a "butterfly" shaped cross-section, can be irradiated with simultaneous protection of the bladder and the rectum, in the case of Ca of the cervix. This case will be treated in detail later on.

2.3. Eye protection.

In the case of the eyes, the two spheres shown in Figure 6A cannot be larger than 2 cm in diameter, because they must not protect the tumour; especially if it is located near one or both eyes. For maximum protection, the spherical protectors have to be made of maximum density material (gold or platinum). Then the dose to the centre of each eye will be about 30% of its dose without protection. This degree of eye protection is usually not adequate.

For this, the device shown in Figure 6B was invented. The protective cylinders can be made of a high density (17 g/cm^3) tungsten alloy or even better of gold (19 g/cm^3) and they can be up to 4cm long providing a beam attenuation equivalent to about seven "half value layers" for the Co-60 beam. The arrangement is shown for eight positions of rotation in Figure 6C. During the rotational irradiation, each cylinder is assigned to protect one eye and its axis remains parallel to the central ray of the beam. The centre of each eye, the centre of the corresponding cylinder and the source are always in a straight line.

Figure 7 shows the dose distribution for 2MV x-rays, in percent of the air dose at the axis of rotation, if two gold cylinders 1,2 cm in diameter and 2,5 cm in length are used. The dose at the centre of each eye is less than 10% of the dose at the surface of the PTV.

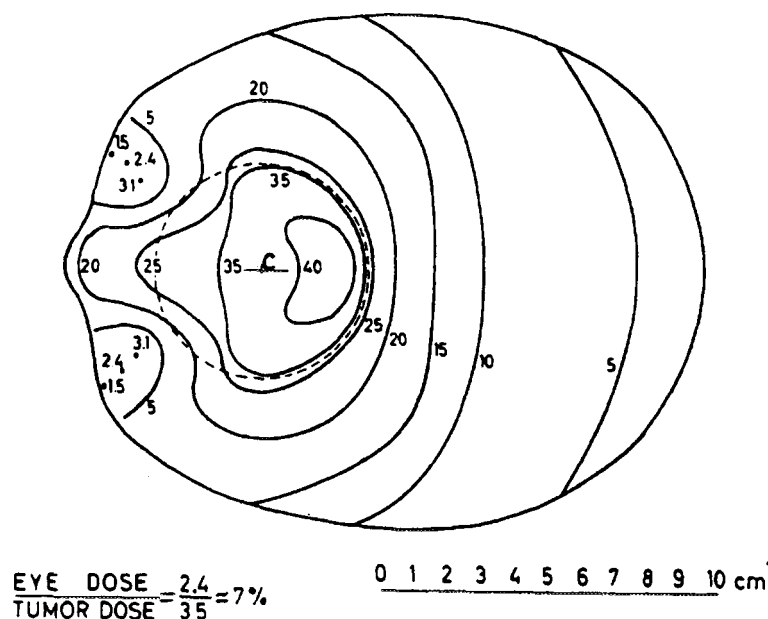


Fig. 7. Distribution of dose corresponding to the arrangement of Figure 6C, for 2 MV X-rays. The dose is in percent of the air dose at the "isocenter" C. (Published in RADIOLOGY, Vol. 77, No.4, October 1961).

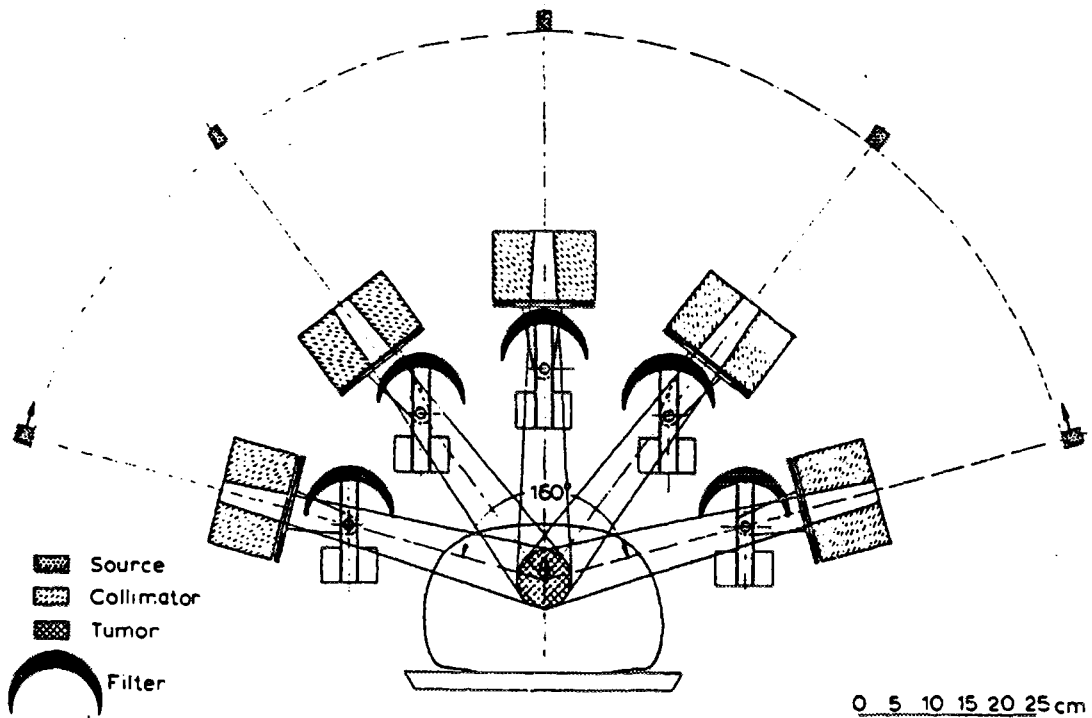


Fig. 8. Arc irradiation of an eccentric tumour of circular cross-section, using a gravity oriented crescent filter. (Published in *RADIOLOGY*, Vol. 87, No.5, November 1966).

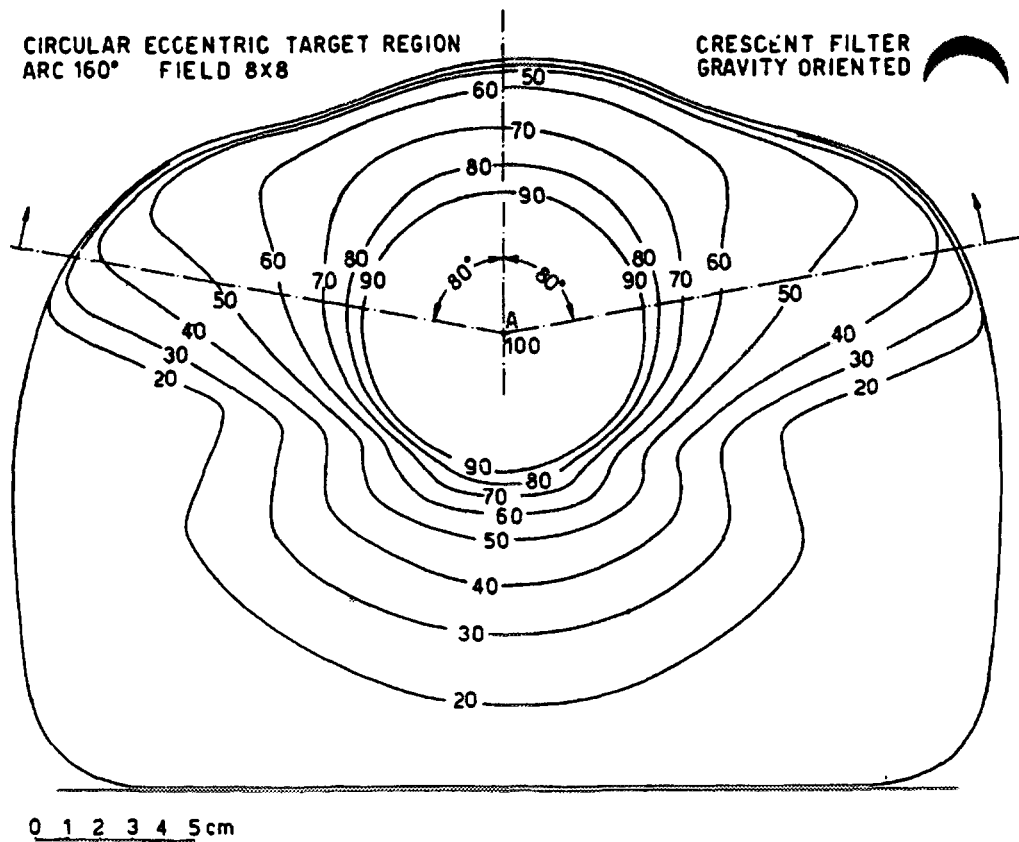


Fig. 9. Dose distribution in percent of maximum dose, obtained by the arrangement shown in Fig. 8, with a Co-60 beam. Published in *RADIOLOGY*, Vol. 87, No.5, Nov. 1966

2.4. Eccentric tumors

Figure 8 shows a gravity oriented crescent filter for five positions of rotation. It modulates the intensity of the beam in a 160° arc irradiation, to achieve: (a) uniform dose distribution in a circular and eccentric PTV (Ca of bladder or rectum or larynx) and (b) uniform and relatively low dose on the skin.

The resulting dose distribution for a Co-60 beam is shown in Figure 9.

2.5. Field shaping

The idea of gravity oriented blocks can also be applied for shaping the two sides of the beam, which are usually parallel to the axis of rotation.

In Figures 10 and 11 two blocks of elliptical cross section are suspended symmetrically in the beam. During the rotation, each block remains parallel to itself, because of a counter weight (black dots in Figure 10 and E and F in Figure 11) attached to it. This way, the beam width changes continuously during the rotation from a maximum, when the beam is vertical, to a minimum, when the beam is horizontal. Only the elongated PTV is always in the beam.

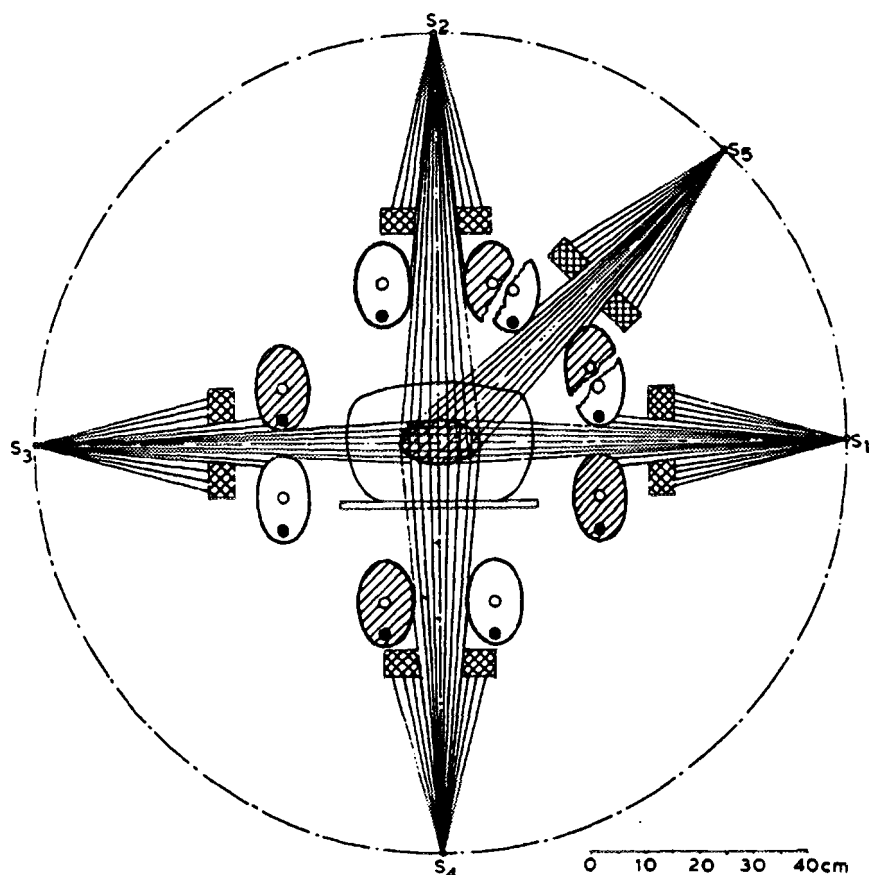


Fig. 10. Vertical section by the plane of source rotation, showing the arrangement of two gravity oriented elliptical blocks for five positions of rotation. The beam width is continuously changing to fit to the width of the PTV as "seen" from the source. (Reprinted from RADIOLOGY, Vol. 81, No.2, Aug. 1963)

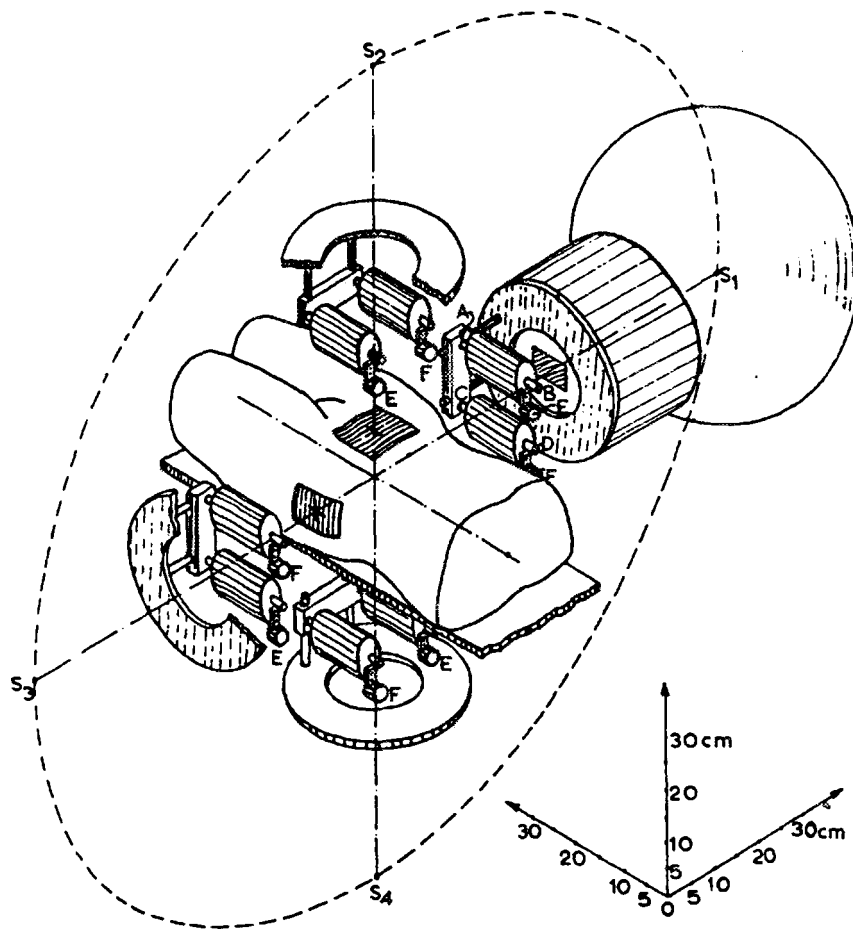


Fig. 11. Beam shaping during rotational therapy. Two cylindrical absorbers, oriented continuously by gravity, are shown for the four vertical and horizontal beam positions. (Reprinted from RADIOLOGY, Vol. 81, No.2, Aug. 1963).

2.6. Simultaneous protection and field shaping.

Figure 12 shows a combination of field shaping and organ protection by synchronous rotation. The two shaded blocks, synchronously rotating about O_1 and O_2 , collimate and direct the beam to follow the rotating about C, tumor B, always. The rotating lead rod D protects the spinal cord A always (even when the cord is out of the collimated beam).

The physical result is shown in Figure 13. The positions of the centre C of rotation, the centre A of the protected region (spinal cord) and the centre B of the PTV can be chosen independently from each other. The location, size and shape of the region to be protected in the patient and the degree of its protection can be defined, during Treatment Planning, by choosing a protector of proper location, size, shape and density, as seen later in this paper. The location, size and shape of the irradiated volume in the patient can be controlled by proper selection of the size, shape and position of the two beam collimating disks.

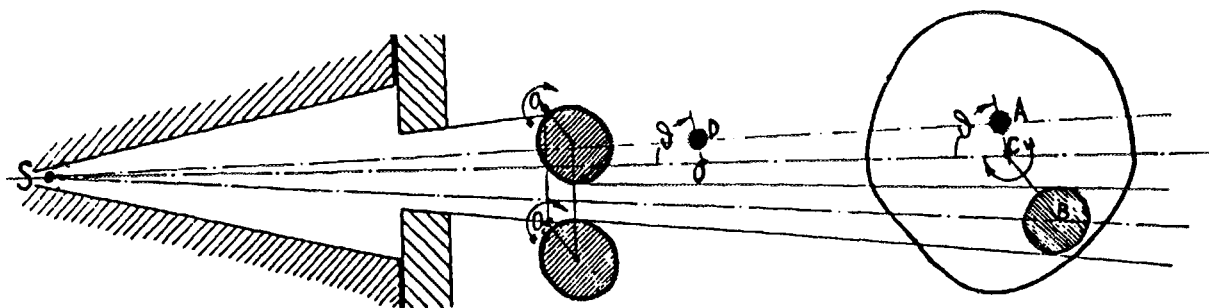


Fig. 12. Schematic diagram of an arrangement showing beam shaping and organ protection. The neck cross section rotates around C . The absorber D , rotating around O synchronously with the neck, protects the spinal cord A at all times. The two shaded blocks, rotating around O_1 and O_2 synchronously with the neck, collimate and direct the beam to the tumour B at all times. (Reprinted from RADIOLOGY, Vol. 77, No.4, October 1961).

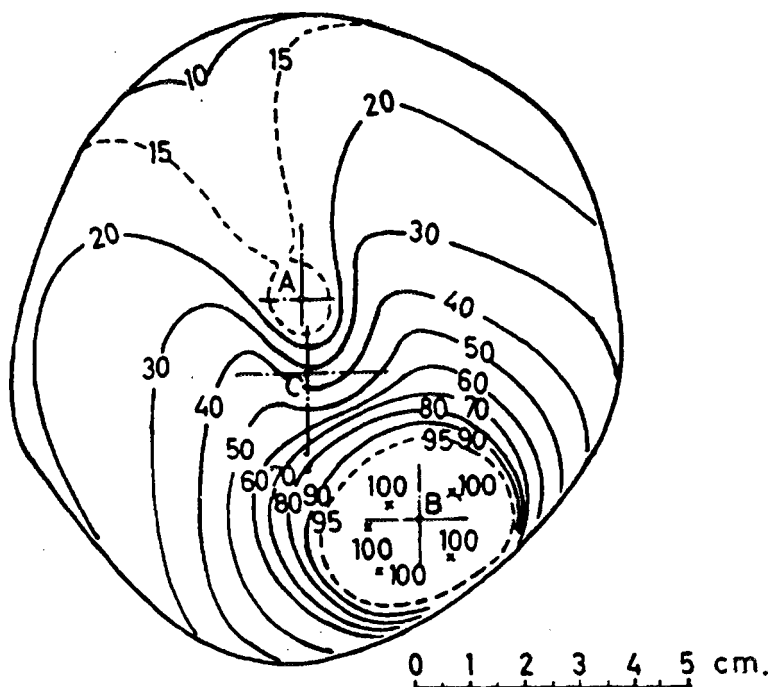


Fig. 13. Distribution of dose on a neck cross-section by the arrangement shown in Fig. 12. Note, the independent positions of the centre A of protected area, the centre B of treated area and the centre C of rotation. (Reprinted from RADIOLOGY, Vol. 77, No.4, October 1961).

3. Problems of practical application.

All of the above technics (from Fig. 2 to Fig. 13) were physically developed more than thirty years ago, but they were not widely implemented for the following reasons :

- 3.1. Radiotherapists, having then a limited education and training in Physics and Geometry preferred in general stationary to rotational fields.
- 3.2. The geometric uncertainty (location, size and shape) of the PTV and the Organs at Risk was then high. The CT, the MRI, and other high resolution diagnostic technics and devices were not invented yet. For this, the possibilities and the physicogeometric accuracy, offered by these Conformal Radiotherapy technics, were not of high value and use.
- 3.3. The study, design and construction of customised gravity oriented absorbers and their application on the corresponding patient, were not very attractive to physicists, therapists and technologists.
- 3.4. The problem of dosimetry and the derivation of the dose distribution required the development of special software for the computer and/or experimental measurements on a customised and hospital made phantom simulating each individual patient.

4. Present solutions to problems 3.1. and 3.2.

The present answers to the above 3.1. and 3.2 problems are the following :

- 4.1. Most radiotherapists are not afraid of Rotational Therapy any more.
- 4.2. The advent of CT, MRI and other high resolution diagnostic technics made possible the accurate geometric definition of the PTV, the Organs at Risk and the neighbouring structures. Devices controlling and duplicating the position of the immobilized patient are also available.

5. Solutions to the problems 3.3. and 3.4. and to the inverse problem.

Solutions to the above 3.3. and 3.4. problems are presented through the Treatment Planning of a specific case of Ca of the cervix.

This presentation also includes a solution to the inverse problem : “ Given the minimum therapeutic requirements (acceptable dose distribution) find a way to satisfy them”.

“DYNARAD” (“Development and Standardisation of New DYNAMIC RADiotherapy Technics”) is a “Concerted Action” of the European Union, involving thirty Medical Centres of Europe.

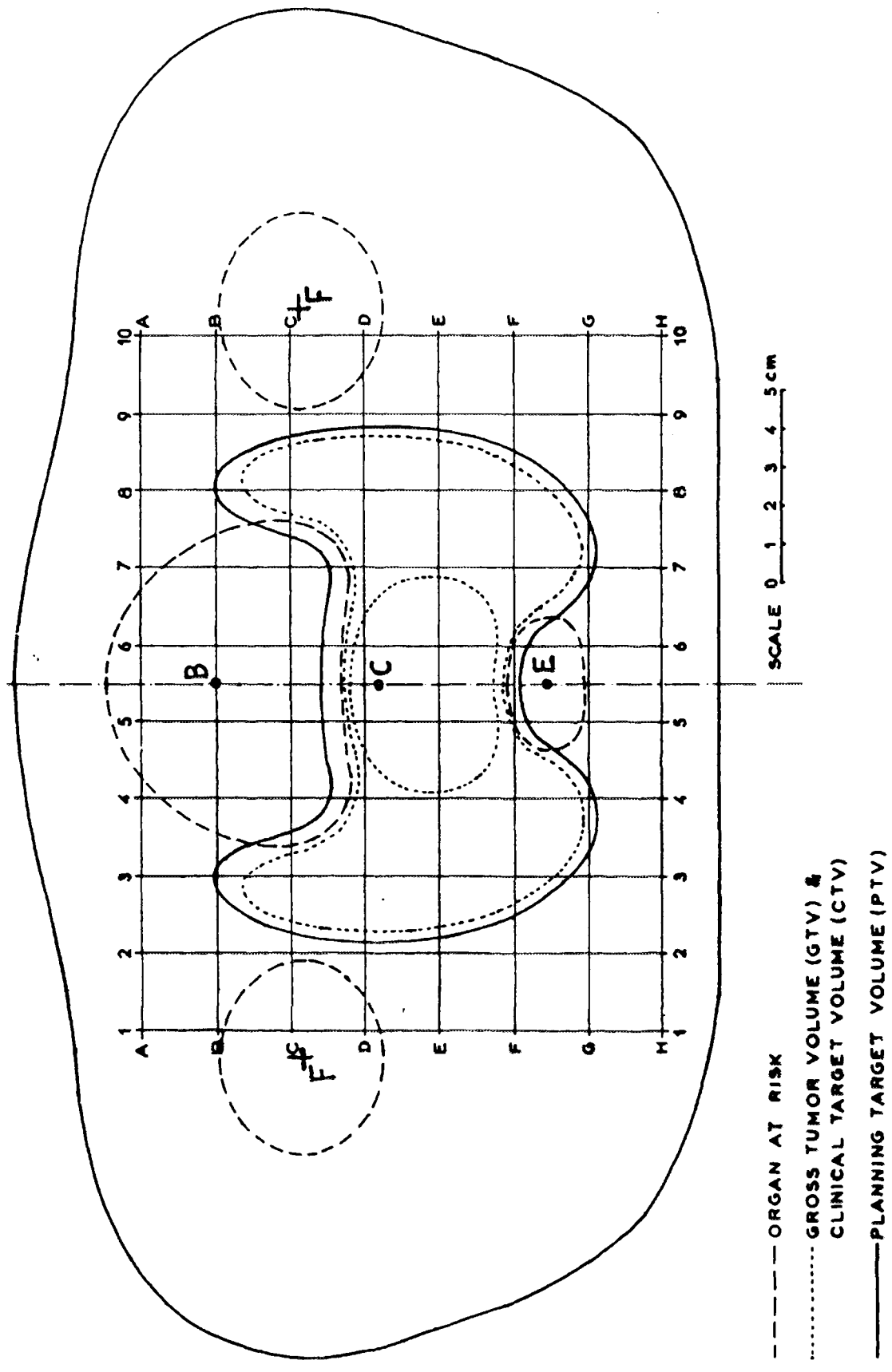


Fig. 14. Transverse cross-section showing the target volumes and the organs at risk in a Ca of the cervix case.

To inter-compare the “Teletherapy” technics applied in Europe, these Centres have agreed to use the case of cervix carcinoma shown in the central transverse cross section of Figure 14.

The following sequential steps are proposed for the Treatment Planning, if gravity oriented absorbers or synchronous protectors are to be used.

- The central transverse cross section is derived by CT and other diagnostic procedures.
- The PTV and the Organs at Risk (bladder, rectum and femurs) are delineated by the therapist, and the cross-section is printed or drawn under scale 1:1.
- The required dose range in the PTV and the permissible doses in the Organs at Risk are specified. Suppose that the goal is to deliver a dose :
 - higher than 60 Gy and lower than 80 Gy in each and every point of the “butterfly” shaped PTV;
 - not higher than 40 Gy at the centre B of the bladder;
 - not higher than 50 Gy at each of the centres R (rectum) and F (femurs);
 - not higher than 60 Gy at the proximal to the PTV region of each of the four Organs at Risk (bladder, rectum and two femurs).
- A circle of about 13cm in diameter, with its centre at C, covers all of the PTV easily. For this, a beam of about 12 cm in width, rotating about C (isocentre) will be employed.

The cross-section is reduced in size through a photocopier by the ratio of homiothesis (source to the machine axis of rotation distance divided by the source to the device axis of suspension distance). This is the factor by which the “shade” of each absorber is magnified as it is projected by the beam on the corresponding protected organ.

- The so reduced cross-section gives the shape, size and position of the absorbers, to be used for the protection of the Organs at Risk. That is, the absorbers are already drawn and located in scale 1:1, in the form of reduced in size cross sections of the Organs at Risk.
- The two femurs are completely outside the PTV. For this, the dose in the proximal to the PTV regions of the femurs will not be larger than 60 Gy (for an average dose of 70 Gy in the PTV). Therefore, most likely, no specific protection is necessary for the femurs, in 360° rotational therapy.
- The other two Organs at Risk need protection by two corresponding absorbers. Let’s call the bladder: “Organ 1” and the rectum “Organ 2”.

- The reduced cross-section solves the geometrical problem. It defines the shape and size of the protective absorbers and their position on the device. In the following, the material of each absorber will be defined through its attenuation coefficient (μ_1 for the bladder protector P_1 and μ_2 for the rectum protector P_2).
- S_1 is the area of the cross-section of the bladder protector P_1 . The average thickness $W_1 = 2 r_1$ of that protector, penetrated by any ray that meets the bladder center B, can be found from: $S_1 = \pi r_1^2$, if we assume that the cross-section of P_1 is about equivalent to a circle of the same area S_1 . In the same way, the radius r_2 of an equivalent circle is defined from the area S_2 of the rectum protector P_2 .
- D_0 is the yet unknown but too high dose that would be given through the same amount of radiation (same number of monitor units) on the circular high dose region of center C and radius $R = W / 2$ if no absorbers were used. Where $W=12$ cm, is the field width. All three points B, C, and E of Figure 14 are in the high dose region. They would receive the dose D_0 , if no protectors were used.
- The diagramme of Figure 15 expresses in a simple and condensed way the essence of Rotational Therapy.
 - a) It gives the fraction of irradiation time (f_i = time factor) that any point (A or B) of any patient cross section is irradiated by a rotating beam of any width ($W=2R$) and of any photon energy. On the horizontal axis is the distance of the point from the center C of rotation (isocenter), measured in multiples of the half width of the beam R. In Figure 15, for the point A it is: $L_A=0,84 R$. That means $L_A < R$ and $f_i= 1$. For the point B, it is $L_B= 1,40 R$ and $f_i= 0,50$. Therefore, the point B remains in the beam 50% of the irradiation time.
 - b) It also gives the fraction of time that any point of any patient cross-section remains under the protection of any constant width absorber, which protects a circular area of radius R in the patient. Now the numbers on the horizontal axis give the distance of the point from the center of protection measured again in multiples of R (radius of protected circular region).
- In solving the inverse problem we have to derive approximately the numerical values of μ_1 , μ_2 and D_0 . Then the absolute dose and its distribution will be verified computationally and/or experimentally, for the so derived values of μ_1 , μ_2 and D_0 .
- For this, we may neglect the dose given to B by a part of the radiation scattered by the surrounding outside of the bladder tissue. This part of the scatter radiation is due to the

difference of beam intensity between the beam irradiating the surrounding bladder region and the weakened by the protector beam which irradiates the bladder.

- The point B receives a dose:

$$D_B = D_0 (f_{B1} - f_{B2}) \cdot e^{-2\mu_1 r_1} + D_0 f_{B2} \cdot e^{-2(\mu_1 r_1 + \mu_2 r_2)}$$

- Where f_{B1} is the fraction of time that B stays in the shade of protector 1. That is $f_{B1} = 1$. The time fraction that B is simultaneously protected by both the rectum and the bladder absorbers is f_{B2} and it can be found from the curve of Figure 15. If L_B is the distance of B from E in cm. L_B / r_2 is the same distance in units r_2 and Figure 15 gives f_{B2} .

- In the same way, the dose D_E given at point E is:

$$D_E = D_0 (f_{E2} - f_{E1}) \cdot e^{-2\mu_1 r_1} + D_0 f_{E2} \cdot e^{-2(\mu_1 r_1 + \mu_2 r_2)}$$

Where again $f_{E2} = 1$

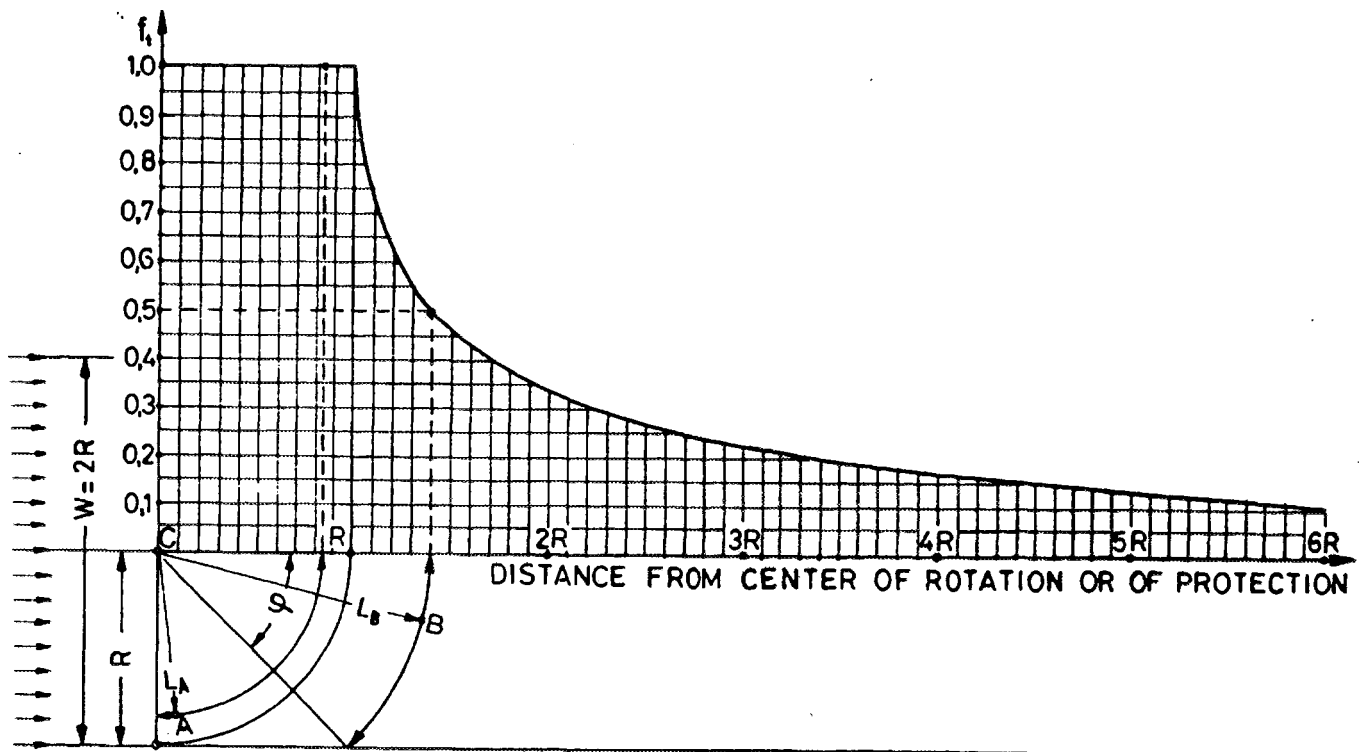


Fig. 15. Diagramme giving the fraction f_t of the treatment time that any point (A or B)
(a) stays in the beam versus its distance from the isocenter C for a rotational field of width $W = 2R$
(b) is protected by an absorber of constant width which protects a circular region of $W = 2R$ versus its distance from the center C of the protected region.

- As long as the point C is protected, it is either in the shade of P_1 or in the shade of both P_1 and P_2 .

Let f_{C1} and f_{C2} be the fractions of the irradiation time that the point C is protected by the protectors P_1 and P_2 respectively. Then $(f_{C1} - f_{C2})$ is the time fraction that C is protected by P_1 only. During the time fraction $(1 - f_{C1} - f_{C2})$ the point C is not protected at all.

Therefore the dose D_C given at point C (isocenter) is:

$$D_C = D_0(f_{C1} - f_{C2}) \cdot e^{-2\mu_1 r_1} + D_0 f_{C2} \cdot e^{-2(\mu_1 r_1 + \mu_2 r_2)} + D_0(1 - f_{C1} - f_{C2})$$

- In these three equations we can substitute the known numerical values of the permissible to B and E doses $D_B=40\text{Gy}$ and $D_E=50\text{Gy}$ as well as the required for C dose $D_C=70\text{Gy}$. The values of f_{B1} , f_{B2} , f_{E1} , f_{E2} and f_{C1} , f_{C2} are taken from the diagram of Figure 15.

- Naming: $e^{-2\mu_1 r_1} = x$ and $e^{-2\mu_2 r_2} = y$, the system becomes:

$$D_B = D_0(f_{B1} - f_{B2}) \cdot x + D_0 f_{B2} \cdot x \cdot y$$

$$D_E = D_0(f_{E2} - f_{E1}) \cdot y + D_0 f_{E1} \cdot x \cdot y$$

$$D_C = D_0(f_{C1} - f_{C2}) \cdot x + D_0 f_{C2} \cdot x \cdot y + D_0(1 - f_{C1} - f_{C2})$$

- The solution of the three equation system gives the three unknowns D_0 , x and y . As a result we have the values of D_0 , μ_1 and μ_2 .
- Therefore we know what material we must use for the protector P_1 and what for the protector P_2 . We also know the dose D_0 that would be given at C under ordinary rotational therapy (without protectors). Using the proper TMR for this patient's cross section, we find from D_0 the number of monitor units for the linear accelerator and through the TAR we find the irradiation time for the Co-60 unit.
- The above derivation is greatly simplified if instead of two we have only one organ to protect.
- A plaster model of each Organ at Risk can be made in reduced size, by the ratio of homiothesis, size.
- A warm low melting point "thermoplastic" sheet can be wrapped around the above plaster model.
- After the so formed plastic shell cools off, it can be cut in two pieces to remove the plaster model from the shell.

- The so-obtained plastic container can be filled with a material in form of small spheres (lead and/or steel and/or aluminium) to achieve the above calculated attenuation coefficient for each protector.
- Computational methods were and are being developed for deriving the dose distribution in each case.
- Customized phantoms of unit density “hardboard” leaves (compressed by products of wood) are inexpensive and easy to build. A calibrated film exposed between two slabs of such a custom made phantom can give or verify the dose distribution.

6. Conclusions

Rotational Therapy with gravity oriented absorbers is a rather easy and inexpensive Conformal Radiotherapy compared to Rotational Therapy employing computer controlled motion of multileaf collimator.

REFERENCES

1. WRIGHT, K.A., PROIMOS, B.S., TRUMP, J.G.: Physical Aspects of Two Million Volt X-ray Therapy. *The Surgical Clinics of North America*, Vol. 39, No. 3, June 1959.
2. PROIMOS, B.S.: Synchronous Field Shaping in Rotational Megavolt Therapy. *Radiology* 74: pp. 753-757, May 1960.
3. TAKAHASHI, S., KITABATAKE, T., MORITA, K., OKAJIMA, S., AND IIDA, H.: Methoden zur besseren Anpassung der Dosisverteilung an tiefliegende Krankheitsherde bei Bewegungsbestrahlung. *Strahlentherapie* 115:pp. 478-488, July 1961.
4. PROIMOS, B.S.: Synchronous Protection and Field Shaping in Cyclotherapy. *Radiology* 77:pp. 590-599, October 1961.
5. WRIGHT, K.A., PROIMOS, B.S., TRUMP, J.G., SMEDAL, M.I., JOHNSTON, D.O., SALZMAN, F.A.: Field Shaping and Selective Protection in 2-million-volt Rotational Therapy. *Radiology* 76:275, 1961.
6. TAKAHASHI, S.: Conformation Radiotherapy: Rotation Techniques as Applied to Radiography and Radiotherapy of Cancer. *Acta Radiologica*, 1964, Suppl.242.
7. PROIMOS, B.S.: Beam Shapers Oriented by Gravity in Rotational Therapy. *Radiology* 87:pp. 928-932, November 1966.
8. PROIMOS, B.S., TSIALAS, S.P., COUTROUBAS, S.C.: Gravity-Oriented Filters in Arc Cobalt Therapy *Radiology*, vol. 87, No. 5, pp. 933-937, November 1966.
9. PROIMOS, B.S.: Shaping the Dose Distribution through a Tumor Model. *Radiology* 92, No. 1, pp. 130-135, January 1969.
10. KELLEY, C.D., REID, A., SIMSON L.D., HILARIS, B.S.: The Proimos Device: A Gravity Oriented Blocking System for use in External Radiation Therapy. *Clinical Bulletin*, Memorial Sloan-Kettering Cancer Center, Vol. 6, No. 3, pp. 107-113, 1976.
11. PROIMOS, B.S., GOLDSON, A.L.: Dynamic Dose-Shaping by Gravity-Oriented Absorbers for Total Lymph Node Irradiation. *Int. J. Radiat. Oncol. Biol. Physics* 7:pp. 973-977, 1981.
12. ENGLER, M.J., HERSKOVIC, A.M., PROIMOS, B.S.: Dosimetry of Rotational Photon Fields with Gravity-Oriented Eye Blocks. *Int. J. Radiation Oncology Biol. Physics*, Vol. 10, pp. 431-438, 1984.

BE 9700028



BE9700028

In Vivo Dosimetry with L- α -Alanine

Boey R.⁽¹⁾, Van Der Velden K.⁽¹⁾, Janssens H.⁽¹⁾, Schaeken B.⁽²⁾

(1) Industriële Hogeschool van het Gemeenschapsonderwijs Limburg, Maastrichterstraat 100, B3500 Hasselt

(2) Department of Radiotherapy

Academisch Ziekenhuis Middelheim, Lindendreef 1, B2020 Antwerp, Belgium

ABSTRACT

When organic substances are irradiated, stable unpaired electrons can be formed. The concentration of these electrons is detected via electron paramagnetic resonance (EPR), a non-destructive form of dosimetry.

L- α -Alanine is extremely suited as a detector because of its high stability and high yield of unpaired electrons.

With an EPR spectrometer, we measure the peak-to-peak value (Hpp) of the first derivative of the resonance-spectrum. This value is proportional to the concentration of unpaired electrons and therefore with the absorbed dose.

Prior to the in vivo measurements in teletherapy, a calibration curve had to be established. This clearly showed a linear relationship between the EPR-signal and the absorbed dose, except for very low dose where precision was low (20% 1SD). This indicates that the background signal of the dosimeter is strongly orientation dependent. For this reason we decided to use pre-irradiated detectors.

With this in mind we performed a number of in vivo measurements, from which it became clear that error propagation plays a major role with the calculation of the measured absorbed dose, in the range 1 Gy - 6 Gy.

Contrary to in vivo measurements in brachytherapy, where higher doses are measured (10 Gy-60 Gy), large uncertainties (30% 1SD) on our entry dose calculations were perceived.

We therefore propose to use a statistical method of reducing this standard deviation to an acceptable level. Our method, consisting of 2 detectors and the usage of weightcoefficients on our standard deviations, gave promising results.

However, theoretical calculations and in vivo measurements show that this method is still not satisfactory to reduce the uncertainty to an acceptable standard in clinical situations.

The only way to avoid the problem of error propagation would be not to pre-irradiate our detectors. In other words, we ought to have detectors that show a small background signal and a high precision, which brings us to pure alanine-powder.

The usage of this powder produced the required precision on our in vivo measurements and is relatively cheap (1500 francs/250g).

INTRODUCTION

The International Commission on Radiation Protection stated in its 1990 recommendations (ICRP Publication 60): "The assessment of doses in medical exposure, i.e. doses to patients, is of critical importance in radiotherapy."

Therefore one has to be capable to perform immediate control-measurements, when encountered with complaints from the patient. When these complaints arise a certain time after the treatment, one has to possess the necessary data to perform an investigation.

Precise measurements, or in other words precise detectors and the possibility of dose-archivation are therefore very important.

The detectors need to comply to certain basic standards, such as linear response in the desired dose-range, no energy dependence, the capability to detect low doses, high reproducibility and small in dimensions.

The very good features of alanine dosimetry, which is now a world-wide technique in high-dose dosimetry, could be put to use in the radiation therapy level.

This brings us to the goal of our research: "Is it possible to use alanine detectors in the low-dose range?"

EXPERIMENTAL

All measurements were performed with an EMS 104 EPR Spectrometer (Brucker) equipped with a standard cavity and quartz holder.

Experiments with 1 detector per patient (teletherapy - Cobalt)

We used pre-irradiated AWM-detectors ⁽¹⁾ with a diameter of 4.8 mm and a length of 5 mm.

Owing to the fact that an un-irradiated detector is strongly orientation dependant, we had to give our detectors an initial dose of at least 10 Gy, in order to keep the variation in repetitive measurements (reproducibility) below 1% (1σ) (Figure 1).

With this in mind we performed a number of in vivo measurements, from which it became clear that error propagation plays a major role with the calculation of the measured absorbed dose.

The reason is as follows:

One of the features of alanine detectors is that they accumulate the given doses.

So, our detectors already have an initial dose, with a standard deviation of 1% or less.

If we administer a certain dose, we will measure a new accumulated dose, with a standard deviation of 1% or less.

¹ AWM: Albrecht Wieser Meßtechnik München

To calculate the administered dose, it suffices to subtract both doses.

However, due to error propagation, the error on the calculated dose, calculated with statistical formulas, is large with respect to the dose.

Figure 2 shows that a standard deviation of 30% was common.

If we premise a maximum uncertainty of 5% on the result, we can calculate theoretically, the maximum permissible accumulated dose that our detector may have, prior to the irradiation in our experiments.

Figure 3 clearly shows that in order to measure a dose of 2 Gy, with a maximum uncertainty of 5%, the detector may have a maximum initial reading of approximately 40 Hpp0.5-units.

The calibration curve for the AWM-detectors has the following equation:

$$R = 3.5447 + 6.8327 \times D$$

with **R** the reading in Hpp-units, normalised to 0.5g alanine (Hpp0.5)

D the dose corresponding to the Hpp0.5 reading

Since these detectors needed to be pre-irradiated with at least 10 Gy, we perceive according to the equation an initial Hpp0.5-value of approximately 70.

In other words, using this method with one detector, we are unable to perform precise measurements of low doses.

Review of the method:

This method does not provide the necessary precision on our measurements. However this does not mean a complete rejection. The method is suitable with brachytherapy, where doses in the range 5-60 Gy are registered. Pre-irradiation becomes superfluous and we evade the problem of error propagation.

Experiments with 2 detectors per patient (teletherapy - Cobalt)

A possible solution to avoid the high standard deviation on our results could be the usage of 2 detectors.

Pre-irradiated AWM-detectors with a diameter of 4.8 mm and a length of 5 mm were used.

As a final result we calculated the average of the two detector readings.

The error on this result can be calculated using the following formula:

$$\sigma_{\text{result}}^{-2} = \sigma_{\text{detector1}}^{-2} + \sigma_{\text{detector2}}^{-2}$$

With this knowledge we performed a series of in vivo measurements (Figure 4), from which it became clear that this method successfully reduced the error on our results, but this error was still too large: up to 20% (1σ).

If we premise a maximum uncertainty of 5% on the result, we can calculate theoretically, the maximum permissible accumulated dose that our detector may have, prior to its use.

Figure 5 & Figure 6 are used in the following way:

If one wishes to administer for example a dose of 1.5 Gy, it suffices to select a point beneath the graph 5. This point refers to the σ of the 2 detectors, after administration of the dose. In the graph 6 one can then find the maximum initial Hpp0.5-value of the 2 detectors separately.

The only problem is once again that with the administering of low doses, one of the detectors according to the our graphs, must have an initial Hpp0.5-value that is lower than initial Hpp0.5-value resulting from the pre-irradiation process.

Review of the method:

By using this method we are able to reduce the error on our results, since the error will always be smaller than the error on the individual measurements of our detectors.

The method was promising, but not good enough to reduce the error to an acceptable standard.

Experiments with pure alanine powder (teletherapy - Cobalt)

In the experiments described above, the major problem encountered is that of error propagation, which resulted in an unacceptable error on our results.

This problem can be avoided if we are no longer forced to pre-irradiate our detectors.

This is only possible if we possess detectors that have a very low background signal.

(We also observed that the 'cavity loading' can reduce the fluctuations in background readings. This effect will be studied in the future.)

We can produce detectors with a low background signal, namely pure alanine powder (SIGMA Chemical Co). We therefore continued our in vivo experiments with this powder, from which it became clear that this method would provide satisfactory results.

Using alanine powder, we were able to reduce the standard deviation on our results to 2% - 3%, what can be regarded as an acceptable standard, figure 7.

Review of the method:

This method provides accurate results, but is more time consuming and the powder needs to be evenly distributed in the quartz tube. However this does not diminish the advantages, e.g. the cost of a single detector is several times the cost of the powder used and one is not dependant on the manufacturers of the detectors.

Remark:

Very recently researchers (Wieser et al.) have been able to produce a solid alanine detector with the same precision as powder. However, these detectors, are rather expensive (± 100 franks per detector).

Figure 8 shows a comparison between alanine powder and these new detectors.

FUTURE PROSPECTS

- The further optimisation of the procedure of alanine dosimetry.
- The study of the 'cavity loading' effect, which can contribute to the reduction of the uncertainty on our results.
- The study of the dependence on the grain size of the alanine powder, and the possible effects of this dependence on the measurements.

REFERENCES

- Bartolatta A., Fattibene P., Onori S., Pantaloni M., Petetti E., Sources of Uncertainty in Therapy Level Alanine Dosimetry, Appl. Radiat. Isot. Vol. 44, Pergamon Press Plc. (1989)
- Descours S., Assayrenc J., Bermann F., Couderc B., de Choudens H., Delard R., Rassat A., Servoz-Gavin P., Etude par RPE des radicaux libres créés sous irradiation dans certaines substances organiques, application en dosimétrie de la mesure des radicaux libres créés dans l'alanine, Rapport CEA-R-3913 (1970)
- Ettinger K. V., Free Radical Dosimetry Techniques and Their Suitability for Precise and Accurate Measurements of Radiation, Appl. Radiat. Isot. Vol. 44 No. 10 - 12 p.865 - 870, Pergamon Press Plc. (1989)
- ICRP, Annals of the ICRP - 1990 Recommendations of the International Commission on Radiological Protection, Pergamon Press (1991)
- Johns H. E., Cunningham J. R., The Physics of Radiology, Charles C. Thomas (1983)
- Khan F. M., The Physics of Radiation Therapy, Williams & Wilkins (1984)
- Knoll G. F., Radiation Detection and Measurement, John Wiley & Sons, Inc. (1989)
- Kudynski R., Kudynska J., Buckmaster H. A., The Application of EPR Dosimetry for Radiotherapy and Radiation Protection, Appl. Radiat. Isot. Vol. 44 No. 6 p.903 - 906, Pergamon Press Ltd. (1993)
- Van Dam J., Marinello G., Methods for In Vivo Dosimetry in External Radiotherapy, ESTRO & Garant (1994)
- Van Der Velden K., EPR Dosimétrie met alanine in het dosisbereik 1 Gy-100 Gy, Afstudeerwerk ingediend tot het behalen van het diploma Industrieel Ingenieur Kernenergie Richting Medisch Nucleaire Technieken, Hogeschool Limburg (1995)

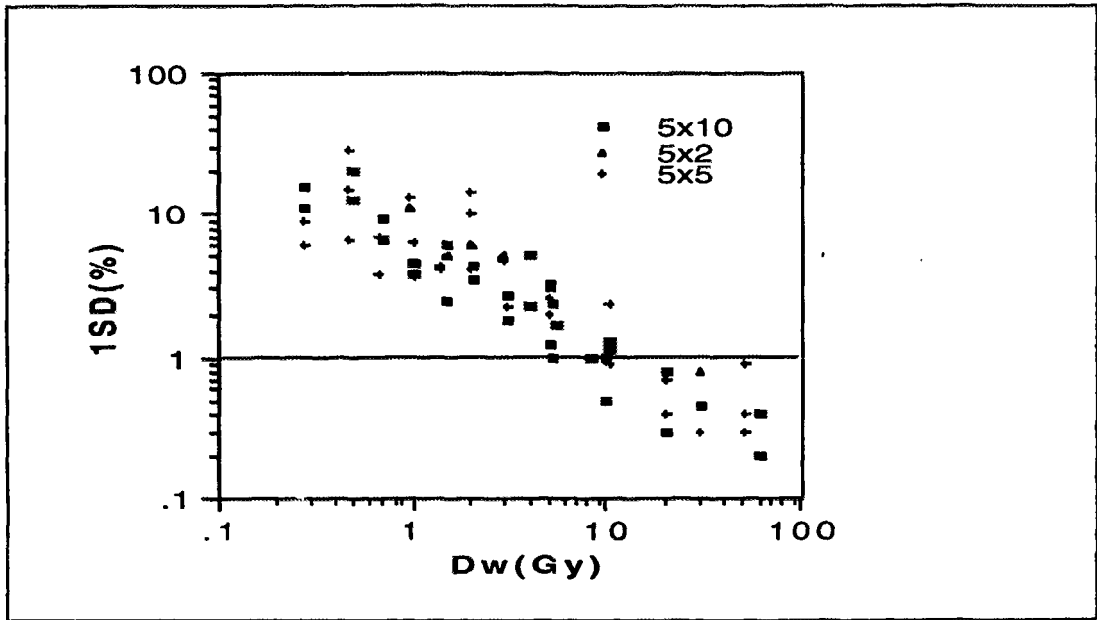


Figure 1

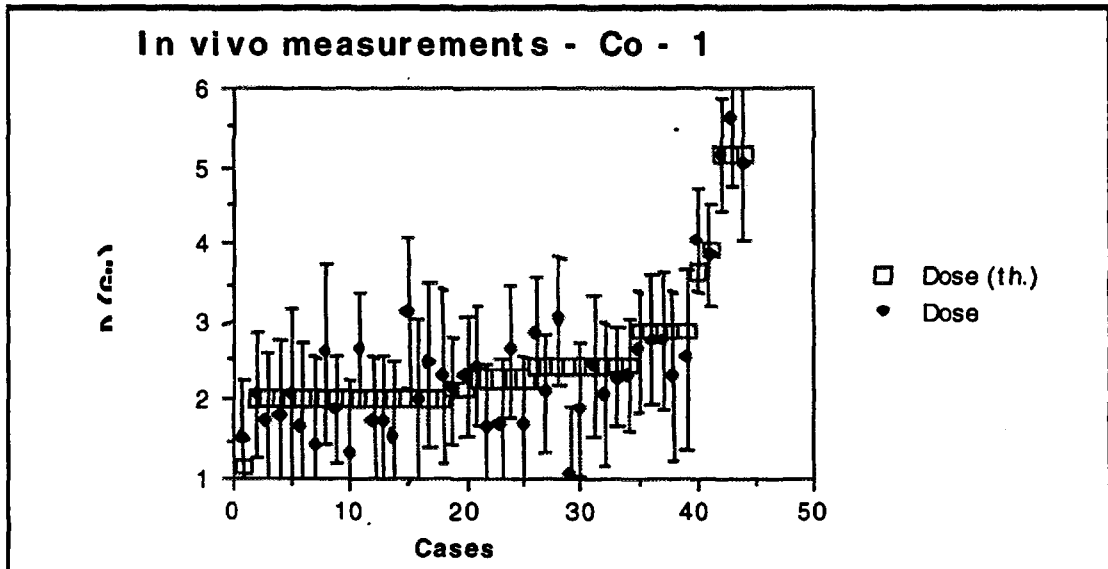


Figure 2

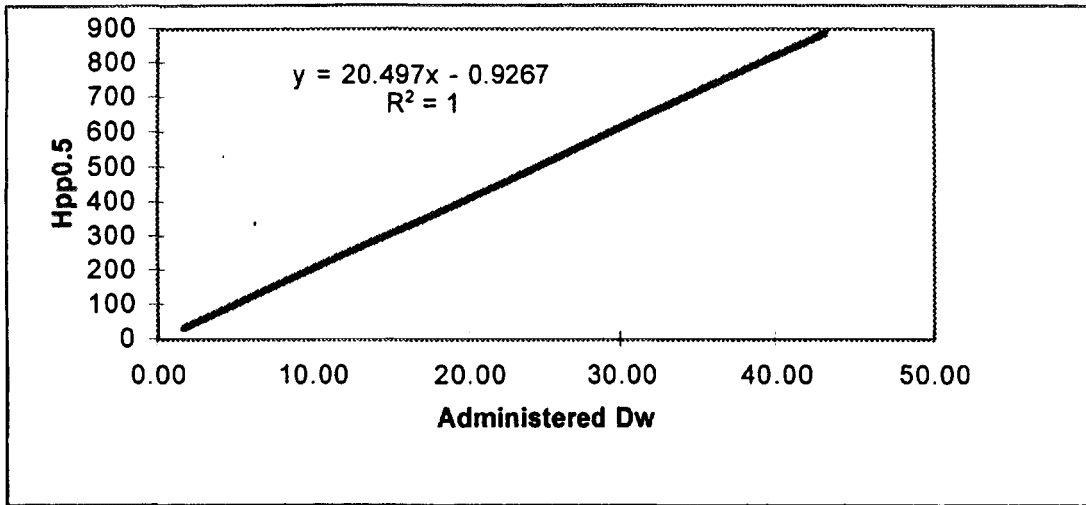


Figure 3

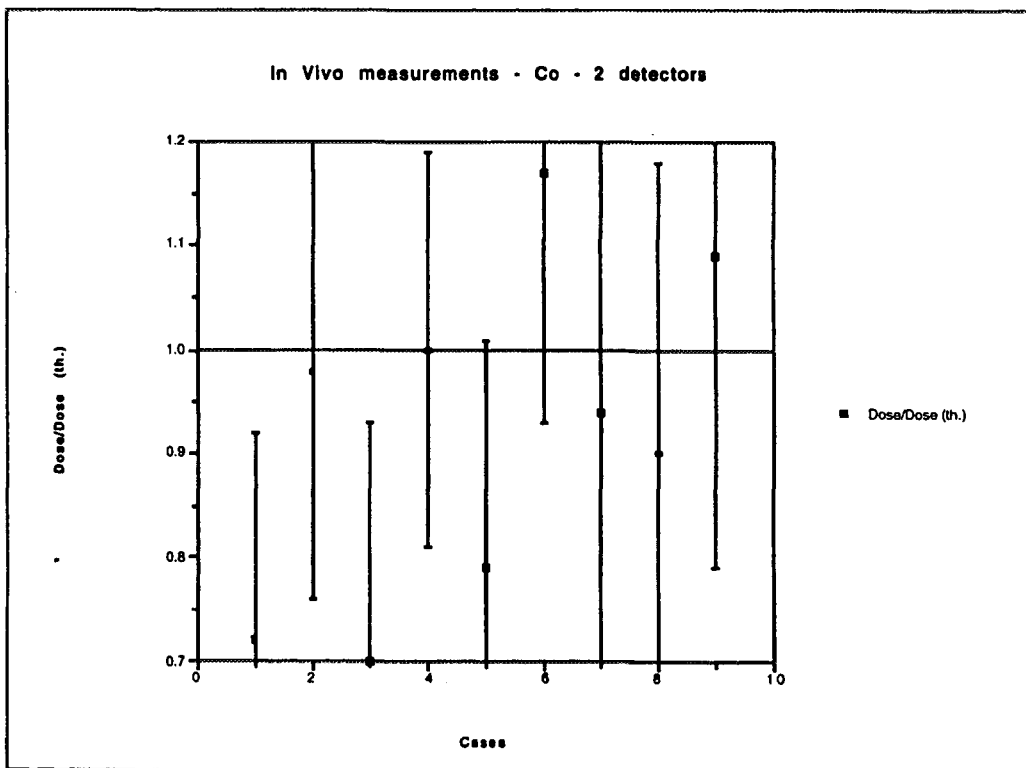


Figure 4

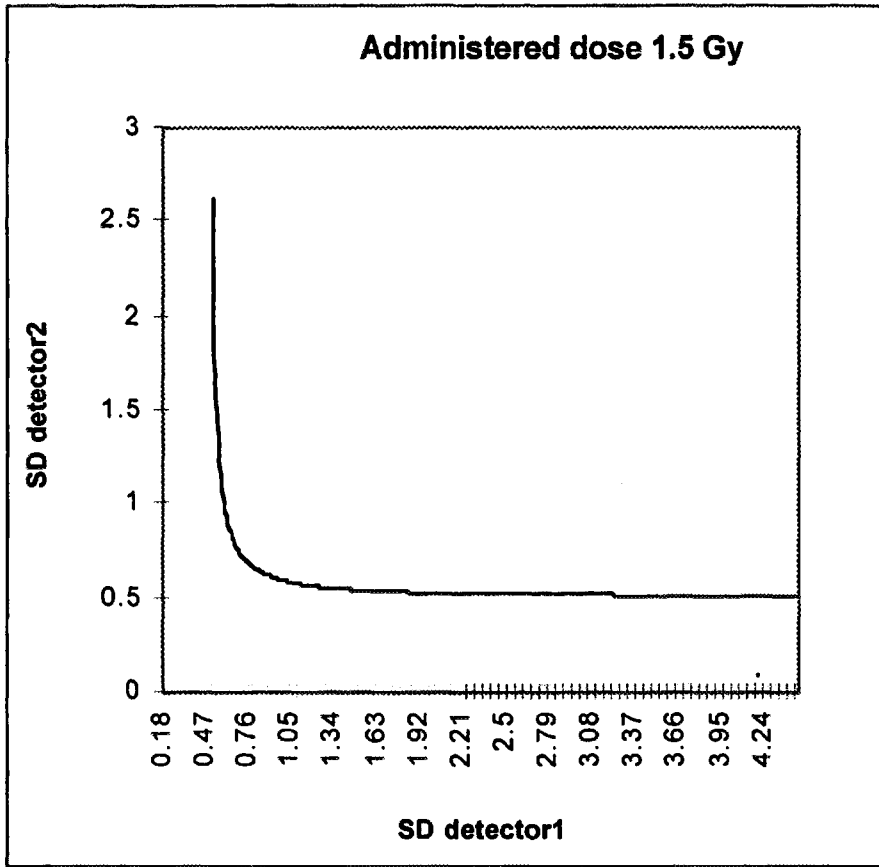


Figure 5

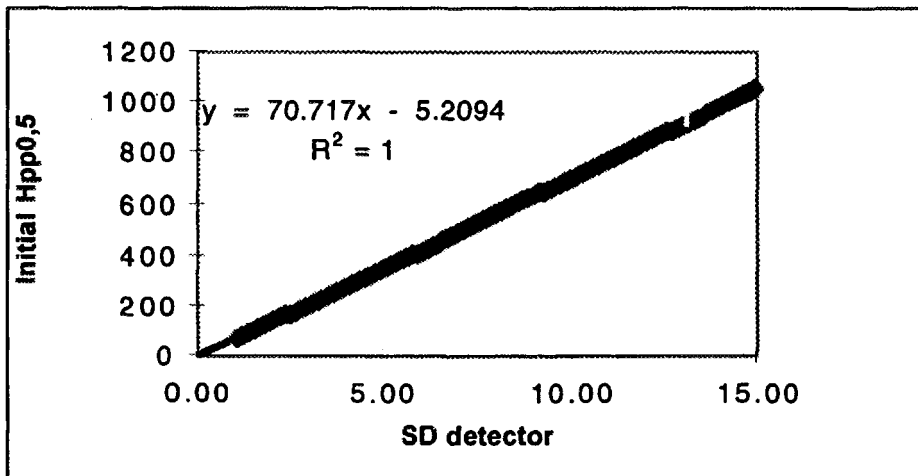


Figure 6

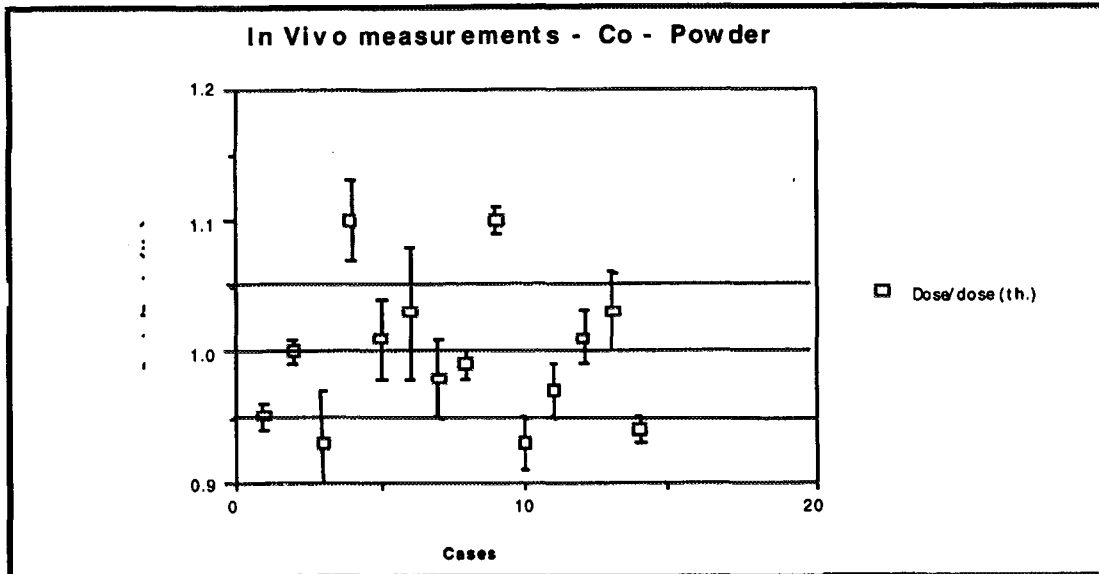


Figure 7

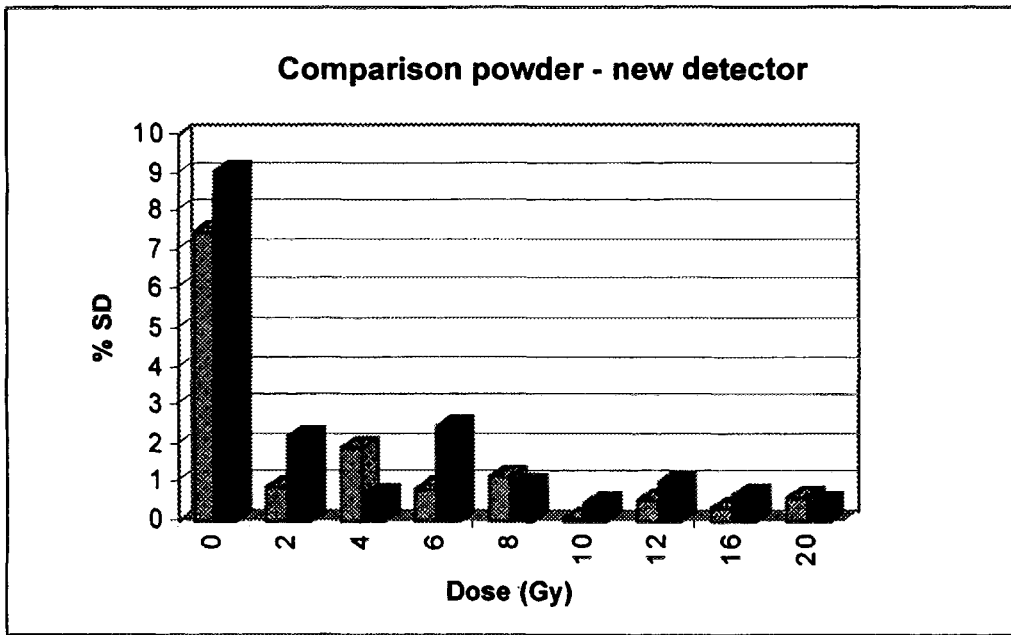


Figure 8

BES700029

In vivo dosimetry using thermoluminescence dosimeters during brachytherapy with a 370 GBq Ir¹⁹² source.

S. Cuepers, M. Piessens, L. Verbeke, A. Roelstraete.
Radiotherapy and Oncology, O.L.V. Ziekenhuis, Aalst, Belgium.

Abstract : When using LiF thermoluminescence dosimeters in brachytherapy, we have to take into account the properties of a high dose rate Ir¹⁹² source (energy spectrum ranging from 9 to 885 keV, steep dose gradient in the vicinity of the source) and those of the dosimeters themselves (supralinearity, reproducibility, size). All these characteristics combine into a set of correction factors which have been determined during in phantom measurements.

These results have then been used to measure the dose delivered to organs at risk (e.g. rectum, bladder, etc.) during high dose rate brachytherapy with a 370 GBq Ir¹⁹² source for patients with gynaecological tumours.

1. Introduction.

Optimal radiotherapeutic management of carcinoma of the cervix or of the endometrium represents a major challenge. Intracavitary brachytherapy in combination with external beam radiation plays an important role in achieving local control. However when brachytherapy is applied care must be taken to avoid significant complications involving the genitourinary tract, parts of the intestine, or both. While doses to bladder and rectum from external beam radiation therapy can easily be determined, the assessment of the dose contribution from brachytherapy to these organs is not easy without a CT-assisted planning system. In order to determine the dose delivered to organs at risk during HDR brachytherapy we measured the dose using thermoluminescence dosimeters. These results are compared with the dose calculated with the orthogonal film pair method.

2. Materials and methods.

2.1 Ir¹⁹² High dose rate.^{1,3,4,6,14}

The Ir¹⁹² source has a nominal activity of 370 GBq (10 Ci). The active source has a length of 3.5 mm and a diameter of 0.6 mm. Its encapsulation is made out of a 0.34 mm thick stainless steel sheath. The source is housed in a Gammamed 12I Remote Afterloading System (Isotopen - Technik Dr. Sauerwein GmbH). The reference air kerma rate of the source (the air kerma rate at a distance of 1 m of the source) was measured using a 0.6 cm³ graphite wall Farmer ionisation chamber (type 2571), with buildup cap, in combination with a Farmer electrometer, type 2570/1. The Ir¹⁹² kerma calibration factor for our chamber was determined by the "Standaard Dosimetrie Laboratorium" of the University of Ghent, Belgium.

2.2. LiF Thermoluminescence dosimeters.

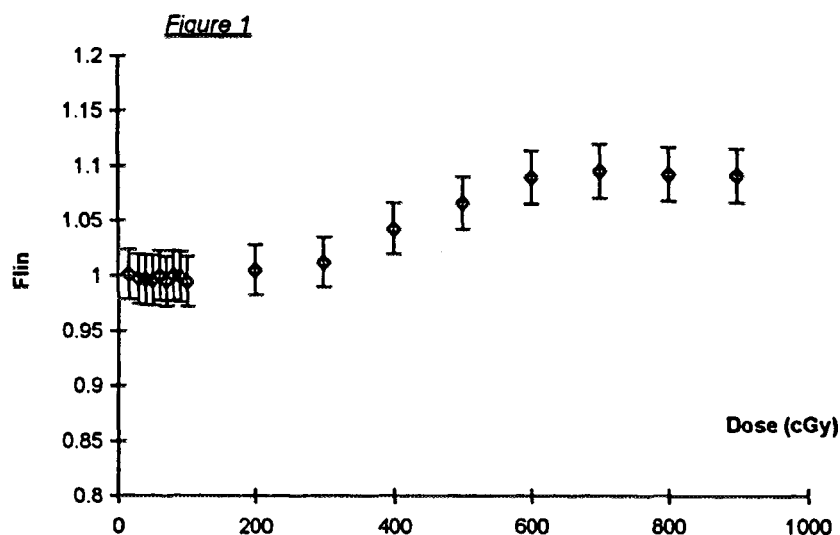
Measurements of the dose delivered to bladder, urinary tract and rectum during intracavitary brachytherapy were performed using Harshaw LiF TLD 100 rods, 1 x 1 x 6 mm³. Before each experiment, the TLDs were annealed at 400°C for 1 h and then kept at 100°C during a period of 2 h. After irradiation the TLDs were heated to 100°C for 10 min prior to the readout procedure. The responses of the TLD rods were read out with a Harshaw 3500 Manual TLD Reader.

2.2.1. Chip factor.

If we would have an ideal batch of TLDs, all rods would give the same response when exposed to the same amount of radiation. However due to differences in properties such as mass, size, etc. the responses can be different from one another. We therefore compared the response of each individual rod with the average response of the entire batch. The relative responses were determined by irradiating the rods with a 4 MV photonbeam (10 x 10 cm) from a Siemens Mevatron linear accelerator. The rods were placed in holes made into a slab of polymethylmetacrylate (PMMA) and at least 10 cm of backscatter material was provided. The chip factors were measured three times and rods which showed more than 3.5% variation were discarded.

2.2.2. Supralinearity.^{8,9,19,25,34}

At relatively low absorbed dose values (depending on what type of TL material is used) the dose response of the TLD is linear. Above a threshold dose, the response becomes supralinear, before reaching a saturation value and then falling off. The occurrence of non linearity in the dose region used in brachytherapy requires the application of a correction factor, F_{lin} . It is defined as the ratio of the measured TLD response to the predicted value for the same absorbed dose by linear extrapolation of the values corresponding to the doses between 50-100 cGy. The values of F_{lin} are shown in Figure 1.



2.2.3. Volume correction.

The TLD results have been corrected for the finite size of the dosimeter. Due to inverse square effects, dose varies over the volume of the TLD such that the dose at the centre of this volume as measured by a point dosimeter may be different from the average dose received by that volume. Thomason et al.³¹ have calculated a geometrical correction factor to compensate for this effect when the longitudinal axis of the dosimeter is perpendicular to the source axis. This factor is listed in table 1, in which r is the distance between the centre of the source and the central axis of the dosimeter.

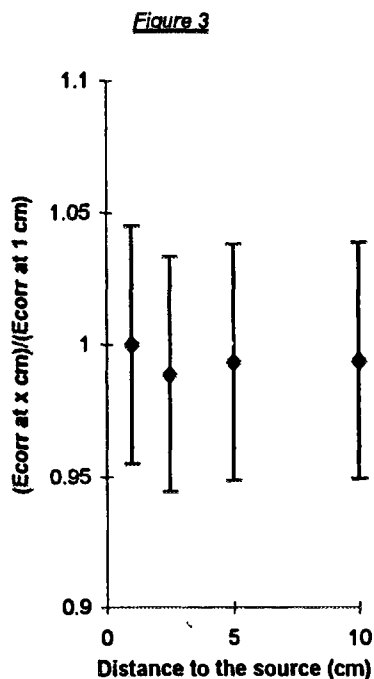
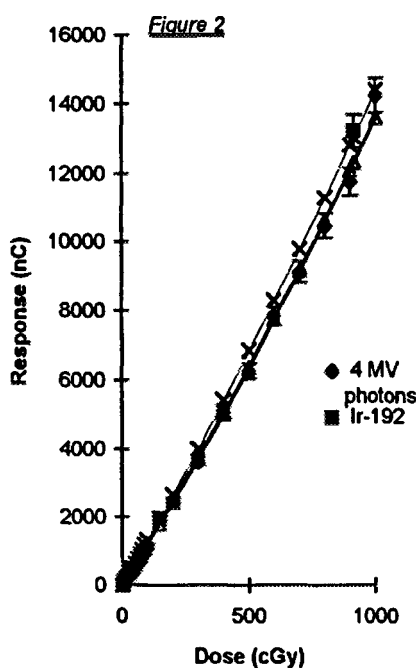
Table 1 Volume correction factor

r (cm)	Correction
1	1.028
2	1.008
3	1.003
4	1.002
5	1.001

2.2.4. Energy correction.^{1,7,8,19,20,31}

LiF shows a higher response to lower photon energies. The energy spectrum of Ir¹⁹² ranges from 9 to 885 keV. However the photon spectrum shifts significantly toward lower energies with increasing depth in the phantom and hence a depth-dependent correction of the response could be required. To determine the energy correction when using LiF TLDs in brachytherapy, we placed the rods in a PMMA phantom. It has been shown that PMMA is equivalent to water under full scattering conditions²² for the dosimetry of Ir¹⁹² sources. The rods were placed in holes milled in a slab of PMMA at known distances from the centre of the source. The longitudinal axis of the rods were perpendicular to the axis of the source. We measured the response of the TLDs at distances of 1, 2.5, 5 and 10 cm from the source and under different angles (0°, 30°, 60° and 90° with respect to the longitudinal axis of the source).

The results are shown in figure 2. It depicts the response of the TLDs in function of the dose for a 4 MV photonbeam and the TLD response along the transversal axis of the Ir¹⁹² source. Figure 3 shows the ratio of the response for an Ir¹⁹² source to the response in a 4 MV photonbeam in function of the distance from the source. The results in Fig.3 are normalized to the energy correction at 1 cm from the source. We can clearly see from this that within the accuracy of the measurements no depth-dependent correction is required.



2.3. In vivo dosimetry.

In the HDR treatments a urethral catheter with Foley balloon is inserted into the bladder of the patient. The balloon is filled with contrast medium and then retracted in order to determine the position of the bladder neck. Once the catheter is in place we insert a smaller tube filled with TLDs and a metallic marker into the urethral catheter.

The rectal tube contains a piece of lead wire to visualize the bowel. After it is inserted into the rectum a similar tube filled with TLDs is also placed inside the rectal catheter. The rectal tube is then attached to the applicator, which is held in place by a table fixation device. To simulate the source positions during the making of the pair of orthogonal films dummy sources are introduced into the applicator. Vaginal gauze packing is performed in an attempt to displace the anterior rectal wall and the base of the bladder and thus reducing the administered dose.

The bladder dose was calculated at the bladder neck (as visualized by the Foley balloon) and along the tube containing the TLDs. The doses to the anterior rectal wall were evaluated by

calculating different points along the lead wire inside the rectal tube and by the TLDs placed in the tube itself.

3. Results.

During our first measurements, we did not attach the rectal tube to the applicator. The tube was partially retracted when placing the patient back in her bed after taking the pair of orthogonal films. This was shown in the measurements with the TLDs : the measured doses were approximately 28% lower than the calculated doses along the rectal tube. Since then the rectal tube has always been immobilized. The dose delivered to the bladder neck was also measured on that occasion and corresponded with the calculated dose within the accuracy of the TLDs (3.5%).

The effect of vaginal gauze packing became obvious when performing measurements in two consecutive fractions with and without it. In both fractions a dose of 7 Gy was requested at 2 cm from the stopping positions of the source. The measured maximum bladder dose was reduced from 6.06 Gy to 4.32 Gy. The maximum dose received by the anterior wall of the rectum was 2.44 Gy during fraction 1 and was reduced to 1.64 Gy during fraction 2. The deviation between measured and calculated dose for this patient is stated in table 2.

	Fraction 1	Fraction 2
Rectum	3.75%	3.7%
Bladder	4.45%	4.3%

We performed our most recent measurements on a patient with a cervical carcinoma. The bladder neck is situated in the middle of the two ovoids of the colpostat on the AP radiograph. On the lateral radiograph we see that the closest point of the bladder neck is only 2 cm away from the stopping position of the source. It is therefore imperative that the external spreading of the colpostat is correct and that the vaginal gauze packing is correctly applied. Due to the fact that this patient has just started with brachytherapy, we have only been able to check the dose delivered to the bladder for the first two fractions. Until now the placement of the applicator has been correct : the maximum measured bladder dose was 4.29 Gy in accordance with the treatment planning. The internal opening of the colpostat seems not to be hampered by the tensing of lower abdominal muscles.

4. Conclusions.

Until now the in vivo measurements have not shown any grave discrepancies between measured and calculated dose. If there would be any differences, then the cause (bad placement of the applicator, movement of the patient and subsequent movement of the applicator, localization errors, etc.) should be found and corrected. Although the actual doses received by portions of the bladder and rectum may differ from the calculated dose due to bladder distension and bowel mobility during treatment, these variations have been minimized with rectal fixation techniques and catheter drainage of the bladder.

It is still too early to make any further comments or to draw any more conclusions as it is the aim of this study to perform further measurements on patients treated in our department with HDR brachytherapy.

¹Attix F.H., " Introduction to radiological physics and radiation dosimetry." J.WILEY INTERSCIENCE PUBLICATION, Chicester, 1986.

²Bagne F., " A comprehensive study of LiF TL response to high energy photons and electrons." RADIOLOGY 123, p. 753-760, 1977.

³Dutreix A., Marinello G., Wambersie A., " Dosimétrie en curiethérapie."

- MASON, Paris, 1982.
- ⁴Ezzell G., " Evaluation of calibration techniques for the Microselectron HDR." BRACHYTHERAPY 2 : Proceedings of the 5th international SELECTRON users' meeting, The Hague, Netherlands, 1988.
- ⁵Fairbanks E.J., De Werd L.A., " Thermoluminescent characteristics of LiF:Mg:Ti from 3 manufacturers." MED. PHYS., Vol. 20, No. 3, p. 729-731, 1993.
- ⁶Goetsch S.J., Attix F.H., Pearson D.W., Thomadsen B.R., " Calibration of ¹⁹²Ir high-dose-rate afterloading systems." MED. PHYS., Vol. 18, No. 3, p. 462-467, 1991.
- ⁷Hammerstein G.R., Miller D.W., White D., Masterson M., Woodard H.Q., Laughlin J.S., " Absorbed radiation dose in mammography." RADIOLOGY 130, p. 485-491, 1979.
- ⁸Horowitz Y.S., " Thermoluminescence and thermoluminescent dosimetry." CRC PRESS, INC., BOCA RATON, FLORIDA, U.S.A., 1984.
- ⁹Horowitz Y.S., " Study of the annealing characteristics of LiF:Mg,Ti using computerised glow curve deconvolution." RADIATION PROTECTION DOSIMETRY, Vol. 33, No. 1/4, p. 225-258, 1990.
- ¹⁰ICRU Report 38, 1985, " Dose and volume specification for reporting intracavitary therapy in gynaecology."
- ¹¹Julius H.W., " Instrumentation in thermoluminescence dosimetry." RADIATION PROTECTION DOSIMETRY, Vol. 17, p. 267-273, 1986.
- ¹²Kapp K.S., Stueckelschweiger G.F., Kapp D.S., Hackl A.G., " Dosimetry for intracavitary placements for uterine and cervical carcinomas : results of orthogonal film, TLD and CT-assisted techniques." RADIOTHERAPY AND ONCOLOGY, Vol. 24, No.3, p. 137-146, 1992.
- ¹³Kirby T.H., Hanson W.F., Johnston D.A., " Uncertainty analysis of absorbed dose calculations from thermoluminescence dosimeters." MED. PHYS., Vol. 19, No.6, p.1427-1433, 1992.
- ¹⁴Kondo S., Randolph M.L., " Effect of finite size of ionization chambers on measurements of small photon sources." RADIAT. RES. 13, p. 37-60, 1960.
- ¹⁵Loftus T.P., " Standardization of Ir-192 gamma-ray sources in terms of exposure." J. Of Research of the National Bureau of Standards 85, p. 19-25, 1980.
- ¹⁶Marinello G., Barthe J., Pollack J., Portal G., " "PLC" a new fast automatic reader suitable for in vivo dosimetry." RADIOTHERAPY AND ONCOLOGY, Vol. 25, No.1, p. 63-66, 1992.
- ¹⁷Marinello G., Pierquin B., Grimard L., Barret C., " Dosimetry of intraluminal brachytherapy." RADIOTHERAPY AND ONCOLOGY, Vol. 23, No.4, p.213-216, 1992.
- ¹⁸Marinello G., Raynal M., Brulé A.M., Pierquin B., " Utilisation de fluorure de lithium en dosimétrie clinique. Application á la mesure de la dose délivrée á la région axillaire par l'iridium 192 dans l'endocurietherapie des cancers du sein." J. RADIOL. ELECTR., No.56, p. 791-796, 1975.
- ¹⁹McKinlay A.F., " Thermoluminescence Dosimetry." MEDICAL PHYSICS HANDBOOKS 5, Adam Hilger, Bristol, 1981.
- ²⁰Meigooni A.S., Meli J.A., Nath R., " Influence of the variation of energy spectra with depth in the dosimetry of Ir¹⁹² using LiF TLD" PHYS. MED. BIOL., Vol. 33, No. 10, p. 1159-1170, 1988.
- ²¹Meigooni A.S., Mishra V., Panth H., Williamson J.F., " Instrumentation and dosimeter-size artifacts in quantitative thermoluminescence dosimetry of low-dose fields." MED. PHYS., Vol. 22, No. 5, p. 555-561, 1995.
- ²²Meli J.A., Meigooni A.S., Nath R., " On the choice of phantom material for the dosimetry of ¹⁹²Ir sources." INT. J. RADIATION ONCOLOGY, BIOL., PHYS., Vol. 14, No.3, p. 587-594, 1988.
- ²³Meli J.A., Meigooni A.S., Nath R., " Comments on "Radial dose distribution of ¹⁹²Ir and ¹³⁷Cs seed sources" ". MED. PHYS., Vol. 16, No. 5, p. 824, 1989.
- ²⁴Meisberger L.L., Keller R.J., Shalek R.J., " The effective attenuation in water of the gamma rays of Gold 198, Iridium 192, Cesium 137, Radium 226 and Cobalt 60." RADIOLOGY 60, p. 953-957, 1968.
- ²⁵Mijnheer B.J., Weeda J., " Some experimental observations on the supralinearity of the response TLD-100 for radiotherapeutical applications." Contributions to the symposium on thermoluminescence dosimetry, Maart 1988.
- ²⁶Muller-Runkel R., Cho S.H., " Anisotropy measurements of a high dose-rate Ir-192 source in air and in polystyrene." MED. PHYS., Vol. 21, No.7, p. 1131-1134, 1994.
- ²⁷Nath R., Meigooni A.S., Meli J.A., " Dosimetry on transverse axes of ¹²⁵I and ¹⁹²Ir interstitial brachytherapy sources." MED. PHYS., Vol. 17, No.6, p. 1032-1040, 1990.
- ²⁸Nath R., Anderson L.L., Luxton G., Weaver K.A., Williamson J.F., Meigooni A.S., " Dosimetry of interstitial brachytherapy sources : Recommendations of the AAPM Radiation Therapy Committee Task Group No. 43." MED. PHYS., Vol. 22, No.2, p. 209-234, 1995.
- ²⁹Nederlandse Commissie voor Stralingsdosimetrie, subcommissie Brachytherapie, 1989, " Aanbevelingen voor dosimetrie en kwaliteitscontrole van radioactieve bronnen bij brachytherapie."
- ³⁰Portal G., " Review of the principal materials available for thermoluminescent dosimetry." RADIATION PROTECTION DOSIMETRY, Vol. 17, p. 351-357, 1986.
- ³¹Thomason C., Higgins P., " Radial dose distribution of ¹⁹²Ir and ¹³⁷Cs seed sources." MED. PHYS., Vol. 16, No.2, p. 254-257, 1989.
- ³²Thomason C., Higgins P., " Reply to comments of Meli, Meigooni and Nath." MED. PHYS., Vol. 16, No.5, p. 825, 1989.

- ³³Valicenti R.K., Kirov A.S., Meigooni A.S., Mishra V., Das R.K., Williamson J.F., " Experimental validation of Monte Carlo dose calculations about a high-intensity Ir-192 source for pulsed dose-rate brachytherapy." MED. PHYS., Vol. 22, No.6, p. 821-829, 1995.
- ³⁴Van Dam J., Marinello G., " Methods for in vivo dosimetry in external radiotherapy." Physics for clinical radiotherapy, Booklet No.1, ESTRO 1994.
- ³⁵Williamson J.F., Li Z., " Monte Carlo aided dosimetry of the microselectron pulsed and high dose-rate Ir¹⁹² sources." MED. PHYS., Vol. 22, No.6, p. 809-819, 1995.



FILM DOSIMETRY IN CONFORMAL RADIOTHERAPY

BE9700030

Claudia Danciu, Basil S. Proimos

Department of Medical Physics, University of Patras, 26500 Patras, Greece

1. INTRODUCTION

More than half of cancer patients are treated by Radiotherapy.

Deep seated tumours are usually irradiated by external photon beams ("Teletherapy"). Therefore, obtaining the dose distribution in the patient is of great importance.

The dose distribution can be experimentally derived through dosimetric measurements in a "phantom", which simulates in shape, size and consistency the important part of the patient's body.

Film dosimetry offers a relatively fast, easy, accurate and inexpensive way of qualitatively seeing and quantitatively deriving the dose distribution in any cross section of a solid phantom, provided that the film is:

- a. "slow", reaching a "density" of about 3, even for therapeutic doses of about 200 cGy
- b. independent of the energy spectrum of the photons attacking each point of the film.

This investigation aims to:

- a. identify "slow" films
- b. derive the film's response (density versus dose curve) for most of the photon beams used in Radiotherapy (Cobalt-60, 6 MV, 15 MV and 45 MV).

2. MATERIALS

2.1. Films

The industrial films "Structurix" of Agfa-Gevaert and "X-Omat V" of Kodak are two of the most frequently used films for field verification in Teletherapy. For this, they are readily available and inexpensive.

The first ("Structurix") was found to be too fast (too sensitive) for our purpose.

The second ("X Omat-V") reaches a density between 2.8 and 3.5 for 200 cGy, delivered by any of the above four different beams. Consequently, the Kodak "X Omat-V" film was finally chosen.

2.2. Phantom

“Hardboard” or “masonite-presdwood” is an inexpensive material made of compressed by-products of wood. It has a density of about 1 g/cm^3 and an effective atomic number of about 7.

For this, free leaves of 38x38 cm and 3 mm in thickness, were used as absorbers. About one hundred such horizontal leaves were superimposed to each other, with horizontal film strips interplaced at six depths of the so formed “stack”.

2.3. Instruments

a. A “PTW” dosimeter connected to a cylindrical ionisation chamber, with 6 mm in external diameter and 0.1 cm^3 in volume, was used in a plexiglas slab 30x30x1 cm in dimensions.

b. A densitometer “Densoquick Pehamed” was used for measuring the density of the films.

2.4. Machines

The following units were used:

a. The Cobalt-60 unit, called “Alcyon”, made by “General Electric” and installed in the “Cancer Hospital-Metaxa” of Piraeus.

b. The 6 MV Linear Accelerator, built by Philips and installed in the “University Hospital” of Patras.

c. The 15 MV Linear Accelerator, called “SL 18”, made by Philips and installed in the “Anticancer Hospital, Saint Savas” of Athens.

d. The 45 MV Betatron, built by Brown Boveri Company. and installed in the “Anticancer Hospital, Saint Savas” of Athens,

3. PROCEDURE AND RESULTS

3.1. Procedures

Each “hardboard” leave of 38x38 cm was weighed. Its mass (in grams) was divided by its surface area (in cm^2). The so found area density (in g/cm^2) was written on one of its corners. By interplacing such leaves and film strips, the “stack” shown in Figure 1 was formed.

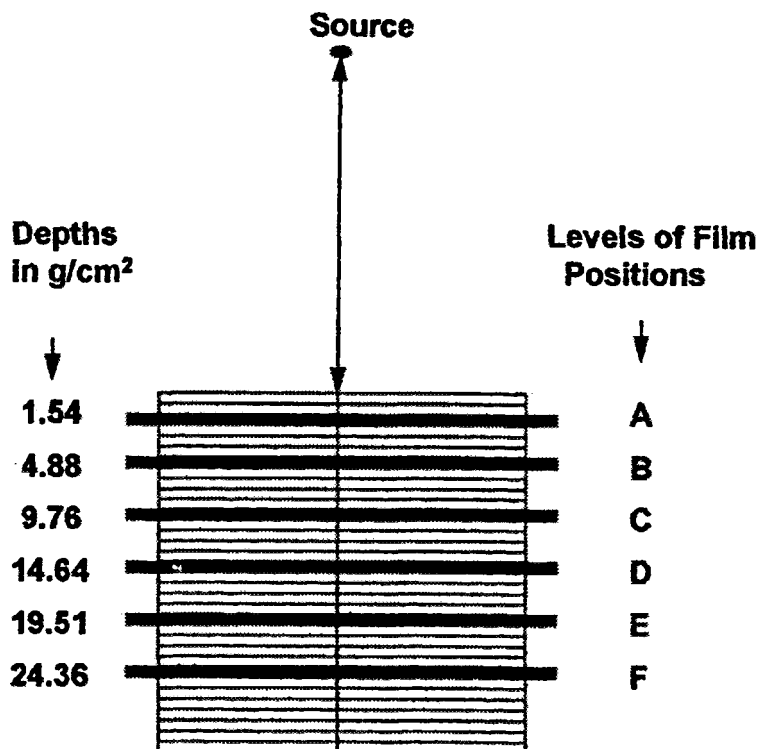


Figure 1: The experimental arrangement of the irradiation, with the film strips placed in the levels A, B, C, D, E and F between the hardboard blocks.

For all six levels (in which the films were positioned) and for each of the four different beams, the Percentage Depth Dose (PDD) was computed from the data existing in the corresponding Department. These PDD values were verified by direct measurements through the above ionisation chamber in its plexiglas plate, which was inserted at the above six levels of the stack. The central ray, of each of the four beams, was perpendicular to the upper surface of the stack. The field size was 15x15 cm at the entrance of the beam to the phantom. The distance from the source to the upper surface of the phantom was 100 cm for Cobalt-60, 6 MV and 15 MV photons beams; but it was 110 cm for the 45 MV photon beam.

During the actual exposure of the film in a transverse cross-section of the phantom, the photon beam is almost parallel to the film, while in the above arrangement (Figure 1) the beam was perpendicular to the film. To check, whether the response of the film remains independent of the relative direction of the beam with respect to the film, we have also applied the two arrangements shown in Figure 2 and Figure 3.

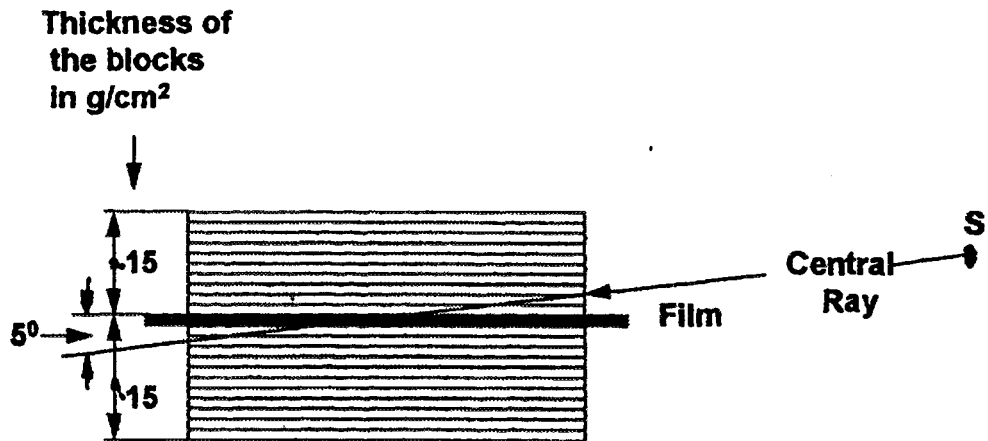


Figure 2: The film strip is placed between two blocks 15 cm thick each and the photon beam is inclined at 5° with the horizontal film. The 'SSD' was 100 cm for the 15 MV photon beam and it was 110 cm for the 45 MV photon beam.

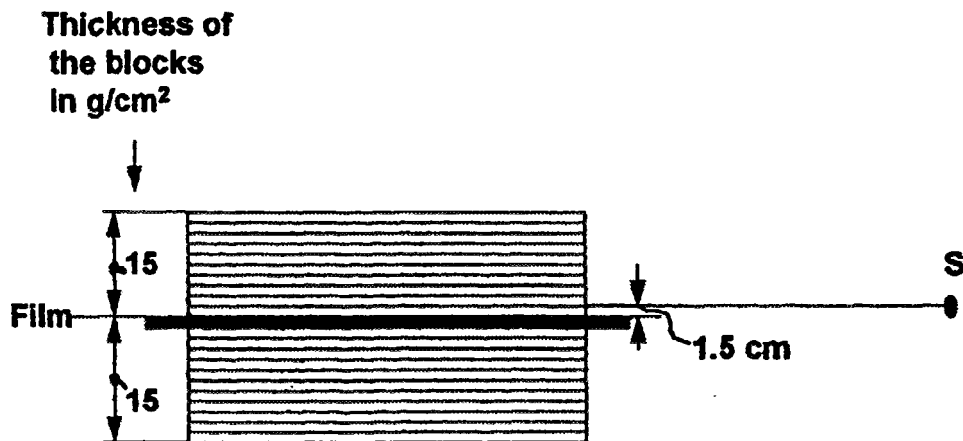


Figure 3: Experimental arrangement for exposing the film by a 45 MV photon beam. The central ray was parallel and at 1.5 cm distance from the horizontal film. The 'SSD' was 110 cm and the field size 15x15 cm.

The arrangement of Figure 2 was applied to 15 MV and 45 MV photon beams.

The arrangement of Figure 3 was applied to 45 MV photon beam, only.

3.2. Results

Following the application shown in Figure 1, the characteristic curves shown in Figures 4, 5, 6 and 7 were derived.

Obviously, for each beam the response of the film (density versus dose) is the same at all important depths (up to 25 cm) of the phantom. This means that the film response is not influenced by the change in the photon energy spectrum caused by the attenuation and the scattering of the corresponding beam in its penetration through the phantom.

The change of the characteristic response curves from beam to beam is shown in Figure 8. The 45 MV curve is not comparable to the other three curves because it was derived under different conditions (different film batch, different film processor, different temperature and time of development).

Figure 9 shows the film response for 15 MV and 45 MV photon beams at an angle of 5° with respect to the film. The density was measured along the strip at many depths from that of maximum dose to 35 cm and it was associated to the corresponding dose values.

Figure 10 shows the characteristic curve of the film , if the central ray is parallel to and at 1.5 cm from the film. The curve was again derived as in Figure 9.

By comparison of Figures 6,7, 9 and 10 we observe that there is not appreciable difference in the response of the film, even if its direction with the respect to the beam changes by 90° .

4. CONCLUSIONS

4.1. Construction and use of 'hardboard' phantoms

"Hardboard" is a good material for phantom construction because:

- a. It is more or less water (tissue) equivalent.
- b. It can be easily glued at several layers and cut by a band-saw to the shape of any transverse cross-section of the patient. The lung space can be filled with wooden-saw dust of 0.35 g/cm^3 density. This way a "phantom" consisting of a pair of two such identical slabs can be made.

c. It is inexpensive. The phantom costs usually less than the fee paid by the patient for each fraction or session of his/her treatment. For these reasons, we could use custom-made phantoms of "hardboard" in order to find the isodose patterns in many individual cases or to investigate new techniques to be applied, using film dosimetry.

4.2. Film dosimetry

Film dosimetry, in association with "hardboard" or other solid phantoms, provides a fast, accurate and easy way of obtaining the dose distribution in any cross-section, provided the film response is independent of photon energy.

Film dosimetry using the "X-Omat V" film of Kodak presents the following advantages:

- a. Including its paper cover, it forms a thin layer which can be easily inserted in any transverse cross-section of a solid phantom.
- b. It can be easily developed in an automatic processor, to give immediately an optical qualitative idea (picture) of the dose distribution, through the distribution of its "density" (blackness)
- c. It is "slow" reaching a density of about 3 for a dose of 200 cGy
- d. Its response at each point depends only on the dose absorbed at that point. Therefore, it can be easily calibrated (density versus dose curve) through a film strip exposed in the phantom by a stationary beam parallel to the film. This way, the desired dose and its distribution in the corresponding cross-section is found for any of the ordinary photon beams (Co-60 to 45 MV).
- e. In any technique (multiple stationary or rotational fields) the beam passes through the patient in different directions. Often the entrance of one field into the patient, coincides geometrically with the exit of an opposite field. Especially, in 360° rotational therapy, each and every point of the transverse cross-section gets into the rotating beam at least twice in every full rotation of the beam. For this reason, the average energy spectrum of the photons is not so different from point to point as it would be, if only one stationary field was applied. Therefore, even if the response of the film presented small differences at different depths for stationary fields, this film could still be used for dosimetry in rotational therapy.

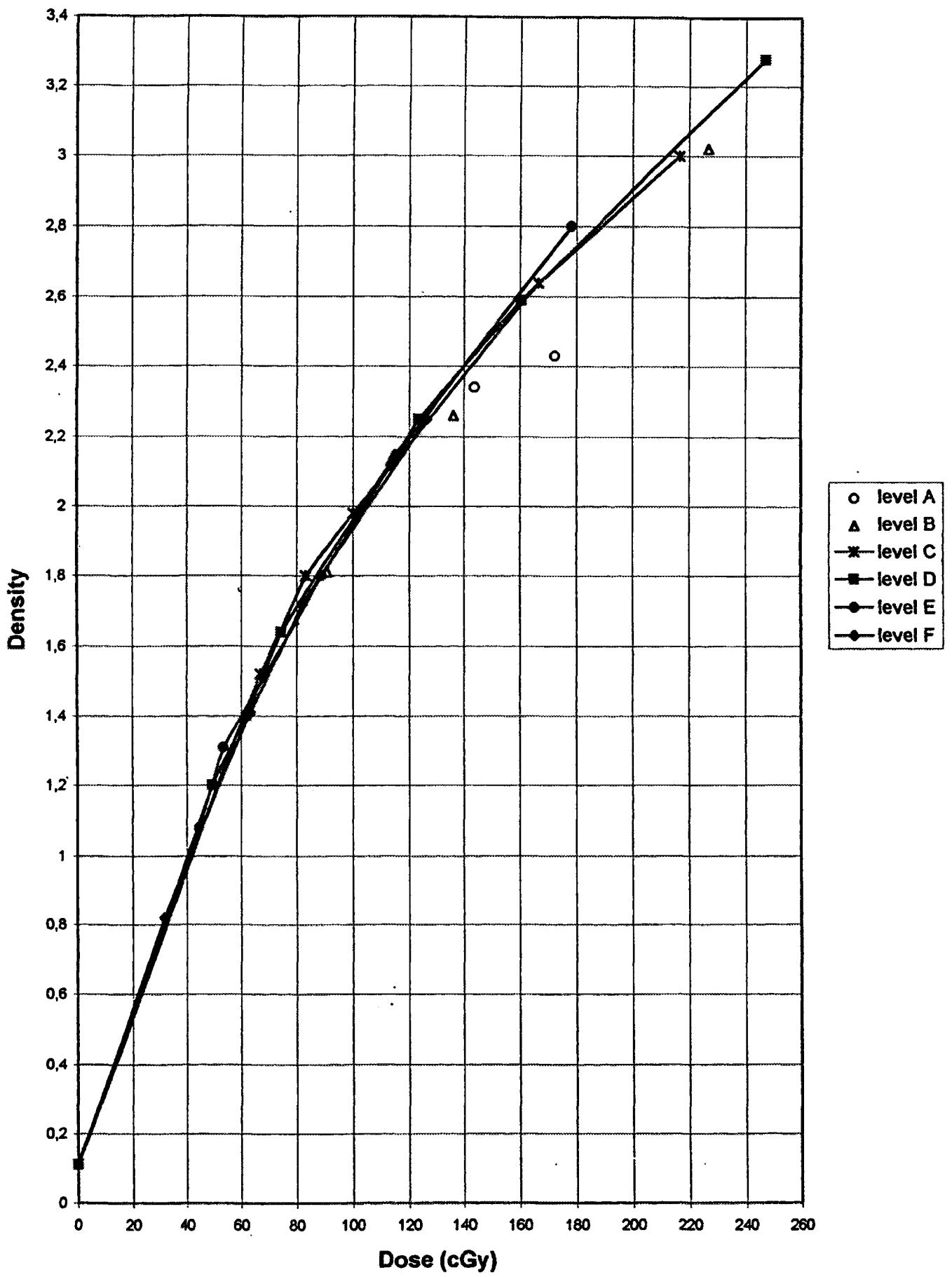


Figure 4: The characteristic curves for an "Alcyon" Cobalt-60 unit.

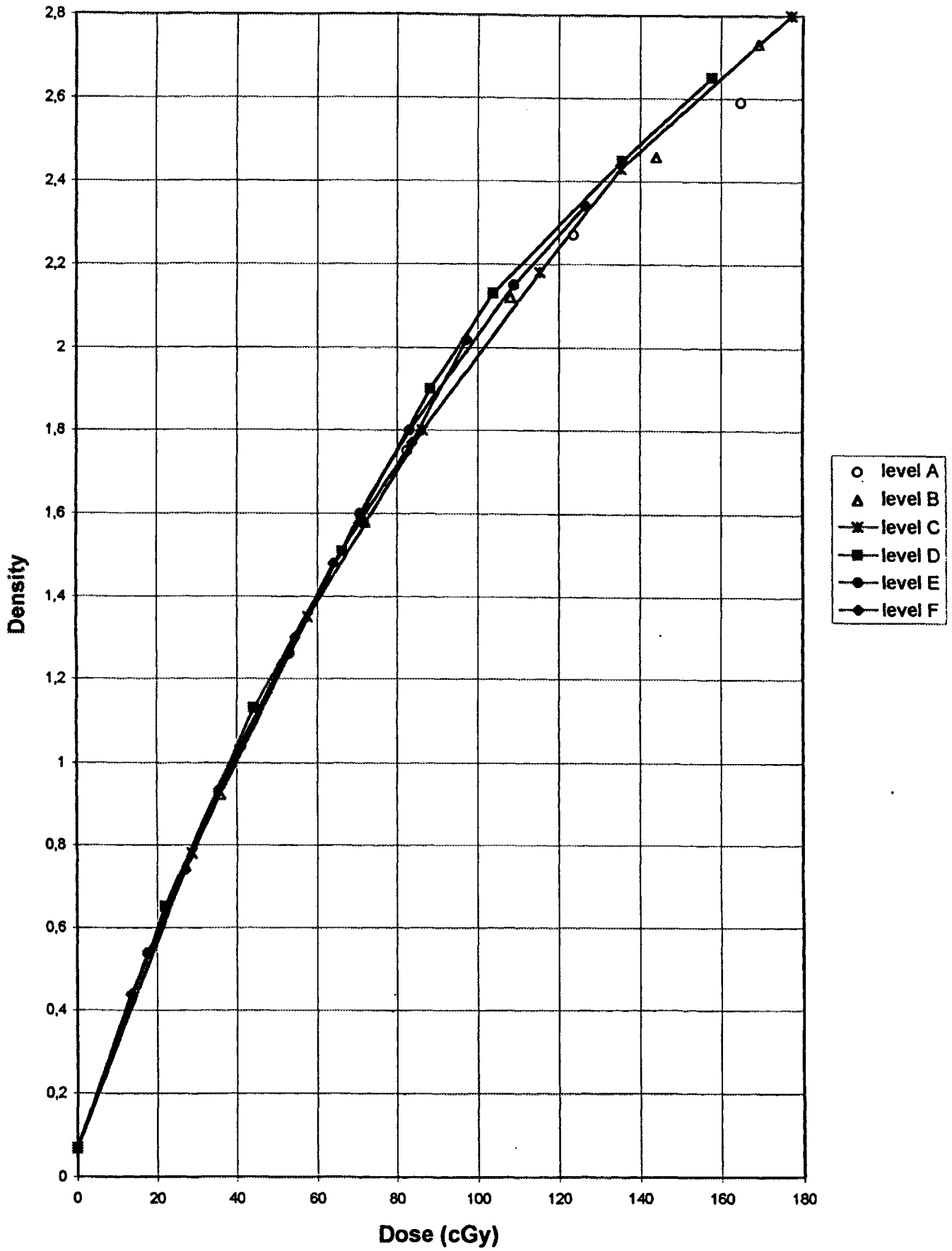


Figure 5: The characteristic curves for a Linac "RX" of 6 MV photon beam.

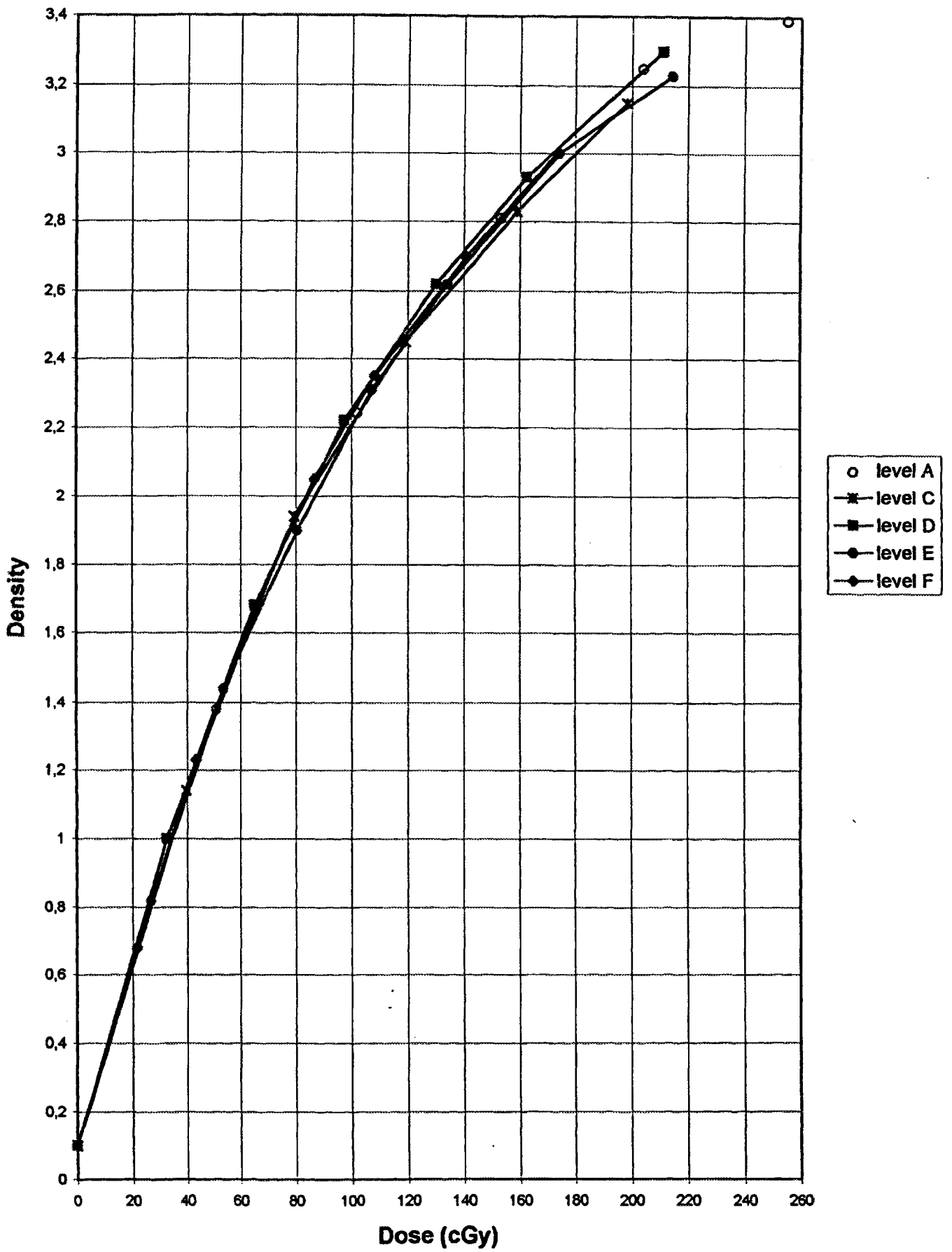


Figure 6: The characteristic curves for a Linac "SL" of 15 MV photon beam.

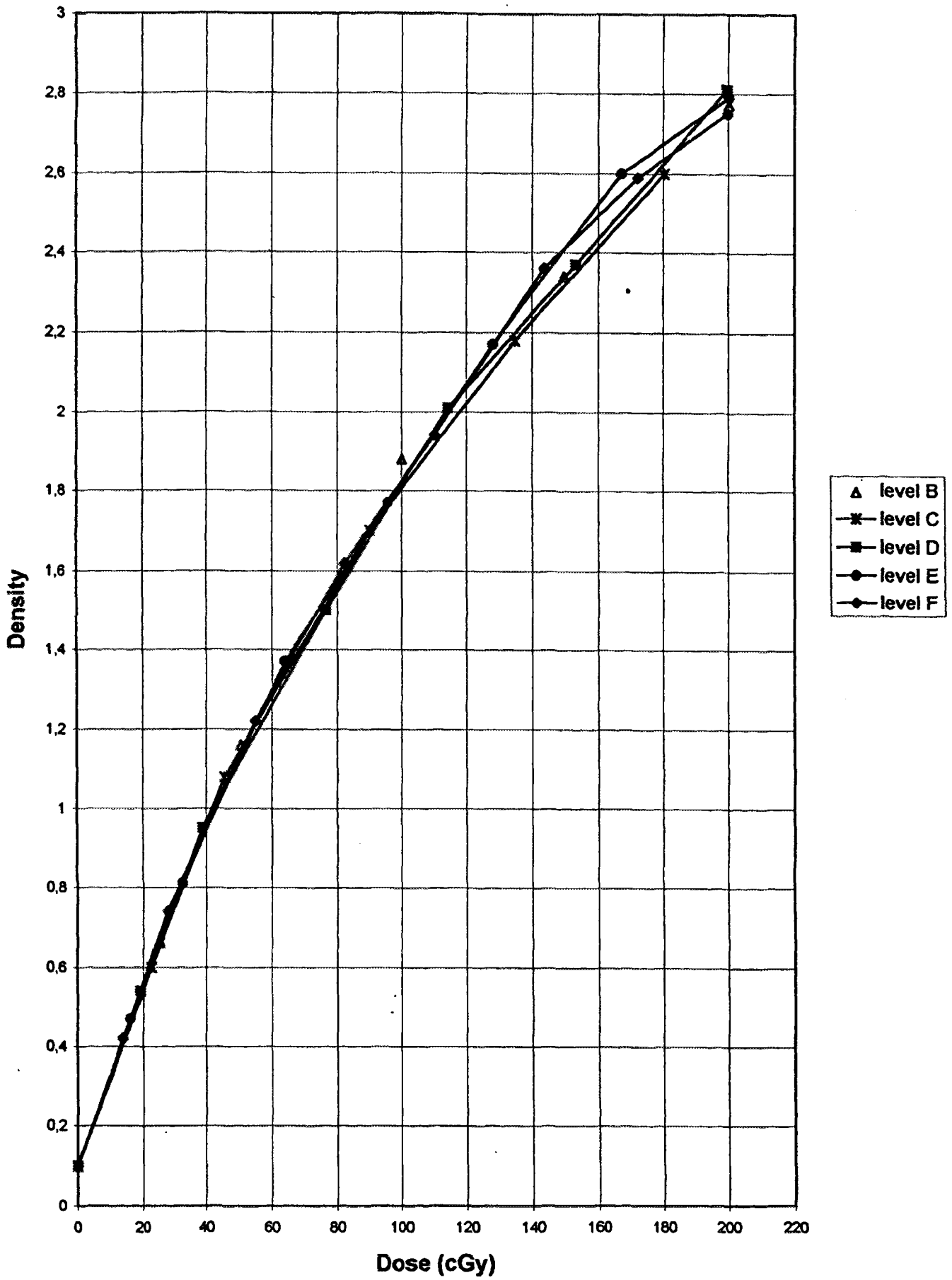


Figure 7: The characteristic curves for a Betatron of 45 MV photon beam

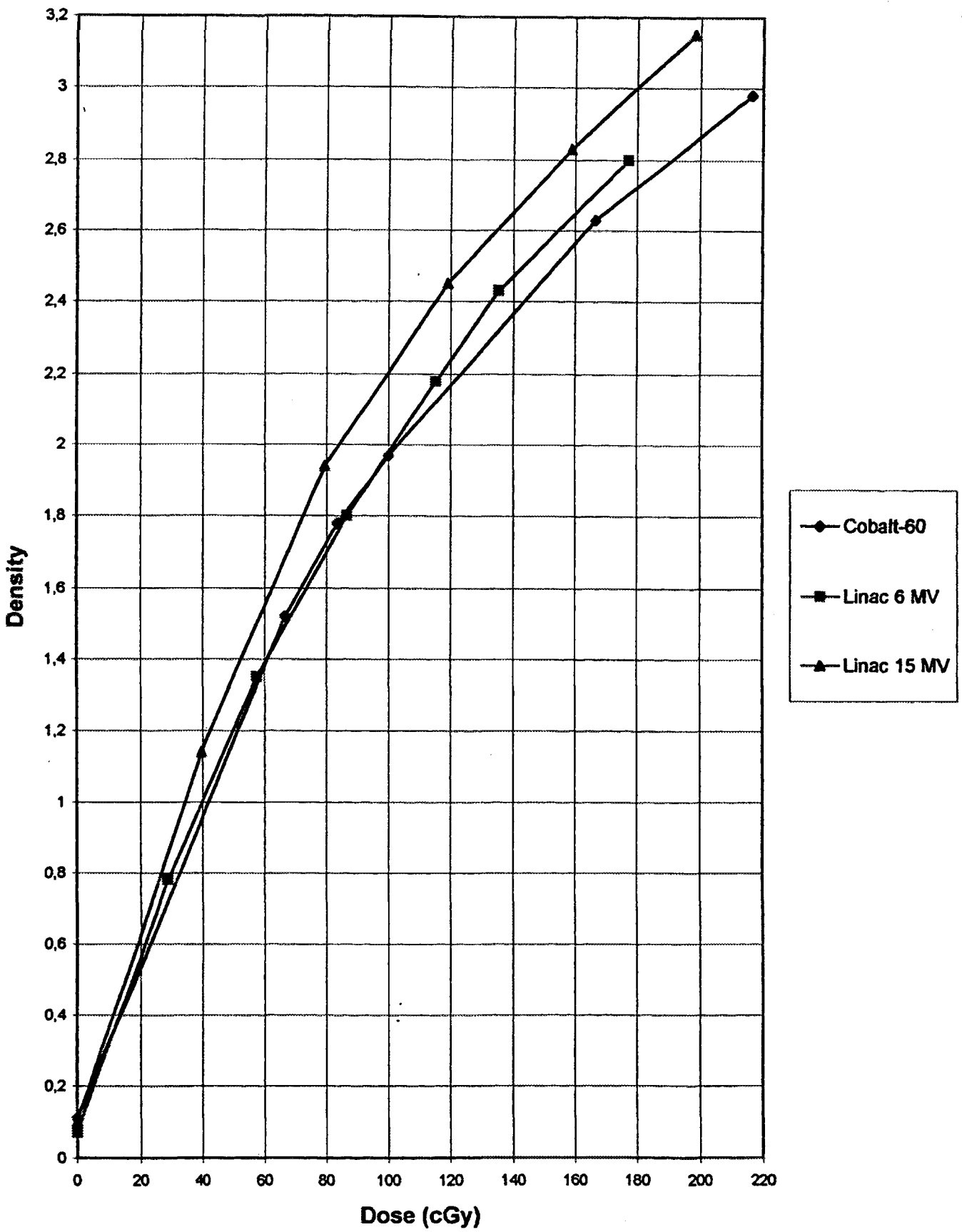


Figure 8: Comparison of the characteristic curves for a Cobalt-60, a Linac 6 MV and a Linac 15 MV photon beams and for a depth of 9.76 g/cm²

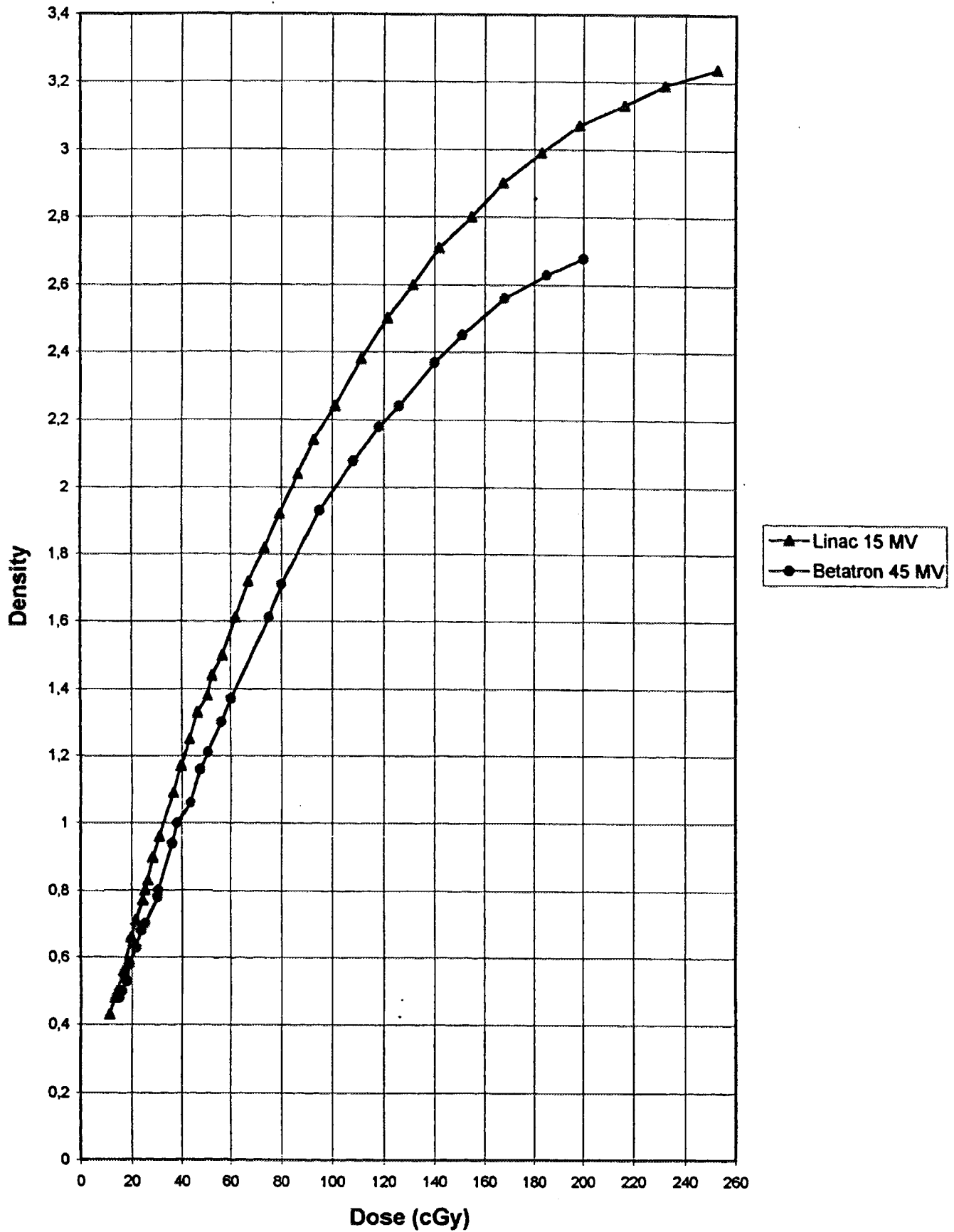


Figure 9: The characteristic curves derived from one film strip each. The photon beam was inclined at 5° with the horizontal plane of the film, for 15 MV Linac and 45 MV Betatron

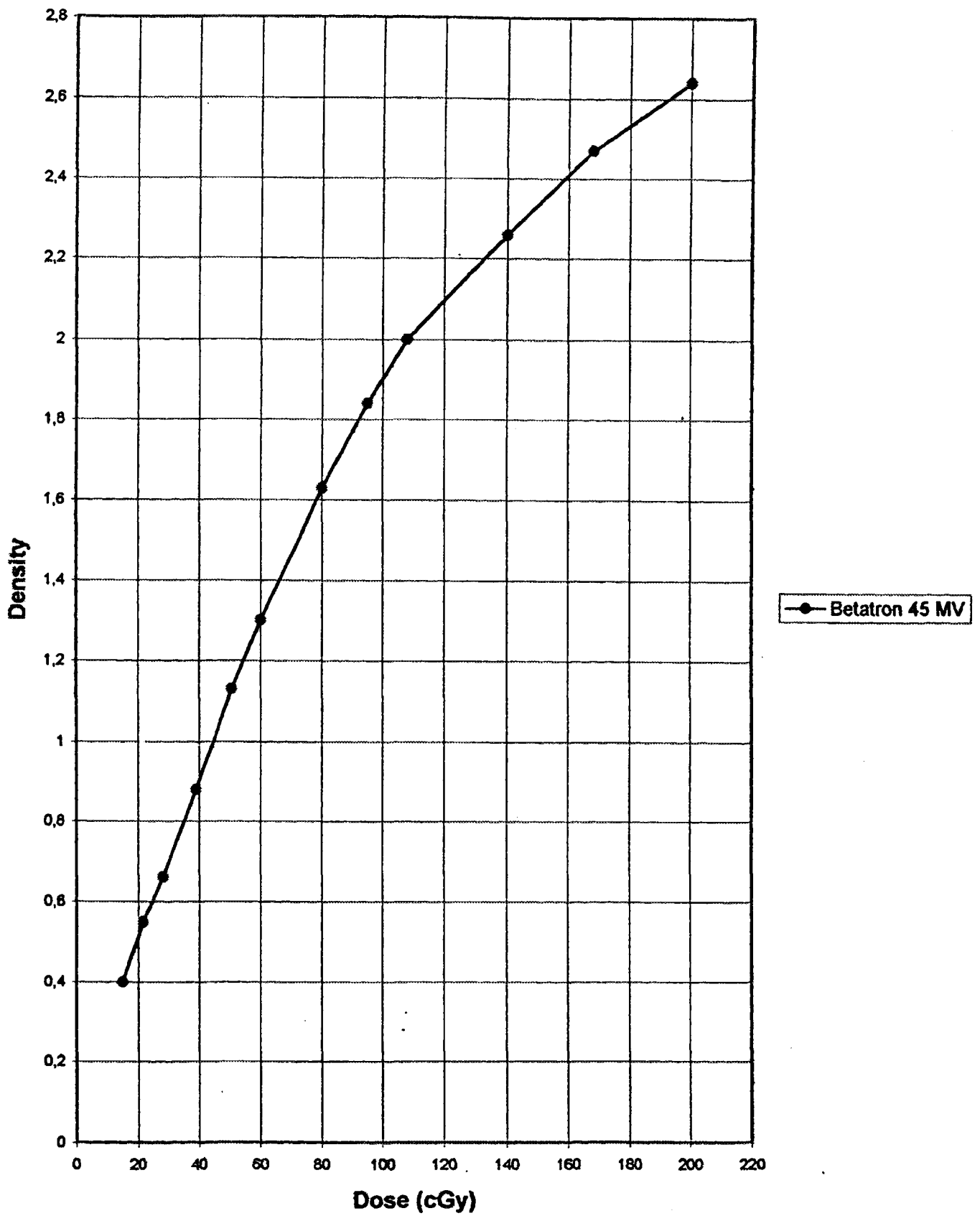


Figure 10: The characteristic curve of the film with the central ray parallel to and at 1.5 cm distance from the film, for the Betatron 45 MV photon beam

References:

1. Harold E. Johns, John Robert Cunningham, *The physics of Radiology*, Springfield, Illinois, U.S.A, 1983
2. Faiz M. Khan, *The Physics of Radiation Therapy*, Baltimore, London, U.K. 1984
3. Basil S. Proimos, Anthony G. Perris, *Dosimetry Using "Kodak RP/V2" Film in "Presdwood" Phantoms for Cobalt-60 and 45 MV Beams*, International Congress of Radiology, Rio de Janeiro, Brasil, 1977
4. Ebert-M, Kron-T, *Portal Films for Relative Exit Dose Determinations*, J. Australas-Phys-Eng. - Sci-Med., 17(2),71-8, 1994
5. Van-Bree-NA, Idzes-MH, Huizenga-H, Mijnheer-BJ, *Film Dosimetry for Radiotherapy Treatment Planning Verification of a 6 MV Tangential Breast Irradiation*, J. Radiotherapy-Oncology, 31(3), 251-5, 1994



Three Dimensional Gel Dosimetry by use of Nuclear Magnetic Resonance Imaging (MRI)

Y. De Deene², C. De Wagter², J. De Poorter¹, B. Van Duyse², W. De Neve², H. Van Hecke², A. Ravier² and E. Achten¹

¹Dept. of Magnetic Resonance - University Hospital of Gent

²Dept. of Radiotherapy and Nuclear Medicine - University Hospital of Gent

BE9700031

1. Introduction

In a previous study we discussed the application of gel dosimeters in the determination of three dimensional dose distributions¹. Two kinds of dosimeters were proposed. We focused mainly on the Fricke gel dosimeter. Special attention was paid on the major disadvantage of these gels. The ferric and ferrous ions may diffuse in the gel. As such a lack of spatial accuracy can be observed.

A second kind of gel is the polymer-gel. The BANG²-gel is composed of the comonomers *N,N'*-methylenebisacrylamide and acrylamide. The BANG-gel is bubbled with nitrogen to expel oxygen and the gelmatrix is formed by gelatine. This kind of gel performs a more stable behaviour than the Fricke gel dosimeter.

The dose-response was measured for different sets of test tubes. Depth dose profiles were performed and compared with PDD-curves. The dependence of the dose-response on temperature was observed.

The gel dosimeter was used in three different clinical applications and compared with planning and the outcome of other dosimetry techniques.

2. Materials and methods

2.1. The comonomers

(3% (w/w) acrylamide, 3 % (w/w) *N,N'*-methylenebisacrylamide)

Acrylamide and *N,N'*-methylenebisacrylamide are dissolved in a gel composed of gelatine and water. Both monomers were obtained from Sigma-Aldrich and were of electrophoresis grade. By irradiation, the comonomers are polymerized to polyacrylamide (Figure 1). Because of the presence of the cross-linking agent, *N,N'*-methylenebisacrylamide, three dimensional polymer networks must be formed. It is supposed that the three dimensional polymer networks consist of small spherical aggregates³. The higher the deposited radiation dose, the larger the number of three dimensional polymer aggregates that are formed. The small polymer aggregates are not able to diffuse through the gel matrix. The chemical propagation reaction only takes place very locally at the site of initiation.

This must result in a proportional behaviour between the T2 relaxivity and the radiation dose.

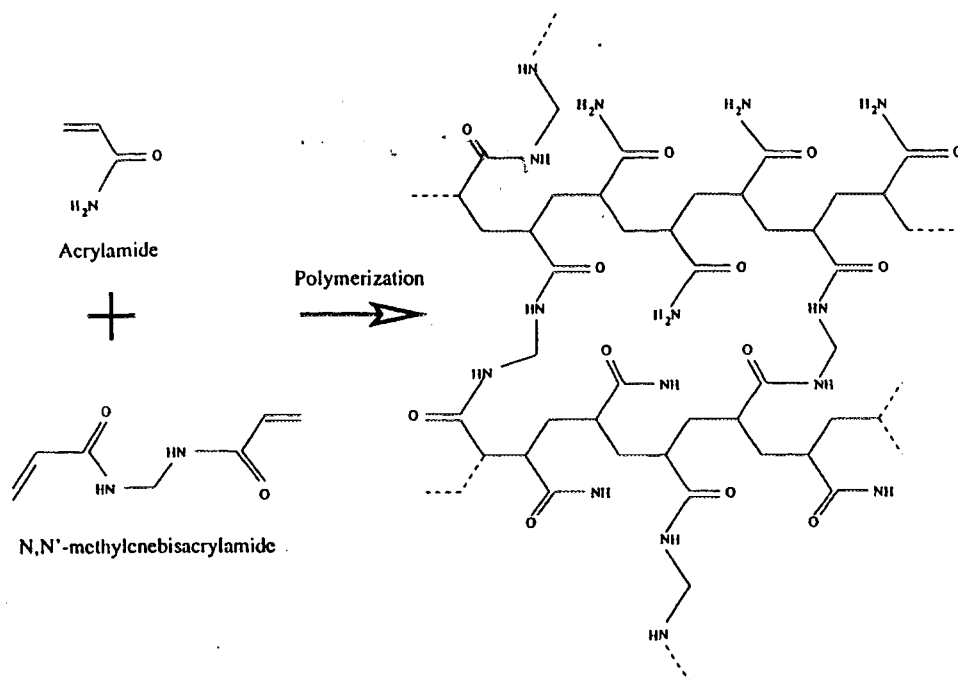


Fig. 1. The polymerization reaction of the monomers through irradiation

2.2. The gelatine (6 % (w/w) gelatine)

Gelatine was fabricated by Systems Bio-industries BENELUX and was obtained from animal skin tissue by partial hydrolysis of collagen. It contains all human amino-acids with the exception of tryptophan (Figure 2). The molecular weight of the gelatine co-polymers lies between 10.000 and 100.000 Dalton⁴. The gelatine has two functions. At first the gelatine network must hold the resulting polymer aggregates that are formed after irradiation. The mesh of the gelatine polymer network must be smaller than the polymer aggregates. Secondly, the T2-value of gelatine is large compared to the T2-value of sacharide gels such as agarose or pectin. The major advantage is that the measuring range in R2-values is larger and thus a higher signal-to-noise ratio is achieved in the R2-images.

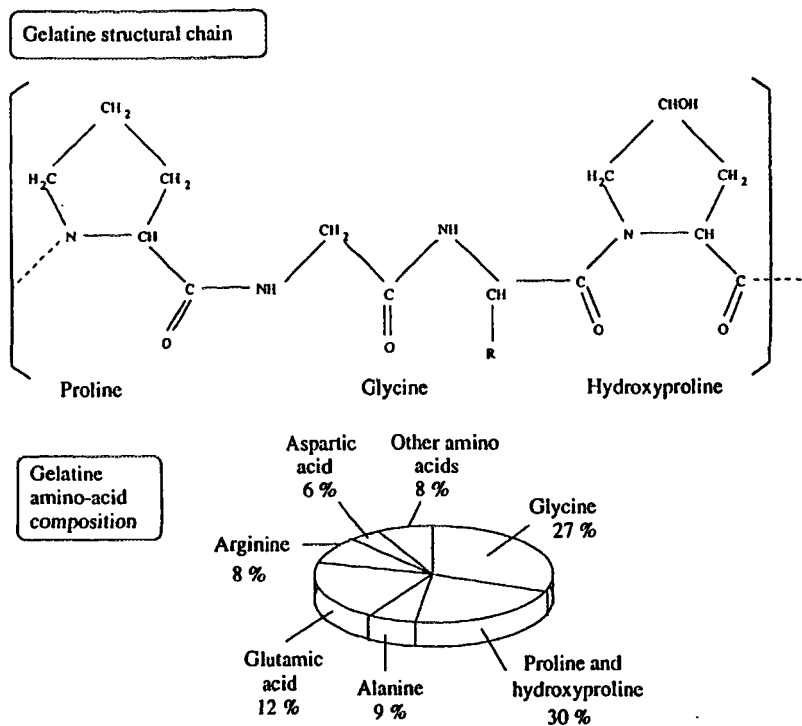


Fig.2. Chemical structure and components of gelatine

2.3. The manufacturing

The amount of water was divided up in two equal amounts (Figure 3). The monomers were dissolved in the first part. To dissolve the cross-linking agent the solution must be heated to about 50 degrees of Celsius. The gelatine was dissolved in cold water in which the gelatine was able to swell. After the swelling of the gelatine particles the gelatine solution was heated to 45 degrees Celsius. As such the gel-to-sol transition of the gel was obtained. The two solutions were bubbled by nitrogen to expel oxygen. After heating both solutions, the solutions were cooled down to 30 degrees Celsius. Then the solutions were mixed and the remaining solution was bubbled by nitrogen again. All processing steps were completed in one set-up equipped with airtight recipients, temperature and oxygen meters and pumps (Figure 4). The final gel was pumped over to the humanoid phantom recipient. This recipient was composed of PVC plate. The filling of the humanoid phantom was performed in a nitrogen atmosphere. The filled phantom was placed in a refrigerator in which nitrogen was flushed. The oxygen concentration was controlled by use of an oxygen measuring indicator.

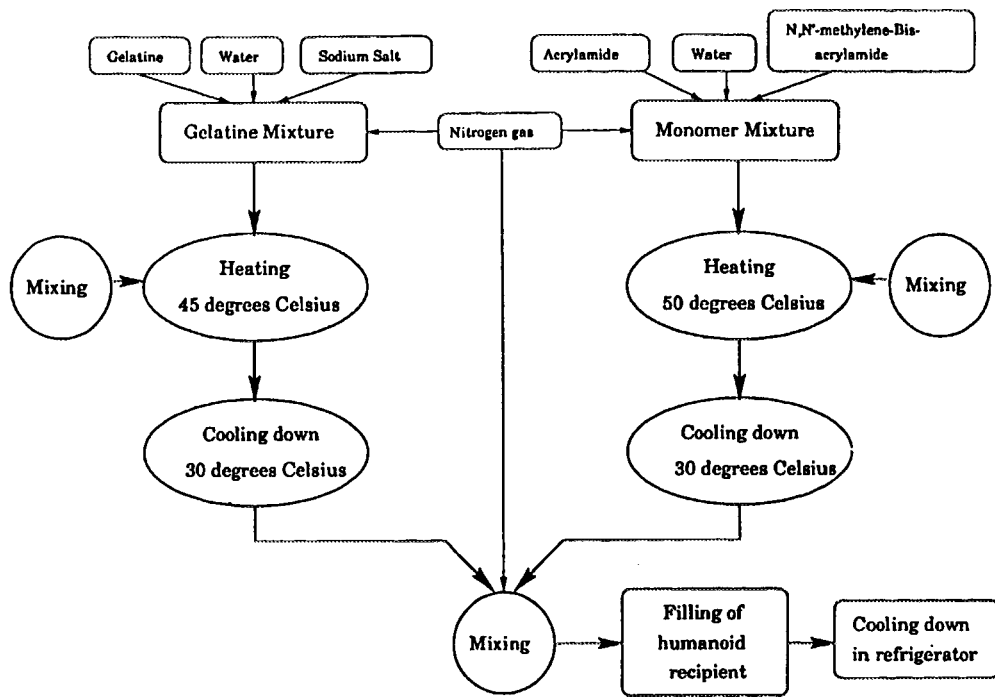


Fig. 3. Functional scheme of the manufacturing of the BANG dosimeter gel

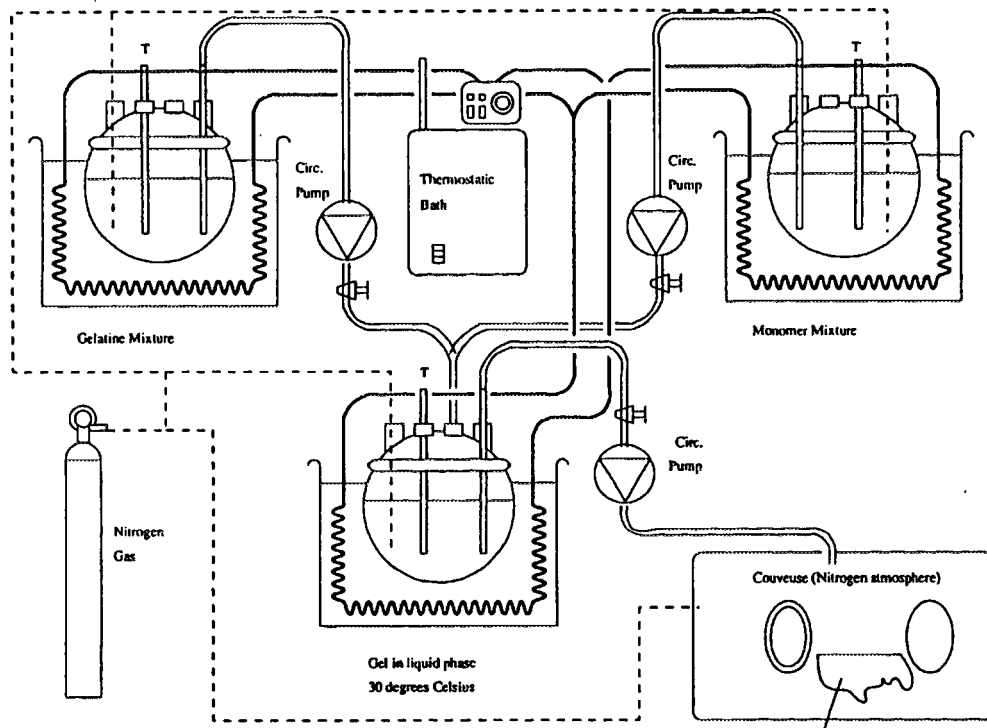


Fig. 4. Laboratory set-up for manufacturing of the BANG dosimeter gel

2.4. The irradiation

The dosimeter gels were irradiated isocentrically by a 6 MV photon beam produced by a linear accelerator type Philips SL75-5, with a dose rate of about 360 cGy/min. The gels were exposed to a maximum dose of about 10 Gy. In one case the radiation was done by beam intensity arc therapy.

2.5. The MR-scanning

The gels were scanned on a Siemens 1.5T clinical MR-scanner. A spin echo sequence performing 32 echoes was used. The echoes were equally separated by 50 ms. CPMG encoding was done to compensate for multiple stimulated echoes. A repetition time of 5 seconds was used to ensure total T1 relaxation for each phase line. The total measurement time for a relaxivity image was 42 minutes.

2.6. The post processing

The set of 32 different T2-weighted images was transferred to a DECstation 5000/200 on which the resulting R2-images were calculated by exponential fitting through the Levenberg-Marquardt algorithm⁵. The relaxation time and the magnetization density were fitted on a pixel-by-pixel basis. After rescaling of the relaxivity images based on the dose response relation, dose images were obtained. The dose response relation was obtained by test tubes irradiated at different doses. A second method is to compare the relaxivity images with dose maps of the same region but obtained by other independent dosimetry techniques such as thermo luminescent dosimeters (TLD's) or film dosimetry. All other calculations were performed on the same DECstation.

3. Results

3.1. The dose response relation

The dose response relation was determined by irradiating test tubes filled with the BANG dosimeter gel at several doses. During irradiation the tubes were placed in a cubic water phantom (22 cm x 22 cm x 22 cm) used for daily dose verification by use of an ionization chamber. The test tubes were irradiated at the calibration depth of 5 cm. After irradiation, the tubes were placed in a cylindrical recipient through which water is pumped (Figure 5) that was cooled or heated by a thermostatic bath.

The cylindrical recipient containing the test tubes was positioned in the MR scanner and the 32 differently T2-weighted images were recorded.

The temperature in the test tubes was measured during the recording of the images.

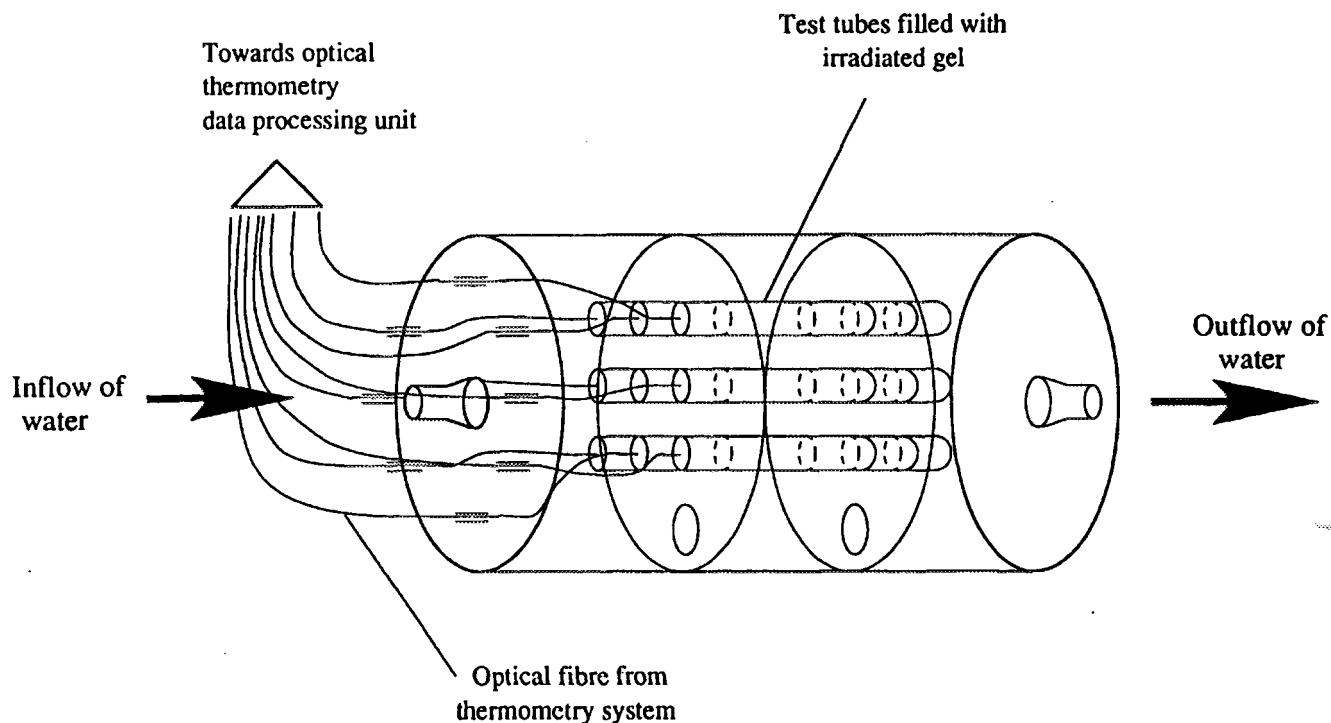


Fig. 5. Measurement set-up for measuring at different temperatures

A linear response was found between the spin-spin relaxation and the irradiation dose (Figure 6a). However this dose response relationship shows a clear dependence on the measuring temperature. We found a linear dependence between the temperature and the slope of the dose response curves in the temperature range of 6.5 degrees to 25 degrees Celsius (Figure 6b). Also the intercept of the dose response curves is linear dependant on temperature in that temperature interval (Figure 6c). This temperature dependence is in correspondence with the theoretical behaviour as predicted by the Bloembergen-Purcell-Pound theory of nuclear spin relaxation in liquids and the Stokes relationship between viscosity and the rotational correlation time⁶ in the presumed temperature interval.

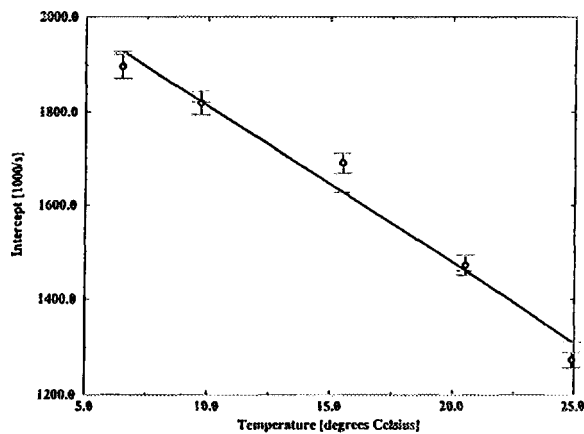
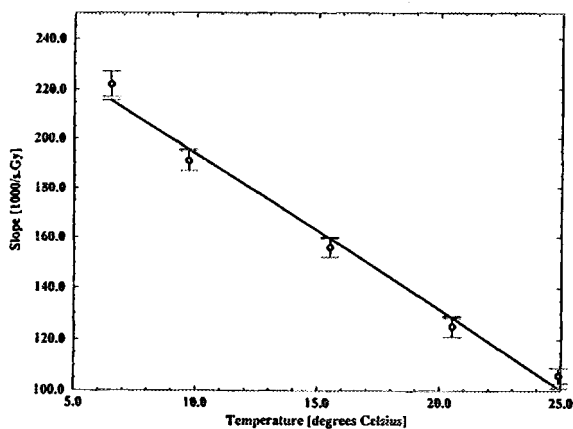
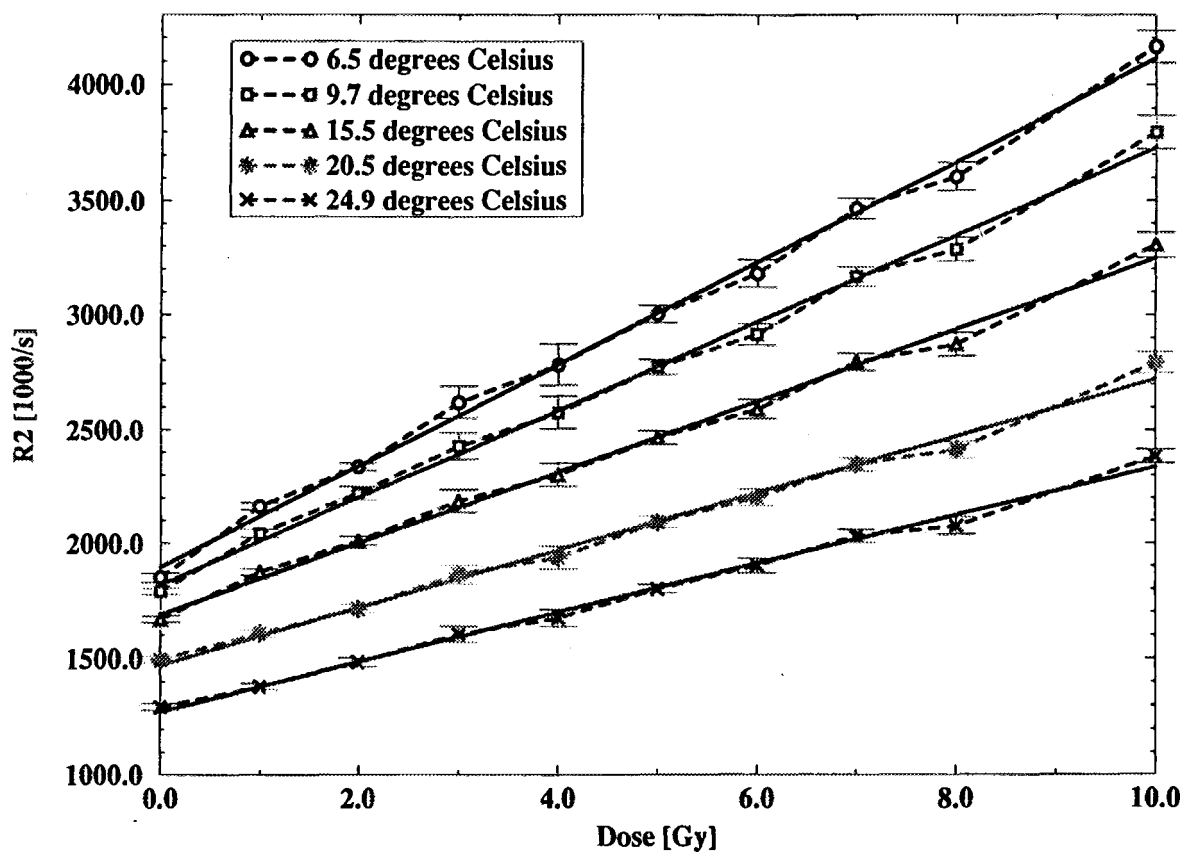


Fig. 6. (a) Dose-R2 curve at different measuring temperatures.
 (b) Temperature dependence of the slope in the dose-R2 curve
 (c) Temperature dependence of the intercept in the dose-R2 curve

3.2. Depth dose curves

Two different radiation beams were given at the same erlenmeyerflask filled

with dosimeter gel. The first beam was a 6 MV photon beam. The second one was a superficial 50 kV photon beam. (Figure 7)

The MR images were acquired using the standard RF head coil. The field of view was 150 mm for the lateral view and 120 mm for the cross-sectional view.

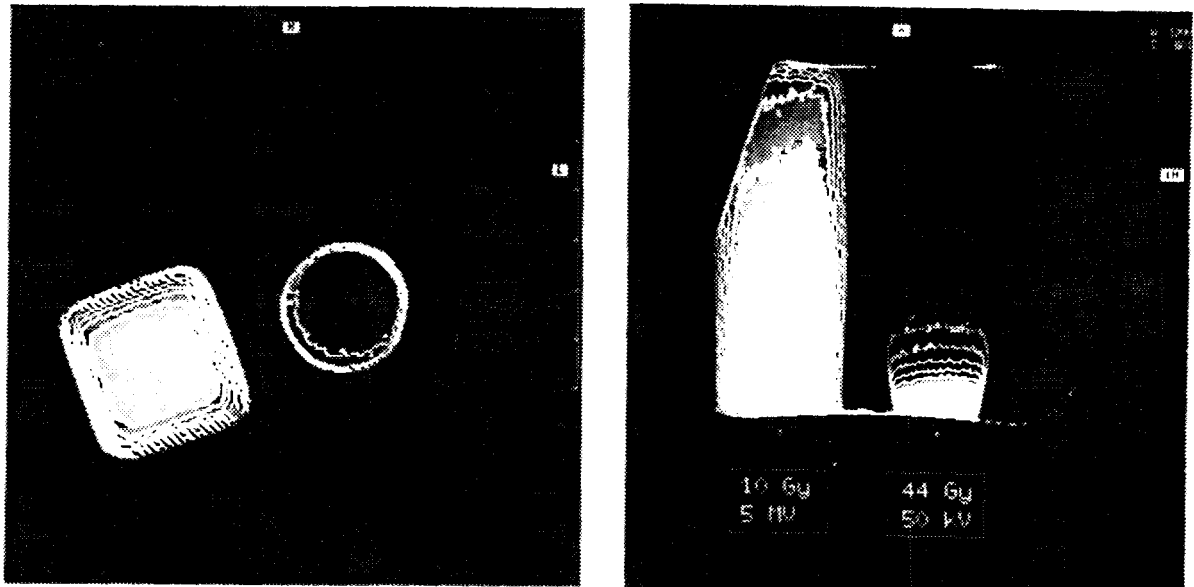


Fig. 7. Dose images of the beams after irradiating an erlenmeyer containing the BANG dosimetry gel.

(left) Image taken in a cross-sectional plane at 1 cm depth.

(right) Image taken in a plane parallel with the beam axis.

3.2.1. The 6MV photon beam

The shape of the beam was rectangular having sides of 4 cm. The maximum dose was 10 Gy. The depth dose curve was compared with the percentual depth dose curve (PDD) as recorded with an ionization chamber for the same beam configuration. The intercomparison was performed by minimization of the mean square deviation of the R2-depth-profile from the PDD. Three variables were optimized. The most evident two were the offset and scale that occur in the dose response relationship. The third variable is the distance at which the depth dose curve of the gel dosimeter starts. This value was found to be about 4 mm and is due to the part of the profile that belongs to the glass vessel and that is not seen on the MR images. (Figure 8)

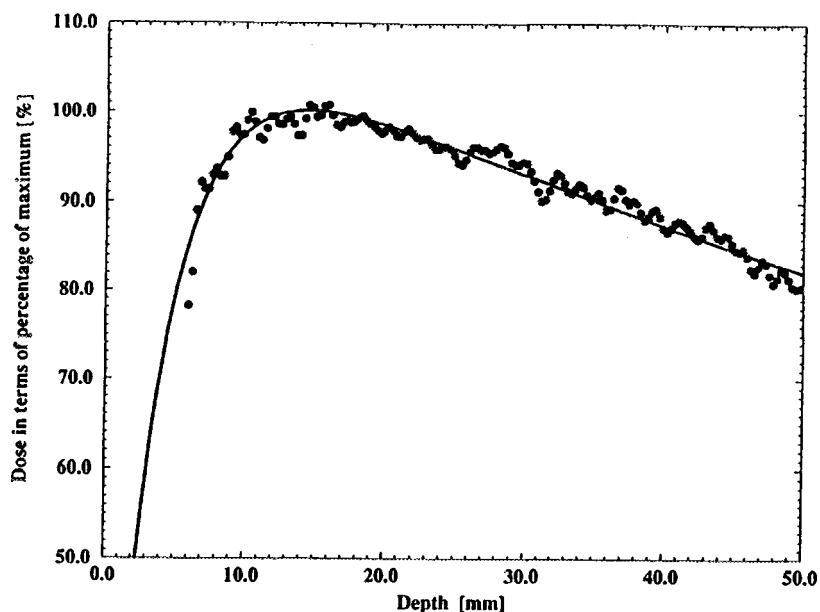


Fig. 8. Depth dose profile for a 6MV photon beam.
Circular dots represent the doses recorded by gel dosimetry.

3.2.2. The 50 kV photon beam

The homogenizing filter was made of Aluminium and had a thickness of 1 mm. The source-to-skin distance was 40 mm. The cross-section of the beam had a circular shape with a diameter of 2 cm. The ion dose of the beam was 5000 R. The depth dose curve was fitted to a mono-exponential curve and was rescaled such that the maximum of the fit was at 100%. The half value distance was found to be at 7 mm. (Figure 9)

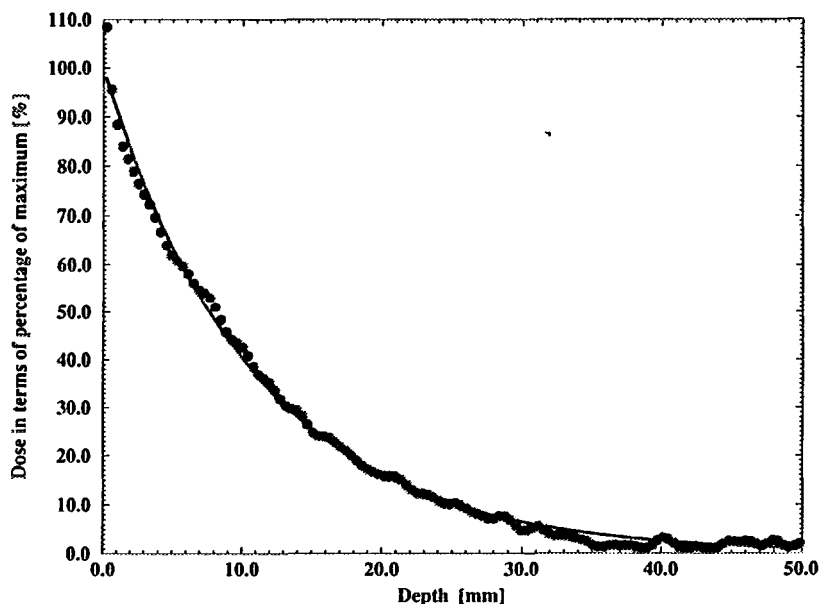


Fig. 9. Depth dose profile for a 6MV photon beam.
Circular dots represent doses as recorded by gel dosimetry.

3.3. Cross-sectional profiles

A cylindrical recipient filled with BANG dosimeter gel was irradiated by a square field having a size of 5 cm. Cross-sectional R2-images were taken at a depth of 50 mm and at a depth of 100 mm. Again, the obtained images were compared with measurements performed with a diamond detector that was scanned in the plane (Figure 10). Restricting to the main axis in the two planes we become the beamprofiles in X- and Y-direction (Figure 11). The reason that the profiles are more shaped when measured with the diamond detector must be sought in some partial volume effect. Notice that the amount of this partial volume effect is different for X- compared to Y- profiles. The fact that in all measurements the penumbra is slightly larger when measured with the dosimeter gel is due to the glasswall (where the beam impinges) that was not taken into account for the gel dosimetry. The resulting overall root mean square deviation between the two measuring techniques amounted to 3 % for the X-profiles and 5 % for the Y-profiles.

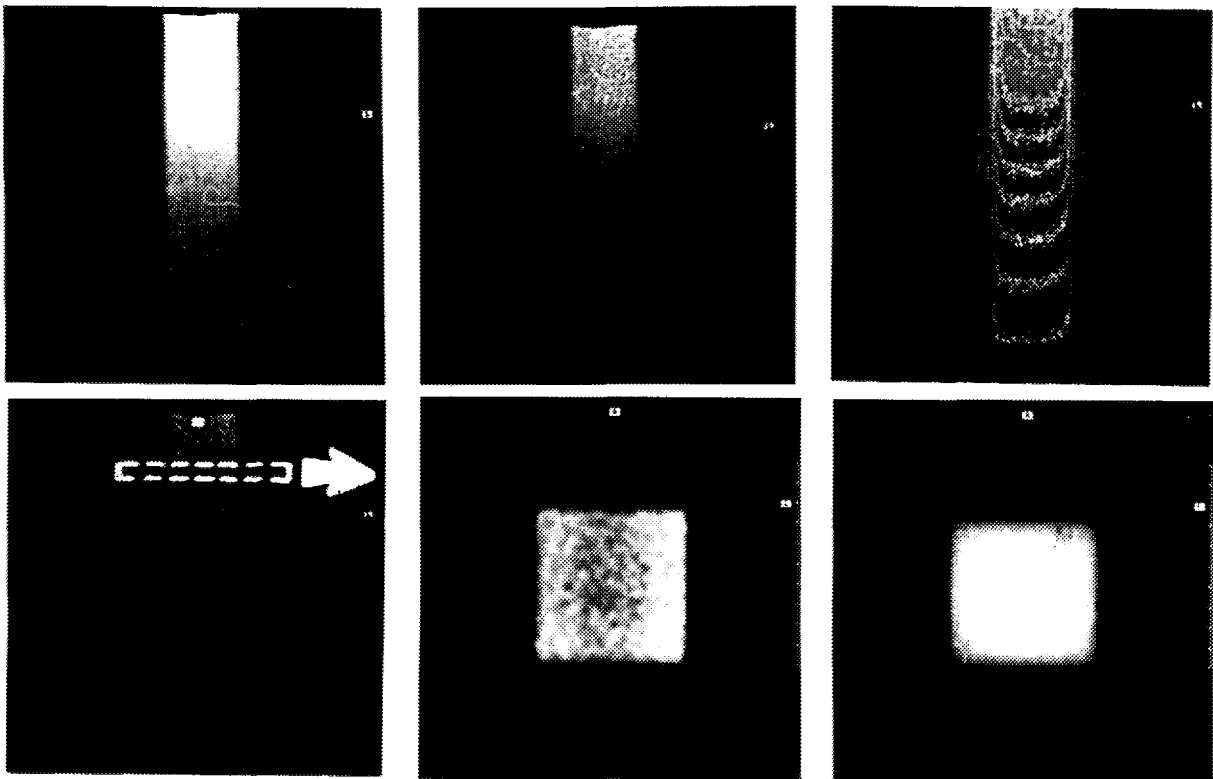


Fig. 10. (a-f) Dose related images of some planar sections.

- a. R2-image parallel to the beam axis.
- b. Corresponding dose image obtained after normalisation of (a)
- c. Image in (b) after contouring at 10 % dose intervals
- d. Image in (b) after windowing at 10 % dose intervals
Corresponding slice in (e) is indicated.
- e. Dose image derived from R2-image perpendicular to beam axis
- f. Dose image spanned by point measurements with a diamond detector

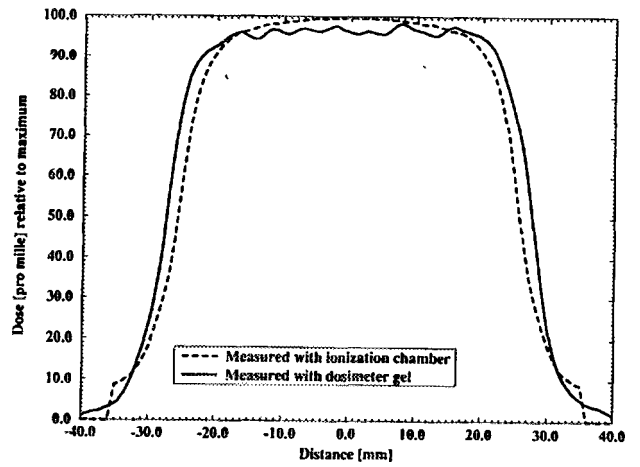
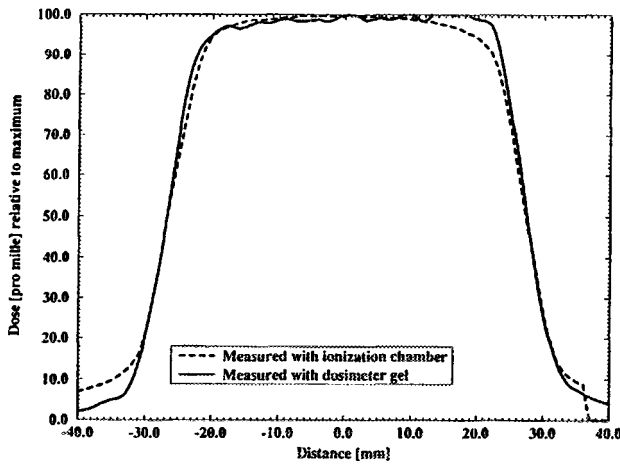
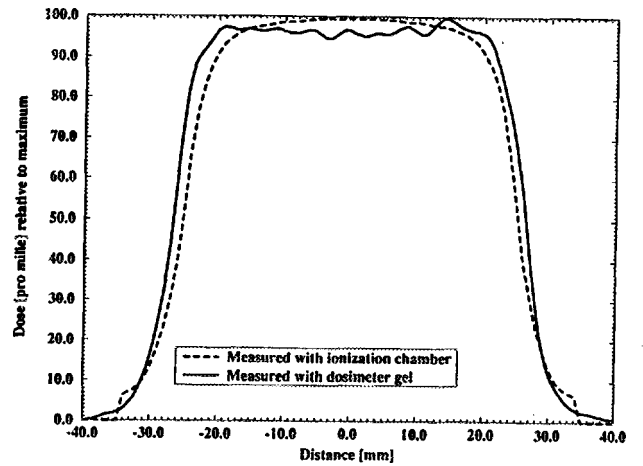
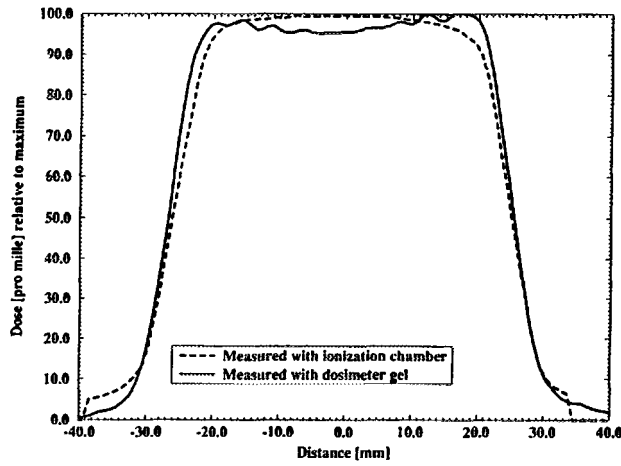


Fig. 11. Beamprofiles at two different depths in the water phantom measured by gel dosimetry and by a scanning diamond detector
 (a) Profile in X-direction at depth of 50 mm
 (b) Profile in Y-direction at depth of 50 mm
 (c) Profile in X-direction at depth of 100 mm
 (d) Profile in Y-direction at depth of 100 mm

3.4. Clinical applications in conformal radiotherapy: Treatment verification of a head and neck treatment

Common to the previously mentioned measurements is that they involved canonical beams. The advantage of these configurations is that they can be verified by other very quantitative measurements, namely by use of an ionization chamber. However, this is not the case if humanoid shapes and clinical beams are used. Until now, we treated three humanoid configurations: macular degenerations in the eye treatment, head and neck cancer and a prostate tumour. Other dosimetry techniques were used to verify the three dimensional gel dosimetry technique in humanoid phantoms. We will restrict ourselves in this abstract to the case of the head and neck tumour.

Threedimensional moulds of the Rando phantom were made in PVC. The moulds were filled with the BANG dosimeter gel and closed in a nitrogen atmosphere (Figure 12). The dosimeter gel was given the considered radiation treatment and scanned as already mentioned.

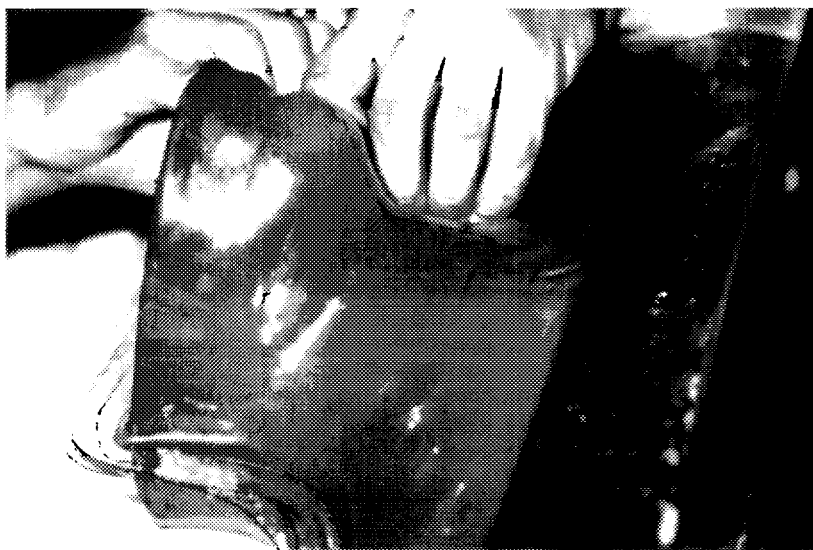


Fig. 12. *The BANG dosimeter gel for the verification of a radiotherapy treatment in the lower-neck*

CT scans were taken from the Rando phantom (Figure 13a). The scans were transferred to the computer in the planning room and a 3D-computer planning was performed by use of the GRATIS software (Figure 13b). At the places of interest, corresponding with the target and areas to spare, radiographic films and TLD's were inserted between two slices of the rando phantom (Figure 14). The response of each TLD was calibrated individually. The Rando phantom was irradiated in the same way as the dosimeter gel and as simulated by computer.

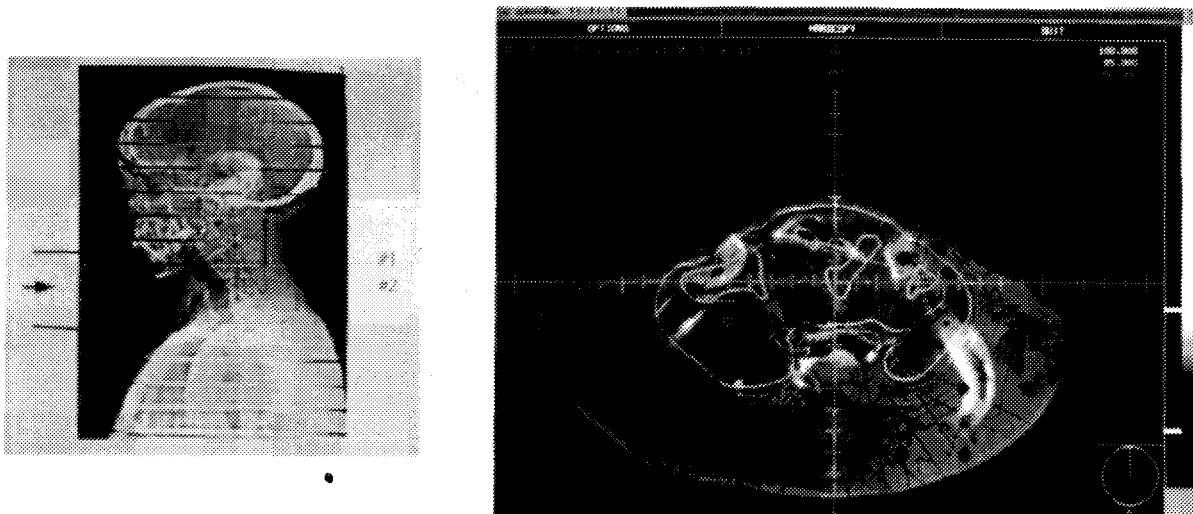
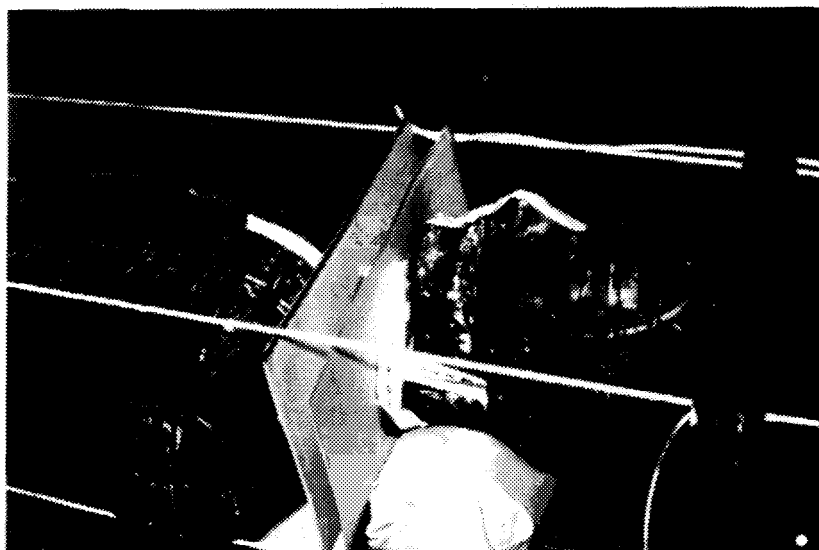


Fig. 13. CT images of the Rando phantom and computer planning



*Fig. 14. The Rando phantom positioned at the linear accelerator
(Two radiographic films and several TLD's were inserted.)*

A comparison was made between the results obtained by the three different dosimetry techniques. The doses measured by the TLD-probes were used to calibrate the other dosimetry methods (Figure 15-16). The scaling and intercept of the dose response relationship were fitted from those calibration values.

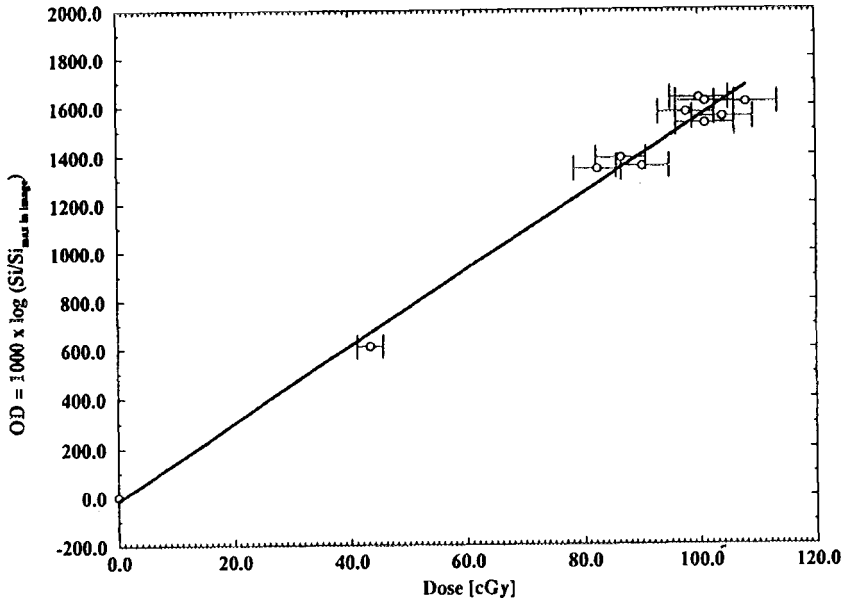


Fig. 15. Optical density versus the dose as measured by TLD's

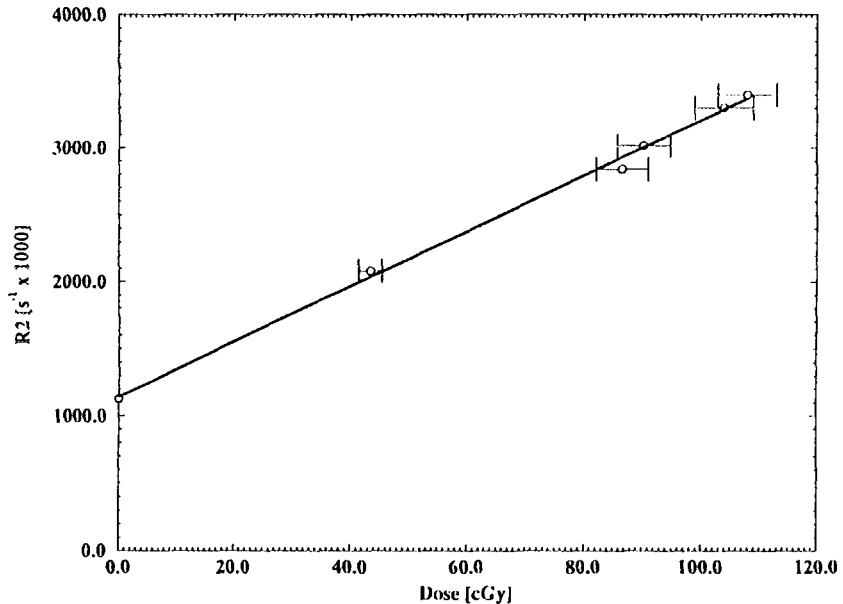


Fig. 16. R2 versus the dose as measured by TLD's in one slice

The resulting doses as obtained by use of the radiographic film and the gel dosimetry and as predicted by the computer planning were brought in the same image format. The comparison of the different dosimetry methods was done in two slices (Figure 17).

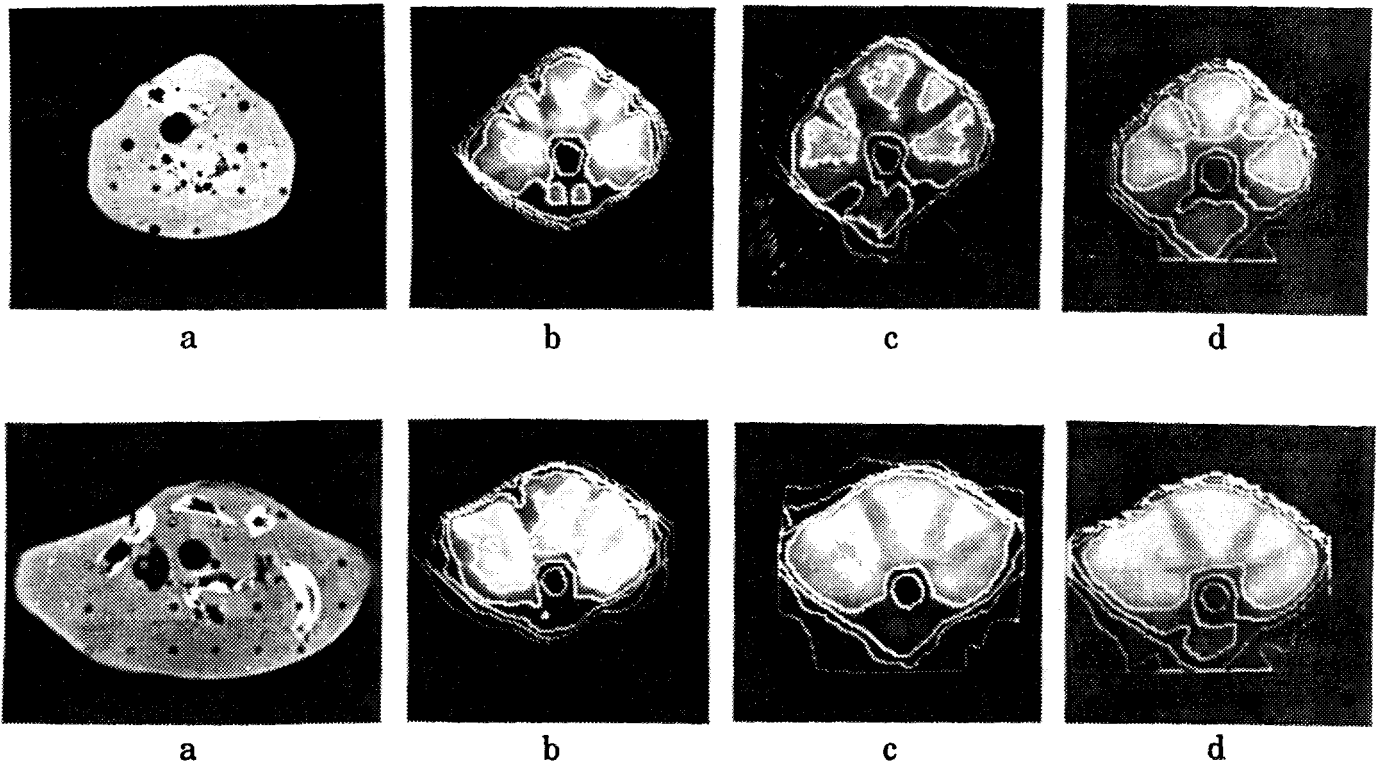


Fig. 17. Overview of the dose images obtained by three different methods
(a) CT images of Rando phantom
(b) Dose images obtained by gel dosimetry
(c) Dose images obtained by radiographic film dosimetry
(d) Dose images obtained by computer planning

4. Conclusions

The polymerization kinetics of the BANG dosimeter gel are quite complex. The linear response of the spin-spin relaxation on radiated dose relies mainly on the formation of small polymer aggregates. The whole mechanism of radical formation by ionizing radiation, diffusion of the radicals, propagation and termination reactions remains a source of further investigation.

For canonical beams, the gel dosimetry by a BANG dosimeter gel corresponds very well with the measurements using an ionization chamber or a diamond detector.

However, special attention must be paid to the gel temperature during the acquisition of the T2 weighted images, as the T2 value in the BANG dosimeter gel is strongly dependent on temperature.

For humanoid configurations, the correlation of R2-values and radiation dose are obtained using TLD's or radiographic films inserted in a humanoid phantom, such as the Rando phantom. The dose images have been compared with the dose distributions calculated by the GRATIS software.

5. References

1. De Deene, Y., De Wagter, C., "Radiation Dosimetry by use of Magnetic Resonance Imaging (MRI): Preliminary Results", Book of abstracts: 10 th Annual Symposium of the Belgian Association of Hospital Physicists, (1994).
2. Maryanski, M.J., Schulz, R.J., Ibbott, G.S, Gatenby, J.C., Xie, J., Horton, D., Gore, J.C., "Magnetic Resonance Imaging of Radiation Dose Distributions using a Polymer-gel Dosimeter", *Phys. Med. Biol.* **39**, 1437-1455 (1994).
3. Kulicke, W.M., Nottelmann, H., "Structure and Swelling of some Synthetic, Semisynthetic, and Biopolymer Hydrogels", *Polymers in Aqueous Media*, 15-44, (1989).
4. Sanofi Bio-Industries, "Structure", Technical brochure: Gelatine, 6-7, (1995).
5. W.H. Press, B.P. Flannery, "Levenberg-Marquardt Method", *Numerical Recipes in C*, 542-547, (1995).
6. Simpson, J.H., Carr, H.Y., "Diffusion and Nuclear Spin Relaxation in Water", *The Physical Review*, Vol. 111 (5), 1201-1202, (1958).



BE9700032

Limits of dose escalation in lung cancer : a dose-volume histogram analysis comparing coplanar and non-coplanar techniques

Derycke, S., Van Duyse, B., Schelfhout, J., and De Neve, W.

Department of Radiotherapy, Nuclear Medicine and Experimental Cancerology, University Hospital, Gent, BELGIUM.

INTRODUCTION

At present radiotherapy is undergoing a revival. Better understanding of normal tissue and tumor radiobiology and the large scale implementation of computer technology have lead to improved radiotherapy techniques and an increase in demand for radiotherapy.

However, in non-small cell lung cancer (nslc) the potential for improved radiotherapy is ill defined.

Anno 1995, the role of any non-surgical treatment is controversial in nslc. Whether improved radiotherapy could increase local control and survival, remains in doubt. Biased comparisons with surgery in early stage disease, insufficient radiation doses to locally advanced disease and life-treating toxicity by poor delivery techniques have discredited radiotherapy and may explain, in part, reluctance to study advanced radiotherapy in nslc.

As a result, data on conformal radiotherapy in nslc are, anno 1995, essentially absent (see further in discussion). The aim of conformal radiotherapy is to shape the dose distribution accurately to the 3-dimensional geometry of the tumor. Selectively decreasing the radiation dose to critical tissues usually allows for significant dose escalation to the tumor.

Existing radiobiological and clinical data of nslc indicate the potential for increased local control and survival by dose-escalation. The 40-70 % 5-year survival obtained by radiotherapy in selected but medically inoperable early stage nslc (*Graham et al., 1995*) and the dose-response relation with radiotherapy in RTOG-studies make nslc an exiting, although technically difficult, disease for conformal dose escalation studies.

The technical difficulties arise from a target nodes that is surrounded by highly radiosensitive critical organs, in casu spinal cord posteriorly, both lungs laterally

and the heart inferiorly. The dose that can be delivered to the target-volume is rapidly limited by these surrounding tissues.

The purpose of this study was to get an answer to the question if there was a demonstrable potential for dose escalation using a conformal, non-coplanar (3D) technique as compared to the classically used coplanar (2D) method.

METHODS AND MATERIALS

From December 1994 till October 1995 ten patients with lung cancer entered the 2D versus 3D planning study. All patients had stage IIIA or IIIB disease, according to the TNM staging system (*UICC TNM Atlas, 1992*), although patients with clinical or pathological N3 disease were excluded. All patients had histologically proven nsclc. Five patients received radiotherapy as only treatment, immediately after diagnosis. Two patients underwent radiotherapy after induction chemotherapy. One patient was referred for radical radiotherapy after pneumectomy with positive resection margins and invasion of mediastinal lymph nodes. At last, two patients were sent for irradiation of a relapse after previous surgery (1 pneumectomy and presently stage rT4N1M0 and 1 lobectomy and now stage rT2N2M0). For all patients, the aim was to design a treatment with curative intent.

All patients underwent a serial CT-scan of the chest, with a 1 cm interval between consecutive slices at the non-target area and a 0.5 cm interval at the target zone. The slice thickness was respectively 1 cm and 0.5 cm in the respective zones.

Whenever possible, intravenous Iodine contrast was administered for better interpretation of anatomical structures. Planning was performed using G.W. Sherouse's GRATIS planning system (*Sherouse et al., 1989*).

The following anatomical structures were drawn, slice by slice, partially automatically, partially by hand : skin, lungs and spinal cord. For planning, two target-volumes (TV1 and TV2) were defined. These target-volumes were drawn with the help of a diagnostic radiologist, specialized in thoracic CT-scanning. TV1 consisted of the Gross Tumor Volume (GTV). TV2 included TV1 plus all lymph node areas that had a probability of invasion of at least ten percent (*Minet et al., 19xx*). Lymph nodes that are incompatible with cure were not included in TV2. These are ATS (American Thoracic Society) regions 1, 8, 9 and 14 all left and right, as well as heterolateral regions (see figure 1). TV1 had to be irradiated upto the highest possible dose, while a dose of 56 Gy was the

aim for TV2. This definition of target-volumes was different from the ICRU guidelines, since the subjective parts defined within the Clinical Target Volume were not drawn and a PTV was not defined. However, the subjective parts in CTV and PTV were taken into consideration in the virtual simulation, where a two centimeter margin was drawn around TV1 and TV2, to correct for penumbra, microscopic extensions and motion uncertainty.

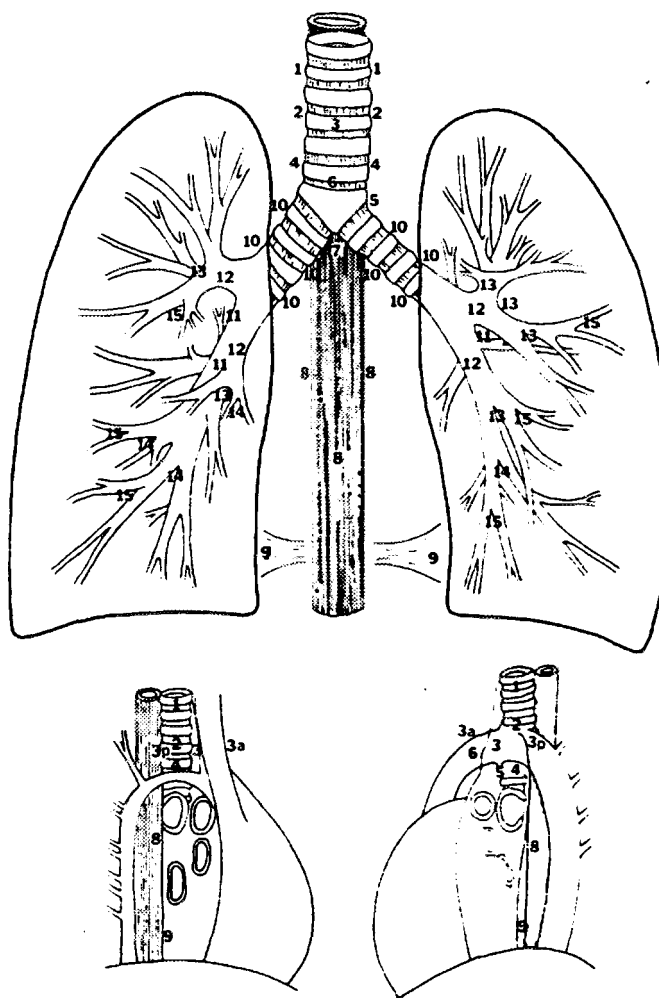


Figure 1 : Lymph node regions according to the American Thoracic Society

Using the GRATIS virtual simulator (Sherouse et al.,1991), 2D and 3D plannings were performed. Each planning was made using Beam's Eye View (BEV).

For the 2D treatment planning, only coplanar beams in a transverse plane were used. TV2 was treated by APPA fields.

If appropriate, shielding blocks to protect normal lung tissue, projected within the treatment portal, were drawn by hand, taking into account the predetermined safety margin of 2 cm. A dose of 46 Gy was delivered with this technique. For boosting TV1, two oblique parallel opposed beams, tangential to

the spinal cord were planned, again with a 2 cm margin.

For the 3D planning, three or four non-coplanar beams were used. Beam incidences with maximal angular separation were searched using the BEV, restricting the number of portals passing through the spinal cord to one out of three or two out of four. Before acceptance, all beam incidences were tested for feasibility on the treatment machine (Philips SL25 with a multileaf collimator). Conformal beam outlines were obtained by using the "Autobeam" tool, which draws automatically beam outlines conformal to the BEV projection of any chosen anatomical structure with a user defined margin around it. The aim was to deliver a dose of 56 Gy to TV2 and a dose of at least 70 Gy to TV1, if permitted by spinal cord and lung tolerance constraints (see further).

For all planning techniques 25 MV photons were used. Dose calculations were run with a grid side of 0.5 cm. No optimization tools (such as wedges) were used for 2D planning. To optimize the 3D planning, a beta version of "Superdot", a tool developed by G.W. Sherouse, was used. This optimization technique is based on a dose-gradient-vector-annihilation method (*Sherouse, in press*). Superdot computes for each set of gantry angles, selected during virtual simulation, the optimal collimator and wedge angles.

Spinal cord and lung tolerance constraints were defined as follows : Dose Volume Histograms (DVH) were calculated for spinal cord and lungs. The maximum dose at any point of the spinal cord was limited at 50 Gy and at least 50 % of the lung volume had to receive 20 Gy or less. Under these constraints, the corresponding absolute dose levels at TV1 and TV2 were defined.

RESULTS

Our results are listed in Table 1.

With the 2D technique, the dose that could be delivered to TV2 varied from 36 Gy to 46.3 Gy. The minimum doses that were achievable for TV1 were between 58.9 Gy and 67.7 Gy and maximum doses varied from 65.7 Gy to 73.3 Gy. In none of the patients, dose to the lungs was a limiting factor in 2D. The amount of lung tissue irradiated upto 20 Gy or less with this technique, varied from 53 % to 70 %.

On the other hand, with the 3D technique, dose to the lungs (with a maximum of 50 Gy to any point of the spinal cord), was a dose-limiting factor in five patients. In these patients, 52 % to 63 % of the lung volume received 20 Gy or more. For TV2, doses from 51.9 Gy to 92.7 Gy could theoretically be given. For TV1 dose

ranged from 61 Gy to 118 Gy minimally and from 62.4 Gy to 123.3 Gy maximally.

For TV2, 3D actually allowed higher doses in all patients, in comparison with 2D. In two patients however, for TV1, 2D was allowed higher doses than 3D, probably due to the large amount of lung tissue irradiated. In those five patients where lung was the limiting tissue, maximum dose to the spinal cord was between 25.8 Gy and 44.8 Gy.

The ratio between volume of TV1 and lung volume ranged from 0.014 to 0.042. Taking all patients together, there was no significant correlation between this ratio and the minimum dose that could be delivered to TV1, as well in 2D as in 3D ($p = 0.9$ and $p = 0.3$). When considering those patients where lung was the limiting tissue, in 3D there was a trend for correlation ($p = 0.06$). The small numbers of patients require a cautious interpretation of these statistics.

DISCUSSION AND CONCLUSION

In literature, few data are available on conformal radiotherapy of nsclc. Most published data, as well as our own results, show some benefit of 3D treatment planning as compared to 2D planning, but the advantage is rather marginal. Overwhelming successes are not exactly reached. In most studies, performed on small patient groups, doses upto 70 Gy could be delivered to GTV, with an acceptable normal tissue toxicity (*Armstrong et al, 1993; Graham et al., 1994*). Doses of 70 Gy unfortunately are too low to obtain local control in a large proportion of patients with stage III disease, since in these patients disease progression within the irradiated field was still the predominant first site of treatment failure (*Hazuka et al., in press*).

Langer et al. (1991) could deliver minimal tumor doses of 80 Gy or more, but had to accept a more than 20 % inhomogeneity limit. Minimal tumor dose fell to the range of 44-64 Gy when the inhomogeneity limit was tightened to 13-17 %.

Ha et al. (1993) found that the gain from computer controlled radiation therapy strongly depended on the chosen lung tolerance limit. A 10-20 Gy gain in minimum target dose could be found for some patients, but this gain was significantly reduced for a relatively small decrease in the amount of lung permitted a dose above 20 Gy.

Weil et al. (1995) described in an abstract a sagittal coplanar Y technique, from which especially patients with centrally located thoracic tumors should benefit. Dose to 30 % of the lung volume could be reduced from 30 % to 5 %. However,

dose to the spinal cord and the heart was increased and minimum target dose was not specified in this abstract.

With the currently available techniques, we are not able to perform substantial dose escalation in all patients with nscl. We will have to search for other treatment positions of the patients in order to find alternative beam entry modalities, in such way that fall off dose can be deposited in less radiosensitive organs, such as the retrocardial area or paraspinal muscles. Perhaps there's also a future in beam intensity modulation techniques. We will further explore this interesting subject.

ACKNOWLEDGEMENTS

S. Derycke is a recipient of a grant of the "Sportvereniging tegen Kanker". The "UZG project Conformal Radiotherapy" is sponsored by the "Vereniging voor Kankerbestrijding" and the "Centrum voor Gezwelziekten, University Gent".

Table 1 :

Patient - Plan	vol (cc)	TV1		TV2		Spinal cord max (Gy)	% Lung vol < 20 Gy	Lung volume (cc)	Ratio TV1/Lung
		min (Gy)	max (Gy)	vol (cc)	min (Gy)				
1 - 2 D	123	66.6	71.9	645	42.7	50.0	53	3506	0.035
1 - 3 D		61.0	62.4		51.9	44.8	46		
2 - 2 D	132	67.7	71.0	434	45.0	50.0	62	4974	0.027
2 - 3 D		74.5	79.1		63.8	41.7	46		
3 - 2 D	123	63.0	70.9	198	42.3	50.0	63	4060	0.030
3 - 3 D		65.9	67.4		55.2	50.0	54		
4 - 2 D	113	62.2	68.1	277	43.6	50.0	70	3514	0.032
4 - 3 D		98.9	101.6		78.9	50.0	73		
5 - 2 D	118	66.9	71.3	344	43.5	50.0	67	5813	0.020
5 - 3 D		118.0	123.3		92.7	50.0	53		
6 - 2 D	244	62.5	68.9	542	36.0	50.0	57	6662	0.037
6 - 3 D		65.5	68.0		52.7	41.1	48		
7 - 2 D	195	58.9	65.7	341	42.8	50.0	62	6277	0.031
7 - 3 D		111.8	118.7		84.4	50.0	53		
8 - 2 D	155	65.4	71.4	327	38.5	50.0	70	3702	0.042
8 - 3 D		61.4	64.1		48.4	42.1	47		
9 - 2 D	148	60.0	73.3	242	38.0	50.0	53	6987	0.021
9 - 3 D		80.0	97.0		80.0	50.0	57		
10 - 2 D	66	64.8	68.3	192	46.3	50.0	56	4710	0.014
10 - 3 D		76.3	82.9		57.9	25.8	37		

REFERENCES

Armstrong, J., Burman, C., Leibel, S., Fontenla, D., Kutcher, G., Zelefsky, M., and Fuks, Z. Three-dimensional conformal radiation therapy may improve the therapeutic ratio of high dose radiation therapy for lung cancer. *Int J Radiat Oncol Biol Phys* 1993; **26** : 685-689.

Graham, M., Matthews, J., Harms, W., Emami, B., and Purdy, J. 3-D radiation treatment planning study for patients with carcinoma of the lung. *Int J Radiat Oncol Biol Phys* 1994; **29** : 1105-1117.

Graham, P., Gebiski, V., and Langlands, A. Radical Radiotherapy for Early Nonsmall Cell Lung Cancer. *Int J Radiat Oncol Biol Phys* 1995; **31** : 261-265.

Ha, C., Kijewski, P., and Langer, M. Gain in target dose from using computer controlled radiation therapy (CCRT) in the treatment of non-small cell lung cancer. *Int J Radiat Oncol Biol Phys* 1993; **26** : 335-339.

Hazuka, M., Turrisi, A., Lutz, S., Martel, M., Ten Haken, R., Strawderman, M., Borema, L., and Lichter, A. Results of high-dose thoracic irradiation incorporating beam's eye view display in non-small cell lung cancer: a retrospective multivariate analysis. *Int J Radiat Oncol Biol Phys* (in press).

Langer, M., Kijewski, P., Brown, R., and Ha, C. The effect on minimum tumor dose of restricting target-dose inhomogeneity in optimized three-dimensional treatment of lung cancer. *Radiother Oncol* 1991; **21** : 245-256.

Minet, P., Constant, M., Biquet, I., and Lemaire, M. Probability of lymph node invasion in lung cancer. In : *Three-Dimensional Treatment Planning* : Ed. P. Minet : 57-68.

Sherouse, G., Thorn, J., Novins, K., Margolese-Malin, L., and Mosher C. A portable 3D radiotherapy treatment design system. *Medical Physics* 1989; **16** : 466-.

Sherouse, G., and Chaney, E. The portable virtual simulator. *Int J Radiat Oncol Biol Phys* 1991; **21** : 475-482.

UICC TNM Atlas, Third Edition, 2nd Revision, 1992.

Weil, M., Roach, M., Pickett, B., Young, B., Kuerth, S., and Phillips, T. 3D conformal radiotherapy in the sagittal plane for centrally located thoracic tumors. *Medical Dosimetry* 1995; **20** : 11-14.



SPECTROMETRIC METHODS USED IN THE CALIBRATION OF RADIODIAGNOSTIC MEASURING INSTRUMENTS

W. de Vries
NMI Van Swinden Laboratorium
Department of Temperature and Radiation
POBox 80.000, NL 3508 TA Utrecht, The Netherlands

BE9700033

Abstract

This paper describes the determination of the photon spectra of the X-ray qualities for the calibration of dosimetric instruments used in diagnostic radiology. The detector used for these measurements is a planar HPGe-detector, placed in the direct beam of the X-ray machine. To convert the measured pulse height spectrum to the actual photon spectrum corrections have to be made for fluorescent photon escape, single and multiple Compton scattering inside the detector, and detector efficiency.

From the calculated photon spectra a number of parameters of the X-ray beam are calculated. The calculated half value layers in aluminum are compared with the measured values of these parameters to validate the method of spectrum reconstruction.

Recently a set of radiation qualities for use in diagnostic radiology was established at the Nederlands Meetinstituut (NMI). The establishment of these radiation qualities required re-evaluation of the correction factors for the primary air-kerma standards. The correction factors were calculated for the NMI free-air chamber by Monte Carlo simulations for monoenergetic photons in the energy range from 10 keV to 320 keV. The actual correction factors are derived by weighting these mono-energetic correction factors with the air-kerma spectrum of the photon beam.

Moreover the spectrum measurements offer the possibility to calibrate the X-ray generator in terms of maximum high voltage. The maximum photon energy in the spectrum is used as a "standard" for calibration of kVp-meters.

Introduction

For the measurement of the quantity air kerma for X-rays, generated at potentials between 50 kV and 320 kV, the Nederlands Meetinstituut (NMI) uses a free-air chamber based on a design by Wyckoff and Attix [1]. To correct the measured signal from the free-air chamber to air-kerma several (beam quality dependent) correction factors are applied. Some correction factors can easily be determined by measurements. Other correction factors -especially those for electron loss, scatter contribution and transmission of the diaphragm and the front wall of the chamber- are very difficult to measure without modification to the primary standard. To get a better understanding of their energy dependence these correction factors were recently evaluated for the free-air chamber. The correction factors were calculated for mono-energetic photon beams using Monte Carlo simulations [2]. By weighting these energy dependent correction factors with the air kerma spectrum of the photon beam, the actual correction factors for all kinds of X-ray qualities can be calculated.

This paper describes the method used to reconstruct the photon spectrum and air kerma spectrum from the pulse height spectrum recorded in the direct beam using a semiconductor

(HPGe-)detector. Results of the spectrum measurements are presented for X-ray qualities for the calibration of dosimeters used in diagnostic radiology. Comparison of calculated and measured values of half value layers in aluminum are used to validate the method of spectrum reconstruction.

An extra parameter coming from the spectrum is the maximum photon energy in the spectrum that is used to calibrate the X-ray generator in terms of high voltage. This way the spectrometric method serves as a reference for the calibration of kVp-meters.

Materials and methods

The spectrometry system used for the measurements consists of a planar HPGe-semiconductor detector (25 mm diameter, 13 mm thickness) with a beryllium window, modular (NIM-) electronics and a PC-based multi channel analyser (2048 channels). X-rays are generated by means of a 320 kV constant potential generator and a tungsten-anode X-ray tube.

For the spectrum measurements the detector was placed in the primary X-ray beam. The beam was collimated using a tungsten diaphragm of 1, 0,5 or 0,1 mm in diameter depending on the photon

fluence rate of the beam, while the X-ray tube current was also adjusted in order to obtain a relative dead-time of the spectrometry system of 10% or less. Nevertheless a correction proved necessary for effects of pulse summing. This effect is expressed in the pulse height spectrum as a "tail" at the high-energy end of the spectrum.

The response of the detector to a pencil beam of mono-energetic photons in the energy range of 3 keV to 400 keV was calculated using the Monte Carlo code EGS4. The geometry in the Monte Carlo code contained the Be-window, the spacing between window and Ge-crystal and the crystal itself.

The calculated response of the detector to a pencil beam of 150 keV photons is shown in figure 1 .

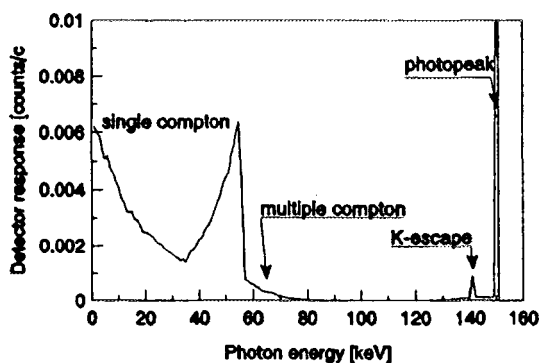


figure 1 Calculated detector response for monoenergetic 150 keV photons

As can be seen from figure 1 there are four corrections necessary to convert the measured pulse height spectrum to the actual photon spectrum:

- 1 escape of fluorescent X-rays from the detector
- 2 single compton scattering inside the detector
- 3 multiple compton scattering inside the detector
- 4 photopeak efficiency of the detector

Effects due to escape of electrons from the detector are of less importance than the mentioned effects, but are included in the corrections.

In the next paragraphs the corrections will be described individually.

Pulse summing

Pulse summing is expressed as a high energy "tail" in the pulse height spectrum. The form of the "summing-spectrum" $s(E)$ is calculated from the

original pulse height spectrum $n(E)$ by:

$$s(E) = \sum_{E_1=0}^{\frac{1}{2}E} n(E_1) \times n(E - E_1)$$

For the summing correction the summing-spectrum $s(E)$ is scaled to the high-energy tail and subtracted from the pulse height spectrum.

The correction for pulse summing is shown together with the other corrections in figure 7.

The correction in the example is small but of the same order of magnitude as the other corrections applied. The correction becomes more important at high count rates.

Escape of fluorescent X-rays

The correction for escape of fluorescent X-rays from the detector is derived from the Monte Carlo simulations. The effect of escape of fluorescent X-rays is expressed in the spectrum as a peak in the spectrum just below the photopeak. The energy of the escape peak E_{escape} is:

$$E_{escape} = E_{phot} - (E_K - E_b)$$

, where E_{phot} is the energy of the photopeak, E_K the energy of the K-X-rays of germanium and E_b the binding energy of the K-electrons.

The correction, expressed as a fraction of the photopeak area and shown in figure 2, is calculated and subtracted from the relevant part of the spectrum.

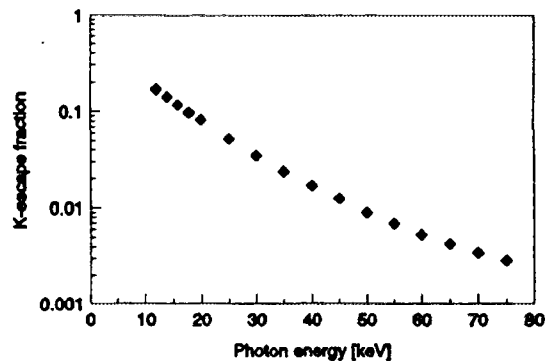


figure 2 K-escape fraction as a function of photon energy

Since the energy of fluorescent K-X-rays for Ge is very low (11 keV, representing a half value layer in Ge of 35 μm) the effect of fluorescent photon escape is larger at low photon energies because the fluorescent photons are produced closer to the surface of the detector. The correction is almost independent of the dimensions of the detector for

the same reason. The calculated escape fraction is in good agreement with the data for five different detectors from reference [3].

Single compton scattering

The correction for single compton scattering is applied through a polynomial function $h_1(E, E_0)$, derived from the Monte Carlo calculations. In order to facilitate interpolation of the Monte Carlo data the independent variable in the function was chosen to be the energy of the photopeak, E_0 , as proposed in ref. [4]:

$$h_1(E, E_0) = \sum_{i=0}^{n_1} a_i(E) \cdot E_0^i$$

The correction is applied for photon energies E between 0 keV and the energy of the compton edge E_c :

$$E_c = \frac{E_0^2}{255.5 + E_0} \text{ keV}$$

To prevent overdimensioning the degree n_1 of the polynomial function h_1 is varied from 6 to 2 as the photon energy E increases from 0 keV to 250 keV. The correction for single compton scattering is calculated, expressed as a fraction of the photopeak area, and subtracted from the relevant part of the spectrum.

Multiple compton scattering

In analogy to the correction for single compton scattering the correction for multiple compton scattering is applied through a polynomial function $h_2(E, E_0)$, derived from the Monte Carlo calculations also. h_2 has the form of a second degree polynomial function:

$$h_2(E, E_0) = \sum_{i=0}^2 b_i(E) \cdot E_0^i$$

The correction is applied, expressed as a fraction of the photopeak area, for photon energies E between the energy of the compton edge E_c and the energy of the photopeak E_0 .

To illustrate the calculation of the correction for single and multiple compton scattering the correction for mono-energetic 150 keV photons is shown in figure 3, together with the Monte Carlo simulation.

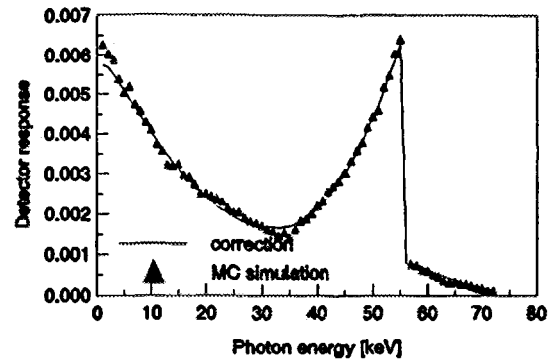


figure 3 Comparison of MC simulation and correction for compton scattering

Detector efficiency

The final correction being made is the correction for detector photopeak efficiency that also follows from the Monte Carlo simulation and that is checked by means of multiple-line low-energy photon emitting radionuclides like ^{57}Co , ^{133}Ba and ^{241}Am .

The results of both Monte Carlo simulation and radionuclide measurements are shown in figure 4. Error bars in figure 4 indicate two standard deviations.

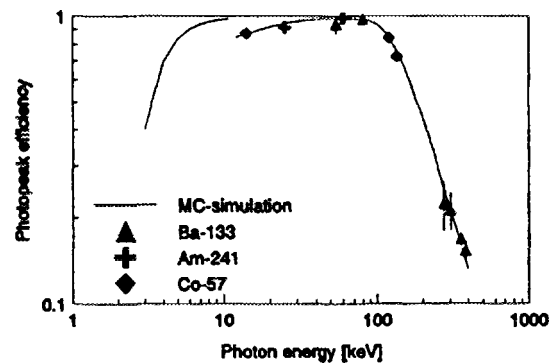


figure 4 Photopeak efficiency of the HPGe-detector as a function of photon energy

Determination of maximum photon energy

An extra parameter coming from the spectrum measurements is the maximum photon energy, used as a reference for the calibration of kVp-meters. The maximum photon energy is calculated from the pulse height spectrum by determination of the point of intersection of two straight lines (see figure 5).

The first line is a fit to the part of the spectrum just below the maximum photon energy, the second line is a fit to the part of the spectrum just above the maximum photon energy. The representation of the spectrum parts just below and just above the maximum photon energy by straight lines is restricted to small energy ranges for these spectrum parts.

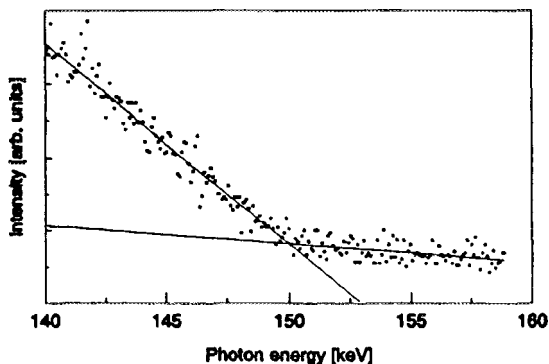


figure 5 Determination of maximum photon energy

This way the setpoint of the X-ray generator is calibrated as a function of tube current (figure 6).

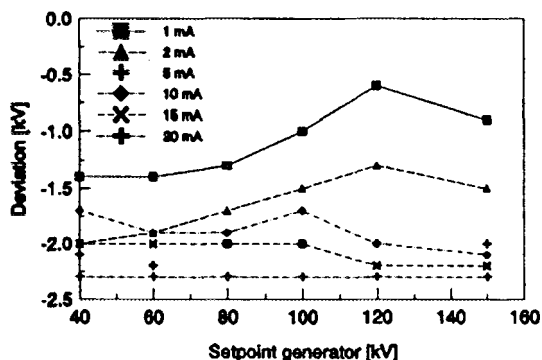


figure 6 Calibration of the setpoint of the generator

Results and conclusions

The first step in the spectrum reconstruction is the determination of maximum photon energy. After that the measured pulse height spectrum is corrected for pulse summing. Finally the corrections to the measured pulse height spectrum due to the photon interaction mechanisms inside the detector are applied starting at the channel with the maximum photon energy.

The successive corrections applied to the pulse height spectra result in the photon spectra for the X-ray qualities used for calibration of diagnostic

dose- and dose-rate meters. This set of X-ray qualities is described in the standard IEC 1267 [5]. As an example the main corrections to the pulse height spectrum are shown in figure 7 for the 150 kV quality RQR10.

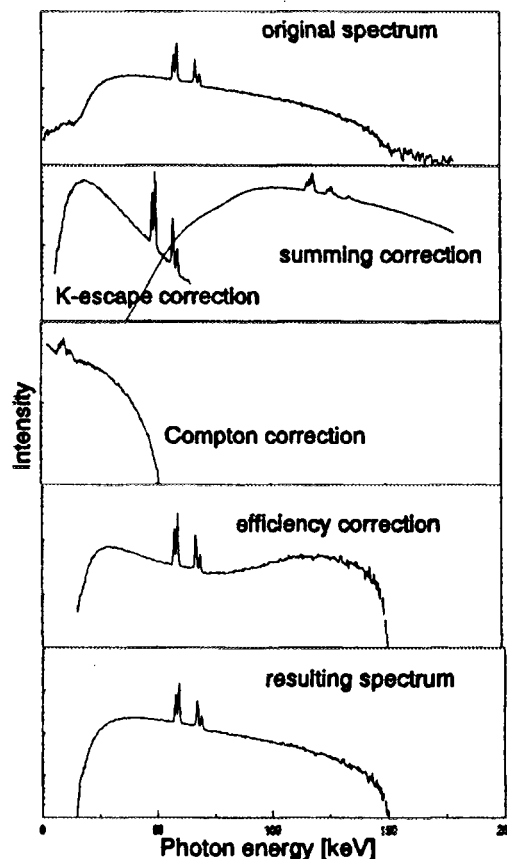


figure 7 Pulse height spectrum, corrections and resulting photon spectrum for RQR10.

The photon spectra resulting from the spectrum measurements are converted to air-kerma spectra by

$$K(E)dE = \left(\frac{\mu_{en}}{\rho} \right)_{air,E} \times E \times N(E)d(E)$$

From the air-kerma spectra the correction factors for the NMI free-air chamber are determined as described in [2].

From the air-kerma spectra the 1st and 2nd half value layer (HVL) in aluminum and in copper are determined. The values of the first HVL in aluminum are compared with the values measured using the free-air chamber. The results of the comparison of the measured and calculated HVL's are shown in table 1 for the unattenuated X-ray qualities RQR. Since the IEC-qualities are characterized by their first HVL there is no

difference between nominal and measured first HVL.

table 1 Comparison of measured and calculated HVL's

Radiation quality	IEC 1267 1 st HVL [mm Al]	Calculated 1 st HVL [mm Al]
RQR2	1,0	1,03
RQR3	1,5	1,48
RQR4	2,0	2,04
RQR5	2,5	2,43
RQR6	2,9	2,84
RQR7	3,3	3,31
RQR8	3,7	3,70
RQR9	4,5	4,43
RQR10	5,7	5,75

Calculated and measured HVL's agree well showing that the method of spectrum reconstruction is valid. For other X-ray qualities similar agreement has been found.

The calibration service at NMI for dosimeters and kVp-meters used in diagnostic radiology is in operation since August 1995. Apart from the radiation qualities RQR, the attenuated X-ray qualities RQA are offered as well as a set of mammographic X-ray qualities containing the IEC-RQN-M mammographic quality. The mammographic qualities are produced using a molybdenum-anode X-ray tube.

References

- [1] Wyckoff, H.O. and Attix, F.H., NBS Handbook 64 (1957)
- [2] Petersen, J.J., Grimbergen, T.W.M., Dijk, E. van and Aalbers, A.H.L., Correction factors for the NMI free-air chamber for 50-320 kV X-rays, Proceedings of the IXth symposium of the Belgian Association of Medical Physicists, Brussels, 1993
- [3] Seelentag, W.W. and Panzer, W., Stripping of X-ray Bremsstrahlung Spectra up to 300 kV_p on a desk type computer, Phys. Med. Biol. 24(4), 767-780 (1979)
- [4] Laitano, R.F., Toni, M.P., Pani, R. and Pellegrini, R., Energy distributions and air kerma rates of ISO and BIPM reference filtered X-radiations, ENEA report, (1990)
- [5] IEC 1267, Medical diagnostic X-ray equipment - Radiation conditions for use in the determination of characteristics (1994)

**NEXT PAGE(S)
left BLANK**



TREATMENT PLANNING IN RADIOSURGERY: PARALLEL MONTECARLO SIMULATION SOFTWARE

Scielzo G.*, Grillo Ruggieri F.**, Modesti M.^o, Felici R.^o, Surridge M.^{oo}

*Hospital Physics, **Radiation Therapy, Galliera Hospitals, Genova, Italy

^oEDS - Electronic Data System, Roma, Italy

^{oo}Parallel Application Centre, University of Southampton, UK

INTRODUCTION

Most current treatment planning applications are based on absorbed dose calculations with convolution methods or precomputed tables. Drawbacks of these systems are inaccuracy in small beams simulation, in particular when targets are small, and/or vital organs are close, for example in stereotactic radiosurgery.

Direct use of Montecarlo random sampling methods is a way to obtain precise dose absorption prediction with which inhomogeneities can easily be taken into account.

Until recently this was not regarded as feasible because of the high computational requirements.

The decreasing cost/performance ratio for computer systems allowed the development of RAPT (Radiotherapy Application on Parallel Technology), a prototype for treatment planning system making use of a parallel Montecarlo code derived from the public domain EGS4 code.

MATERIALS AND METHODS

RAPT is part of the Europort-2 project and is partially funded by the European Union ESPRIT project 8863.

Three institutions are involved in the RAPT consortium.

The Department of Hospital Physics of Galliera Hospitals is responsible for the scientific direction and the validation environment.

The Southampton based Parallel Application Centre is a parallel computer system expert and is in charge of the development of the parallel Montecarlo code.

Electronic Data System Corp. is the global project coordinator and is responsible for development of the data acquisition and visualization tools and the user interface.

The RAPT project is aimed at developing a fast and cost effective treatment planning system based on direct use of Montecarlo simulation techniques employing parallel software, embedding also 3D anatomy reconstruction with data directly acquired from medical imaging equipments and 3D visualization tools, all driven by an easy-to-use graphical interface.

The CT or MRI images are acquired directly from medical imaging equipments using ACR-NEMA standards and are stored on database which is managed by high-end PC. This is capable of storing images as well as data relative to the patient and the adopted treatment plans.

Image data are processed to obtain a full 3D rendering of the anatomical volume with a linear interpolation algorithm.

The radiation therapist specifies details on treatment plan and on region of interest acting through a user-friendly graphical interface then he starts dose absorption calculation.

The system sends the 3D rendering of patient anatomy, together with beam specification, to the parallel Montecarlo server.

After short time calculated absorbed doses in the anatomy are returned and the radiation therapist can check the absorbed doses making use of the graphical interface.

The whole system makes use of a simple Local Area Network, although it is possible to use a specialized high-speed network for the parallel Montecarlo server.

The radiation therapist can check CT scans one by one and outline areas of particular interest. At the same time it is possible to adjust the gray scale to density conversion functions, which is necessary for the anatomy reconstruction phase.

The parallel Montecarlo code is based on the public domain EGS4 code; this has been chosen because it is simple, flexible and can be expanded, because it allows the user to define most of data structures, and it is also widely referenced in radiotherapy.

The parallelization has been kept simple adopting a "task decomposition" approach and brought us to some interesting challenges as the development of special memory saving techniques, which have permitted us to use cheaper low-end workstations and the realization of a special parallel number generator.

The tuning of the RAPT code has required at first the acquisition of the Linear Accelerator data in order to allow correct beam modelling.

Setting of the code parameters has been made using water phantoms and use of complex beam configurations for stereotactic applications on PMMA and anthropomorphic phantoms.

RESULTS

The calculated results are displayed in different ways.

The absorbed doses on specified planes are visualized using a color-wash technique and at the same time it is possible to select regions of particular interest where to display the calculated absorbed doses.

The user may also select any plane on which to show the results and is not limited to the planes defined by the CT images.

The absorbed doses can be displayed over a three-dimensional reconstruction of the anatomy obtained by employing a linear interpolation algorithm.

Single processor typical run-times were obtained simulating a 6MV 2cm square beam using 10 million photons.

It can be seen that although times were extremely long (57.3 hours) on the Intel iPSC 860 (which is the development machine), more satisfactory results were obtained (9.0 hours) using the Parsytec GC Power Plus which can employ up to 128 80-MHz Power PC processors, and the DEC 3000-1000 (5.7 hours) which employs Alpha 233 MHz processors.

The portability of the code is shown by the use of different architectures.

The results obtained on parallel architectures show that speed-ups are almost linear, and that by employing 8 processors times go under the 1 hour mark with the Alpha machine. This is an high-end machine, but the simple parallelization strategy and the low memory requirements of the code make it possible to obtain acceptable run-times by employing entry-level machines, with higher number of processors but lower costs.

Further refinements in the code, as automatic stop of simulation based on statistical uncertainty of partial results should furthermore reduce average execution time.

The treatment beam arcs specified by the radiation therapist are separated for the Montecarlo simulation into a number of separate pencil beams, to which spatial distribution is given based on the measured lateral dose distribution, and the energy characteristics are given employing the typical energy spectrum of the machine.

An example of the results obtained is the stringent consistency of calculated and measured curves of relative absorbed doses employing 4 million photons for a 6MV 2cm square beam in water.

DISCUSSION AND CONCLUSIONS

The first benchmarking and tests on parallel Montecarlo simulation software conducted so far have indicated that the goal of short computing times can effectively be met even keeping the system cost affordable.

The current phase of the project is aimed to be completed by the end of 1995, and RAPT will continue under the name RAPT2 with a deployment phase, which the objective of prototype installation based on Parsytec hardware for testing in a hospital environment.

It will be possible to test the system on real patient cases and a comparison with current treatment planning systems will be possible.

REFERENCES

Nelson W.R., Hirayama H., Rogers D.W.O.: The EGS4 code system. Stanford Linear Accelerator Center Report SLAC-265 (Stanford) 9, 1985.

Bielajew A.F., Mohan R., Chui C.S.: Improved bremsstrahlung photon angular sampling in the EGS4 code system. National Research Council of Canada PIRS-0203, 1989.

Brismester J.F.: MNCP - A general Montecarlo N-Particle transport code, Version 4A, Los Alamos National Laboratory Report, LA - 12625, 1993.

**NEXT PAGE(S)
left BLANK**



BE9700042

BE9700042

Thienpont M., van Eijkeren M., Van Hecke H., Boterberg T., De Neve W.

Department of Radiotherapy and Nuclear Medicine, University Hospital, Gent, Belgium.

Abstract :

We analysed 154 applications using a pulsed dose brachytherapy technique in 138 patients over a 2 year period with emphasis on technical aspects influencing the overall treatment time.

Vaginal ovoids were used in 59 cases, plastic tubes in 52, a Fletcher - type in 18, vaginal cylinders in 14 and a perineal template in 11 cases. Pulses were given at hourly intervals with a median dose rate of 0.6 Gy per pulse (range 0.4 to 3 Gy). The number of pulses per application varied from 3 to 134 (median 32). The number of dwell positions varied from 1 to 542 over 1 to 18 catheters.

Patient related problems were few. The room was entered almost every 77 minutes. We noted 561 status codes in 147 applications. Of the 25 different codes, the most frequent one was due to the door left open when a pulse had to be given (35%) or due to constriction of the plastic catheters at the transfer tube junction (26%). However, the median total treatment time was increased by only 5 minutes.

With pulsed dose rate brachytherapy at hourly pulses we can treat our patients within the planned time despite frequent room entrance and occurrence of an appreciable number of status codes. This technique seems to fulfill its promise to replace low dose rate brachytherapy.

Introduction :

Since August 10th, 1993 we used a pulsed dose rate brachytherapy system (PDR) to replace the continuous low dose rate technique (LDR) (1). Radiobiological equivalence with LDR can be assumed when the same dose over an identical total treatment time is given at hourly pulses (2,3,4). To study the feasibility of this technique we analysed 154 applications using PDR in 138 patients.

Material and Methods :

A MicroSelectron - PDR ^{192}Ir Remote Afterloading Machine loaded with a 1 Ci stepping source was used in all applications. The sources were replaced every 3 months, recalibrated in air and compared with the activity specified by the manufacturer (Mallinckrodt Medical B.V., Petten, The Netherlands). Computer treatment planning was made with PLATO vs. 12.00.

The study group consisted of 28 male and 110 female patients. The median age was 62.9 years (range 2.3 to 86.6 years). The most frequently treated pathologies were gynecological tumours (n = 94) and soft tissue sarcomas (n = 14).

In this study we used vaginal ovoids in 59 patients, plastic tubes in 52, a Fletcher - type applicator in 18, vaginal cylinders in 14 and a perineal template in 11 cases. The median dose rate was 0.6 Gy per pulse (range 0.4 to 3 Gy). The number of pulses per application varied from 3 to 134 (median 32) with 1 to 542 dwell positions in 1 to 18 catheters.

Results:

We noticed only a few patient related problems : one accidental removal of the implant, once kinking of an endobronchial tube and one patient fell out of her bed.

We noted 561 status codes in 147 applications. In one single application we recorded a median of 2 codes (range 0 to 27). Codes due to technical machine - related problems occurred mainly during the first months of operation. Those produced a status code indicating that the source had moved out of its central position in the safe and then initiated an emergency stop action. This code occurred 134 times in 21 applications and was eventually found to be due to enhanced friction between different parts of the stepper motor.

After resolving these problems, the most frequent one of the 25 different codes was due to the door left open when a pulse had to be given (35%), due to constriction of the plastic catheters at the transfer tube junction (26%) or due to the fact that the most distal dwell position was located too close to the tip of the catheter (5%). This last code occurred in the plastic tube and needle applicators exclusively.

We registered up to 4 different status codes per application ; in 34 cases no status code occurred.

The room was entered almost every 77 min ; this ranged from every 64 min in perineal implants to every 85 min in applications involving ovoids. Although there seemed to exist some relationship with the number of status codes in these applications, it was mainly due to the need of more nursing care in perineal implant and plastic tube techniques.

The median total treatment time was increased by only 5 minutes in all applications (range from - 2h to + 15.5h). The increase was only 2 min when using ovoids and increased by 28 min when using a perineal implant ($p = 0.005$). This increase was correlated with the number of pulses, pulse time, total treatment time and frequency of room entrance.

Discussion - Conclusion :

Over a 2 year period we used a pulsed dose rate brachytherapy technique in 138 patients. A total of 154 applications were performed.

After resolving some machine related problems, most of the status codes were due to a door left open when a pulse had to be given or kinking of a plastic tube.

Most treatments were tolerated well. Since most applications were in gynecology or peri-operative, patients had to stay in bed, so remaining connected to the machine posed no extra problem. In selected cases, it was possible to disconnect the patient between pulses.

Although the room was entered several times during the applications, most of the treatments could be given within the prescribed time.

It is clearly a great advantage that the room can be entered without radiation exposure to the personnel and without prolonging the overall treatment time ; the latter is not the case with remote afterloading LDR.

This technique seems to fulfill its promise, at least technically, to replace low dose rate brachytherapy.

-
1. van Eijkeren M. Initial PDR brachytherapy experience at Ghent, Belgium. *Activity* 1994 (5) : 22-23.
 2. Brenner DJ, Hall EJ. Conditions for the equivalence of continuous to pulsed low dose rate brachytherapy. *Int J Radiat Oncol Biol Phys* 1991 ; 20 : 181-190.
 3. Fowler J, Mount M. Pulsed brachytherapy : the conditions for no significant loss of therapeutic ratio compared with traditional low dose rate brachytherapy. . *Int J Radiat Oncol Biol Phys* 1992 ; 23 : 661-669.
 4. Fowler JF. Why shorter half-times of repair lead to greater damage in pulsed brachytherapy. . *Int J Radiat Oncol Biol Phys* 1993 ; 26 : 353-356.

Three dimensional conformal radiation therapy may improve the therapeutic ratio of radiation therapy after pneumonectomy for lung cancer.

R.Trouette, N.Causse, M.El Khadri, M.Caudry, J.Ph.Maire, J.P. Houlard, L.Récaldini and H.Demeaux.

BE9700043

INTRODUCTION

Despite strong rationale for recommending radiation therapy in patients with metastatic nodal disease after pneumonectomy, there is no statistically sound evidence to demonstrate the beneficial survival effect. Moreover, pneumonitis or radiation-induced cardiac disease are sometimes life-threatening complications of radiation therapy for lung carcinoma. The incidence and degree of these injuries depend on the dose and volume of lung and heart incorporated within the radiation field.

Three dimensional conformal radiation therapy would allow to decrease the normal tissue dose while maintaining the same target dose as standard treatment. To evaluate the feasibility of lung and heart dose reduction after postpneumonectomy radiation therapy, we determined the dose distribution with 3D conformal treatment planning (3D-CTP) and conventional treatment planning (CTP).

METHODS AND MATERIALS

Ten patients with mediastinal lymph nodes metastasis were treated 4 to 6 weeks after pneumonectomy for lung cancer with 18 MV photons from a Varian Linac 2100C. Fourty Gy in 4 weeks were delivered in the supraclavicular areas and the totality of the mediastinum, followed by a 10 Gy boost with reduced portals to the volume of known metastatic involvement. Nevertheless in our study, the possibility of lung and heart dose reduction was only studied after 40 Gy.

For each patient a CT scan with 8 mm jointive slices was performed in treatment position. Then data was transfered to the Dosigray treatment planning console and automatic external contouring was undertaken by the physicist whereas semi-automatic or manual contouring of the clinical target volume and organs at risk (lung, heart, spinal cord) was done by the radiotherapist.

For conventional treatment, opposed anteroposterior beams were planned with automatical determination of all beams parameters and automatical definition of complex fields encompassing the clinical target volume with a 1 cm security margin by the Dosigray system. For 3 dimensional conformal treatment, 2 oblique ipsilateral beams were planned after automatical 3 dimensional reconstruction of the clinical target volume and the surrounding organs at risk. By offering us the possibility to turn round this 3D reconstruction, the Dosigray system help us to choose the gantry angles of rotation for each patient. Likewise automatical definition of complex fields was produced.

At the end of the previous step, complex fields were available for each patients. Then the dose was prescribed on a reference isodose encompassing the clinical target volume as usual in our department, followed by calculation of dose distribution. The differences of dose distribution for volumes with CTP and 3D-CTP were evaluated by calculating organs at risk dose-volume histograms for each treatment planning. Two relevant level of doses were choosen for each organ (20 and 40 Gy), then comparisons of dose volume histograms were performed.

RESULTS

	Mean Percentages of Volumes			
	40 Gy		20 Gy	
	CTP	3D-CTP	CTP	3D-CTP
Lung	14% (4.4-22.5)	8.8% (4.4-13.8)	20.6% (6.7-27.5)	21.9% (11.7-35.1)
Heart	43.5% (20.1-67.5)	16.3% (0.5-29.1)	62.7% (40-85.2)	63.6% (50.5-77.8)

Finally, the mean percentages of lung and heart volumes which received 40 Gy with 3D-CTP were respectively 63% (8.8/14) and 37% (16.3/43.5) of the mean percentages of lung and heart volumes which received the same dose with CTP. Nevertheless this reduction bring with it a minimal increase of lung and heart mean volumes receiving 20 Gy (respectively 6.3% and 1%).

CONCLUSION

These preliminary reslus suggest that conformal therapy may improve the therapeutic ratio by reducing risk to normal tissue



BE9700002

Reprinted from "International Radiotherapy Review", Vol. 1, based on "The Philips 1995 International Radiotherapy Users' Meeting", Ed. R.F. Mould, pp. 149 - 158, 1995.

BE9700002

Implementation of Intensity Modulation with Dynamic Multileaf Collimation

J. W. Wong, C. Yu, and D. Jaffray

Departments of Radiation Oncology and Physics,

W. Beaumont Hospital, 3601, West 13 Mile Road, Royal Oak, MI 48073-6769, USA

Introduction

The introduction of the computer-controlled multileaf collimator (MLC) marks one of the most important technological advances made recently in radiation therapy. Not only does the device efficiently replace manual blocking to shape fields, it can also be used to modulate beam intensity. Intensity modulation allows optimisation of the dose distribution in depth direction and plays an important role in the delivery of optimal treatment (Brahme 1988).

Several investigators (Convery & Rosenbloom 1992, Bortfeld *et al* 1994, Svensson *et al* 1994, Spirou & Chui 1994, Yu *et al* 1995) have demonstrated that by dynamically controlling each leaf motion while the beam is on, highly complex intensity distributions can be delivered using the MLC. The simple theory is demonstrated in the schematic of **Figure 1**.

The movement of the opposing left and right leaf pairs produces intensity profiles of opposing gradients. The effective gradient of the final intensity profile is determined by the sum of the left and right gradients. Since each leaf gradient is dependent on the velocity of leaf travel, any desirable final gradient can be delivered by moving the left and right leaves at different velocities. For example, the one-dimensional (1D) sinc function of **Figure 2 (top)** can be delivered by having the left and right leaves move according to the two positional profiles shown in **Figure 2 (centre)**.

1 The Dynamic Intensity Modulation Programme at William Beaumont Hospital

At William Beaumont Hospital, a research programme has been established to bring dynamic intensity modulation into clinical use. The study focuses on using the computer-controlled MLC available on our SL 20 accelerator. The technical and scientific collaboration with Philips plays an important part in the success of our efforts.

1.1 The Translator

A *translator* software utility has been implemented to convert any prescribed two-dimensional (2D) intensity distribution into appropriate MLC segments for delivery. The 2D distribution is first separated into a set of 1D profiles corresponding to the 1 cm leaf spacing

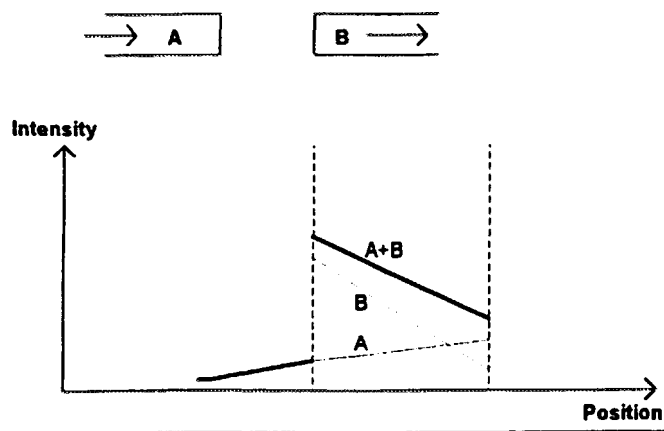


Figure 1. Schematic diagram showing that movement of the left and right leaves produced profiles of opposing gradients. The effective gradient of an intensity profile is the sum of these profiles.

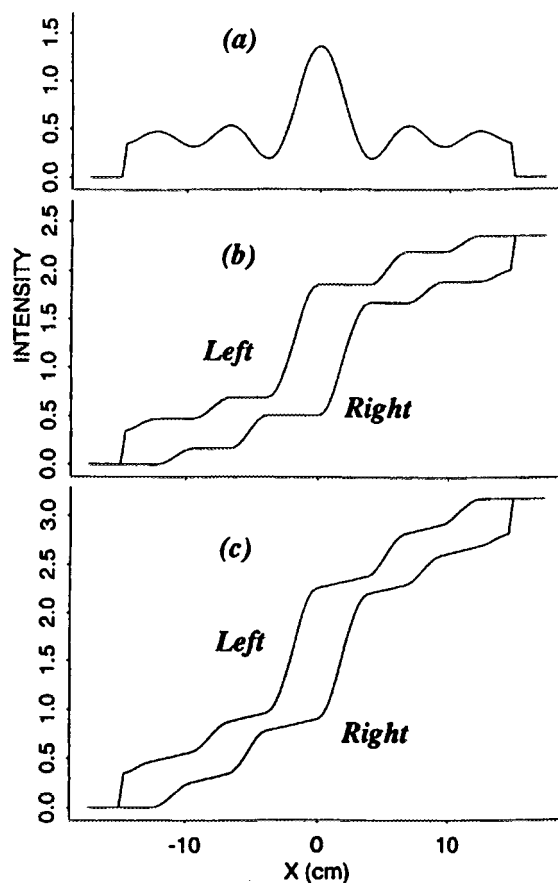


Figure 2. (top) A 1d sinc function depicting an intensity profile with multiple maxima and minima. (centre) The positional profiles of the left and right leaves which can be used to deliver the 1D sinc function. (bottom) The modified positional profiles for the left and right leaves to account for the finite speed of leaf travel.

at the isocentre. With the beam on, movement of each leaf pair is computer-controlled to deliver the assigned 1D profile. Instead of delivering a continuous profile, each 1D profile is subdivided into a sequence of left and right leaf positions at fixed dose increments. At the end of each dose increment, as measured by the machine monitor chambers, each leaf is moved as quickly as possible to the next assigned position. Thus, using this dynamic *step and shoot* scheme, a continuous 1D profile is approximated with multiple segments of linear gradients as shown in **Figure 3**.

In deriving the multiple MLC segments, the *translator* utility also needs to consider other control parameters of the machine. These include the dose rate, speed of the MLC, mechanical limits to avoid MLC collision, movement of the upper and lower collimators. For example, because of the finite speed of leaf travel, it is not possible to deliver a flat gradient by moving one leaf instantaneously from one position to another. Instead, the *translator* prescribes that both leaves move at identical speed between the two positions. The effective gradient, being the difference of the left and right gradients, is then flat.

Figure 2 (bottom) shows the modified positional profiles for the left and right leaves to deliver the sinc function of **Figure 2 (top)**. Because of the many complex machine parameters involved, there are usually several solutions for the multiple MLC segments. The important task of the *translator* is to find the optimal solution to ensure smooth delivery of dynamic intensity modulation.

1.2 Dosimetry of Dynamic Intensity Modulation

For clinical use, the dosimetry of dynamic intensity modulation has to be evaluated. Most interest has been focused on applying the technique to deliver complex intensity distributions optimised using three-dimensional (3D) inverse planning. However, intensity modulation treatment should benefit, not only advanced conformal therapy, but radiation therapy in general. A simple 1D wedge is an example of a very important beam modifier. With that

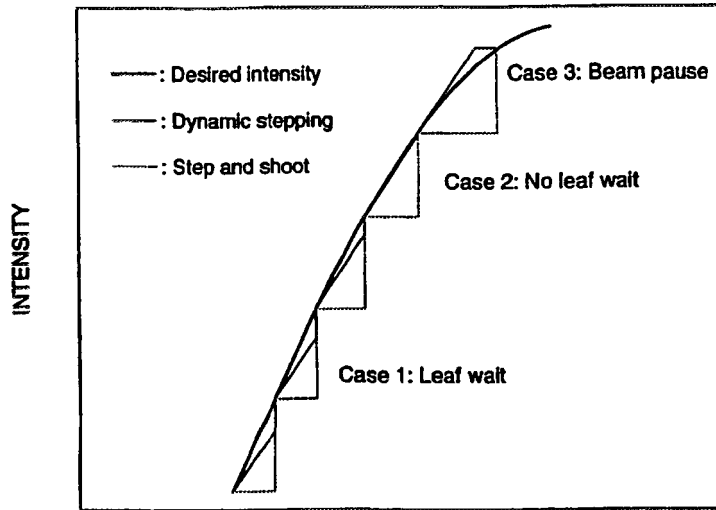


Figure 3. Approximation of a continuous 1D profile with multiple MLC segments of linear gradients using the dynamic 'step and shoot' method. Note that the beam remains on throughout the entire sequence of leaf travel.

in mind, we have adapted a systematic approach to implement dynamic intensity modulation for use in the clinic. Results from our early studies are presented qualitatively in this section. In-depth quantitative analysis of the dosimetry is on-going at our institute.

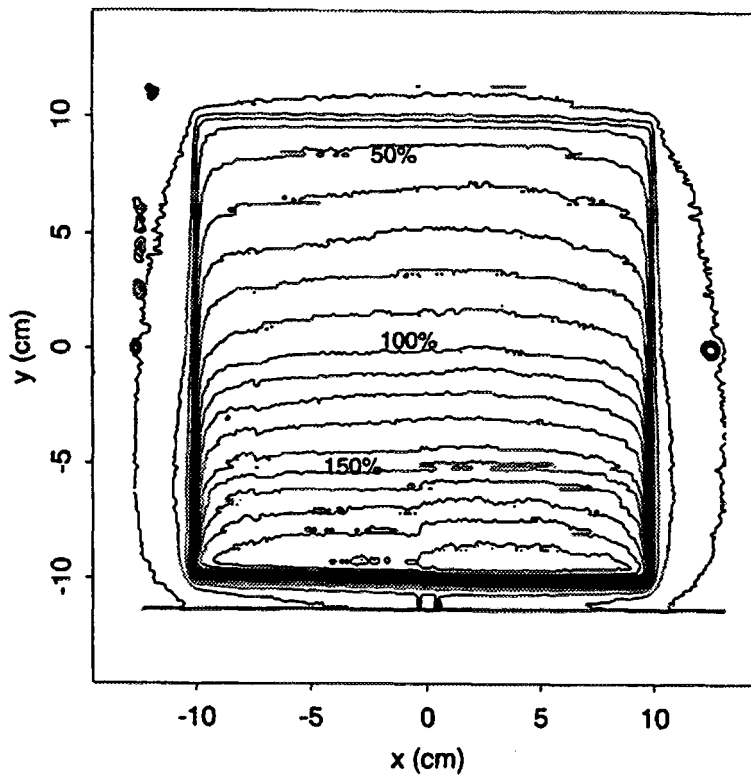
Three classes of intensity modulation using dynamic MLC are being studied. In the 1D model, a dynamic wedge distribution was delivered along the direction of travel of the leaf banks. Square and circular fields irradiated with 6 MV X-ray beams were used. Film dosimetry was acquired at a depth of 10 cm in a solid water phantom.

Figure 4 shows the beams-eye-view (BEV) dosimetry for a 60° wedge delivered with dynamic MLC. For comparison, **Figure 5** shows the results obtained with the universal wedge of the SL 20. The circular field in **Figure 5 (bottom)** was shaped using a cerrobend block. Excellent agreement was achieved between the universal and dynamic wedges for the square field. Good agreement was also achieved for the circular fields. However, field shape dependent differences in the BEV dosimetry appeared as the MLC was also used to form the circular field.

In the 2D model, the 60° dynamic wedge distribution was delivered at an arbitrary orientation to the collimator rotation. In these cases, even square fields would be challenging as each leaf pair was required to deliver a different monotonic intensity profile across the field. **Figure 6** shows the BEV results for the square and circular fields, with the 60° dynamic wedge delivered at 45° to the collimator orientation. Qualitatively, good agreement of BEV dosimetry was achieved for the rotated dynamic wedge and universal wedge. Shape dependent effects were again observed in these cases.

Finally, in the 3D model, the *in air* intensity profiles no longer have monotonic gradients. Missing tissue compensators are representative clinical examples. **Figure 7** shows the 2D intensity distribution delivered by dynamic MLC to compensate for the irregular surface of the breast. The measurement was made with film at a depth of 1 cm. The required 2D

60 degree dynamic wedge



60 degree dynamic wedge

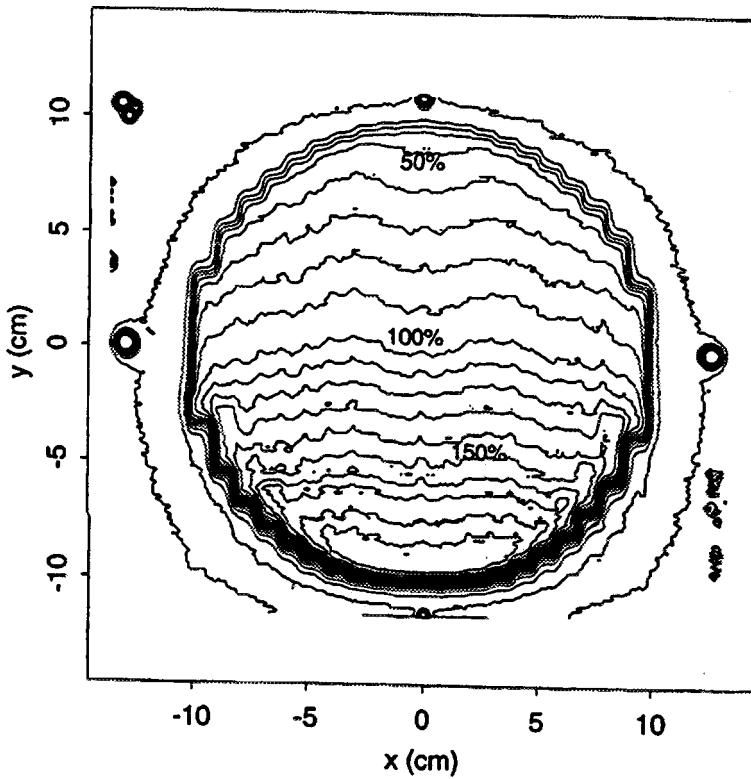


Figure 4. Beam's-eye-view film dosimetry of a 6 MV photon beam with 60° dynamic MLC wedge for (top) a square field, and (bottom) a circular field. Measurements were made at a depth of 10 cm in solid water.

60 degree universal wedge

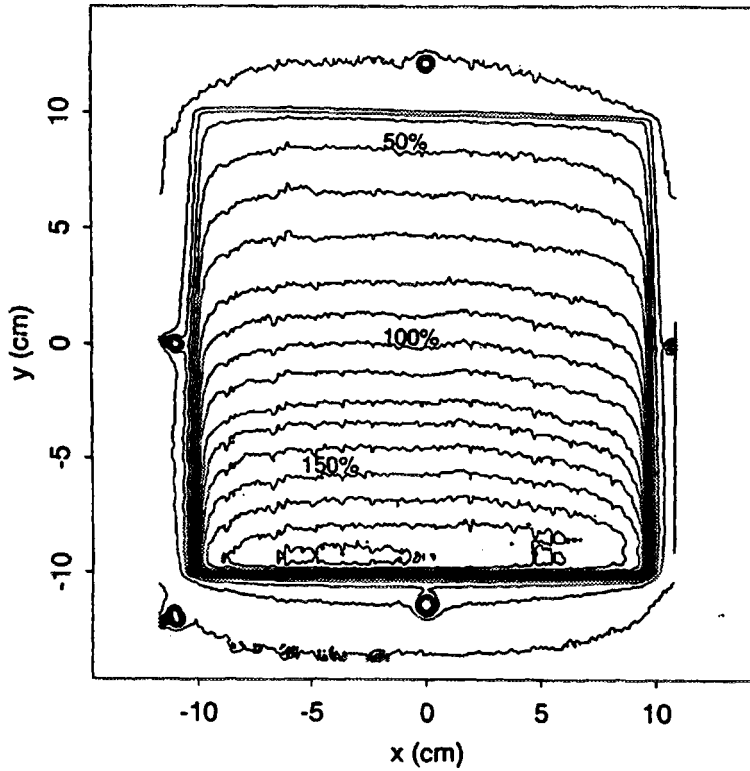
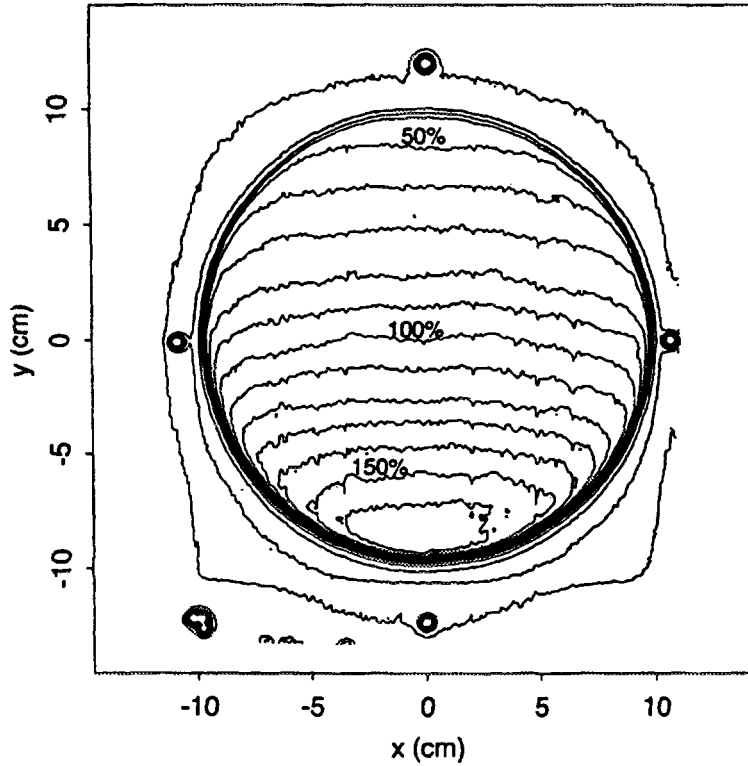


Figure 5. Beam's-eye-view film dosimetry of a 6 MV photon beam with 60° universal wedge for (top) a square field and (bottom) a circular field. Measurements were made at a depth of 10 cm in solid water.

60 degree universal wedge



60 degree dynamic wedge

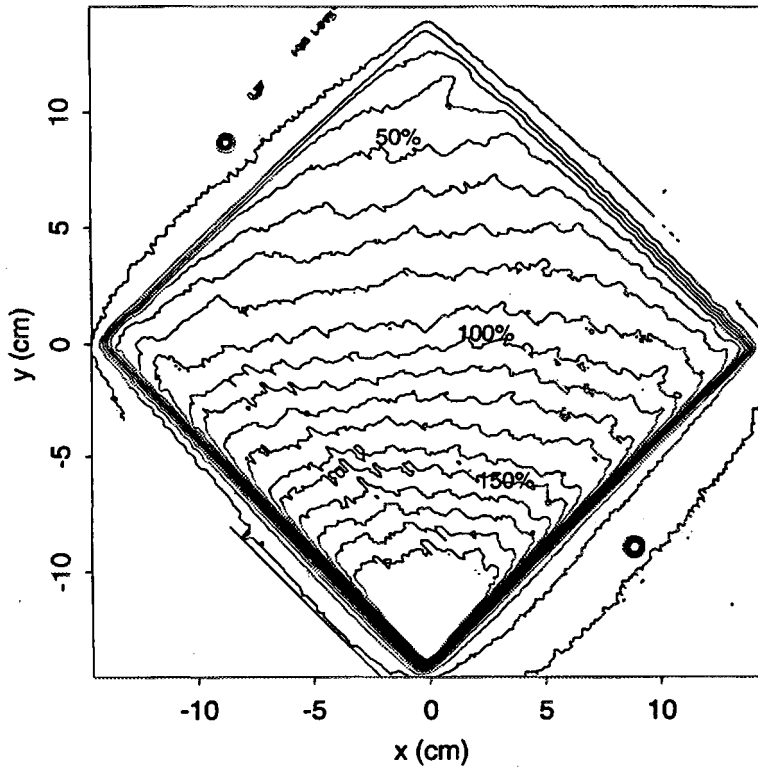
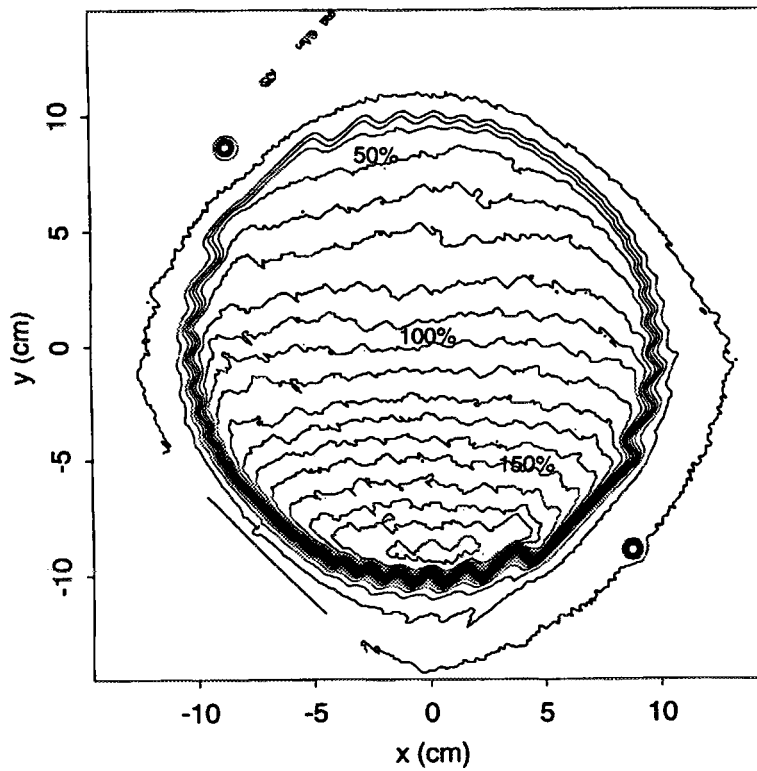


Figure 6. Beam's-eye view film dosimetry of a 6 MV photon beam with 60° dynamic MLC wedge for (top) a square field. The wedge distribution was delivered at an angle of 45° to the collimator orientation. Measurements were made at a depth of 10 cm in solid water.

60 degree dynamic wedge



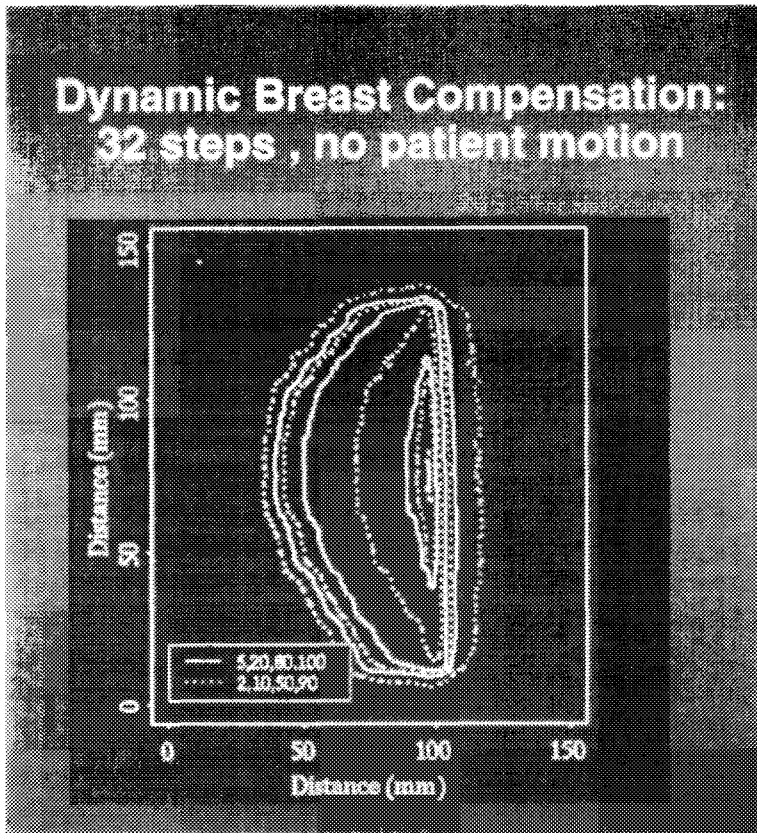


Figure 7. The *in-air* intensity distribution, measured with film, delivered by dynamic MLC to compensate for the irregular surface of the breast.

intensity data were derived from a transmission portal image (Evans *et al* 1994) and was kindly provided by Mr P.M. Evans from the Royal Marsden Hospital. The result was qualitatively correct and the smoothness of the delivered distribution was encouraging.

In the general 3D cases, multiple maxima and minima could exist in the intensity distributions as derived for conformal therapy with 3D inverse planning. As a test case, **Figure 8 (top)** shows the 2D *in air* intensity distribution representing a 2D sinc function that was prescribed for delivery by dynamic MLC. **Figure 8 (bottom)** shows the *in air* distribution delivered with 50 dynamic MLC segments as measured with film dosimetry. Again, good qualitative agreement was achieved between the prescribed and delivered distributions. There was an apparent *tilt* in the measured distribution which could be due to changes in the transmission through the MLC segments as they moved from one side of the field to another.

2 Discussion

Clearly, recent efforts demonstrate the great potential of dynamic MLC to achieve complex modulation of intensity. Results from our dosimetry studies, although presented qualitatively in these proceedings, are encouraging. Times for delivery are also reasonable. For the dynamic wedge, treatment times are usually less than those using the universal wedge. For more complex intensity distributions, treatment times are not more than twice those using physical beam modifiers. More in-depth analysis of our results is being conducted in preparation for future publication.

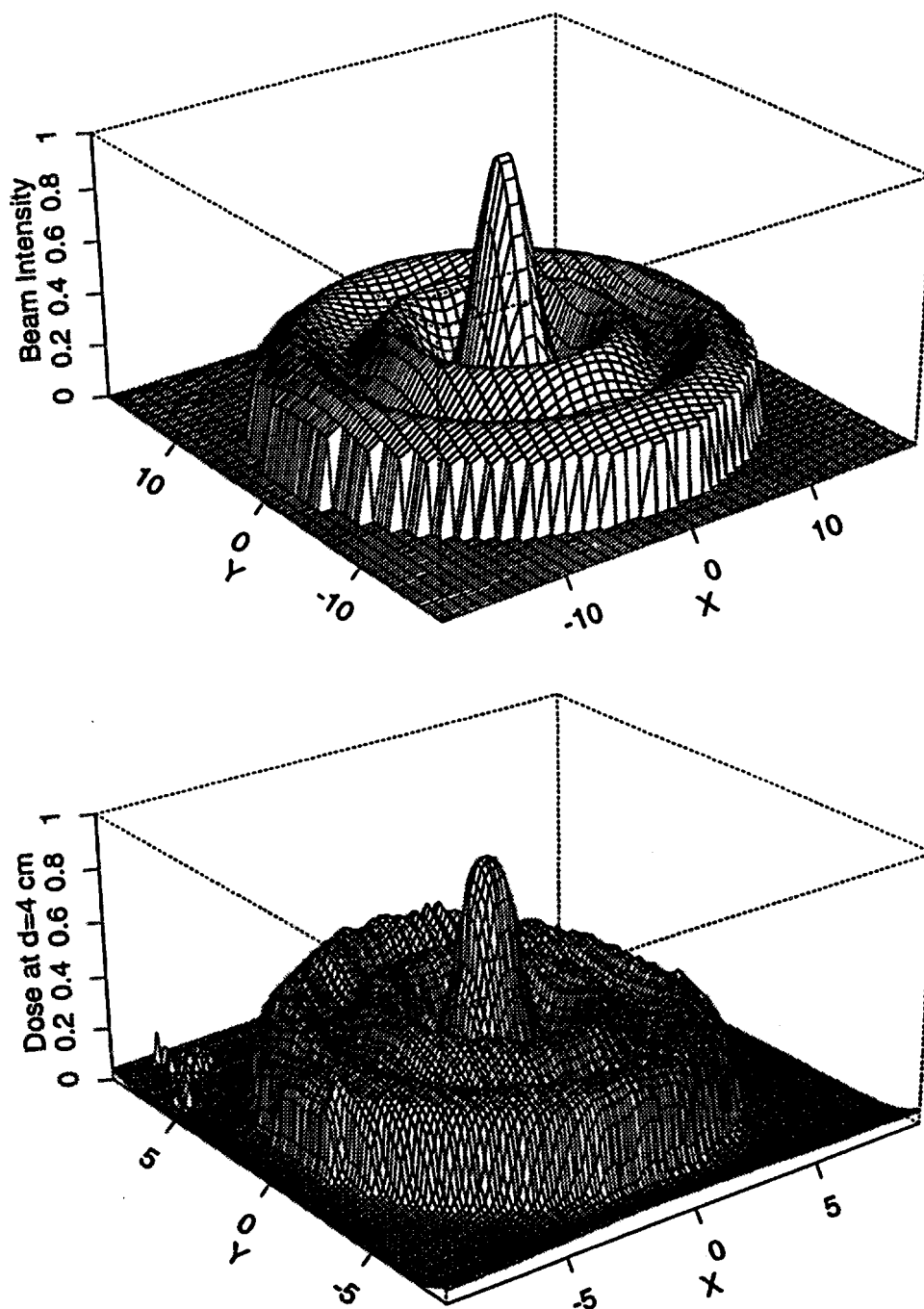


Figure 8. (top) The prescribed in-air intensity distribution depicting a 2D sinc function. (bottom) The corresponding in-air intensity distribution delivered with 50 dynamic MLC segments as measured with film.

In our 1D and 2D dynamic wedge models, comparisons with the well-established dosimetry of the universal wedge allowed us to evaluate dynamic intensity modulation in a systematic fashion. Important insights can be obtained. Issues such as dose due to radiation leakage through each MLC segment, field shape dependent effects on dose distribution, calculation of dynamic wedge factors, calculation of monitor units for each MLC segment, can be addressed. The findings can be used to further refine the *translator* utility for optimising dynamic MLC delivery. Clinically, the ability to deliver a dynamic wedge at arbitrary orientation to the collimator rotation will also enhance the use of the MLC for optimal field shaping, bypassing the need to use the universal wedge at fixed collimator orientation.

Much more work is needed before clinical implementation. Because of the dynamic nature of the delivery, complex issues such as the effects of the patient's breath motion and treatment verification must be addressed. However, judging from the rapid advances made in the past two years, it would not be far fetched to expect that some form of dynamic intensity modulation will be used clinically in the near future.

References

Bortfeld T. R., Kahler D. L., Waldron T. J. & Boyer A. L., *X-ray Field Compensation with Multileaf Collimators*. Int. J. Radiation Oncology Biology & Physics, 723-730, 1994.

Brahme A., *Optimization of Stationary & Moving Beam Radiation Therapy Techniques*. Radiotherapy & Oncology, 12, 129-140, 1988.

Convery D. J. & Rosenbloom M. E., *The Generation of Intensity-modulated Fields for Conformal Radiotherapy by Dynamic Collimation*. Physics in Medicine & Biology, 37, 1359-1374, 1992.

Evans P. M., Hansen V. N., Swindell W., Toor M., Mayles W. P. M., Neal A. J., Brown S. & Yarnold, J. R., *The Use of Portal Imaging System to Design Tissue Compensators for Radiotherapy of the Breast*. in: *Proceedings XIth International Conference on the Use of Computers in Radiation Therapy*, Manchester, 1994, Hounsell, A.R., Wilkinson, J.M., & Williams, P.C., (Eds), 118 - 119, ICCR: Manchester, 1994.

Spirou S. & Chui C. S., *Generation of Arbitrary Intensity Profiles by Dynamic Jaws or Multileaf Collimators*. Medical Physics, 21, 1031-1042, 1994.

Svennsson R., Kallman P. & Brahme A., *An Analytic Solution for the Dynamic Control of Multileaf Collimators*. Physics in Medicine & Biology, 39, 37-61, 1994.

Yu, C. X., Symons M. J., Du M. N., Martinez A. A. & Wong J. W., *A Method for Implementing Dynamic Photon Beam Intensity Modulation Using Independent Jaws & Multileaf Collimator*. Physics in Medicine & Biology, 40, 769-787, 1995.



**CONFORMAL RADIOTHERAPY
USING MULTILEAF COLLIMATION
QUALITY ASSURANCE AND IN VIVO DOSIMETRY**

BE9700017

**P. ALETTI
Centre A. Vautrin - NANCY - FRANCE**

I - INTRODUCTION

The goal of radiation therapy has been always to cure cancer locally without excessive side effects on toxicity. Several techniques are used to deliver a high dose with high precision in the target volume :

- brachytherapy delivering a high dose in the tumor with good protection of surrounding normal tissues,
- intraoperative and stereotactic radiotherapy.

The evolution of the external beam radiotherapy has continuously resulted in better local control and reduced toxicity and improved survival.

The newest of these advancements is called three dimensional conformal therapy (3D CRT). Then, innovative technology has improved the understanding of the spatial relationship between the tumor and normal tissues, the definition of the target volume and the distribution of the irradiation dose in the treated volume. These developments increase the ability to conform irradiation portals to the volume of interest. Multileaf collimators facilitate application of complex treatment planning to the daily treatment of patients with conformal irradiation technique.

The figure 1 shows the basic components and function, which has been identified in the whole process of the 3D conformal therapy.

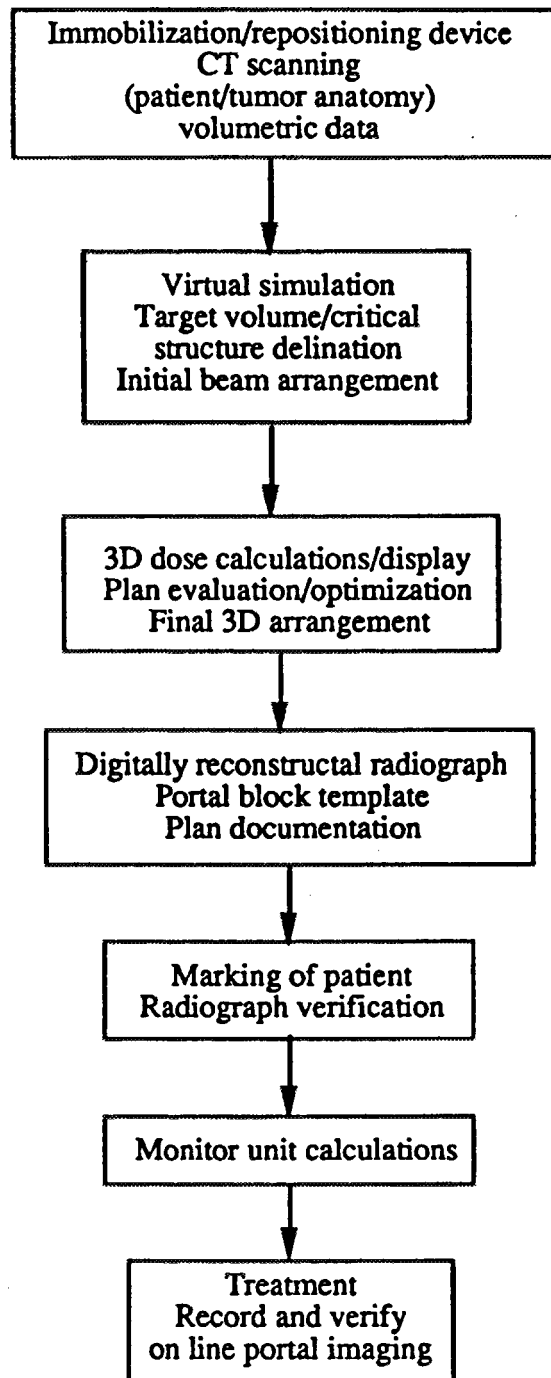


Figure 1 : Elements of an integrated 3D planning conformal therapy from Perez - St Louis (USA) Radiotherapy and Oncology, 36 (1995); 32-43.

The concept of the 3D conformal therapy is to deliver higher doses to selected target volumes while relatively sparing adjacent normal tissues thus improving tumor control probability without increasing treatment morbidity.

Critical requirements in conformal therapy are :

a) The patient immobilization :

The patient must be positioned and rigidly fixed in such a way that the reproductibility of this position is accurate from the CT to the simulator (if used) and to the treatment machine from the first session to the last session of the treatment.

b) The localization :

The different target volumes must be accurately delineated in three dimensional terms corresponding to the ICRU 50 definitions :

- GIV : Gross Tumor Volume
- CTV : Clinical Target Volume
- PTV : Planning Target Volume.

c) The dose delivery :

The radiation dose must be highly concentrated within a well defined volume and fall quickly outside this volume.

The ultime goal of quality assurance in external radiotherapy is to ensure that an accurate dose has been delivered in the defined volume within the scheduled time with limited dose to surrounding normal tissues. Quality assurance is the total compliance with the prescription and the strictness of its execution using all the means available.

The need for QA is universally acknowledged and there now exist general guidelines and recommendations for proper QA programs (AAPM - Task Group 40 1994 - SFPH-SFRO 1995, Kutcher and Purdy 1992,...).

II - GENERAL RECOMMENDATIONS

II.1 - Technical level

A quality assurance program includes systematic controls on :

- equipment,
- beam calibration,
- safety of the personnel

according to therapeutic prescriptions, modulated controls and recommendations loading to the different technical levels :

- level 1 : simple technique
- level 2 : sophisticated technique
- level 3 : high technical treatment.

The setting up and development of new techniques are classified in the level 3. Conformal radiation therapy is necessary classified in level 3 during the period of development and afterwards in level 2.

Technical levels 2 and 3 justify more human and technical means than level 1.

II.2 - SFPH-SFRO recommendations (personnel and equipments).

Table 1 presents the recommendations for different configurations :

- two treatment units,
- three or more treatment units.

Table 1 : Full time staff and equipment of the radiation therapy department for two treatment units and more : SFRO-SFPH recommendations

	Two treatment units (one cobalt unit or equivalent +one multi-energies accelerator)	Three treatment units or more
Number of patients treated /year	600 to 1000	≥ 1000
Technical level	1 and 2 (3*)	1, 2 and 3
Low energy X-rays	yes	yes
Simulator	yes	yes
CT scan access	yes	yes
Treatment planning system	yes	yes (3 D)
<i>Manpower resources</i>		
Radiation oncologist	1/150** to 350 patients/year (according to number at level 2 or 3)	1/150** to 250 patients/year
Radiation physicist	1/400*** to 600 patients/year	1/400 to 600 patients/year
Maintenance technician	1	2
Engineer	-	1 (if level 3)
Physics aid technologist	(according to organisation)	(according to organisation)
Radiation technologist		
- for each treatment unit	2 simultaneously (3 if special techniques)	2 simultaneously (3 if special techniques)
- simulation - dosimetry - immobilisation system (moulds, masks) - shielding blocks - low energy X-rays	at least 2 simultaneously (+ according to organisation)	at least 2 simultaneously (+ according to organisation)

* the level 3 needs an availability of the equipment and of the staff difficult to obtain with this configuration

** for the structures with level 3, research and education.

*** at least two radiation physicists.

These recommendations don't take the specificity of the 3D conformal therapy into account.

II.3 – Time and effort for 3D conformal therapy

Perez (1995) gives information on the time and effort for the various steps of 3D conformal therapy recorded by the physician, physicist and dosimetrist.

Table 2 shows the time and effort per patient using a fast and user friendly commercial CT scan (ACQSIM).

Table 2 : Time and effort for 3D treatment planning (average (min) per patient) with ACQSIM (Picker Corp.).

Procedure	Head and neck*	Thorax	Prostate
No. of patients, T&E	40	20	39
Average no. of CT slices	101	77	77
Immobilization	18	15	18
CT scanning/reconstruction/filming	44	40	37
Contouring			
Normal tissues	76	44	73
Tumor/target volumes	110	35	38
Virtual simulation/dose computation	231	82	190
Plan evaluation/optimization			
By physician	37	17	23
By physicist	28	30	28
Plan documentation preparation	114	77	125
Verification simulation	53	36	57
Treatment devices	20	16	23

T&E, time/effort analysis.

*Includes pediatric patients.

The maximum and median average patient treatment times with conformal or standard therapy are summarized in table 3.

Table 3 : Comparison of time and effort in 3D conformal irradiation and standard techniques (from Perez and al).

Anatomic site	No. of patients	Average no. of fractions	Average treatment times recorded (min)		
			Maximum	Median	SD
Conformal technique					
Brain	12	31	31.8	14	±4
Head and neck	45	34	32.9	12.5	±3.3
Thorax (lung)					
Cerrobend*	70	34	28.4	13.2	±3.6
Multileaf collimation	5	30	20	12	
Hepatobiliary/pancreas	23	28	28.9	11.8	±2
Prostate					
Cerrobend*	50	34	39	19	±4
Multileaf collimation	9	34	24	14	
Standard technique					
Brain	24	31	29.6	11.5	±4
Head and neck	80	34	35.2	12.1	±3.6
Thorax (lung)	105	34	31	11.2	±4.3
Hepatobiliary/pancreas	5	28	42	11.7	±4
Prostate					
Cerrobend*	84	34	24.3	9.8	±5

*Cerrobend tailored blocks or bilateral arc rotation.

III – QUALITY ASSURANCE OF EXTERNAL BEAM RADIATION THERAPY EQUIPMENT

For conformal therapy, the equipment subject to QA procedures includes treatment machines, simulators, CT scanners, treatment planning systems and treatment verification systems.

III.1 – Computer controlled accelerators

Protocols and recommendations have been established by national and international groups (AAPM, IAEA, ICRU, SFPH, NACP,...) for standard machines.

However computer controlled accelerators are used in 3D conformal therapy and it is more difficult to perform proper operation than it is for a standard machine particularly if there is a multileaf collimator.

Quality assurance for a computer controlled accelerator starts with acceptance testing to verify the proper and safe operation of the particular machine. All of the tests traditionally performed on non computerized accelerators are performed plus tests to verify operation of software, communications and hardware, software/user interfaces.

Periodic routine QA procedures and measurements monitor the operation of the machine and guide the user in keeping it running according to its mechanical and radiation specification.

While acceptance and periodic QA tests are often easy to perform in a "service" mode, on computer controlled machines such tests may not always accurately predict the behavior of the equipment in clinical modes of operation (Rosen, Radiation Therapy Physics, 1995).

Therefore, it is recommended that whenever possible, tests be performed in the operation modes used to treat patients. Safety interlocks especially should be tested in clinical modes.

A report on the safety issues for computer controlled accelerator has been recently published by the AAPM Task Group 35 : Medical Accelerator Safety considerations.

The new technology for the 3D conformal therapy (Fraas, 1994) treatments creates the need for much additional routine quality assurance work, both in accepting and commissioning the machine and in routine QA checks. Additional consideration include :

- table motion under computer control
- gantry / collimator / table angle motion under computer control
- multileaf collimator shaping
- computer-controlled intensity modulation devices (dynamic wedge, scanned beams, ...)
- collision avoidance technology (software and/or hardware)

The Q A program approach to each items depends on its use in the clinical practice. For example, if a key feature in all modern 3D conformal therapy approaches is the use of a computer controlled multileaf collimator. While it is possible to create any field shape with poured blocks, one cannot use treatment plans that routinely employ more than 4 to 6 fields with fixed blocks because of the time that it takes the therapist to enter the room, manually switch the blocks, and leave the room. Multileaf collimator allow to change the shape of the field in complex ways without entering the accelerator room.

Q A of this particular part of the linac consists of

1 - For the acceptance test (example : Philips MLC)

- the check leaf bank alignment (to ensure that the leaf bank is correctly centred with the respect to the head) ; (film at the isocenter exposed with a height adjustment) : figure 2
- standart irregular beam for centeringang : figure 2

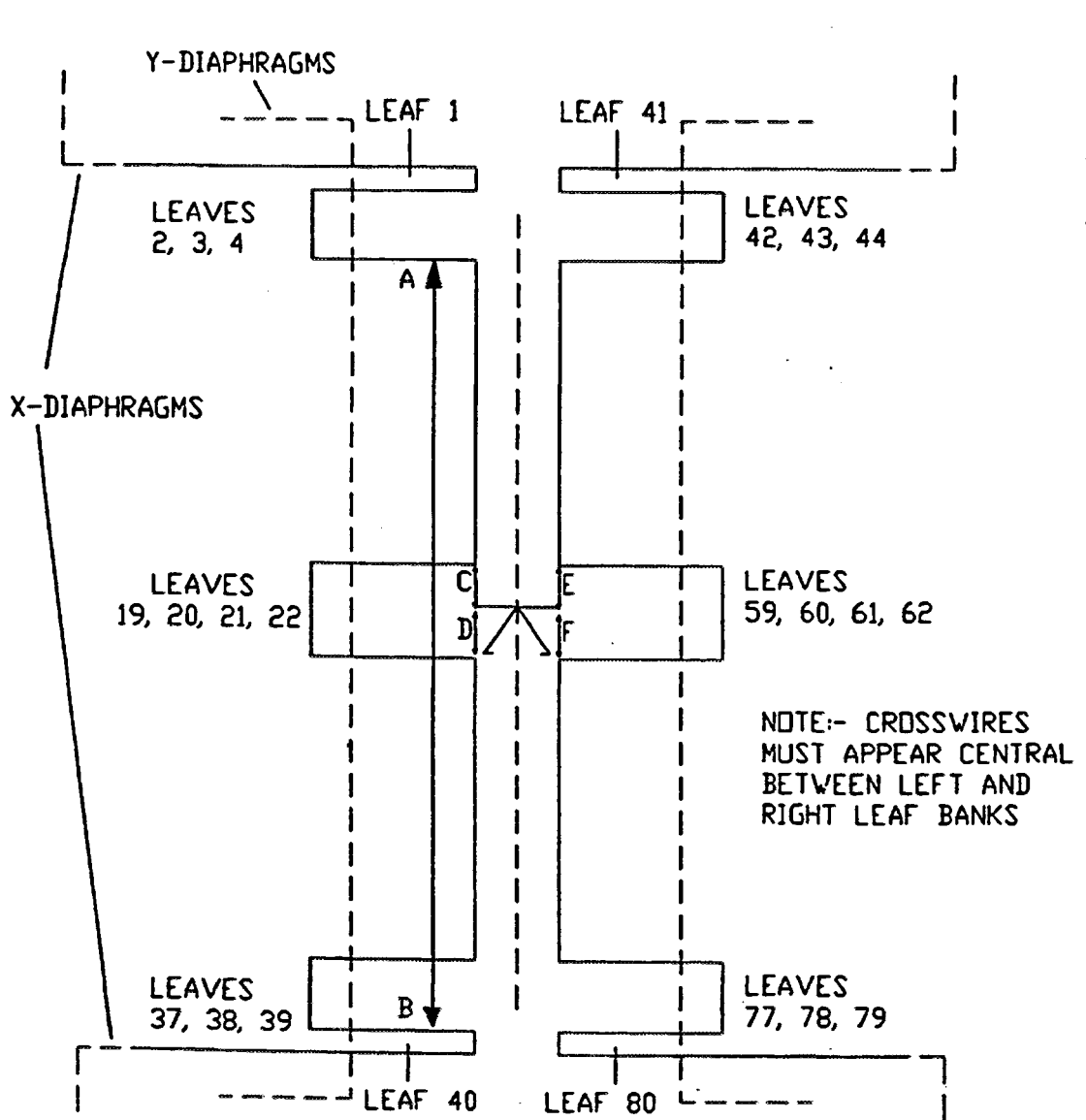


Figure 2 : Check irregular beam (Philips acceptance test)

The alignment of the leaf bank to the backup Diaphragm face (figure 3).

$$(D1 = D2 / D3 = D4 / \pm 1 \text{ mm})$$

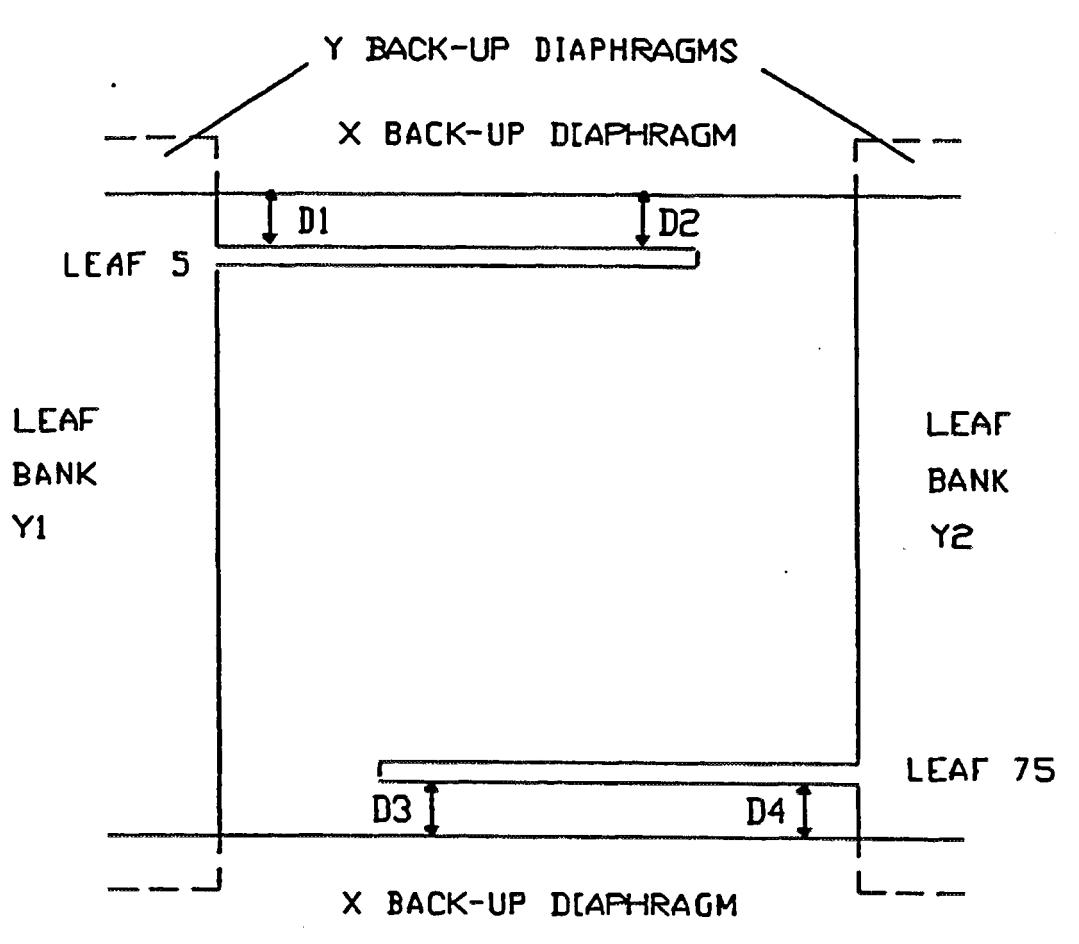


Figure 3 : Standard irregular beam for alignment of Diaphragms with leaf.

- and
- the check calibration of the leaves (agreement between the x ray field size the indicated field size)
 - the output factors (square, rectangular fields and irregular fields)
 - the transmission through the leaves with different head angles
 - the effective penumbra (80 - 20 % or 90 - 20 % as Brahm suggested) in different situations (X penumbra, Y penumbra according to the angle between the back up diaphragm and the direction of the leaves (figure 4).

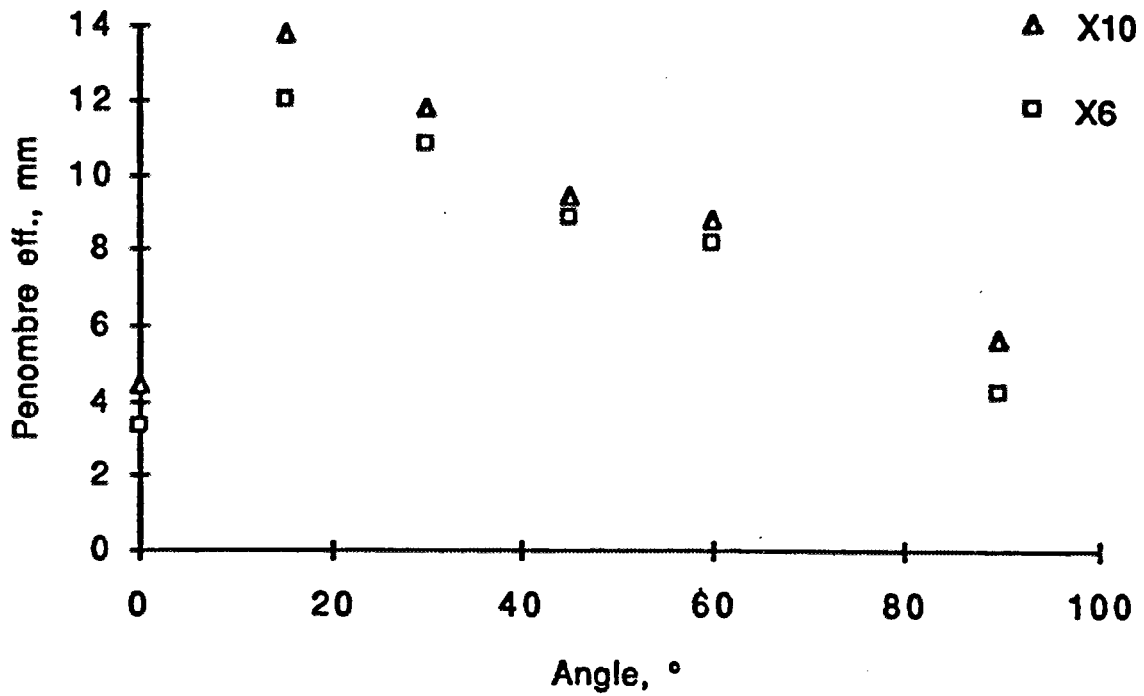
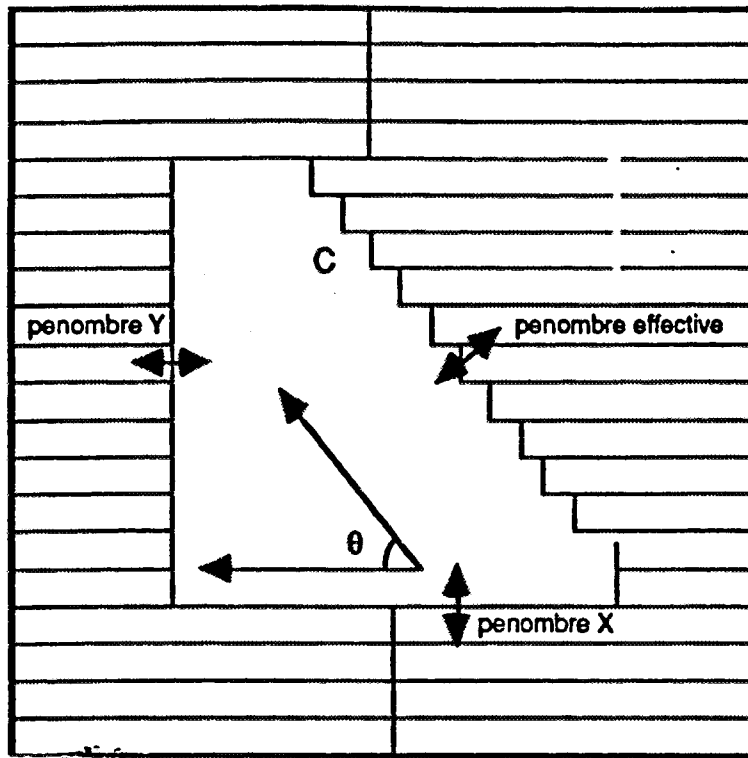


Figure 4 : Variation of the effective penumbra according to the angle between leaves and back up diaphragm

2 - For the routine Q A

- the check of the leaf alignment
- the check of the positions of the leaves
- the check calibration of the leaves

Before using MLC in clinical practice it is imperative to perform a comparative study of MLC and cerrobend blocks penumbras (table 4)

ENERGY	Depth (dmax)	MLC (mm) 0° 15° 45°	Cerrobend Blocks
6 MV 15 MV	1,5 cm 3,0 cm	3,5 4,8 7,7 4,5 5,7 8,4	3 4,5

Table 4 : Comparaison of penumbra for MLC and divergent cerrobend blocks (from Powlis - 1992)

Work on beam shaping has delineated several different methods for setting MLC edges relative to a desired beam aperture (figure 5)

- set each leaf so that the aperture touches the innermost part of the leaf
- set each leaf so the aperture touches the outermost part
- set the leaf so that the area which is overlapped by the leaf end equals the area underlapped

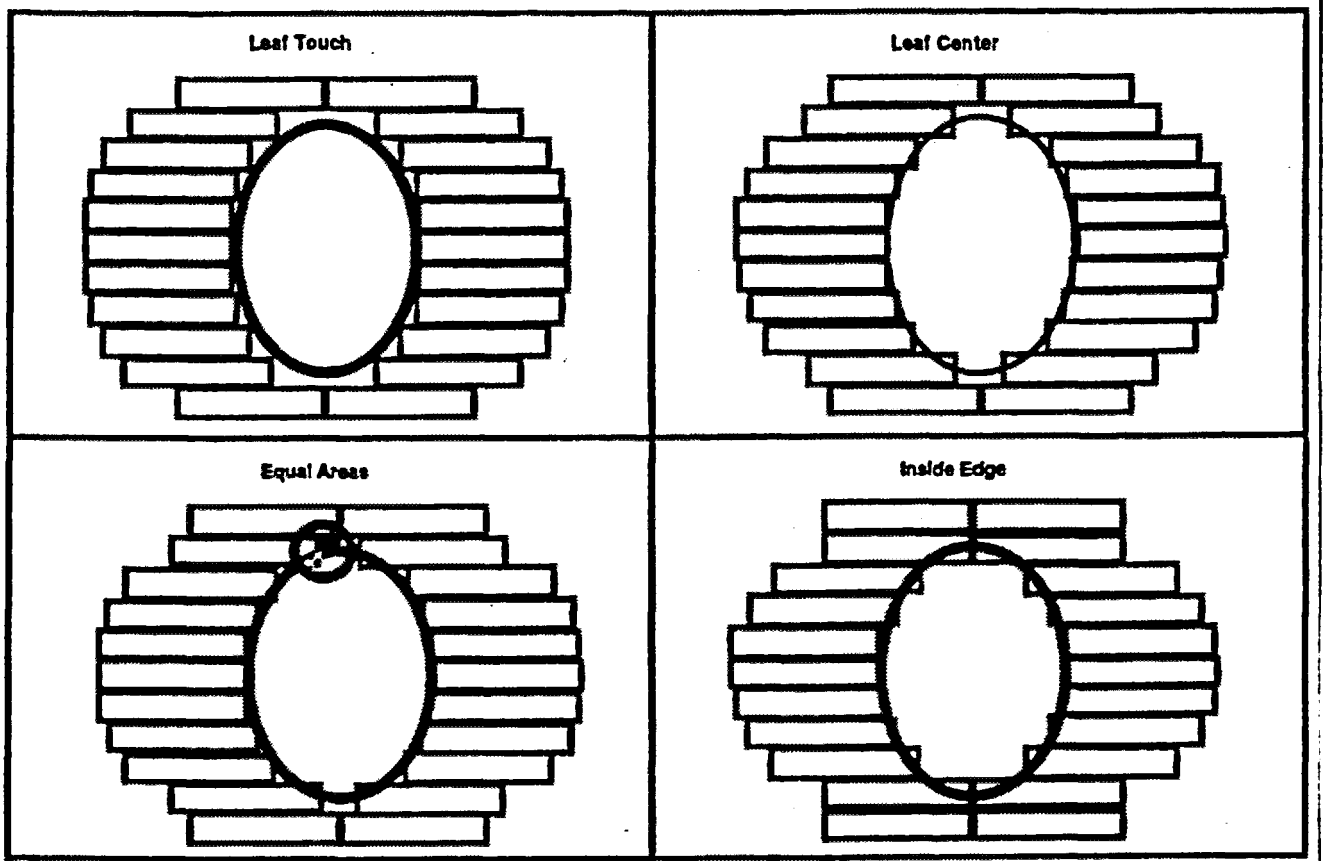


Figure 5 : Different methods for setting MLC edges relative to a desired aperture (from Fraas, 1994)

III.2 – CT scanners and simulator

The most important problem in the use of the CT Scans for treatment planning is the table top because of the difficulty to reproduce the radiation therapy couch top and then the position of the patient.

The correlation of the CT numbers with electron densities and the variation of CT numbers with position and phantom size should be determined.

The simulator should be subjected to the same mechanical checks as accelerators. In addition the simulator should be checked for image quality according to established guidelines for diagnostic radiography units.

III.3 – Treatment planning systems

3 D conformal therapy treatments rely heavily on treatment planning systems to delineate the different volumes (GTV, CTV and PTV) and to design individual patient treatments.

Treatment planning software is used to create beam outlines based on the 3 D shape of the target volume and normal tissues to select beam directions, to define the shape of the fields and the location of the leaves (if MLC is used) to compute the optimal dose to be delivered from each beam and to calculate the dose volume histogram. Geometric and dosimetric errors in the treatment planning can be adversely affect the quality of the treatment and defeat the gains from using a conformal technique.

There are four distinct areas of QA for treatment planning systems (Rosen 1994) :

- dose model evaluation
- algorithm verification
- accuracy of hardware peripherals
- database accuracy

Some tests for 3 D calculation are proposed (J. C Rosenwald - Dynarad, 1995) to evaluate the accuracy of the 3 D dose calculation taking inhomogeneities, the shape of the external surface of the patient into account.

The penumbra must be checked in different situations (particularly in case of the use of MLV)

IV – EXTERNAL BEAM TREATMENT PLANNING

In 3D conformal therapy, treatment planning is a process that begins with the localization, and continues through imaging, graphical planning plan implementation, treatment verification and finishes with the plan summary. It entails interactions between radiation physicists, radiation oncologists, radiation technologists and the engineer.

Each step of the complex treatment planning process involves a number of issues relevant to quality assurance.

IV.1 – Localization :

This step is designed to find the optimal treatment position and create the adequate immobilization device that are going to be used to retain the patient in that position. Markers are located in the patient and the immobilization system.

IV.2 – Imaging

The patient is placed in the immobilization device and is scanned in CT scan or MRI, special markers are repaired

IV.3 – Data transfer to the TPS

IV.4 – Contouring/ target volume and normal organ definition

CT is used and the geometrical accuracy should be checked.

The different volumes (GTV, CTV, PTV) must be correctly defined.

The first step involved defining margins to account for possible extracapsular extension of tumor to be added to the GTV (Gross tumor volume) : the CTV (Clinical target volume is obtained)

The second step is to defined the PTV (planning target volume) from the CTV. the planning target volume (PTV) is a geometrical concept, and it is defined to select appropriated beam sizes and beam arrangements, taking into consideration the set effect of all the possible geometrical variations, in order to ensure that the prescribed dose is absorbed in the CTV (ICRU 50 : prescribing, recording, and reporting photon beam therapy)

The concept of the PTV includes CTV and margins :

- margin due to the movements of the tissues which contain the CTV (e g with respiration), as well as movements of the patient,
- variations in size and shape of the tissues that contain the CTV (e.g different filling of the bladder)
- variations in the beam geometry characteristics (e.g beam sizes, beam directions)

The evaluation of the different margins is fundamental in conformal therapy. The figures 6 shows the impact of different margins on rectal dose (Roach, 1993) for patient treated with a localized prostate cancer.

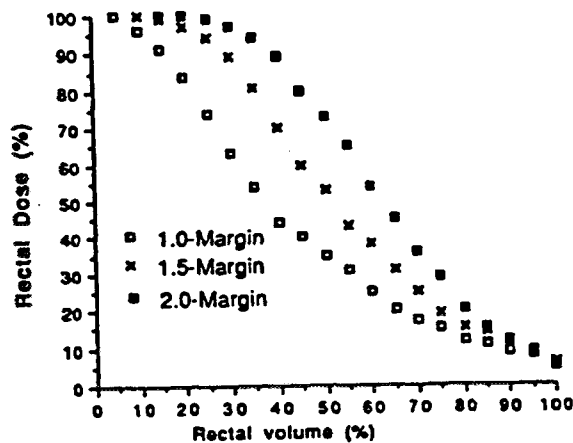


Figure 6 : Impact of margin size on rectal dose (Roach 1993)

Roach has evaluated the two types of movements (patient and prostate) and has defined the ideal margin for the different fields : table 6 and table 7

Magnitude of deviation	Patient movement	A-P prostate movement*	SI prostate movement*
Average	0.4 cm	> 0.5 cm anterior	< 0.5 cm superior
Median	0.4 cm	0.5 cm	0.0 cm
Minimum	0.0 cm	0.0 cm	0.0 cm
Maximum	1.4 cm	2.0 cm	~ 1.1 cm
≤ 0.25 cm	49 (24%) [†]	25 (50%)	37 (74%)
≤ 0.5 cm	132 (66%) [†]	30 (60%)	48 (96%)
≤ 0.75 cm	184 (92%) [†]	36 (72%)	49 (98%)
≤ 1.0 cm	196 (98%) [†]	41 (82%)	49 (98%)

Note: Based on measurements made on 22 patients, modified from Rosenthal *et al.* (27).

* Estimated from the report by Ten Haken *et al.* based on 50 patients studied with and without their rectums filled with contrast (35).

[†] *p* value < 0.001 compared to those patients treated without immobilization.

Table 6 : Patient and prostate movement assumptions (from Roach 1993)

Prostate interfaces	"ideal margins"
Posterior-lateral	0,75 - 1,75 cm
Posterior-oblique	1,5 - 2,0 cm
Superior	1,75 - 2,0 cm
Inferior	2,25 cm
Anterior lateral	2,0 cm
Anterior oblique	1,75 cm

Table 7 : ideal margins due to the organ movement (prostate)

IV.5 – Aperture design

Field apertures can be defined interactively using beam's eye view (BEV) computer displays in which volumes are projected into a plan along ray lines that emanate from the source. BEV accuracy as a function of gantry angle, collimation angle, field size and isocenter distance should be confirmed prior to use and checked as part of going QA. The location of each leaf is determined for each field according to the rule defined in the figure 5

IV.6 – Computation of dose distributions

The dose computation algorithms should be checked as part of the commissioning and on going QA of the treatment planning system

IV.7 – Plan evaluation

Dose volume histograms (DVHs) must be used to the plan review process

IV.8 – Computation of monitor units

The accuracy of the calculation of monitor units is affected by a great number of factors which must be checked regularly.

IV.9 – Quality control of daily treatment

External beam therapy includes different steps requiring correct data transfer. A good agreement between preparation of the treatment and the first patient set-up, as well as a good reproducibility for each treatment session is essential. Any error occurring during the preparation of the treatment will lead to a systematic deviation repeated at each session.

Errors occurring during daily sessions are mainly random and of human origin. They concern dose level or geometrical data of irradiation, through misadjustments of the treatment unit or inaccurate patient set-up.

a) Source of errors (SFRO-SFPH recommendations)

Agreement between the preparation of the treatment and the first patient set-up.

Before performing any adjustment of the treatment parameters on the therapy unit, it is necessary to check the critical step which is the data transfer from the treatment preparation to the treatment execution.

Assuming a correct geometry, dose calculations require knowledge of the following parameters : beam quality, energy, adjustment of the timer or the monitor, dose rate, accessories (shielding blocks, block holders, compensating filters, bolus, additional collimators, beam scattering filters).

As for geometry, the following parameters must be considered : SSD (source-skin distance) and/or STD (source-tumour-distance), beam direction (gantry, collimator, treatment couch), leaves positions.

In addition, the following parameters concerning the patient himself must be taken into account: identification, position related to immobilization and support devices.

Possible errors can be related either to data transmission, interpretation or lack of attention.

- Reproducibility of the treatment sessions :

All the parameters mentioned above can be the subject of random errors while performing the treatment sessions, in addition to systematic errors remaining after the first patient set-up.

- Checking and recommendations

Checks of the treatment conditions can be performed according to three main modalities after the validation of the treatment plan :

- initial comprehensive checking during the first set-up or before the first treatment session,
- systematic check before each session,
- check by samples.

Additional clinical and paraclinical checks must also be considered, at least weekly. Whatever the technical level, it is mandatory to use a treatment sheet as simple as possible, well designed, allowing any qualified person to check it easily, properly filled so that all the data required for the treatment are available without ambiguity.

An independent checking of both physical and medical treatment data has been considered as mandatory to ensure the coherence and the compliance of the treatment with the prescription.

- b - Recommendations for 3 D conformal therapy :

The treated volume is very closed to the clinical volume.

The following quality control systems are recommended

a) personalised immobilization system and/or a use of a system for a very strict immobilization periodically checked in time.

The use of computer system to :

- create
- transfer
- control
- verify
- the treatment parameters, allowing the random errors to be reduced, after careful check of the data introduced.

The presence of the radiation oncologist, the physicist and the technologist who performed simulation, for the first session.

- portal images at the first set-up and at a modification of the technique and at least once a week, with EPID (electronic portal imaging device) From these checks, it is important to evaluate the uncertainties of the set-up of the patient (evaluation of the margin)

- in vivo measurements are recommended for the first session (for each field, entrance dose at the level of the central axis of the field).

It is useful to perform such measurements periodically and if possible at the level of sites of interest and in other areas.

The role of in vivo dosimetry is :

- to detect errors in individual patient and then to avoid systematic errors (Noel, Aletti 1995),

- to evaluate the quality of specific treatment techniques (LEUNENS, 1990, 91, 92)

CONCLUSION

To have an effective quality assurance program for the 3D conformal therapy using multileaf +collimator it is required to assure that resources are available, including :

- personnel

- QA test tools and equipment

- assigned time for performance of QA program

- assigned time for the training of all personnels.

In addition to these recommendation it is mandatory to participat at different comparisons between radiotherapy centers :

- dose calibration

- evaluation of the accuracy of the dose calculation algorithms

- the contouring of the target volume and normal organ

- the evaluaaion of the margins

REFERENCES

ALETTI P., BEY P., Recommendations for a quality assurance programme in external radiotherapy. Physics for clinical radiotherapy. ESTRO Boohlet n° 2

EMANI B.? 3D conformal radiation therapy clinical aspects. Teaching cause. ASTRO 1994

FRASS B., Computer controlled 3D treatment delivery. Teaching cause 36 th Annual Meeting ASTRO SAN FRANCISCO

KUTCHER G., Comprehensive QA for radiation oncology : report of AAPM. Radiation therapy committee. Task Group 40

LEUNENS G., VESHAETE S., Human errors in data transfer during the preparation and delivery of irradiation treatment affecting the final result : "garbaye in", "garbaye out" Radiother. Oncol. 25 : 245-250, 1992

NOEL A.; ALETTI P.. Detection of errors in individual patients in radiotherapy by systematic in vivo dosimetry. Radiotherapy and oncology 34 (1995) 144-151

POWLIS W. Initiation of multileaf collimator conformal radiation therapy. Into radiation oncology Biol. Phys. Vol 25, pp 171-179

ROACH M. Defining treatment margins for six fields conformal irradiation of localized prostate cancer int J. Radiation oncology Biol. Phys. Vol 28 pp 267-275

ROSEN L, Quality assurance in conformal radiation therapy

List of participants, in alphabetical order (as of 01/12/95) :

- ★ Aird Edwin
Mount Vernon Hospital - Medical Physics Department
Middlesex , United Kingdom
- ★ Alaimo Rosanna
Institut Supérieur Industriel de Bruxelles
Zaventem , Belgium
- ★ Aletti Pierre
Centre Alexis Vautrin - Radiotherapy Department
Vandœuvre-Les-Nancy , France
- ★ Baas Erwin
University Hospital Leiden - Dept. Clinical Oncology
Leiden , The Netherlands
- ★ Bakker Marlies
UZ-Gent, Dept of Radiotherapy and Nuclear Medicine
Gent , Belgium
- ★ Bate M-Thérèse
UZ-Gent, Dept of Radiotherapy and Nuclear Medicine
Gent , Belgium
- ★ Bel Arjan
AZ - VUB, Department of Radiotherapy
Brussel , Belgium
- ★ Bellekens Ludwig
Sint-Vincentiusziekenhuis - Afd. Radiotherapie
Antwerpen , Belgium
- ★ Bings Iris
Klinikum St. Marien Amberg - Institut für Strahlentherapie
Amberg , Germany
- ★ Boellaard Ronald
A. van Leeuwenhoek Ziekenhuis - The Netherlands Cancer Institute
Amsterdam , The Netherlands
- ★ Boey Robby
AZ-Middelheim
Antwerpen , Belgium
- ★ Bogman Mr.
Bogman Medical Equipment
Hamme-Merchtem , Belgium
- ★ Bogman Mrs.
Bogman Medical Equipment SPRL
Hamme-Merchtem , Belgium
- ★ Bokhorst Joop
Isotopen-Technik Dr. Sauerwein
Haan , Germany
- ★ Bosmans Hilde
UZ-Gasthuisberg, KUL, Radiology and Lab. for Medical Imaging Research
Leuven , Belgium

- ★ Boterberg Tom
UZ-Gent - Kliniek voor Radiotherapie en Kerngeneeskunde
Gent , Belgium
- ★ Bouiller Annick
CHU Tivoli
La Louviere , Belgium
- ★ Brendan Vahey
Philips Medical Systems - Radiotherapy
Crawley, West Sussex , United Kingdom
- ★ Bressers Eddy
Virga Jesse Ziekenhuis - Afd. Radiotherapie
Hasselt , Belgium
- ★ Briot Edith
Institut Gustave-Roussy, Physics Department
Villejuif , France
- ★ Brown Kevin
Philips Medical Systems - Radiotherapy
Crawley, West Sussex , United Kingdom
- ★ Buelens Stefaan
MCR
Braine-L'Alleud , Belgium
- ★ Buls Nico
Industriële Hogeschool van het Gemeenschapsonderwijs Limburg
, Belgium
- ★ Causse Nicole
Hôpital Saint-André
Bordeaux , France
- ★ Coghe Marc
St-Vincentiusziekenhuis
Antwerpen , Belgium
- ★ Colle Christophe
UZ - Gent, Dept. Radiotherapy and Nuclear Medicine
Gent , Belgium
- ★ Cortoos Jeff
GE Medical Systems
Wommelgem , Belgium
- ★ Cottens Erik
Ministerie van Volksgezondheid DBIS/SPRI
Brussels , Belgium
- ★ Coutant Jean-Paul
Kliniek Maria's Voorzienigheid
Kortrijk , Belgium
- ★ Cuepers Sarah
O.L. Vrouw Ziekenhuis , Aalst - Dienst Radiotherapie
Aalst , Belgium

- ★ Daeninck Patrick
Sercolab B.V.B.A.
Mechelen , Belgium
- ★ Danciu Claudia
University of Patras - Department of Medical Physics
Patras , Greece
- ★ Davelaar Jacob
University Hospital Leiden - Dept. Clinical Oncology
Leiden , The Netherlands
- ★ David Marc
Theratronics - CIS BIO
Eysines , France
- ★ De Beukeleer Mark
AZ - VUB Oncologisch Centrum
Brussels , Belgium
- ★ De Boer Roel W.
Antoni van Leeuwenhoek Ziekenhuis - The Netherlands Cancer Institute
Amsterdam , The Netherlands
- ★ De Deene Yves
UZ-Gent, MR-department
Gent , Belgium
- ★ De Jans Jo
Heilig Hart Ziekenhuis, Radiotherapie
Roeselare , Belgium
- ★ De Luyck Inge
AZ-VUB
Brussel , Belgium
- ★ De Maeyer David
Institut Supérieur Industriel de Bruxelles
Brussels , Belgium
- ★ De Meerleer Gert
UZ - Gent, Dept. Radiotherapy and Nuclear Medicine
Gent , Belgium
- ★ De Mulder Bart
Dutoit Medical
Wommelgem , Belgium
- ★ De Nayer Bart
UZ - Gent, Dept. Radiotherapy and Nuclear Medicine
Gent , Belgium
- ★ De Neve Wilfried
UZ - Gent, Dept. Radiotherapy and Nuclear Medicine
Gent , Belgium
- ★ De Ost Bie
AZ Middelheim
Antwerpen , Belgium

- ★ De Patoul Nathalie
Evere , Belgium
- ★ De Poorter John
UZ-Gent, MR-department
Gent , Belgium
- ★ De Smet Ghislaine
UZ - Gent, Dept. Radiotherapy and Nuclear Medicine
Gent , Belgium
- ★ de Vries Willem
Nederlands Meetinstituut Van Swinden Lab.
Utrecht , The Netherlands
- ★ De Wagter Carlos
UZ - Gent, Dept. Radiotherapy and Nuclear Medicine
Gent , Belgium
- ★ Debecker Marina
St. Elizabeth Ziekenhuis
Brussel , Belgium
- ★ Decroos Pol
Reninge , Belgium
- ★ Degreef Robert
UZ - Gent, Dept. Radiotherapy and Nuclear Medicine
Gent , Belgium
- ★ Denis Jean-Marc
UCL - Neutron and Proton Therapy
Louvain-la-Neuve , Belgium
- ★ Derie Cristina
UZ-Gent, Dept. of Radiotherapy and Nuclear Medicine
Gent , Belgium
- ★ Derycke Sylvie
UZ - Gent, Dept. Radiotherapy and Nuclear Medicine
Gent , Belgium
- ★ Desmedt Inglof
MCR
Braine-L'Alleud , Belgium
- ★ Dessy Frederic
Hôpital de Jolimont
Namur , Belgium
- ★ Devriendt Gaby
Zeneca NV
Destelbergen , Belgium
- ★ Dierckx Danielle
Industriële Hogeschool van het Gemeenschapsonderwijs Limburg
, Belgium

- ★ Dirkx Maarten
Dr. Daniel den Hoed Cancer Center
Rotterdam , The Netherlands
- ★ Dwarswaard Marjan
A. van Leeuwenhoek Ziekenhuis - The Netherlands Cancer Institute
Amsterdam , The Netherlands
- ★ Essers Marion
The Netherlands Cancer Institute - A. van Leeuwenhoek huis
Amsterdam , The Netherlands
- ★ Fortan Ludwig
UZ - Gent, Dept. Radiotherapy and Nuclear Medicine
Gent , Belgium
- ★ Gill Carole
Ministerie van Volksgezondheid DBIS/SPRI
Brussels , Belgium
- ★ Goffart Pascal
Virga Jesse Ziekenhuis - Afd. Radiotherapie
Hasselt , Belgium
- ★ Götz Uwe
St. Vincenz Hospital - Institut Für Strahlentherapie
Limburg , Germany
- ★ Graindor Valérie
Institut Supérieur Industriel de Bruxelles
Brussels , Belgium
- ★ Greffe Jean-Louis
UCL - Dept. Radiotherapy
Marcinelle , Belgium
- ★ Grillo Ruggieri Fillipo
Galliera Hospitals - Radiation Therapy
Genova , Italy
- ★ Haedinger Ulrich
Universitaet Wuerzburg
Wuerzburg , Germany
- ★ Haest Karen
Grobbendonk , Belgium
- ★ Hamal Michel
Centre d'Oncologie et de Radiothérapie de Chaumont le Bois
Chaumont , France
- ★ Hamers Ronald
CURAD
Wijk bij Duurstede , The Netherlands
- ★ Hermans Jan
AZ St Jan van het OCMW
Brugge , Belgium

- ★ Huyghe Chris
AZ St Jan Brugge
Brugge , Belgium
- ★ Huys John
UZ - Gent, Dept. Radiotherapy and Nuclear Medicine
Gent , Belgium
- ★ Infantino Silvana
Biomed Engineering
Namur , Belgium
- ★ Janssens Herwig
Hogeschool Limburg
Berchem , Belgium
- ★ Jarbinet Valerie
Clinique Louis Caty
Baudour , Belgium
- ★ Julia Frederic
Institut Gustave Roussy
Villejuif , France
- ★ Kiricuta Christian
University of Würzburg, Dept. of Radiation Oncology
Würzburg , Germany
- ★ Knöös Tommy
University Hospital Lund, Dept. Radiation Physics and Oncology
Lund , Sweden
- ★ Koken Phil
A. van Leeuwenhoek Ziekenhuis - The Netherlands Cancer Institute
Amsterdam , The Netherlands
- ★ Kroes Guus
A. van Leeuwenhoek huis - The Netherlands Cancer Institute
Amsterdam , The Netherlands
- ★ Lafay Frédéric
Centre Léon Bérard
Lyon , France
- ★ Linthout Nadine
AZ - VUB, Department of Radiotherapy
Lokeren , Belgium
- ★ Loncol Thierry
Cliniques Universitaires St-LUC Radiotherapy Dept.
Bruxelles , Belgium
- ★ MacLeod Aileen
Western General Hospital - Clinical Oncology, Physics
Edinburgh , United Kingdom
- ★ Mareel Mark
UZ - Gent, Dept. Radiotherapy and Nuclear Medicine
Gent , Belgium

- ★ Matthys Tim
UZ - Gent, Dept. Radiotherapy and Nuclear Medicine
Gent , Belgium
- ★ Maurel Patricia
Centre de Radiothérapie - Arras
Arras , France
- ★ Menninga M.H.
EG & G, Ortec
Breda , The Netherlands
- ★ Mersseman Bart
UZ - Gent, Dept. Radiotherapy and Nuclear Medicine
Gent , Belgium
- ★ Mertens Nadine
St. Norbertus Ziekenhuis - Duffel
Duffel , Belgium
- ★ Messens Eric
AZ Middelheim
Antwerpen , Belgium
- ★ Mestrom Lau
Arnhems Radiotherapeutisch Instituut
Arnhem , The Netherlands
- ★ Minken André
A. van Leeuwenhoek Ziekenhuis - The Netherlands Cancer Institute
Amsterdam , The Netherlands
- ★ Moelans Michelle
Industriële Hogeschool van het Gemeenschapsonderwijs Limburg
, Belgium
- ★ Møller Søren
Sercolab B.V.B.A.
Mechelen , Belgium
- ★ Monsieurs Myriam
RUG - Student Biomedical and Clinical Engineering
Gent , Belgium
- ★ Nissen Xavier
Chartex - Cerro Metal Products
Sint-Genesius-Rode , Belgium
- ★ Niven Andy
Philips Medical Systems - Radiotherapy
Crawley, West Sussex , United Kingdom
- ★ Oozeer Rashid
Clinique Ste Catherine
Avignon , France
- ★ Overgaauw Ruud
MCR
Braine-L'Alleud , Belgium

- ★ Palmans Hugo
University of Gent, Department of Biomedical Physics
Gent , Belgium
- ★ Peynsaert Jan
UZ - Gent, MR Department
Gent , Belgium
- ★ Piessens Marleen
O.L. Vrouw Ziekenhuis , Aalst - Dienst Radiotherapie
Aalst , Belgium
- ★ Pijpelink Jaap
Nucletron Research
Veenendaal , The Netherlands
- ★ Pilette Pierre
Hôpital Civil de Charleroi, Centre Commun de Radiothérapie
Charleroi , Belgium
- ★ Pinchbeck Sarah
Philips Medical Systems - Radiotherapy
Crawley, West Sussex , United Kingdom
- ★ Piron Auguste
Université Libre de Bruxelles
Bruxelles , Belgium
- ★ Polak Andrezj
Landré - Intechmij, Div. Landré & Glinderman
Aartselaar , Belgium
- ★ Proimos Basil S.
University of Patras - Department of Medical Physics
Patras , Greece
- ★ Rasch Coen R.N.
A. van Leeuwenhoek Ziekenhuis - Netherlands Cancer Institute,
Amsterdam , The Netherlands
- ★ Rebigan F.
Institute of Atomic Physics
Bucharest , Romania
- ★ Rijnders Alex
UZ Leuven
Leuven , Belgium
- ★ Rijsdijk F.
Alphatron Electronic Parts bv
Rotterdam , The Netherlands
- ★ Rotty Michel
Canberra Packard Benelux
Zellik , Belgium
- ★ Sabatier Jacques
CHU Sart Tilman - Radiotherapie
Liège , Belgium

- ★ **Scarlat F.**
Institute of Atomic Physics
Bucharest , Romania
- ★ **Schaeken Bob**
AZ-Middelheim, Department of Radiotherapy
Antwerpen , Belgium
- ★ **Schelfhout Johan**
UZ - Gent, Dept. Radiotherapy and Nuclear Medicine
Gent , Belgium
- ★ **Schipper Jan**
Arnhems Radiotherapeutisch Instituut
Arnhem , The Netherlands
- ★ **Scielzo Guiseppa**
Galliera Hospitals - Hospital Physics
Genova , Italy
- ★ **Segers Bart**
Industriële Hogeschool van het Gemeenschapsonderwijs Limburg
, Belgium
- ★ **Simon Stephane**
Institut Jules Bordet - Labo de Physique
Bruxelles , Belgium
- ★ **Spatz Huguette**
UZ - Gent, Dept. Radiotherapy and Nuclear Medicine
Gent , Belgium
- ★ **Speleers Jacques**
Philips Professional Systems n.v.
Brussel , Belgium
- ★ **Storme Guy**
AZ-VUB - Oncologisch Centrum
Brussel , Belgium
- ★ **Thienpont Muriel**
UZ - Gent, Dept. of Radiotherapy
Gent , Belgium
- ★ **Thierens Hubert**
University Gent
Gent , Belgium
- ★ **Tomsej Milan**
Louvain-la-Neuve , Belgium
- ★ **Tonscheidt Heidemarie**
Knappschafts Krankenhaus
Dortmund , Germany
- ★ **Toy Beau James W.**
University of Michigan - Exchange Student
Avignon , France

- ★ Trouette Renaud
Hôpital Saint-André, Department of Radiotherapy
Bordeaux , France
- ★ Vakaet Luk
UZ - Gent, Dept. Radiotherapy and Nuclear Medicine
Gent , Belgium
- ★ Van Aelst Ronnie
Clinique Générale St.-Jean, RHPO Radiothérapie
Bruxelles , Belgium
- ★ Van Dam Jan
U.H. Gasthuisberg
Leuven , Belgium
- ★ Van Damme Walter
Dutoit Medical
Wommelgem , Belgium
- ★ Van den Heuvel Frank
AZ-VUB, Oncologisch Centrum
Brussel , Belgium
- ★ van der Giessen Piet-Hein
Dr. Bernard Verbeeten Instituut
Tilburg , The Netherlands
- ★ van der Laarse Robert
Nucletron Research
Veenendaal , The Netherlands
- ★ van der Linden P.M.
Best Planning System B.V.
Best , The Netherlands
- ★ Van Der Plaetsen Ann
AZ - St-Vincentius
Gent , Belgium
- ★ Van Der Straeten Reynald
Institut Supérieur Industriel de Bruxelles
Asse , Belgium
- ★ Van Der Velden Koen
Student IHGL-Mol
Ranst , Belgium
- ★ van Dieren Erik B.
Dr. Daniel den Hoed Cancer Center - Dept. of Clinical Physics
Rotterdam , The Netherlands
- ★ Van Duyse Bart
UZ - Gent, Dept. Radiotherapy and Nuclear Medicine
Gent , Belgium
- ★ Van Dycke Michel
Clinique Générale St.-Jean, RHPO Radiothérapie
Bruxelles , Belgium

- ★ van Eijkeren Marc
UZ - Gent, Dept. of Radiotherapy
Gent , Belgium
- ★ Van Gheluwe Jacqueline
UZ - Gent, Dept. Radiotherapy and Nuclear Medicine
Gent , Belgium
- ★ van Herk Marcel
A. van Leeuwenhoek huis - The Netherlands Cancer Institute
Amsterdam , The Netherlands
- ★ Van Herzeele Jean-Jacques
Kodak
Koningslo-Vilvoorde , Belgium
- ★ Van Steelandt Els
AZ Middelheim - Isotopen
Antwerpen , Belgium
- ★ Van Yperzeele Isabelle
Zambon
Brussels , Belgium
- ★ Vandekerkhove Christophe
Institut Jules Bordet - Labo de Physique
Bruxelles , Belgium
- ★ Vandendriessche Jacky
Deckers - Helax
Heverlee-Leuven , Belgium
- ★ Vanneste Françoise
Cliniques Universitaires St-LUC Radiotherapy Dept.
Bruxelles , Belgium
- ★ Vanregemorter Joris
Algemeen Ziekenhuis Middelheim, Radiotherapie / Med. Phys.
Antwerpen , Belgium
- ★ Verellen Dirk
AZ - VUB Oncologisch Centrum
Brussels , Belgium
- ★ Verhaegen Frank
Rijksuniversiteit Gent
Gent , Belgium
- ★ Verhees Jacques
Nucletron
Antwerpen , Belgium
- ★ Verhenne Els
Kliniek voor Maria's Voorzienigheid
Kortrijk , Belgium
- ★ Vermeren Xavier
ULg
Namur , Belgium

- ★ Verniers Didier
H. Hartziekenhuis
Roeselare , Belgium
- ★ Verplancke Bart
Siemens S.A.
Brussel , Belgium
- ★ Verstraete Jan
UZ-Gasthuisberg
Leuven , Belgium
- ★ Verzelen Jos
Philips Professional Systems n.v.
Brussel , Belgium
- ★ Voith Christine
Städtische Kliniken Darmstadt
Darmstadt , Germany
- ★ Vynckier Stefaan
UCL - Cliniques Universitaires St-LUC
Bruxelles , Belgium
- ★ Ward Lennart
Precision Therapy Europe
Stockholm , Sweden
- ★ Wegman Pieter-Jan
Sinmed bv
Reeuwijk , The Netherlands
- ★ Weltens Caroline
UZ-Gasthuisberg - Dept. of Radiotherapy
Leuven , Belgium
- ★ Wember Rainer
Knappschafts Krankenhaus
Dortmund , Germany
- ★ Wirtz Holger
Klinikum St. Marien Amberg - Institut für Strahlentherapie
Amberg , Germany
- ★ Wittkämper Frits
A. van Leeuwenhoek Ziekenhuis - The Netherlands Cancer Institute
Amsterdam , The Netherlands
- ★ Wong John
William Beaumont Hospital - Dept. of Radiation Oncology
Royal Oak , U.S.A.
- ★ Zemzami Abdellah
Clinique du Chapitre, Centre de Radiotherapie
Maubeuge , France
- ★ Zimmer Micheline
A2J
Fontenay sous Bois , France

★ Zimmer Philip A.
A2J
Fontenay sous Bois , France